On the Control of Surface Waves in Integrated Antennas

Analysis and Design Exploiting Artificial Dielectric Layers

Ph.D. Thesis

Waqas H. Syed

On the Control of Surface Waves in Integrated Antennas

Analysis and Design Exploiting Artificial Dielectric Layers

PROEFSCHRIFT

ter verkrijging van de graad van doctor
aan de Technische Universiteit Delft,
op gezag van de Rector Magnificus Prof. ir. K. C. A. M. Luyben,
voorzitter van het College van Promoties,
in het openbaar te verdedigen op dindsdag 16 juni 2015 om 12:30 uur

door

Waqas Hassan Syed
Master of Science in Communications Engineering
RWTH Aken, Duitsland

geboren te Rawalpindi, Pakistan.

This dissertation has been approved by the:

Promotor:	Prof. Dr. A. Neto
Copromotor:	Dr. D. Cavallo

Composition of the doctoral committee:

Rector Magnificus
Prof. dr. ir. A. Neto, promotor
Dr. ir. D. Cavallo, copromotor

Independent members:

Prof. dr. ir. A. Yarovoy	Faculty Electrical Engineering, Mathematics and Computer Science, TU Delft
Prof. dr. ir. P.M. Sarro	Faculty Electrical Engineering, Mathematics and Computer Science, TU Delft
Prof. dr. ing. A. Freni	University of Florence, Italy
Dr. ir. P. de Maagt	European Space Agency, The Netherlands
Dr. ir. P. T. M. van Zeijl	Omniradar, The Netherlands
Prof. dr. ir. A.-J. van der Veen	Faculty Electrical Engineering, Mathematics and Computer Science, TU Delft (reserve member)

The work presented in this thesis has been performed at TU Delft and financed by the Dutch Technology Foundation STW, which is part of the Netherlands Organisation for Scientific Research (NWO) and partly funded by the Ministry of Economic Affairs (project number 10709). This work has also received funding from the European Research Council starting grants ERC-2011-StG Grant AAATSI 278794.

Keywords: Surface waves, artificial dielectrics, superstrates, Green's function method, planar integrated antennas, on-chip antennas, connected arrays.

ISBN 978-94-6186-482-6

Cover Design: Dr. Daniele Cavallo.

To my parents for their love and support
and to the kind memories of my grandfather

Contents

Chapter 1

Introduction

The progressively increasing demand for miniaturization, integration and conformability in wireless applications has led to a substantial growth of the popularity of planar printed antennas [1, 2]. Planar antennas, compared to the complex and bulky three dimensional antenna geometries, are not only light weight and simple to fabricate, but they can also be designed to achieve very high performance. This renders them attractive not only for commercial low-cost mobile devices, but also for the high-end applications such as military radars and satellite communication.

Although planar antennas are simple to realize, their design presents multifaceted challenges to the radio frequency (RF) designers, mainly due to their low radiation efficiency and narrow matching bandwidth. These two parameters are dominated by the dielectric properties as well as the physical dimensions of the substrate on which an antenna is printed i.e., permittivity and height respectively. For instance, antennas printed on electrically thin dielectric layers radiate equal power in the upper and the lower half spaces. Unidirectional radiation patterns on the one hand can be achieved by using electrically thin grounded substrates instead of ungrounded slabs. On the other hand, such antennas can be matched over a narrow bandwidths. An approach to improve the front-to-back ratio and the matching bandwidth simultaneously is to use a dense and electrically thick dielectric slab. However, increasing the height and the permittivity of the substrate leads to a significant increase in the excitation of surface waves. For the hypothetical case of infinitely extended dielectric slabs, the power launched into the surface waves constitutes to a loss in radiation efficiency of the antenna. Whereas, for finite-size slabs, such waves are diffracted from the edges the substrate degrading the quality of the radiation patterns. This is because surface waves spreading is cylindrical thus they decay slow in comparison to spherical spreading of space-wave. In antenna arrays, surface waves excitation results

in undesired mutual coupling between the neighboring antenna elements which can further lead to mismatch, scan-blindness and high cross-polarization levels.
The above highlighted problems are the fuel and the motivation for the investigation into new planar antenna solutions, which can be fabricated using the commercial processes, e.g., printed circuit board (PCB) or monolithic microwave integrated circuit (MMIC) technology. The focal point of this dissertation is centered around the design of planar electromagnetically engineered superstrates, which exhibit high surface-wave efficiency [1], over a broad frequency band, as well as an enhanced front-to-back ratio for antennas/antenna arrays radiating in their presence.

1.1 Planar Antennas: A Perspective

The driving force behind the rapid increase in the use of planar antennas in commercial applications is the advancement of silicon system-on-a-chip (SoC) and system-in-a-package (SiP) technologies. The latter are nowadays enabling the realization of inexpensive, light-weight, portable and reliable consumer products. Some examples of such applications at millimeter-wave frequencies are 60 GHz high data rate short-range communication [3–7]and 77 GHz automotive radars for safety and comfort [8–13]. Recently, sub-millimeter imaging radars systems for security applications, designed at 94 GHz and integrated on a single chip, are also gaining a lot of attention due to their low-profile and cost effectiveness [14–18]. The RF front-ends, in all these cases, are realized using MMIC technology [19–22] together with an off-chip radiator. A simple, compact and a low-profile solution is to integrate the antenna on the same platform/substrate on which the MMIC is mounted. The planarity of the antenna or the antenna array is then crucial to achieve all-integrated miniaturized sensors.
Planar integrated antennas have also found many applications in space instruments. A recent example is a kilo-pixel dual-polarized array of the slots, which is realized using conventional photo-lithographic techniques [23]. This array is used in an instrument called BICEP2 to study the Cosmic Microwave Background (CMB) polarization [24]. The advantage of using planar antennas, when compared with the conventional high-performance 3D horns, is two-fold. Firstly, they are light-weight, secondly, due to the use of standard lithography techniques, fabricating them is a straightforward process which makes them suitable for large antenna arrays.
In satellite communication and military platforms such as unmanned aerial vehicle (UAV),

[1] The term high-surface wave efficiency herein refers to the minimal excitation of surface waves.

a design of an efficient single wideband, wide-scan antenna array is of paramount importance. Since space, weight and conformability are major constraints in these scenarios, it is beneficial to combine several functions in a single antenna aperture. Furthermore, to support communication services, polarization purity is an important aspect to be accounted for. In most of the state-of-the-art designs of dual-polarized (wideband and wide-scan) arrays [25–27], a complicate egg-crate configuration is implemented, which is not only bulky but also costly to realize. To achieve comparable performances using completely planar antenna topologies, a few alternative concepts have been also proposed in the literature [28–30].

1.2 Surface Waves: State-of-Art Solutions

Figure 1.1 shows an example of a planar antenna, realized by etching a slot on a grounded dielectric slab of permittivity ε_{r1} and height h. The slab is typically characterized by a high relative permittivity, so that most of the power is radiated towards this medium, to achieve good front-to-back ratio. Furthermore, to feed the antenna and to reduce the back radiation, a microstrip line printed on an electrically thin slab with a lower permittivity ε_{r2} is usually employed. Such an antenna, despite its simplicity, is inefficient due to the excitation of surface waves inside the dielectric slab for $\varepsilon_{r1} > 1$, which is an undesired phenomenon. The surface waves are the transverse electric (TE) and the transverse magnetic (TM) modes of the dielectric slab, whose intensity, regardless of the nature of planar sources, i.e., electric or magnetic, increases as the height and/or the permittivity of the dielectric slab increase. They are also referred in literature as slow waves, since their phase velocity is lower than that of free space [31].

As depicted in Fig. 1.2, surface waves propagate along a zigzag path inside the substrate. These waves, which are bound by the substrate, are essentially the ones generated by the source at angle between $\pi/2$ and $\sin^{-1}(1/\sqrt{\varepsilon_r})$. Since the propagation constant of the surface waves is real, they do not exhibit exponential attenuation but only spatial spreading. Thus their amplitude can be high when they reach the boundaries of the dielectric slab, where they are reflected or diffracted from the edges, interfering with the space wave radiated by the antenna. Consequently, not only the antenna radiation efficiency is degraded, but this effect also results in deterioration of the far-field patterns and the polarization purity. A detail investigation of the surface wave in the homogeneous slabs is presented in [32–34].

One effective way to solve the issue of surface waves and to obtain simultaneously high

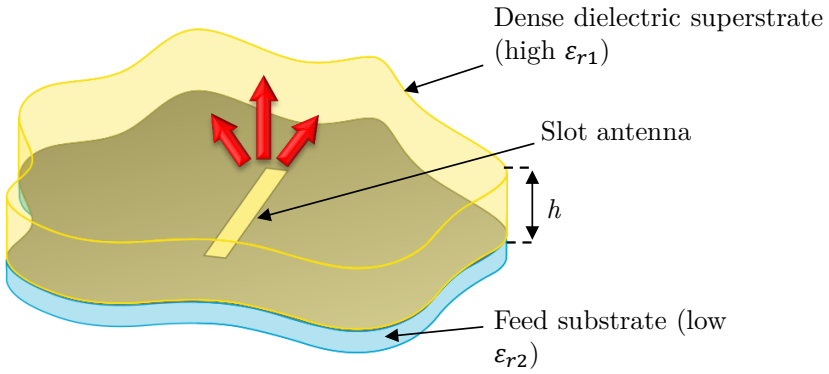

Figure 1.1: A slot etched on the ground plane, radiating in the presence of a dielectric slab.

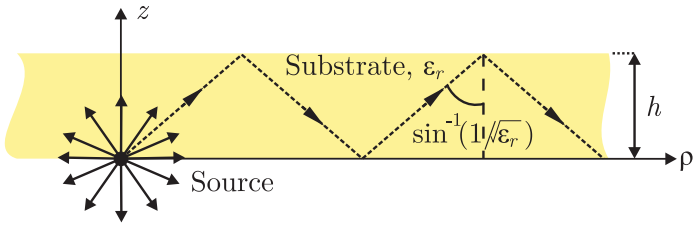

Figure 1.2: Surface waves in a finite height dielectric slab. The parameter ρ denotes the radial distance from the feed.

radiation efficiency and good front-to-back ratio is to use the antenna as a feed of a dielectric lens. A widely used solution in mm and sub-mm wave domain that works over about 15% bandwidth is to feed a dielectric lens with a planar double-slot antenna [35] (see Fig. 1.3). Matching layers can then be used on the lens surface to minimize the effect of multiple reflections inside the lens [36, 37]. Another approach is to feed dielectric lenses with non-dispersive leaky-wave feeds, to achieve very high performances over a decade (1:10) bandwidth [38–40]. However, dielectric lenses are non-planar, bulky and large in terms of wavelength. Therefore their inclusion is not always possible and depends on the frequency and the front-end architecture. This thesis will focus on planar solutions and even of a couple of cases in which they are used as a lens feed are discussed.

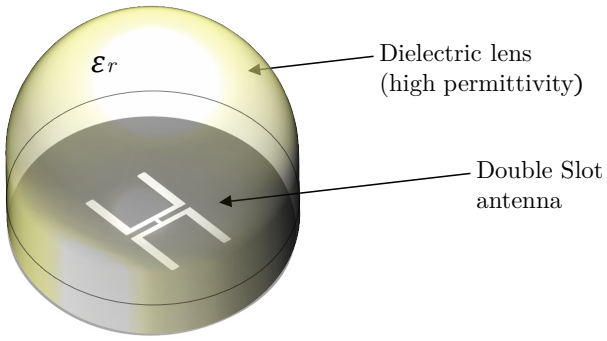

Figure 1.3: A double slot antenna radiating in the presence of a dielectric lens [35].

1.2.1 Planar Solutions

A plethora of planar techniques have been published in the last three decades, aimed at mitigating surface-wave excitation. Although a comprehensive summary including all the scientific contributions would be difficult, this subsection gives a brief overview in terms of performance of a few key antenna concepts typically employed for planar designs.

A planar antenna design that can achieve a very good front-to-back ratio without surface-wave excitation is the aperture-coupled stacked patch antenna (ASP) [41]. An ASP antenna, depicted in Tab. 1.1, consists of a resonant aperture, coupled electromagnetically to a multilayer stack of parasitic elements, such as resonant patches. The parasitic elements are typically printed on a foam substrate (i.e. $\varepsilon_r = 1$) to avoid surface wave modes. This antenna can achieve more than an octave impedance matching bandwidth by tuning the resonance of feeding aperture and the parasitic element simultaneously. ASP antennas are also used in linearly polarized phased array design, which are capable of scanning to 45° in all the azimuth planes while maintaining a very good polarization purity [28,30]. However, their efficiency drops if one is constrained to use higher permittivity dielectric substrates ($\varepsilon_r > 1$) instead of foam to host the antennas [42].

The efficiency of an antenna can also be improved by using so-called Fabry-Perot type resonant cavities [43–45] (see Tab. 1.1). In such configurations, the antenna is loaded with a single or multiple layers of electrically thin homogenous dense dielectric superstrates. To support a strong leaky wave, the source and the superstrate are separated by a distance of half-wavelength along the longitudinal axis. These type of antennas typically work over a narrow frequency band because of the use of resonant cavities.

In the design of planar antennas on single dielectric slabs, a high surface-wave efficiency can also be obtained by shaping the antenna elements themselves or their immediate sur-

Antenna Element	
1). Aperture-Coupled Stack Patch Antenna	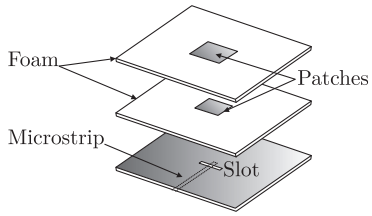
2). Fabry-Perot Resonant Cavity	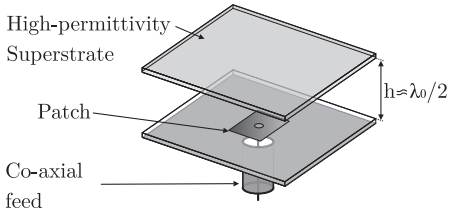
3). Twin-arc slot antenna	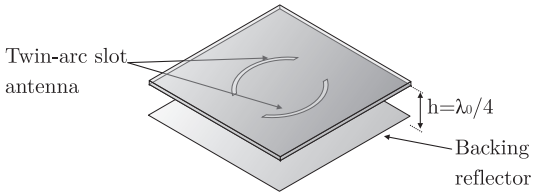
4). Mushroom type EBGs	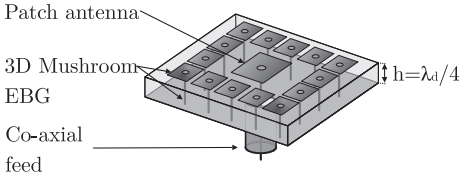
5). Planar EBGs	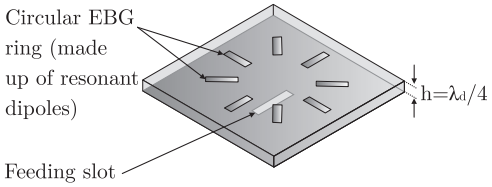

Table 1.1: State-of-art planar antenna solution to address the surface wave problem.

roundings. For instance, in [46] authors show that a radiation efficiency of 99.9% can be achieved over a narrow band by using a twin arc slot antenna, where the slots generate equal and opposite surface wave in every radial direction. This antenna, as depicted in Tab. 1.1, also needs to be backed by a cavity to obtain a uni-directional pattern and works efficiently only over a narrow band.

Another narrow-band planar antenna approach to avoid surface-wave modes is to synthesize the substrate by drilling holes in the vicinity of the antenna such that it emulates

permittivity close to that of free-space [47–49].
A technique which has gained a lot of popularity is to introduce periodic loading in a host dielectric slab to realize frequency bandgaps. At those bandgap frequencies, the substrate does not permit the propagation of surface waves. These periodic inclusions are referred to as electromagnetic band gaps (EBGs) in literature. A practical realization in PCB technology, shown in Tab. 1.1, is obtained by introducing periodic mushroom structures inside the dielectric substrate, which forbids the coupling of power to surface wave modes over 50% of relative bandwidth [50]. Note that, in table only one rings that surrounds the antennas is shown, however, in practical designs, multiple rings of EBGs are required to minimize the loss of power incurred due to the surface wave excitation. The resulting structure is electrically large, thus it would generate grating lobes if used in an array configuration.
A completely planar version of EBG for synthetic aperture radar application is reported in [51,52] (see also Tab. 1.1). In this concept, the frequency bandgap is realized by printing periodic resonant dipoles on the top of the substrate in the form of periodic circular rings. This design works over a bandwidth in the order of 20%. However, usage of the EBGs in array configuration restricts the scanning potential to only one plane because of the large radius of the proposed EBG rings [53].

1.3 Research Objective

In the previous sections, it has been highlighted that the performance of the planar antennas is mostly limited due to the undesired phenomena of the surface waves, inherent of dielectric slabs. All dielectric materials present in nature trade-off surface-wave efficiency for larger bandwidth and enhanced front-to-back ratio.
The goal of this thesis is to design artificial dielectric slabs that present high dielectric constants for the waves propagating orthogonally to slab itself, whereas the dielectric constants are low for the waves that propagates towards grazing direction. Thus the front-to-back ratio of the antenna is enhanced while surface waves due to multiple reflections at the dielectric air interface are not strongly excited.

1.3.1 Electromagnetically Engineered Substrate

Artificial dielectrics (ADs), as widely known in the literature, is an approach to realize dense dielectric ($\varepsilon_r > 1$) on a low-permittivity substrate, such as foam ($\varepsilon_r \approx 1$). They were proposed in late 1940's by W. E. Kock [54] as an alternative to homogeneous bulky

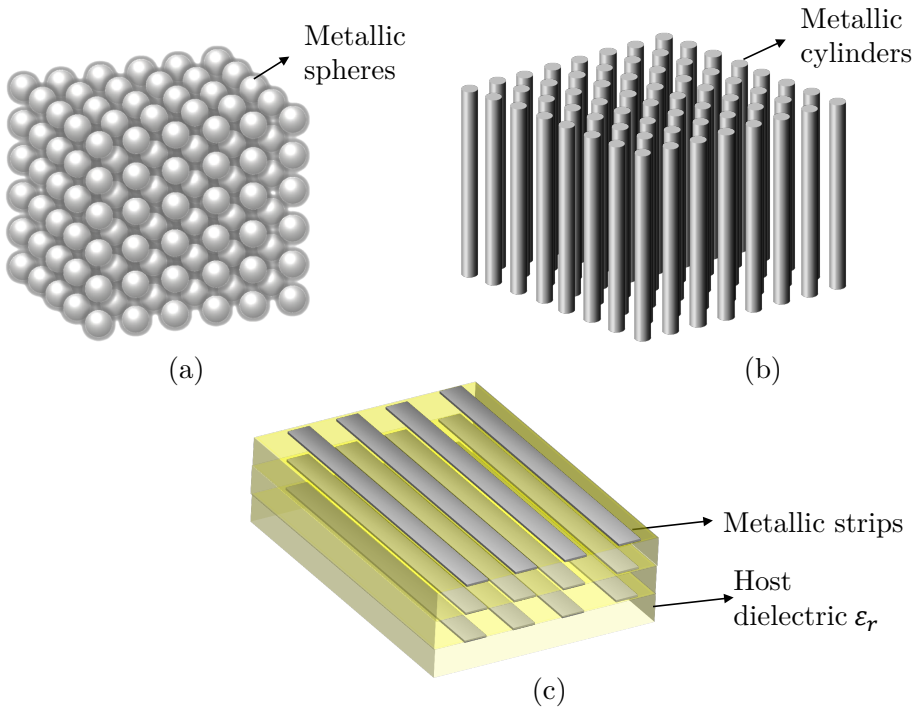

Figure 1.4: Artificial dielectric layer embedded in a host dielectric. (a) Three dimensional sphere and (b) cylinders and (c) planar two dimensional metallic strips.

substrate to design low-loss and light-weight dielectrics for realizing lens antennas. After their introduction, ADs have been extensively studied and used for decades for radar development.

ADs can be considered as a large-scale model of an actual dielectric, realized by embedding periodic metallic obstacles in a host in order to enhance its equivalent relative permittivity [55]. A physical realization of AD includes embedding of metallic spheres, cylinder and stripes inside a dielectric in a regular arrangement as shown is Fig. 1.4. In all these scenarios, the field scattered by the metallic inclusions, when added to the incident field, creates an effective equivalent delay [54–56]. The overall field can then be seen as propagation of the incident field in a new homogeneous material. This material is characterized by an effective dielectric constant, which can be much larger than the host substrate. The effect of the enhancement in the dielectric constant of the host medium is not frequency independent. It is determined by the size and spacing of the metallic inclusions. However, a constant improvement of the dielectric constant over a broadband can be achieved, provided that the size and spacing between the element is less than quarter wavelength at the highest frequency of the operation [54].

The equivalent medium in case of spherically symmetric obstacles, as shown in Fig. 1.4(a) and (b) is isotropic, since the effect of the impressed field on the geometry is independent of the polarization and incidence angle. However, it is anisotropic for the two dimensional artificial dielectrics, such as stripes (see Fig. 1.4(c)), which are suited for planar multi-layer slab designs. This is because the polarization and the angle of the incidence of the external electric field significantly impacts the equivalent properties of the structure. For instance, the enhancement of the dielectric constant ε_r of the host media is possible only if the electric field is orthogonal to the orientation of the stripes. In such case, the increase in the dielectric constant is maximum for the normally incident wave and it decreases as the the angle of the incidence starts to increase. However, this geometry reflects entirely the incident wave in which the electric field is parallel to the stripes.
Recently, the growing demand for silicon integrated front-ends is driving a renewed interest for planar strip-type ADs to improve the performance of passive components by miniaturization. In [57], ADs are implemented in commercial complementary metal oxide semiconductor (CMOS) technology to decrease the length of on-chip passive components, thus significantly reducing ohmic losses.

1.3.2 Planar ADL for Efficient Antenna Design

It is well-known that the near-field radiated by a generic source can be represented as an infinite spectrum of TE and TM plane waves [58]. Therefore, an AD should be simultaneously sensible to TE and TM modes when illuminated by a source located in its close proximity.
In this thesis, artificial dielectric layers (ADLs) are proposed to be realized in a planar topology with the goal of enhancing the antenna efficiency over a broadband. They are composed of multiple layers of periodic patches, as depicted in Fig. 1.5, with dimensions and the period of the patches as well the inter-layer distances that are small compared to the wavelength. Although this geometry presents different anisotropic characteristics for TE and TM incidence, it supports the propagation of waves with both polarizations, unlike ADs made of strips. At the frequencies for which the periodic unit cell is much smaller than the wavelength, ADL slabs can be assigned parameters that describe an equivalent homogeneous dielectric.
This concept is exploited to improve the front-to-back ratio efficiency and enhance the gain of integrated antennas, without supporting surface waves. An attractive feature of this solution is that the ADL can be designed *independently* of the antenna. This is not the case, e.g., of the ASP antenna [41], for which the resonance of the multi-patch antennas

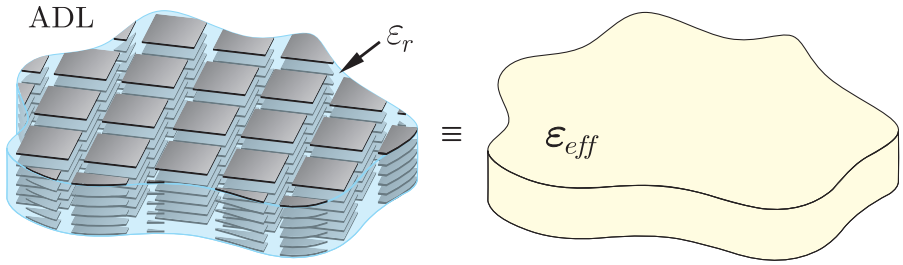

Figure 1.5: Artificial dielectric layer structure and equivalent anisotropic medium.

have to be tuned together. Also, the ADL can be manufactured and placed above the antenna without ensuring a fine alignment between the two. Moreover, this approach can be easily extended to built two dimensional arrays for scanning in both the planes, without incurring into scan blindness introduced by large periodicity or surface waves. Finally, the ohmic losses due to the metallic inclusions are very low, thanks to the non-resonant nature of the patches.

1.4 Scientific Contribution in this Thesis

This thesis deals with the theoretical analysis and the design of artificially dielectric layers (ADLs). The analysis of such structures is based on a spectral Green's function method, which not only gives an insight into the physics of artificial dielectric, but also leads to closed-form expressions to design ADL superstrates. The formalism is then exploited to design efficient unidirectional antennas/antenna arrays. Numerical results are verified from the measurements of prototype antennas at X-band and also at 0.3 THz. The key novel aspects addressed in this thesis are summarized as follows:

- *An analytical method for the characterization of ADLs of finite height, under arbitrary field illumination*: a rigorous equivalent circuit is derived and can be used to calculate, on one hand, the effective parameters of the ADL and, on the other hand, the spectral Green's function (GF) of the ADL. The exploitation of the equivalent circuit and the spectral GF allows to evaluate the dispersion characteristic of finite slabs, and the patterns of a generic antenna in the presence of the ADL.

- *Experimental demonstration in X-band of the performance enhancement of an antenna by loading it with an ADL superstrate:* the slab consists of a thin isotropic dielectric hosting the ADLs and has been proved to be capable of increasing the di-

rectivity and achieving high front-to-back ratio. Although a similar effect would be obtained with a thick standard dielectric slab with high permittivity, such a material also supports strong surface-wave propagation, while an artificial dielectric slab of the same equivalent permittivity does not.

- *Design, fabrication and testing of an antenna prototype at* 0.3 *THz*: on-chip integrated antennas typically radiate in the presence of a lossy silicon substrate or an electrically thin grounded slab. This leads to either high dielectric losses or very narrow bandwidths of operation. To increase the radiation efficiency, an antenna loaded with ADL has been fabricated using in-house integrated circuits (IC) process and tested to demonstrate the effectiveness of AD superstrates also at THz frequencies.

- *Novel concept of wideband wide-scanning phased array designs:* the proposed structure, based on connected arrays of slots loaded with ADL superstrates, has two main advantages with respect to the existing solutions. Firstly, it is completely planar and realized with a single multi-layer PCB, with consequent reduction of the cost and the complexity of the array. Secondly, ADLs are used in place of real dielectric superstrates, to achieve much better efficiency in terms of surface-wave losses.

1.5 Outline of the Thesis

The thesis is organized in seven chapters, which address several aspects of the the analysis, the design and the experimental validation of ADLs. A brief summary about the contents of each chapter is as following:
In chapter 2[2], a closed-form expression is derived to calculate the transverse propagation constant of a plane-wave impressed on a two dimensional artificial dielectric. A two-dimensional method of moment (MoM) tool has then been developed in the framework of this project to show that, although ADL presents the equivalent properties of dense dielectric slabs, they do not support surface waves.
In chapter 3[3], a spectral domain analytical formulation to model a single layer for arbitrary plane-wave incidence is presented. The results of the analysis are useful to highlight the characteristic properties of ADLs and their frequency range of validity. A closed-form solution is derived for the magnetic current distribution, including the reactive near field on

[2]This chapter is an extended version of the article [J1] (a list of the author's publications is included at the end of this dissertation, p. 159)

[3]The content of this chapter is published in [J2] (see p. 159)

the crossing slots, by expanding the total current with ad-hoc entire-domain basis functions. Simple analytical expressions are also derived for the equivalent sheet impedance of the layer.

Chapter 4[4] extends the method developed in Ch. 3 for a single layer to the multi-layer case, by including the higher-order interaction between parallel sheets in analytical form. From the equivalent impedance of the layers, a transmission line model is constructed that provides the spectral Green's function of ADLs in closed form. This allows to characterize the propagation through finite ADLs and to study the dispersion characteristics from the investigation of the Green's function singularities. Finally, by integrating the responses of a continuous set of plane waves, sources at small distances from the ADL slab are treated.

Chapter 5[5] describes the use of ADLs as a means to enhance front-to-back radiation ratio in printed, planar antennas. A simple qualitative description of this concept is followed by an experimental validation which clearly highlights the advantages of the proposed ADL for antenna applications.

Chapter 6[6] presents the development and the experimental test of an antenna loaded with ADLs at 300 GHz. The effectiveness of the ADLs to enhance the front-to-back ratio, demonstrated at microwave frequencies and using PCB technology in Ch. 5, is in this chapter proved also at THz frequencies. The artificial material is now realized with integrated technology, by introducing non-resonant metallic inclusions in a silicon dioxide host material. A prototype antenna was built using an in-house complementary metal-oxide-semiconductor (CMOS) back-end compatible integrated circuits (IC) process. Measured results from the antenna are presented and show a good agreement with the predicted results.

In chapter 7[7], a planar solution for wideband wide-scan phased array is proposed, which is realized with a single multi-layer PCB, with consequent reduction of the cost and complexity of the array. ADLs are used in place of real dielectric superstrates, as they are characterized by very high surface-wave efficiency. The presence of the ADL superstrate allows using slot elements in the array without exciting parallel plate waveguide modes between the array plane and the backing reflector. For the design of the total structure (array loaded with ADL) we used an in-house developed analysis tool, which is based on closed-form expressions and thus resorts to minimal computational resources. The proposed structure achieves in simulations about an octave bandwidth (7 to 14 GHz) for both

[4]The content of this chapter is published in [J3] (see p. 159)
[5]The content of this chapter is published in [J1] (see p. 159)
[6]The content of this chapter is published in [J4] (see p. 159)
[7]The content of this chapter has been submitted for publication in [J5] (see p. 159)

the single- and dual-polarized cases, within a scanning volume of 50° in all azimuth planes. The simulated radiation efficiency of the array is 95%. The maximum cross-polarization level of the dual-polarized array is −10 dB for scanning to 50° in the diagonal plane.
Chapter 8 provides concluding remarks about the results achieved in the project and possible indications about the future research directions.

Chapter 2

Analysis of Two Dimensional Strip-Type Artificial Dielectric Layers

In late 1940's, W. E. Kock proposed artificial dielectrics (ADs) to design low-loss and light-weight lens antennas [54]. An AD consists of non-resonant periodic metallic obstacles embedded in a host material to increase its equivalent relative permittivity. A three dimensional approach for obtaining a high dielectric constant is to introduce identical metallic spheres inside a low-permittivity dielectric medium, such as foam.

A completely planar approach to realize ADs is to embed periodic strips or patches in a host dielectric and they are referred to as artificial dielectric layers (ADLs). The resulting medium simulates a homogeneous anisotropic substrate. Under plane-wave incidence, the effective permittivity depends upon the polarization and the angle of the incidence. In this chapter, a Green's function (GF) based formalism is presented, which allows the analysis of strip-type infinite ADL. The equivalent propagation constant and the enhanced equivalent permittivity are analytically derived for a generic plane-wave incidence by solving the dispersion equation. This discussion is followed by a study of finite ADLs in the presence of a near-source (e.g. a dipole) using method of moments (MoM). The presented numerical results show that the ADL is characterize by high surface-wave efficiency.

This chapter only deals with two-dimensional problems, whereas the three-dimensional case of patch-type ADLs will be discussed in detail in Ch. 3 and 4.

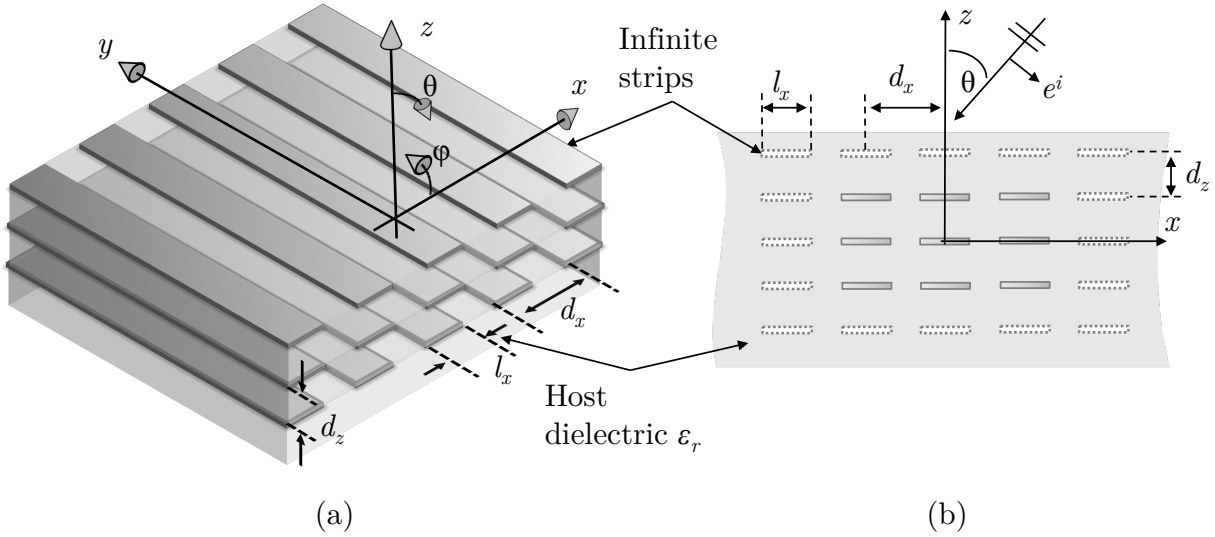

Figure 2.1: (a). Metallic strip-type artificial dielectric medium, and (b) a cross-sectional view of two-dimensional doubly periodic geometry under the plane wave incidence.

2.1 Infinite Strip-Type Artificial Dielectrics

In Fig. 2.1(a), a three-dimensional (3D) illustration of the metallic strip-type artificial dielectric medium is shown. It consists of an infinite array of y-oriented metallic strips, periodically arranged with spacing d_x and d_z along the x- and z-directions. The strips are assumed to be narrow with respect to the wavelength and the periods along x and z are also considered to be electrically small. The metal strips, characterized by width l_x, are invariant along y, perfectly conducting and infinitely thin. The structure is embedded in an infinite lossless dielectric of relative permittivity ε_r.

The geometry under investigation simulates a medium with an enhanced effective dielectric constant $\varepsilon_{r,\text{eff}} > \varepsilon_r$ for a transverse magnetic (TM) incident plane wave, with the electric field polarized on the x-z plane. The effective relative permittivity is dependent on the angle of incidence of the plane wave traveling inside the medium, thus the effective material is anisotropic. Unlike for the TM incidence, this geometry, for electrically small separation between the strips, is totally reflecting for a transverse electric (TE) plane wave. Therefore, a simplified two-dimensional (2D) geometry is investigated, as the one depicted in Fig. 2.1(b). The aim of the study is to obtain a close form expression of the unknown propagation constant along the z-direction in the homogenized material.

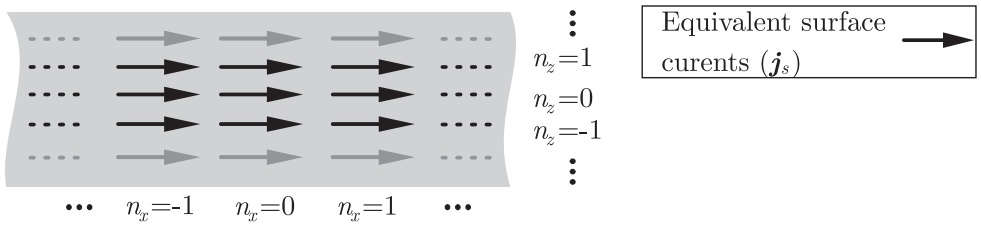

Figure 2.2: The equivalent electric currents oriented along x on each metal strip.

2.1.1 Integral Equation

The integral equation can be set up by applying the equivalence theorem and defining equivalent electric currents on the surface of the strips along the x-direction. These equivalent currents satisfy the boundary conditions of the tangential component of the magnetic field

$$\hat{\boldsymbol{z}} \times (\boldsymbol{h}_+ - \boldsymbol{h}_-) = \boldsymbol{j}_s(x, z = n_z d_z) \tag{2.1}$$

where $\boldsymbol{h}_+$ and $\boldsymbol{h}_-$ represent the magnetic field above and below each layer at $z = n_z d_z \pm \epsilon$, with ϵ vanishingly small. The equivalent problem involves electric surface currents $j_s(x, n_z d_z)\hat{\mathbf{x}}$, which are distributed over the area occupied by each strip, as shown in Fig. 2.2. The integers n_x and n_z are used to indicate the indexes of the layer and the strip, respectively. Once the equivalent currents are defined, the electric field integral equation (EFIE) can be formulated by enforcing the vanishing of the total (incident + scattered) tangential electric field on the strips:

$$\overbrace{\sum_{n_z=-\infty}^{\infty} \sum_{n_x=-\infty}^{\infty} \int_{n_x d_x - \frac{l_x}{2}}^{n_x d_x + \frac{l_x}{2}} g_{xx}^{ej}(x - x', z - n_z d_z) j_s(x', z' = n_z d_z) dx'}^{\text{scattered field}} = \underbrace{-e_x^i(x, z)}_{\text{incident field}} . \tag{2.2}$$

where (x,z) refer to the observation point, whereas (x', z') indicate the point of the local current density. The left hand side (LHS) of Eq. (2.2) represents the electric field scattered by the infinite doubly-periodic metallic strips. The kernel of the convolution integral contains the term g_{xx}^{ej}, which represents the xx-component of the spatial dyadic Green's function, that describes the electric field radiated by an elementary electric dipole. The incident field, on the right hand side (RHS), is assumed to be a plane wave $e_x^i = E^i e^{-jk_{x0}x} e^{jk_{z0}z}$,

characterized by propagation constant $k_{z0} = k_d \cos\theta$ and $k_{x0} = k_d \sin\theta$ along z and x, respectively. The incident angle θ is defined as in Fig. 2.1(b) and k_d refers to the wavenumber in the dielectric. It can be related to the free-space propagation constant k_0 by $k_d = k_0\sqrt{\varepsilon_r}$. Due to the infinite periodicity, the surface current density j_s can be written as:

$$j_s(x', n_z d_z) = j_s(x' - n_x d_x) e^{jk_{zs} n_z d_z} e^{-jk_{x0} n_x d_x} \,. \tag{2.3}$$

The unknown wavenumber k_{zs} represents the linear phase progression of the plane wave traveling along z in the equivalent medium. Including the definition of the current given in Eq. (2.3) in (2.2) and introducing the change of variable $x' = x' - n_x d_x$, we obtain the following expression:

$$\sum_{n_z=-\infty}^{\infty} \sum_{n_x=-\infty}^{\infty} \int_{-\frac{l_x}{2}}^{\frac{l_x}{2}} g_{xx}^{ej}(x - x' - n_x d_x, -n_z d_z) j_s(x') e^{-jk_{x0} n_x d_x} e^{jk_{zs} n_z d_z} dx' = -e_x^i(x, z = 0) \,. \tag{2.4}$$

where, for simplicity, the observation point is fixed at $z = 0$. Under the hypothesis of electrically small strips, the current distribution can be expressed with a single basis function, weighted by an unknown coefficient (i.e., $j_s = I_0 j_b$). This basis function is selected so as to verify the boundary conditions at the edge of the strips [59]:

$$j_b = \frac{2}{\pi l_x} \sqrt{1 - \left(\frac{x}{l_x/2}\right)^2} \,. \tag{2.5}$$

For the determination of the unknown coefficient I_0, Galerkin projection can be applied. This consists of multiplying LHS and RHS of Eq. (2.4) by a test function, which is taken equal to the basis function, and integrating over the region of the strip centered in the origin:

$$I_0 \sum_{n_z=-\infty}^{\infty} \sum_{n_x=-\infty}^{\infty} \int_{-\frac{l_x}{2}}^{\frac{l_x}{2}} j_b(x) \int_{-\frac{l_x}{2}}^{\frac{l_x}{2}} j_b(x') g_{xx}^{ej}(x - x' - n_x d_x, -n_z d_z) e^{-jk_{x0} n_x d_x} e^{jk_{zs} n_z d_z} dx' dx dk_x$$

$$= -\int_{-\frac{l_x}{2}}^{\frac{l_x}{2}} j_b(x) e_x^i(x) dx \tag{2.6}$$

Spectral Domain Expression of I_0

The closed-form expression of the GF is only known in spectral domain. Thus, it is convenient to express the integral equation (2.6) in the spectral domain. The relation between the spatial and the spectral dyadic Green's functions is defined as the following inverse Fourier transform:

$$g_{xx}^{ej}(x,z;x',z') = \frac{1}{2\pi}\int_{-\infty}^{\infty} G_{xx}^{EJ}(k_x,z,z')e^{-jk_x(x-x')}dk_x\,. \tag{2.7}$$

Substituting Eq. (2.7) in (2.6), and grouping the terms that depend on the integration variable x and x' to identify two Fourier transforms, one can write:

$$I_0\frac{1}{2\pi}\int_{-\infty}^{\infty}\sum_{n_z=-\infty}^{\infty}\sum_{n_x=-\infty}^{\infty}\left(\int_{-\frac{l_x}{2}}^{\frac{l_x}{2}} j_b(x)e^{-jk_xx}dx\right)\left(\int_{-\frac{l_x}{2}}^{\frac{l_x}{2}} j_b(x')e^{jk_xx'}dx'\right)$$
$$G_{xx}^{EJ}(k_x)e^{j(k_x-k_{x0})n_xd_x}e^{jk_{zs}n_zd_z}e^{-jk_z|n_zd_z|}dk_x = -\int_{-\frac{l_x}{2}}^{\frac{l_x}{2}} j_b(x)e_x^i(x)dx \tag{2.8}$$

where $k_z=\sqrt{k_d^2-k_x^2}$. The Poisson's summation formula can be used to write the infinite summation on indexes n_x as follows [55]:

$$\sum_{n_x=-\infty}^{\infty} e^{j(k_x-k_{x0})n_xd_x} = \frac{2\pi}{d_x}\sum_{m_x=-\infty}^{\infty}\delta(k_x-k_{xm}) \tag{2.9}$$

where $k_{xm}=k_{x0}+\frac{2\pi m_x}{d_x}$ is the m-th Floquet mode wavenumber. Furthermore, by substituting Eq. (2.9) in (2.8) and using the property of the Dirac δ-function, the infinite integration in k_x reduces to a sum over the discrete spectral Floquet wavenumbers:

$$I_0\frac{1}{d_x}\sum_{n_z=-\infty}^{\infty}\sum_{m_x=-\infty}^{\infty} J_b(-k_{xm})G_{xx}^{EJ}(k_{xm})J_b(k_{xm})e^{jk_{zs}n_zd_z}e^{-jk_{zm}|n_zd_z|} = -J_b(-k_{x0})E^i\,. \tag{2.10}$$

Here, the Fourier transform of $j_b(x)$, indicated as $J_b(k_x)$, is given by [59]

$$J_b(k_x) = \frac{1}{2}\left(J_0\left(k_x\frac{l_x}{2}\right)+J_2\left(k_x\frac{l_x}{2}\right)\right) \tag{2.11}$$

where J_0 and J_2 are the Bessel function of order 0 and 2, respectively. The unknown weight I_0 can be computed finally using

$$I_0 = -\frac{E^i J_b(-k_{x0})}{D(k_{x0})}\,. \tag{2.12}$$

The function $D(k_{x0})$ in the denominator is defined as

$$D(k_{x0}) = \frac{1}{d_x}\sum_{n_z=-\infty}^{\infty}\sum_{m_x=-\infty}^{\infty} J_b(-k_{xm})G_{xx}^{EJ}(k_{xm})J_b(k_{xm})e^{jk_{zs}n_z d_z}e^{-jk_{zm}|n_z d_z|}\,. \tag{2.13}$$

By splitting the spatial summation in $n_z = 0$ and $n_z \neq 0$, the function $D(k_{x0})$ can be written as

$$D(k_{x0}) = Z_{\text{self}} + Z_{\text{mutual},n_z\neq 0} \tag{2.14}$$

where the term Z_{self} can be identified as the self impedance, meaning that it refers to the impedance of a single layer alone. It is given by

$$Z_{\text{self}} = \frac{1}{d_x}\sum_{m_x=-\infty}^{\infty} |J_b(k_{xm})|^2 G_{xx}^{EJ}(k_{xm})\,. \tag{2.15}$$

Whereas, the presence of infinite layers above and below can be associated with Z_{mutual,n_z}. This parameter can be referred to as mutual impedance as it accounts for the higher-order-mode coupling between the layers.

$$Z_{\text{mutual},n_z\neq 0} = \frac{1}{d_x}\sum_{m_x=-\infty}^{\infty} |J_b(k_{xm})|^2 G_{xx}^{EJ}(k_{xm})\left(\sum_{n_z\neq 0} e^{jk_{zs}n_z d_z}e^{-jk_{zm}|n_z d_z|}\right)\,. \tag{2.16}$$

To calculate I_0 using Eq. (2.12), the unknown k_{zs} is required, which is not known a priori. This quantity relates the currents in the entire infinite structure to the current in the $n_x = 0, n_z = 0$ unit cell (see Eq. (2.3)).

Mutual Impedance

With the aim of deriving an analytical expression of k_{zs}, the Floquet mode summation in Eq. (2.16) can be split in fundamental ($m_x = 0$) and the higher order Floquet modes ($m_x \neq 0$).

$$Z_{\text{mutual},n_z\neq 0} \approx \frac{1}{d_x}|J_b(k_{x0})|^2 G_{xx}^{EJ}(k_{x0}) \left(\sum_{n_z\neq 0} e^{jk_{zs}n_z d_z} e^{-jk_{z0}|n_z d_z|} \right) + \sum_{m_x\neq 0} |J_b(k_{xm})|^2 G_{xx}^{EJ}(k_{xm}) \left(\sum_{n_z\neq 0} e^{jk_{zs}n_z d_z} e^{-jk_{zm}|n_z d_z|} \right) . \quad (2.17)$$

The square root defining $k_{zm} = \pm\sqrt{k_d^2 - k_{xm}^2}$ is associated with a first-order branch point with two possible values. For higher order Floquet modes, $|k_{xm}| \gg k_d$, thus one can approximate $k_{zm} \approx \pm\sqrt{-k_{xm}^2} = \pm jk_{xm}$. These modes are characterized by a purely imaginary propagation constant. Also, since $k_{zm} \gg k_{zs}$, the summation in n_z for $m_x \neq 0$ can be approximated as $\sum_{n_z\neq 0} e^{-jk_{zm}|n_z d_z|}$.

To verify the radiation condition, the only physical solution for $m_x \neq 0$ is represented by evanescent waves along z, for which $\mathfrak{Im}\{k_{zm}\} < 0$. As a consequence, the sum in n_z includes very fast decaying terms $e^{-|k_{xm}||n_z d_z|}$, that can be neglected for inter-layer distances that are not too small compared to the transverse period d_x. Note that the error introduced by this approximation increases for very small separations along z. A more accurate solution is formulated for three-dimensional structures in Ch. 3 and Ch. 4, where the validity of the method is not limited by the inter-layer distance.

The propagation along z direction can possibly be described by the the fundamental Floquet mode, for which the summation in n_z can be expressed in a closed-form as [55]:

$$\sum_{n_z\neq 0} e^{jk_{zs}n_z d_z} e^{-jk_{z0}|n_z d_z|} = \sum_{n_z=1}^{\infty} e^{-j(k_{zs}+k_{z0})n_z d_z} + \sum_{n_z=1}^{\infty} e^{j(k_{zs}-k_{z0})n_z d_z} = -1 - \frac{j}{2}\cot\left((k_{zs}+k_{z0})\frac{d_z}{2}\right) + \frac{j}{2}\cot\left((k_{zs}-k_{z0})\frac{d_z}{2}\right) \quad (2.18)$$

which can be simplified further by exploiting the polar representation of the cotangent [55]

$$\frac{j}{2}\cot x = -\frac{1}{2} + \frac{1}{e^{-jx}-1} . \quad (2.19)$$

Simplifying Eq. (2.18) using the identity in Eq. (2.19) leads to

$$\sum_{n_z\neq 0} e^{jk_{zs}n_z d_z} e^{-jk_{z0}|n_z d_z|} = -1 + j\frac{\sin(k_{z0}d_z)}{\cos(k_{zs}d_z) - \cos(k_{z0}d_z)} . \quad (2.20)$$

Consequently, Eq. (2.17) can be expressed as follows:

$$Z_{m,n_z\neq 0} \simeq \frac{1}{d_x}|J_b(k_{x0})|^2 G_{xx}^{EJ}(k_{x0}) \left(-1 + j\frac{\sin(k_{z0}d_z)}{\cos(k_{zs}d_z) - \cos(k_{z0}d_z)} \right) . \quad (2.21)$$

2.1.2 Dispersion Equation

As mentioned earlier, the calculation of the unknown coefficient I_0 requires a prior evaluation of k_{zs}. A unique solutions can be obtained only if, for a distinct value of k_{x0}, exists a single value of k_{zs}. Once it is calculated, the ADL loaded dielectric can be described as an effective homogeneous medium with certain constitutive parameters e.g., effective permittivity. In literature, the procedure for obtaining the description of a periodic structure with effective parameters is referred to as "homogenization process" [60–63].
To find analytically the constitutive parameters, that define strip-type periodic ADLs, at first the pole k_{zs} is needed to be derived in a closed-form. To achieve this goal, one needs to solve the dispersion equation, which implies equating the denominator of Eq. (2.12) to zero:

$$D(k_{x0}) = 0 \tag{2.22}$$

or

$$Z_{\text{self}} + Z_{\text{mutual},n_z\neq 0} = 0\,. \tag{2.23}$$

By substituting Eq. (2.21) and (2.15) in (2.23), we obtain, after some algebraic steps, the following analytical expression of k_{zs}:

$$k_{zs} = \frac{1}{d_z}\cos^{-1}\left(\frac{G_{xx}(k_{x0})|J(k_{x0})|^2}{\sum_{m_x\neq 0} G_{xx}(k_{xm})|J(k_{xm})|^2} j\sin(k_{z0}d_z) + \cos(k_{z0}d_z)\right)\,. \tag{2.24}$$

The free-space spectral Green's function is given by ($G_{xx}(k_{xm}) = -\frac{\zeta_0}{2}\frac{k_{zm}}{k_0}$), where the constant $\zeta_0 = 120\pi$ is the impedance of free-space. In the case of a hosting medium with a relative permittivity ε_r, the impedance modifies to $\zeta = \zeta_0/\sqrt{\varepsilon_r}$. The summation given in Eq. (2.24) converges very fast, since it contains only the sum of strongly attenuated evanescent modes (i.e $m_x \neq 0$). Finally, the effective permittivity can be calculated from the propagation constant by equating k_{zs} to $\sqrt{k_{eq}^2 - k_{x0}^2}$, where $k_{eq} = k_0\sqrt{\varepsilon_{r,\text{eff}}}$. The effective dielectric constant is then given by

$$\varepsilon_{r\text{eff}} = \frac{k_{zs}^2 + k_{x0}^2}{k_0^2}\,. \tag{2.25}$$

2.1.3 Results and Discussion

Figure 2.3 reports the effective dielectric constant $\varepsilon_{r\text{eff}}$ for the different values of the parameters l_x and d_x, as a function of θ. In this graph, d_z is kept constant to $0.01\lambda_d$, λ_d being the wavelength inside the host dielectric, which is taken to be free space $\varepsilon_r = 1$.

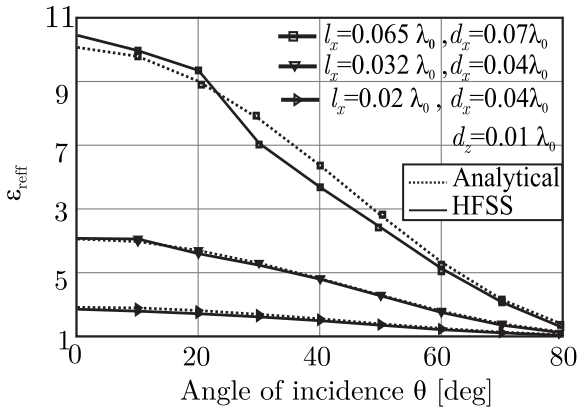

Figure 2.3: Effective dielectric constant ε_{reff} as a function of the incidence angle.

These curves show that for the broadside incidence (i.e. $\theta = 0°$), the ε_{reff} increases by incrementing the values of l_x and d_x. This is expected, since arranging these metallic strips in a dense configuration would increase the capacitive coupling between the neighboring cells. Consequently, higher enhancement of the relative permittivity of the host substrate is obtained.

This figure also shows that the dielectric enhancement factor changes as a function of the angle of incidence (i.e. $\varepsilon_{reff}(\theta)$) [55]. That is, ε_{reff} decreases for increasing values of the angle of incidence. Eventually, when the electric field is orthogonal to the metal strips, the equivalent dielectric approaches the dielectric constant of the host substrate. This anisotropic property renders the ADL advantageous to be located in the proximity of antennas, when compared to the homogeneous dielectric slabs. In fact, an important problem in dielectric loaded antennas occurs when a significant amount of power can be coupled to surface waves, via those rays that are radiated by the antenna at angles larger than the critical angle θ_c (see Fig. 2.4(a)). Since θ_c is associated with the dielectric constant of the dielectric slab via Snell's law, the lower values of ε_{reff} characterizing the ADL for larger angles imply that total internal reflection occurs at higher angles for ADL enhanced slabs (see Fig. 2.4(b)). Since ε_{reff} remains large for the waves radiated by the antenna in direction orthogonal to the ADL slab, thus a good front-to-back ratio can be achieved while preserving high surface-wave efficiency.

In order to validate the analytical results, full wave simulations are carried out with a commercial EM software [64]. Infinite periodic boundary conditions are imposed in the x- and y-directions only. The periodicity along z is accounted for by cascading 4 elements along this direction. Simulations have shown that cascading more unit cells do not effect

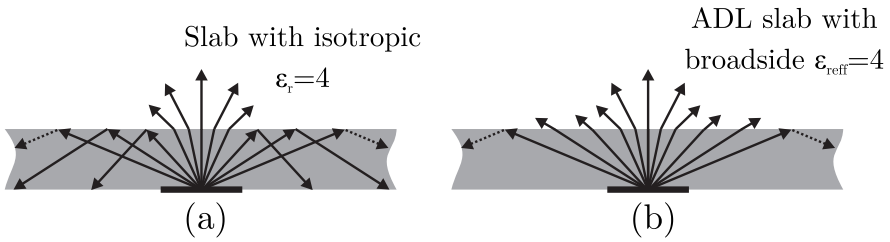

Figure 2.4: A near source radiating in; (a) bare dielectric slab of $\varepsilon_r = 4$ and; (b) ADL enhanced slab of $\varepsilon_{r\text{eff}} = 4$.

the results. A series of two port S-parameter simulations are carried out for TM incidence by varying the incidence angle between 0 and 80 degrees. After that, $\varepsilon_{r\text{eff}}$ is retrieved using S-parameter based extraction technique discussed in [65, 66] (see also Appendix B). For $d_x = 0.04\lambda_0$, a good agreement can be observed in Fig. 2.3, between the results obtained by the numerical and the analytical tool. However, a small error can be seen as d_x is increased from $0.04\lambda_0$ to $0.07\lambda_0$. This is because we have neglected the higher-order-mode contribution (i.e., $m_x \neq 0$) along the z-direction to obtain a simplified expression of the mutual impedance (see Eq. (2.21)). To account for the higher order mode interaction along z accurately, spectral GF based analytical formulation for a three dimensional ADL is presented in Ch. 3 and Ch. 4.

2.2 Near-Source Excitation of the Finite ADL (TM Case)

In this section, the effect of a source placed in the near field of a finite ADL slab is investigated using an in-house method of moments (MoM) tool. The geometry is depicted in Fig. 2.5, it consists of $N_x \times N_z$ metallic strips and is invariant along y. A lossless dielectric slab with relative permittivity ε_r, height h and infinitely extended along x is considered as a host medium. To realize a near source, an electric dipole of length l_s, oriented along x-axis, is located at the height h.

2.2.1 The Integral Equation

The field scattered by the ADL inclusion in the presence of a source at an observation point (x, z) can be derived by finding the actual electric current distribution $j(x, n_z d_z)\hat{\mathbf{x}}$ on all the metallic strips. Accordingly, an EFIE can be formulated by enforcing to zero

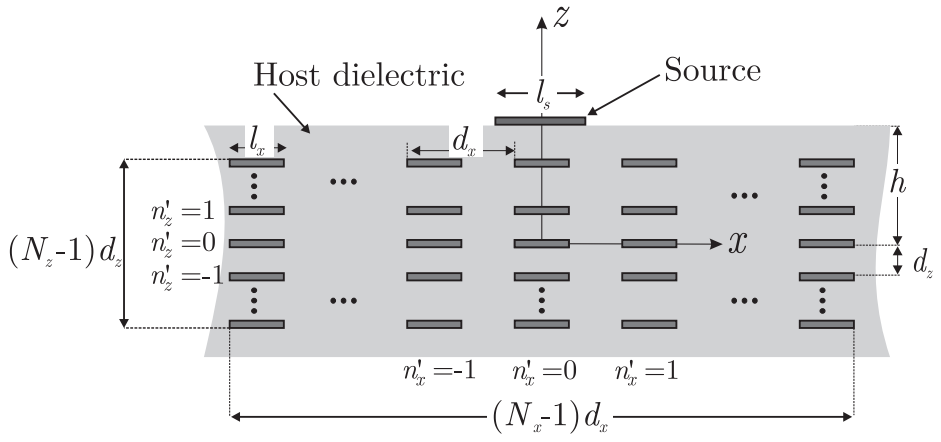

Figure 2.5: Finite ADL in the presence of a near source.

the component of the electric field tangent to the surface of the metal.

$$e^s(x,z) = -e^i(x,z) \tag{2.26}$$

where the incident and the scattered electric fields can be identified by the subscripts i and s, respectively. They can also be represented as a convolution between the spatial domain Green's function and the current as follows:

$$g * j_s = -g * j_i\,. \tag{2.27}$$

The LHS of Eq. (2.27) is the scattered field, which is expressed in terms of the unknown surface electric current density denoted by j_s. The latter can be expanded in terms of an appropriate set of basis functions. Under the assumption that the strips are electrically small, an entire domain basis function j_b given in Eq. (2.5) can be used to describes the distribution of the current density on each metallic obstacle. Finally, j_s can be written as:

$$j_s(x',z') = \sum_{n'_x=-N_x/2}^{N_x/2} \sum_{n_z=-N_z/2}^{Nz/2} I_{n'_x,n'_z} j_b(x'-n'_x d_x)\delta(z'-n'_z d_z) \tag{2.28}$$

where $I_{n'_x,n'_z}$ are the unknown coefficients, with the subscript (n'_x, n'_z) referring to the index of the inclusion. The RHS of Eq. (2.27) refers to the incident electric field radiated in absence of the metallic inclusions by the electric dipole source. The current distribution j_i is a known quantity, it can be expressed in terms of piecewise sinusoidal function [67]:

$$j_i(x) = \frac{\sin\left(k_{eq}(l_s/2-|x|)\right)}{\sin\left(k_{eq}(l_s/2)\right)} \qquad |x| \le l_s/2 \tag{2.29}$$

where $k_{eq} = k_0\sqrt{\frac{\varepsilon_r+1}{2}}$ is the average wavenumber. Conventional Galerkin-MoM procedure can now be applied to Eq. (2.26) in order to determine the unknown expansion coefficients $I_{n'_x,n'_z}$. Projecting LHS and RHS of Eq. (2.27) onto test functions which are taken equal to the basis functions, we obtain a set of equations such as

$$\sum_{n'=-N/2}^{N/2} I_{n'} < j_{t,n}, g * j_{b,n'} >= - < j_{t,n}, g * j_i > \qquad \forall n\,. \tag{2.30}$$

The integer n' and n indicate the pairs of indexes (n'_x, n'_z) and (n_x, n_z), respectively, referring to the basis and the test function. In Eq. (2.30), a reaction operator is also introduced

$$< f_1, f_2 >= \int_{-\infty}^{\infty} f_1(x) f_2^*(x) dx \tag{2.31}$$

where f_1 and f_2 are functions of x. The reaction integral on the LHS of Eq. (2.30) can be associated with an impedance $Z_{n,n'}$, whereas the integral on the RHS represents the forcing term which can be identified as a voltage. A convenient way to solve the integrals of the MoM matrix elements is to use the spectral domain representation, since the GF of a stratified media is known in closed-form in this domain. Therefore, the impedance can be written as

$$Z_{(n_x,n_z),(n'_x,n'_z)} = \frac{1}{2\pi} \sum_{n'_z=-Nz/2}^{Nz/2} \sum_{n'_x=-N_x/2}^{N_x/2} \int_{-\infty}^{\infty} |J_b(k_x)|^2 G_{xx}^{EJ}(k_x) e^{-jk_x(n_x-n'_x)d_x} e^{-jk_z|n_z-n'_z|d_z} dk_x\,. \tag{2.32}$$

The forcing term can be written in spectral domain as follows:

$$V_{(n_x,n_z)} = \frac{1}{2\pi} \int_{-\infty}^{\infty} J_i(k_x) G_{xx}^{EJ}(k_x) J_b(-k_x) e^{-jk_x(n_x d_x)} e^{-jk_z|n_z d_z - h|} dk_x \tag{2.33}$$

where the Fourier transform of $j_i(x)$, indicated as $J_i(k_x)$, is given as follows:

$$J_i(k_x) = 2\frac{\left(k_{eq}\frac{l_s}{2}\right)^2}{k_{eq}\sin\left(k_{eq}\frac{l_s}{2}\right)} \frac{\cos\left(k_x\frac{l_s}{2}\right) - \cos\left(k_{eq}\frac{l_s}{2}\right)}{\left(k_{eq}\frac{l_s}{2}\right)^2 - \left(k_x\frac{l_s}{2}\right)^2} \tag{2.34}$$

Equation (2.30) can be then expressed as

$$\sum_{n'=-N/2}^{N/2} I_{n'} Z_{n,n'} \;=\; V_n \qquad\qquad \forall n \tag{2.35}$$

or, more compactly in matrix form, as

$$\mathbf{ZI} \;=\; \mathbf{V}\,. \tag{2.36}$$

The unknown vector of the coefficients can be calculated as $\mathbf{I} = \mathbf{Z}^{-1}\mathbf{V}$. Once the current weights are known, the field scattered by the ADL in the presence of the source can be found by numerically solving the following integral equation:

$$e_x^s(x,z) = \frac{1}{2\pi} \sum_{n'_z=-N_z/2}^{N_z/2} \sum_{n'_x=-N_x/2}^{N_x/2} I_{n'_x,n'_z} \int_{-\infty}^{\infty} G_{xx}^{EJ}(k_x, z, n'_z d_z) J_b(k_x) e^{-jk_x(x-n'_x d_x)} dk_x\,. \tag{2.37}$$

2.2.2 Numerical Results and Discussion

For the design of planar printed antennas, grounded dielectric slabs are usually employed, which suffers from the excitation of surface waves. In this section, we use the MoM formulation introduced in the previous section to assess the performance of ADLs in terms of surface waves. Comparison with homogeneous dielectric slabs is also made, to highlight the advantages of using ADL slabs. Note that this study is limited to 2D cases for a TM polarized electric field. To calculate the electric field, the Green's function of a grounded dielectric slab is needed, the detailed derivation of which is given in Appendix A of [34,68].

ADL Slab Hosted by Free Space

To understand the effectiveness of the ADL slab, at first a homogenous slab is analyzed. The geometry consists of a source of length $l_s = \lambda_0/5$, positioned at the height $h = \lambda_0/8$ on the top of a grounded dielectric slab with $\varepsilon_r = 4$. Also, an ADL slab is designed by using free-space as a host medium by means of Eq. (2.24) and (2.25). The geometrical parameters of the ADL are adjusted such that for a normal incident plane wave, the permittivity of the free-space is enhanced by a factor 4. These dimensions are given in Tab. 2.1 in terms of the free-space wavelength λ_0. The number of layers along the z-direction (N_z) are chosen to be 3, thus realizing a $\lambda_{\text{eff}}/4$ dielectric slab which has a physical height of $\lambda_0/8$.

Table 2.1: ADL dimensions in term of wavelength

l_s	d_x	d_z	w_x	N_x	N_z
$0.2\lambda_0$	$0.16\lambda_0$	$0.05\lambda_0$	$0.135\lambda_0$	11	3

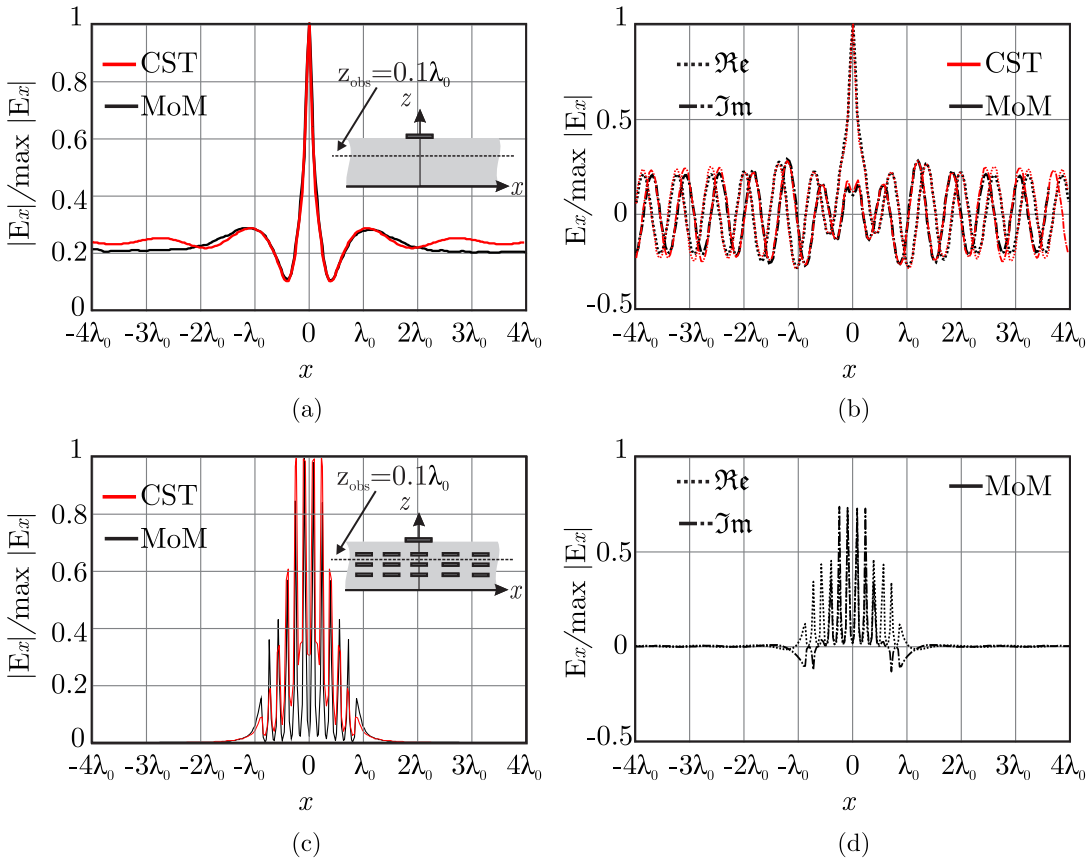

Figure 2.6: The normalized electric field scattered along x by a small electric dipole inside, a homogeneous dielectric slab of relative permittivity 4; (a) absolute value and; (b) real and imaginary part, and a ADL loaded slab in free space having $\varepsilon_{reff} = 4$; (c) absolute value and; (d) real and imaginary part. (The observation point along z is fixed at $z_{\text{obs}} = \lambda_0/10$ for both the slabs (refer to inset).

Figure 2.6 reports the predicted normalized electric field for the ADL and the homogeneous substrate, respectively, each of them having the same, real or equivalent, dielectric constant. It can be observed in Fig. 2.6(a) and (b) that the homogeneous slab supports a propagating surface wave. However, in case of the ADL loaded slab, the electric field intensity which is depicted in Fig. 2.6(c) and (d), decays to zero with a certain geometrical distribution when moving away from the center. The ADL is hosted by air (e.g., foam in a practical design) and thus it does not support surface waves. It can be also noticed that the amplitude of

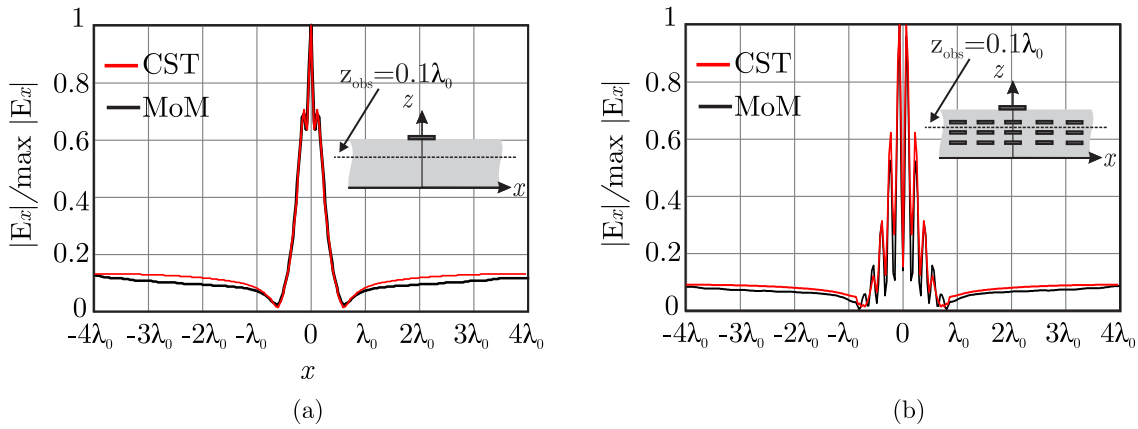

Figure 2.7: The normalized absolute electric field scattered along x by a small electric dipole inside a homogeneous dielectric slab of dielectric constant 2; (a) without and; (b) with the ADL inclusions. The scan is performed at $z_{\text{obs}} = \lambda_0/10$ above the ground plane.

the electric field goes to lower values for observation points close to the metal and peaks in the gaps between metal strips. The absence of surface waves in ADL slabs is a consequence of the angular dependence of the effective dielectric constant (refer to Fig. 2.3).

Simulation results of the precise geometry using the commercial EM solver [69] are also shown in Fig. 2.6, they show a fair agreement with the MoM tool.

ADL Slab in a Homogeneous Dielectric

ADL can also be introduced in a uniform dielectric slab with relative permittivity higher than 1. The slab itself supports a certain amount of surface waves, which depends on its thickness in terms of the wavelength in the dielectric. Accordingly, another simulation is carried out assuming a host with permittivity $\varepsilon_r = 2$ with the aim of obtaining $\varepsilon_{r\text{eff}} = 4$. To achieve this goal, the width of the metallic strips (l_x) is selected as $0.09\lambda_0$. In Fig. 2.7(a) and (b), we compare the absolute value of a near field inside a homogeneous slab of $\varepsilon_r = 2$ with that of an ADL loaded slab hosted by a substrate with $\varepsilon_r = 2$ of the same height ($h = 0.175\lambda_0$) respectively. It can be observed from both figures that the intensity of the surface waves launched in the artificial dielectric slab is the same with or without metallic inclusions.

It should be highlighted that Fig. 2.6 and 2.7 describe the TM surface-wave characteristics of the ADL slab. The exploitation of ADL for improving the front-to-back ratio of planar antennas will be addressed in subsequent chapters (Ch. 5 and 6).

2.3 Conclusions

In this chapter an analytic formula is presented, which is derived for the case of two-dimensional strip type ADLs. The closed-form expression allows to estimate analytically the effective dielectric constant as a function of the ADL geometrical parameters. Although the expression is only valid for the transverse magnetic (TM) polarized incident wave, it highlights an important physical mechanism: ADL is an equivalent dense material for the plane waves incident in directions close to the normal, whereas it exhibits lower effective permittivity for the waves that are incident close to the grazing angle. This peculiar anisotropy, characteristic of ADLs, is a key property for the design of high-efficiency superstrates.

To study the effect of a near-source radiating in the presence of a finite ADL slab, an in-house method of moments tool is built. The numerical results confirm that the ADL inclusions do not support additional surface waves, with respect to the hosting homogeneous dielectric slab.

Chapter 3

Closed-Form Analysis of Patch-Type Artificial Dielectric Layers Part–I: Properties of a Single Layer Under Plane-Wave Incidence

3.1 Introduction

The scattering from a single layer of periodic square patches has been extensively treated in the literature, for example in [70–75]. Some of these methods provide analytical formulas for the equivalent reactance of the layer under generic plane-wave incidence. However, they do not give a description or explanation of the typical properties of these structure, such as the transverse electric (TE) and transverse magnetic (TM) modal decoupling and the azimuthal independence of the equivalent layer impedance. These properties have been empirically observed for rectangular grids and meshes and they are typically assumed to be true in the literature [70–75].

In this chapter, we propose a novel analytical method to describe the scattering from a single rectangular mesh under generic plane-wave incidence. This method allows to derive not only a simple analytical formula for the equivalent layer reactance, but also a closed-form expression for the magnetic current distribution on the array plane. The solution is found in closed form by expanding the total current with appropriate entire-domain basis functions. The accurate description of the current distribution in the structure allows to develop an equivalent circuital model that clarifies and demonstrates the main peculiar properties of the structure, as well as the frequency range in which the circuit model is

valid.

This chapter is the first part of a two-chapter sequence. The closed-form expressions derived for the single layer are then extended to the multi-layer case in the Ch. 4, accounting for the reactive coupling between parallel layers in analytical form. In Ch. 4, we focus more on the use of the models for the real designs of artificial dielectric slabs with finite height, possibly illuminated by a near source.

This chapter is organized as follows. In Sec. 3.2 the magnetic current distribution on the array plane is calculated with a method of moments based on entire domain basis functions. The frequency range of validity of the chosen current expansion is investigated. In Sec. 3.3 we present an analytical solution for the admittance matrix and the unknown weights of the current expansion. The closed-form expressions are used to demonstrate the decoupling properties and the azimuthal independence of the structure for well-sampled arrays. Equivalent circuital representations are given to describe the plane wave scattering mechanism and the low-frequency behavior. A validation of the method is reported in Sec. 3.4, where comparison with commercial electromagnetic solvers are presented. Finally, conclusions are drawn in Sec. 3.5.

3.2 Magnetic Current Solution for a Single Layer

Let us consider the geometry shown in Fig. 3.1. It consists of an infinite doubly-periodic array of patches or, equivalently, of a combination of two orthogonal periodic arrays of infinitely long slots. We assume that the slots (gaps between adjacent patches) are electrically narrow. The periods along x and y are indicated by d_x and d_y, respectively, while w_y and w_x represent the width of the slots oriented along x and y, respectively. Regardless of the fact that in ADLs the dimensions of the patches are typically small with respect to the wavelength, we will subsequently quantify the validity of the proposed method as a function of the electrical size of the unit cell.

An integral equation can be set up as in [76,77], where the unknown is the equivalent magnetic current distribution on the slot region. By using the equivalence principle, magnetic current densities are introduced above and below an infinitely thin metallic layer covering the slot aperture, as shown in Fig. 3.2. These currents are equal and opposite ($\pm\mathbf{m}(x,y)$) to ensure the continuity of the tangential electric field on the slot aperture. The discontinuity of the scattered magnetic field at the slot plane can be expressed in terms of the equivalent magnetic current density as a convolution integral:

$$\mathbf{m}(\boldsymbol{\rho}) * \mathbf{g}(\boldsymbol{\rho}) = \int_{-\infty}^{\infty}\int_{-\infty}^{\infty} \mathbf{g}(\boldsymbol{\rho}-\boldsymbol{\rho}') \cdot \mathbf{m}(\boldsymbol{\rho}') d\boldsymbol{\rho}' = \mathbf{h}_i(\boldsymbol{\rho}) \tag{3.1}$$

where $\boldsymbol{\rho} \equiv (x, y)$ and $\boldsymbol{\rho}' \equiv (x', y')$. The dyadic Green's function $\mathbf{g}$ is related to the free-space Green's function $\mathbf{g}_{fs}$ by the condition $\mathbf{g} = 4\mathbf{g}_{fs}$, where $\mathbf{g}_{fs}$ represents the magnetic field radiated by an elementary magnetic dipole in free space. A factor 2 comes from the image theorem, since the magnetic currents radiate in the presence of a perfect electric conductor. Another factor 2 multiplies the free-space Green's function, since the magnetic current densities above and below the slot aperture must be equal and opposite to satisfy the boundary conditions. The incident field $\mathbf{h}_i$ represents the field in absence of the magnetic current, but in the presence of the ground plane. Thus, it is related to the direct field $\mathbf{h}_{\text{dir}}$ by the condition $\mathbf{h}_i = (1+\Gamma)\mathbf{h}_{\text{dir}} = 2\mathbf{h}_{\text{dir}}$, being the reflection coefficient at the metal plane $\Gamma = 1$:

$$\mathbf{m}(\boldsymbol{\rho}) * \mathbf{g}(\boldsymbol{\rho}) = 2\mathbf{h}_{\text{dir}}(\boldsymbol{\rho}) \tag{3.2}$$

The structure is illuminated by an arbitrary plane wave, associated with a direct magnetic field $\mathbf{h}_{\text{dir}}$ whose tangential component is in general a superposition of transverse electric (TE) and transverse magnetic (TM) modes:

$$\mathbf{h}_{\text{dir}}(\boldsymbol{\rho}, z) = I^+_{\text{TE}}\mathbf{h}_{\text{TE}}(\boldsymbol{\rho}, z) + I^+_{\text{TM}}\mathbf{h}_{\text{TM}}(\boldsymbol{\rho}, z) \tag{3.3}$$

where I^+_{TE} and I^+_{TM} are the complex weights of the plane-wave components, and the magnetic field mode functions are given by

$$\mathbf{h}_{\text{TE}}(\boldsymbol{\rho}, z) = \frac{1}{\sqrt{d_x d_y}}\hat{\mathbf{k}}_\rho e^{-j\mathbf{k}_\rho\cdot\boldsymbol{\rho}} e^{-jk_{z0}|z|} \tag{3.4}$$

$$\mathbf{h}_{\text{TM}}(\boldsymbol{\rho}, z) = \frac{1}{\sqrt{d_x d_y}}\hat{\boldsymbol{\alpha}} e^{-j\mathbf{k}_\rho\cdot\boldsymbol{\rho}} e^{-jk_{z0}|z|}\,. \tag{3.5}$$

Indicating with θ and ϕ the elevation and azimuth angles of incidence, respectively, the propagation constant along x, y and z are given by $k_{x0} = k_{\rho 0}\cos\phi$, $k_{y0} = k_{\rho 0}\sin\phi$, $k_{z0} = k_0\cos\theta$, with k_0 being the free-space wavenumber and $k_{\rho 0} = k_0\sin\theta$. The vector $\mathbf{k}_\rho$ in the exponential is equal to $k_{x0}\hat{\mathbf{x}} + k_{y0}\hat{\mathbf{y}}$ and the unit vectors of the TE and TM components are defined as

$$\hat{\mathbf{k}}_\rho = \cos\phi\hat{\mathbf{x}} + \sin\phi\hat{\mathbf{y}} = \frac{k_{x0}}{k_{\rho 0}}\hat{\mathbf{x}} + \frac{k_{y0}}{k_{\rho 0}}\hat{\mathbf{y}} \tag{3.6}$$

$$\hat{\boldsymbol{\alpha}} = -\sin\phi\hat{\mathbf{x}} + \cos\phi\hat{\mathbf{y}} = -\frac{k_{y0}}{k_{\rho 0}}\hat{\mathbf{x}} + \frac{k_{x0}}{k_{\rho 0}}\hat{\mathbf{y}}\,. \tag{3.7}$$

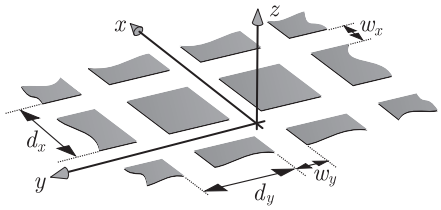

Figure 3.1: Single layer of crossing slots with geometrical parameters.

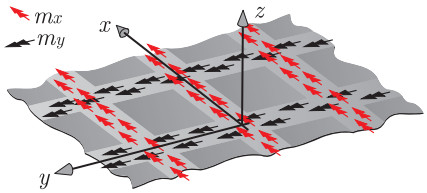

Figure 3.2: Equivalent magnetic current densities on the slot aperture.

3.2.1 Representation of the Magnetic Current

To find a closed-form solution to the integral equation (3.1), we expand the unknown total magnetic current into three basis functions, defined over the entire unit cell:

$$\mathbf{m}(\boldsymbol{\rho}) = a_{\mathrm{TE}}\mathbf{m}_{\mathrm{TE}}(\boldsymbol{\rho}) + a_{\mathrm{TM}}\mathbf{m}_{\mathrm{TM}}(\boldsymbol{\rho}) + a_{\mathrm{d}}\mathbf{m}_{\mathrm{d}}(\boldsymbol{\rho}) \tag{3.8}$$

where a_{TE}, a_{TM} and a_{d} are unknowns to be determined. The three basis functions are defined as follows:

1. The first two contributions to the total magnetic current ($\mathbf{m}_{\mathrm{TE}}$ and $\mathbf{m}_{\mathrm{TM}}$) represent the magnetic current enforced by the incident plane wave on the slots, as if the junctions between crossing slots had no effect. They can be expressed as the projections of the incident field onto the slot axes:

$$\mathbf{m}_{\mathrm{TE}}(\boldsymbol{\rho}) = m_{\mathrm{pw},x}(\boldsymbol{\rho})\cos\phi\hat{\mathbf{x}} + m_{\mathrm{pw},y}(\boldsymbol{\rho})\sin\phi\hat{\mathbf{y}} \tag{3.9}$$

$$\mathbf{m}_{\mathrm{TM}}(\boldsymbol{\rho}) = -m_{\mathrm{pw},x}(\boldsymbol{\rho})\sin\phi\hat{\mathbf{x}} + m_{\mathrm{pw},y}(\boldsymbol{\rho})\cos\phi\hat{\mathbf{y}} \tag{3.10}$$

   where we assume that the magnetic current is the product of separable functions of x and y:

$$\begin{aligned} m_{\mathrm{pw},x}(\boldsymbol{\rho}) &= e^{-jk_{x0}x}\Pi_{[-w_y/2,w_y/2]}(y) \\ m_{\mathrm{pw},y}(\boldsymbol{\rho}) &= e^{-jk_{y0}y}\Pi_{[-w_x/2,w_x/2]}(x)\,. \end{aligned} \tag{3.11}$$

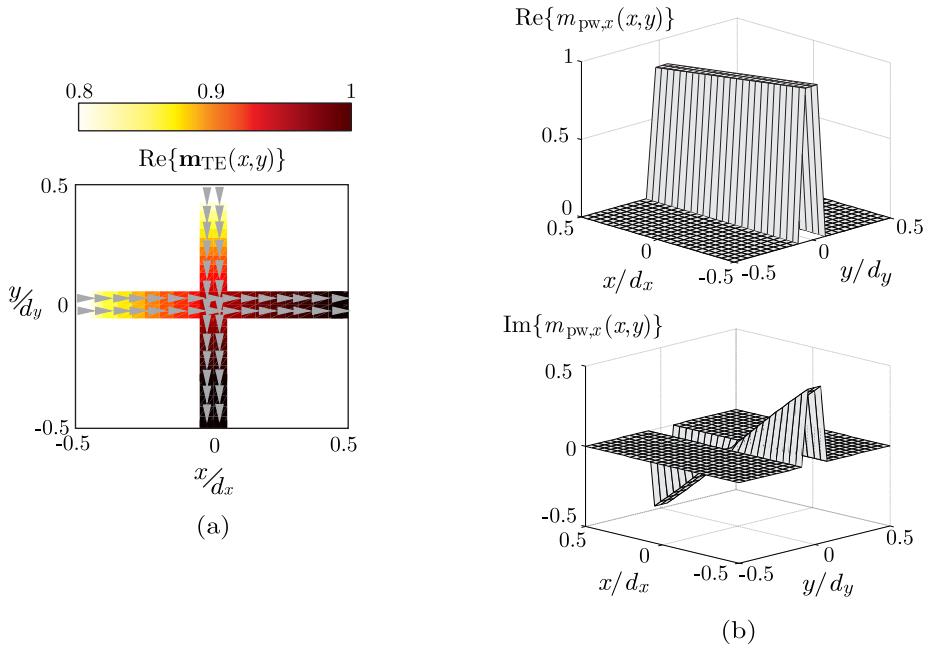

Figure 3.3: Example of the magnetic current distribution associated with the 'pw' basis function in the unit cell: (a) real part of the total magnetic current basis function and (b) real and imaginary part of the projection $m_{\mathrm{pw},x}$ on the x-axis.

The longitudinal voltage distribution along the slots is a linearly progressive phase term that accounts for the oblique angle of incidence, while the transverse distribution is assumed to be uniform, i.e. the function $\Pi_I(\xi)$ equals 1 for $\xi \in I$ and 0 elsewhere. The distributions associated with this basis functions are depending on the angle of incidence and the polarization of the incoming plane wave. As an example, a possible distribution is shown in Fig. 3.3 for incidence from $\theta = 60°$ and $\phi = 45°$: the real part of the total vector magnetic current on the unit cell are reported in Fig. 3.3(a), whereas Fig. 3.3(b) shows the real and imaginary parts of the x-oriented component.

2. The effects of the junction can be included by considering a third basis function that describes the field distribution at the crossing. Since both the basis functions $\mathbf{m}_{\mathrm{TE}}$ and $\mathbf{m}_{\mathrm{TM}}$ verify the Kirchoffs law individually at the crossing, the third basis function must verify the Kirchoffs law too. An appropriate choice is thus a basis function representing the electric field distribution as in Fig. 3.4(a). The current distribution is solenoidal, with the overall magnetic current entering the junction equal to zero.

   The electric field distribution can be associated with two equivalent doublet exci-

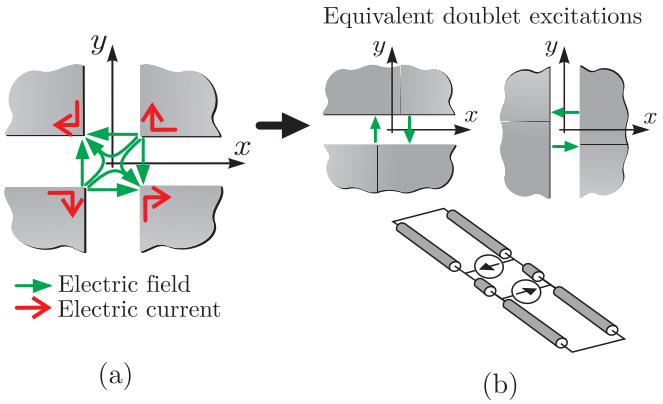

Figure 3.4: (a) Electric field and electric current distribution at the junction. (b) Doublet excitations to represent the crossings of orthogonal slots and equivalent transmission line model.

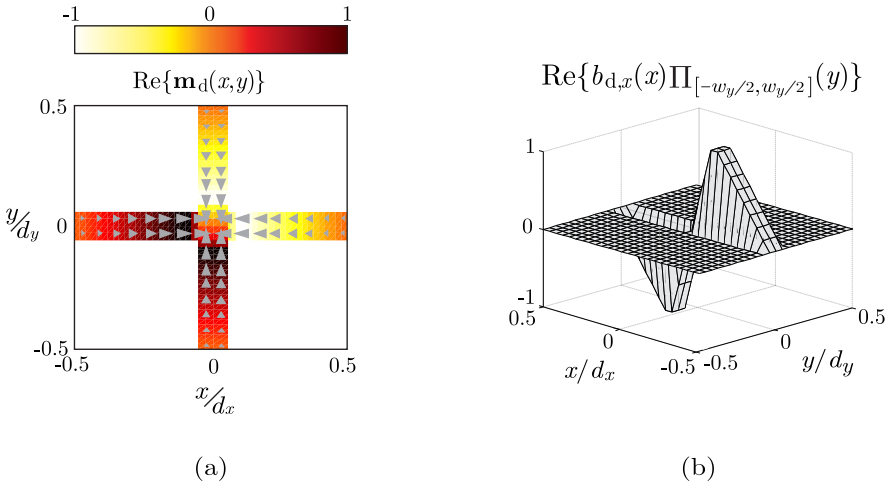

Figure 3.5: Magnetic current distribution associated with the 'doublet' basis function: (a) real part of the total magnetic current basis function and (b) of its projection along the x-axis.

tations, as shown in Figure 3.4(b). With the term 'doublet' we indicate the set of two δ-currents, equal and opposite, spaced by a distance equal to the width of the crossing slots. The magnetic current distribution associated with this basis function is represented in Fig. 3.5: the longitudinal part is equivalent to the voltage solution of a transmission line of length equal to the unit cell period, driven by two equal and opposite generators and terminated with short circuits at $x = \pm d_x/2$ and $y = \pm d_y/2$. Indeed, due to the symmetry, the voltage vanishes in the center as well as at the edges of the unit cells, as shown in Fig. 3.5(b).

We can express the basis function mathematically as follows:

$$\mathbf{m}_{\mathrm{d}}(\boldsymbol{\rho}) = b_{\mathrm{d},x}(x)\Pi_{[-w_y/2,w_y/2]}(y)\hat{\mathbf{x}} - b_{\mathrm{d},y}(y)\Pi_{[-w_x/2,w_x/2]}(x)\hat{\mathbf{y}} \tag{3.12}$$

where the '$-$' sign ensures that the two doublet sources along x and y satisfy the voltage Kirchhoff law at the junction. We assume a constant transverse distribution and we define the longitudinal voltage along x as

$$\begin{aligned} b_{\mathrm{d},x}(x) = &-(e^{jk_0x} + \Gamma e^{-jk_0x})\Pi_{[-d_x/2,-w_x/2)}(x) \\ &+ (e^{-jk_0x} + \Gamma e^{jk_0x})\Pi_{(w_x/2,d_x/2]}(x) + Cx\Pi_{[-w_x/2,w_x/2]}(x)\,. \end{aligned} \tag{3.13}$$

and $b_{\mathrm{d},y}(y)$ in the same way by replacing x with y. In the expression (3.13), C is a constant equal to $(2/w_x)(e^{-jk_0w_x/2} + \Gamma e^{jk_0w_x/2})$ and Γ is the reflection coefficient at the shorts ($\Gamma = -e^{-jk_0d_x}$).

3.2.2 Solution

If one substitutes the expansion in (3.8) into the convolution (3.2) and applies a Galerkin projection, the linear system of equations to be solved becomes the following:

$$\begin{aligned} a_{\mathrm{TE}}Y_{\mathrm{TE,TE}} + a_{\mathrm{TM}}Y_{\mathrm{TE,TM}} + a_{\mathrm{d}}Y_{\mathrm{TE,d}} &= i_{\mathrm{TE}} \\ a_{\mathrm{TE}}Y_{\mathrm{TM,TE}} + a_{\mathrm{TM}}Y_{\mathrm{TM,TM}} + a_{\mathrm{d}}Y_{\mathrm{TM,d}} &= i_{\mathrm{TM}} \\ a_{\mathrm{TE}}Y_{\mathrm{d,TE}} + a_{\mathrm{TM}}Y_{\mathrm{d,TM}} + a_{\mathrm{d}}Y_{\mathrm{d,d}} &= i_{\mathrm{d}} \end{aligned} \tag{3.14}$$

where $Y_{p,q} = \langle \mathbf{g} * \mathbf{m}_p, \mathbf{m}_q \rangle$, $i_q = \langle 2\mathbf{h}_{\mathrm{dir}}, \mathbf{m}_q \rangle$, and p and q can indicate any of the subscripts 'TE', 'TM' or 'd'. A reaction operator has been introduced, which is defined as follows:

$$\langle f_1, f_2 \rangle = \int_{-\infty}^{\infty}\int_{-\infty}^{\infty} f_1(x,y)f_2^*(x,y)dxdy \tag{3.15}$$

where f_1 and f_2 are generic functions of the variables x, y.

3.2.3 Frequency Range of Validity

The system in (3.14) associates only a limited degrees of freedom to the problem under analysis. Accordingly in this section the validity of the expansion in (3.8), as a function of the size of the unit cell, is investigated. By inverting the system of 3 equations in (3.14), one can evaluate the unknown weights of the basis functions. In Fig. 3.6 the

normalized voltages along the x- and y-oriented slots are reported, for different dimensions of the array period. The results of the method of moments (MoM) using three entire domain basis functions are compared with a commercial MoM code (Ansoft Designer [78]), based on small domain basis functions. The incident plane wave is assumed to be TE and incoming from $\theta = 60°$ and $\phi = 0°$, and the width of the slots is $w_x = w_y = \lambda_0/100$.
It can be noted that the agreement is good for unit cells of dimensions up to about a quarter wavelength and gets worse for larger periods. This is because resonant current distributions are not represented by the chosen three basis functions. However, the defined current expansion remains valid for all typical cases of ADL design, for which the array period is well below a quarter wavelength.
A deviation between the two solutions is observed in the crossing region close to the origin, when the junction dimensions are not much smaller than the period, for example for $d_x = d_y = \lambda_0/15$. Such discrepancy is due to the fact that we assume the transverse current distribution to be constant also in the crossing region, where the actual current widens at the junction (Fig. 3.7). However, this approximation of the current is not limiting if one is interested to calculate the equivalent reactance of the layer, which is an integrated quantity, as it will be shown in Sec. 3.4.

3.3 Decoupling Properties of the Structure

The system of equations in (3.14) can be solved for generic plane-wave incidence by inverting the 3×3 admittance matrix to find the unknown weights. However, some considerations can be made that allow the derivation of the solution in a simpler form and, at the same time, provide physical insight.
For visible plane-wave sources, or for very well sampled array structures, the current term i_{d} is approximately equal to zero because it represents the projection of the plane wave onto the doublet function, which is an odd function, as shown in Fig. 3.5. One can then find the expression of a_{d} from the third equation of (3.14) and substitute it in the first two equations, leading to a reduced system:

$$\mathbf{Y}_{\mathrm{red}} \cdot \begin{bmatrix} a_{\mathrm{TE}} \\ a_{\mathrm{TM}} \end{bmatrix} = \begin{bmatrix} i_{\mathrm{TE}} \\ i_{\mathrm{TM}} \end{bmatrix} \tag{3.16}$$

where

$$\mathbf{Y}_{\mathrm{red}} = \begin{bmatrix} Y_{\mathrm{TE,TE}} - \frac{Y_{\mathrm{TE,d}} Y_{\mathrm{TE,d}}}{Y_{\mathrm{d,d}}} & Y_{\mathrm{TE,TM}} - \frac{Y_{\mathrm{TM,d}} Y_{\mathrm{TE,d}}}{Y_{\mathrm{d,d}}} \\ Y_{\mathrm{TE,TM}} - \frac{Y_{\mathrm{TM,d}} Y_{\mathrm{TE,d}}}{Y_{\mathrm{d,d}}} & Y_{\mathrm{TM,TM}} - \frac{Y_{\mathrm{TM,d}} Y_{\mathrm{TM,d}}}{Y_{\mathrm{d,d}}} \end{bmatrix} . \tag{3.17}$$

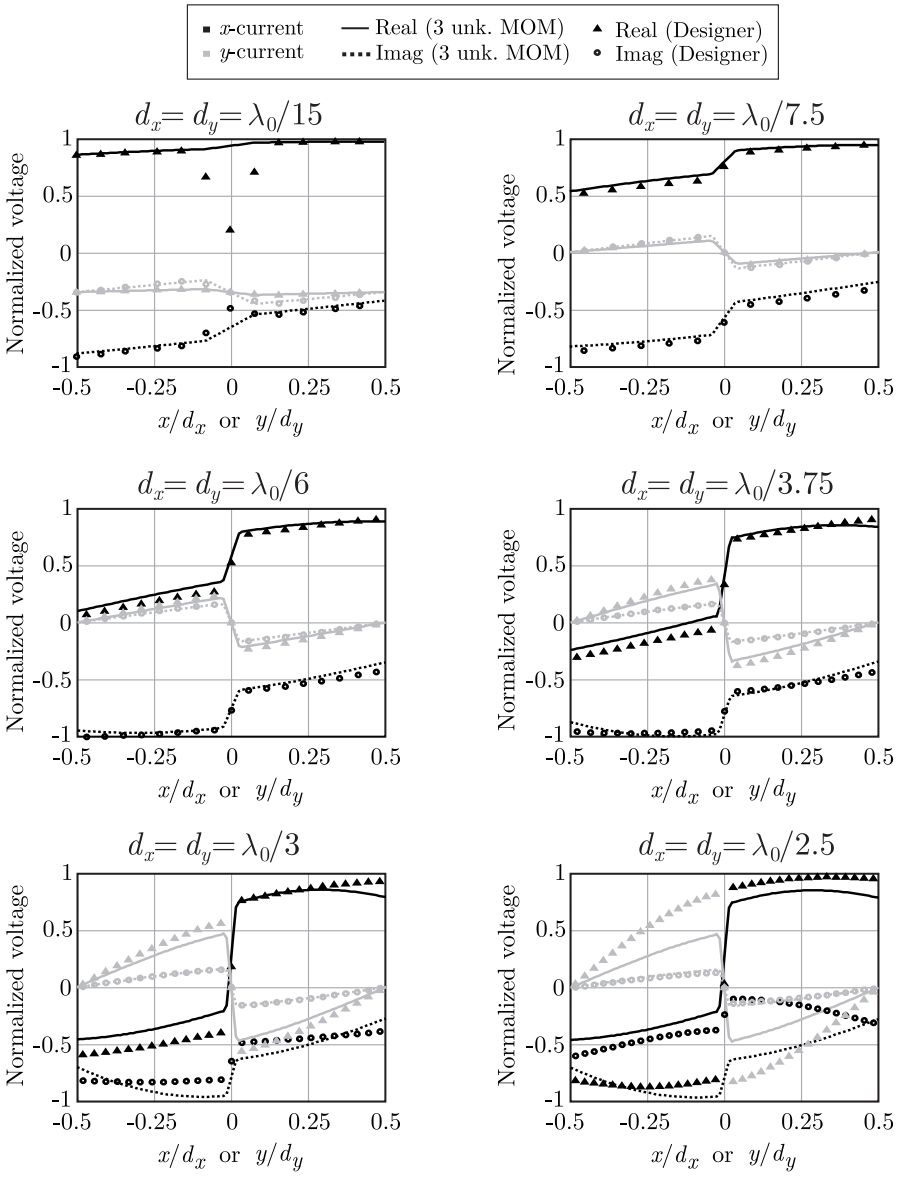

Figure 3.6: Comparison between our entire-domain-basis function MoM and Ansoft Designer [78], for different sizes of the unit cell. TE incidence from $\theta = 60°$ and $\phi = 0°$ is assumed and the width of the slots is $w_x = w_y = \lambda_0/100$.

It is convenient to calculate all admittance elements in the spectral domain, since the Fourier transforms of the basis functions $\mathbf{m}_{\mathrm{TE}}$ and $\mathbf{m}_{\mathrm{TM}}$ contain Kronecker δ functions that only retain the fundamental mode in the Floquet series. As a consequence, all the admittance terms can be calculated in a closed form, as shown in Appendix A.1 (Eq. (A.53)). By substituting these expressions into (3.17), we can write the admittance matrix

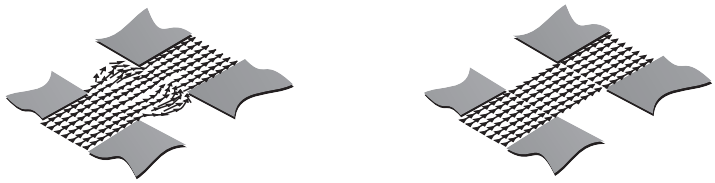

(a) (b)

Figure 3.7: Vector magnetic current distribution in the slot crossing: (a) Ansoft Designer, (b) our approximated model.

$\mathbf{Y}_{\text{red}}$ as the sum of three contributions:

$$\mathbf{Y}_{\text{red}} = \mathbf{Y}_{\text{TL}} + \mathbf{Y}_{\text{layer}} + \mathbf{Y}_{\text{cou}} \tag{3.18}$$

with

$$\mathbf{Y}_{\text{TL}} = -\begin{bmatrix} \frac{2}{Z_{0TE}} & 0 \\ 0 & \frac{2}{Z_{0TM}} \end{bmatrix} \tag{3.19}$$

$$\mathbf{Y}_{\text{layer}} = -\begin{bmatrix} jB_s(1 - \frac{\sin^2\theta}{2}) & 0 \\ 0 & jB_s \end{bmatrix} \tag{3.20}$$

$$\mathbf{Y}_{\text{cou}} = \begin{bmatrix} Y_{\text{c}}\frac{\sin^2\theta\cos^2(2\phi)}{2} & -Y_{\text{c}}\frac{\sin^2\theta\sin(2\phi)\cos(2\phi)}{2} \\ -Y_{\text{c}}\frac{\sin^2\theta\sin(2\phi)\cos(2\phi)}{2} & Y_{\text{c}}\frac{\sin^2\theta\sin^2(2\phi)}{2} \end{bmatrix} \tag{3.21}$$

where we introduced the wave impedances of the TE and TM modes $Z_{0\text{TE}}$ and $Z_{0\text{TM}}$, the slot self-susceptance B_s and a coupling admittance term Y_c, whose expression is given in Appendix A.

We define the slot self-susceptance (capacitance) B_s as the following sum of higher order Floquet modes:

$$B_s = \frac{2k_0}{\zeta_0} \sum_{m_y \neq 0} \frac{|\text{sinc}(k_{ym} w_x/2)|^2}{|k_{ym}|} \tag{3.22}$$

where $k_{ym} \approx \frac{2\pi m_y}{d_y}$.

An equivalent circuit representation of the two-port admittance matrix in (3.18) is shown in Fig. 3.8. The voltages and the total currents at the terminals A-A' and B-B' are the unknowns and the known terms in the system of equations (3.16). The scattering into free space is represented by TE and TM transmission lines, with characteristic impedances $Z_{0\text{TE}} = \zeta_0 k_0/k_{z0}$, $Z_{0\text{TM}} = \zeta_0 k_{z0}/k_0$, with ζ_0 being the free-space impedance. The transmission lines associated with the upper and lower half spaces are in parallel with the equivalent reactances of the layer for TE and TM incidence, given by

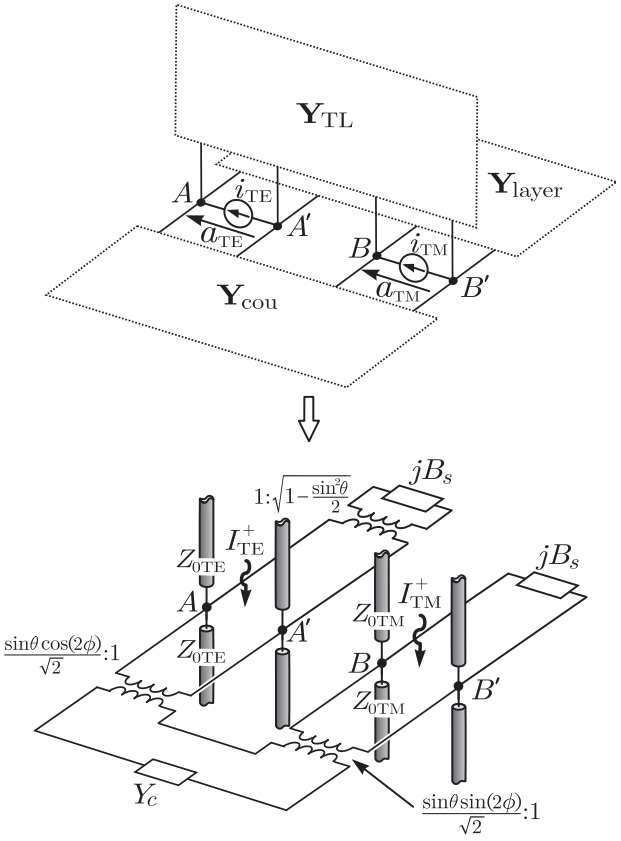

Figure 3.8: Equivalent circuit representation of the admittance matrix in Eqs. (3.18) to (3.21).

$$Z_{\mathrm{layer,TM}} = \frac{-j}{B_s}, Z_{\mathrm{layer,TE}} = \frac{-j}{B_s(1-\frac{\sin^2\theta}{2})}\,. \tag{3.23}$$

The known terms i_{TE} and i_{TM} represent the projection of the direct incident field onto the TE and TM basis functions, respectively:

$$i_{\mathrm{TE}} = \langle 2\mathbf{h}_{\mathrm{dir}}, \mathbf{m}_{\mathrm{TE}}\rangle = 2I^+_{\mathrm{TE}}(\mathrm{sinc}(k_{y0}w_y/2)\cos^2\phi + \mathrm{sinc}(k_{x0}w_x/2)\sin^2\phi) \tag{3.24}$$

$$i_{\mathrm{TM}} = \langle 2\mathbf{h}_{\mathrm{dir}}, \mathbf{m}_{\mathrm{TM}}\rangle = 2I^+_{\mathrm{TM}}(\mathrm{sinc}(k_{y0}w_y/2)\sin^2\phi + \mathrm{sinc}(k_{x0}w_x/2)\cos^2\phi)\,. \tag{3.25}$$

For small width of the slots such that $\mathrm{sinc}(k_{x0}w_x/2) \approx \mathrm{sinc}(k_{y0}w_y/2) \approx 1$, the currents at A-A' and B-B' are obtained by multiplying by 2 the TE and TM currents of incident plane wave evaluated at $z = 0$. This is a consequence of the image theory, and can be also explained applying the Norton equivalence as shown in Fig. 3.9.

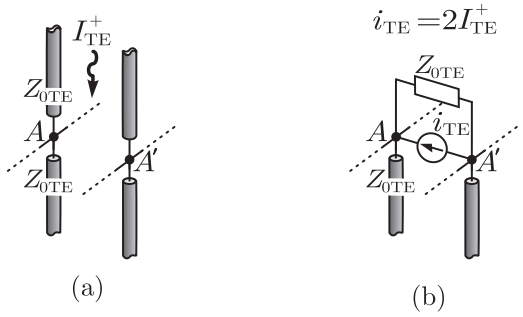

Figure 3.9: (a) Incident direct plane-wave current in the equivalent transmission line and (b) Norton equivalent current generator at the plane $z = 0$.

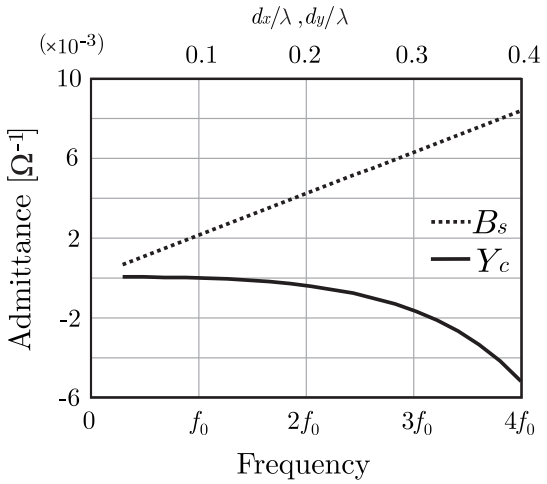

Figure 3.10: Imaginary part of the coupling admittance Y_c, compared with the real susceptance B_s, as a function of the frequency and of the unit cell size.

The matrices $\mathbf{Y}_{\mathrm{layer}}$ and $\mathbf{Y}_{\mathrm{TL}}$ are diagonal and therefore do not account for any coupling between TE and TM modes. The third contribution to the admittance matrix given by (3.21) describes the interaction between TE and TM modes, as it contains also off-diagonal elements. The equivalent circuit of this matrix can be represented as two transformer defined as in Fig. 3.8. The definition of the coupling admittance in (A.56) is general and describes the TE-TM coupling properties of the array of patches under investigation. However, under the assumption of well sampled array, this term asymptotically tends to zero ($Y_c \sim 0$). The demonstration of this condition involves a few algebraic steps that are reported in Appendix A.2. We report in Fig. 3.10 the value of the coupling admittance (Y_c) as a function of the frequency, and thus of the unit cell size. We note that the value of

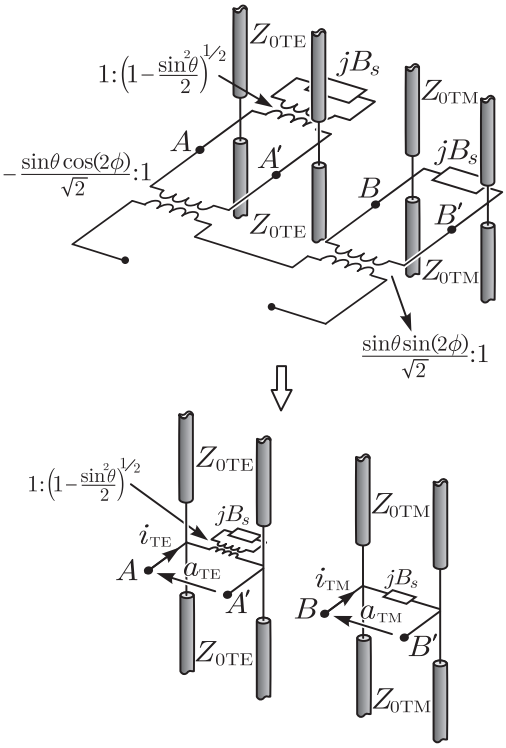

Figure 3.11: Equivalent circuit representation of a single layer for electrically small unit cells.

Y_c can be considered negligible only for cell sizes up to about a quarter wavelength. This means that essentially whenever the representation with three basis function is adequate, the TE and TM Floquet waves are decoupled.

Thus, for unit cells of the array that are small in terms of the wavelength, the coupling term Y_c is approximately an open circuit. Therefore, as shown in Fig. 3.11, no current is flowing in the lower part of the circuit, so that the two equivalent transmission lines models for the TE and TM scattering become decoupled. The resulting equivalent transmission-line representation is depicted in Fig. 3.12, describing a generic plane wave illuminating a patch array with electrically small periods. A similar circuit was developed in [79] for singly polarized arrays of strips. In that case the TE and TM Floquet waves were coupled one to another, unlike for the orthogonal crossing arrays.

The physical meaning of this condition is that a periodic electrically dense array of patches can only scatter TM waves under TM incidence, and only TE waves under TE incidence. It can be also pointed out that the expressions of the equivalent reactance in (3.23) are non dependent on ϕ, which is a proof of the azimuthal invariance of the scattering from the structure under analysis. These properties were previously observed or assumed in [71, 75],

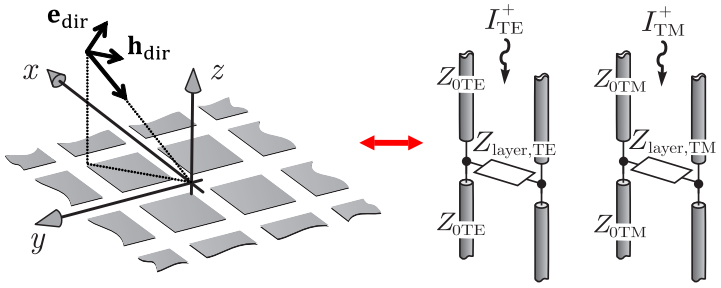

Figure 3.12: Equivalent transmission lines of a patch array with electrically small periods, under generic plane-wave illumination.

whereas the range of validity of the approximation is shown here.
Finally, it is straightforward from the expressions in (3.19) and (3.20) to calculate the magnetic current distribution in analytical form. The weights of the basis functions are given by

$$\begin{aligned} a_{\text{TE}} &= -i_{\text{TE}} \left(\frac{2}{Z_{0TE}} + jB_s \left(1 - \frac{\sin^2\theta}{2} \right) \right)^{-1} \\ a_{\text{TM}} &= -i_{\text{TM}} \left(\frac{2}{Z_{0TM}} + jB_s \right)^{-1} \end{aligned} \tag{3.26}$$

and

$$a_{\text{d}} = \begin{cases} a_{\text{TE}} \frac{jB_s \sin\theta \cos(2\phi)}{2\widetilde{Y}} & \text{for TE incidence} \\ -a_{\text{TM}} \frac{jB_s \sin\theta \sin(2\phi)}{2\widetilde{Y}} & \text{for TM incidence} \end{cases} . \tag{3.27}$$

3.4 Validation of the Method

The equivalent layer capacitance given by (3.23) for TE and TM incidence is shown in Fig. 3.13, compared with Ansoft HFSS simulations [64]. The geometrical parameters are $w_y = w_x = 0.02\lambda_0$ and $d_y = d_x = 0.15\lambda_0$, with λ_0 being the free space wavelength at the frequency f_0, and the plane wave is incident from four different angles. A good agreement can be observed between the analytical solution and the full-wave simulations performed with the commercial solver.
The expressions (3.26) and (3.27), together with Eq. (3.8), define in analytical form the voltage distribution on the slots for generic and arbitrarily polarized plane wave. As an example, Fig. 3.14 shows the voltage along the x-oriented slot for normal incidence, while

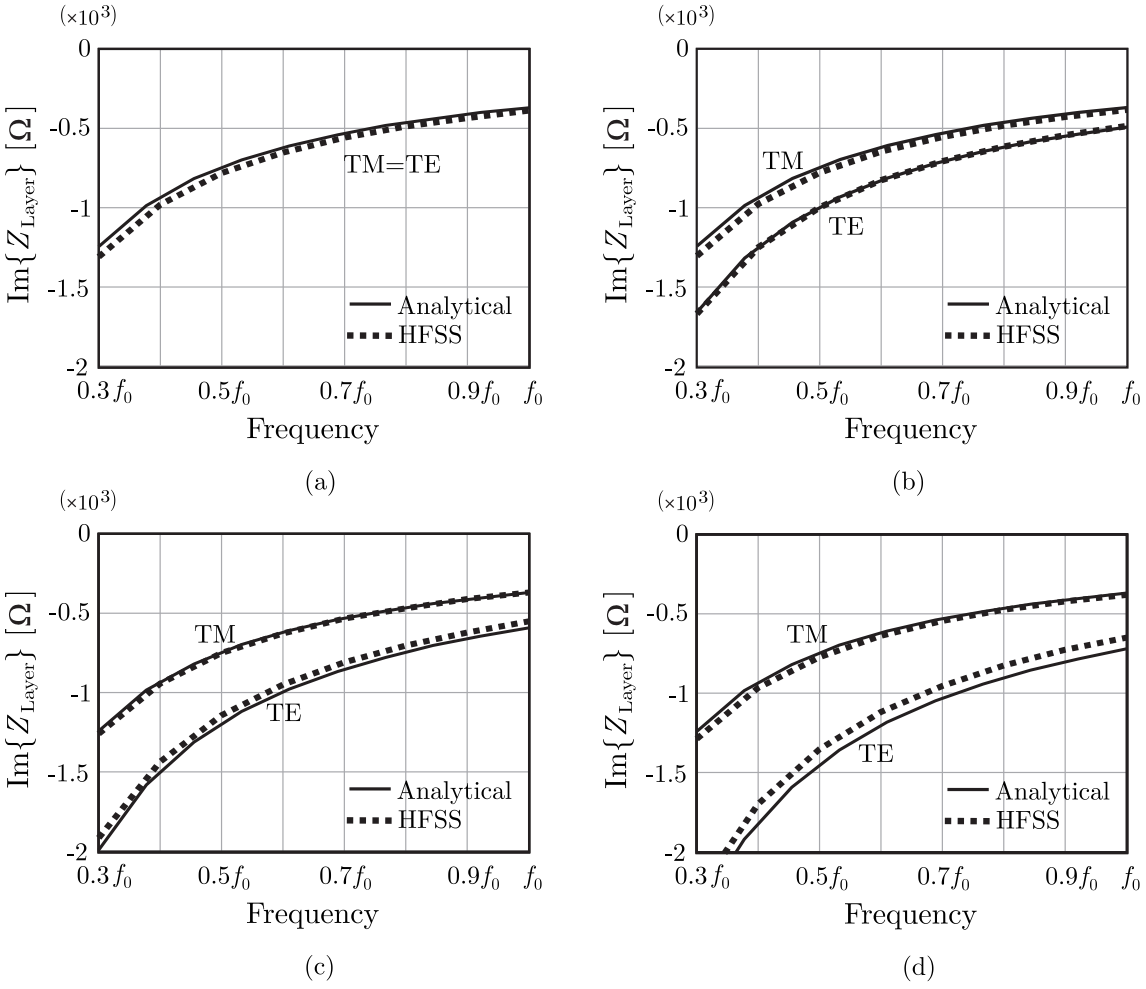

Figure 3.13: Equivalent capacitance of the single layer for transverse electric (TE) and transverse magnetic (TM) incidence for (a) $\theta_i = 0°$, (b) $\theta_i = 45°$, (c) $\theta_i = 60°$ and, (d) $\theta_i = 80°$. The parameters are $w_y = w_x = 0.02\lambda$ and $d_y = d_x = 0.15\lambda$, with λ being the wavelength at the frequency f_0.

Fig. 3.15 (a) and (b) refer to the voltage on the x- and y-oriented slots, respectively, for transverse electric (TE) incidence from the direction $\theta = 60°$, $\phi = 0°$. Both voltages are normalized to the maximum magnitude of the voltage on the x-oriented slot. This is done in order to highlight the relative magnitude difference of the two components of the magnetic current density. The geometrical parameters are set as $w_x = w_y = 0.01\lambda_0$ and $d_x = d_y = 0.0785\lambda_0$ with λ_0 being the wavelength at the calculation frequency. Figures 3.16 and 3.17 show the normalized voltages along the x and y slots, for TE and TM incidence, respectively, when the incidence angle are $\phi = 40°$ and $\theta = 60°$, while the geometrical parameters are $w_x = w_y = 0.02\lambda_0$ and $d_x = d_y = 0.15\lambda_0$.

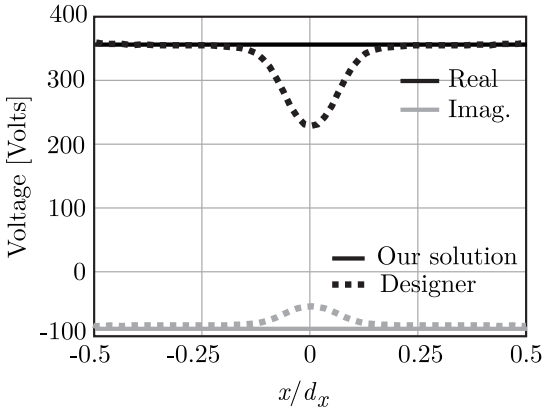

Figure 3.14: Voltage distribution on the slot axis for normal incidence. The geometrical parameters are set as $w_x = w_y = 0.01\lambda_0$ and $d_x = d_y = 0.0785\lambda_0$ with λ_0 being the wavelength at the calculation frequency.

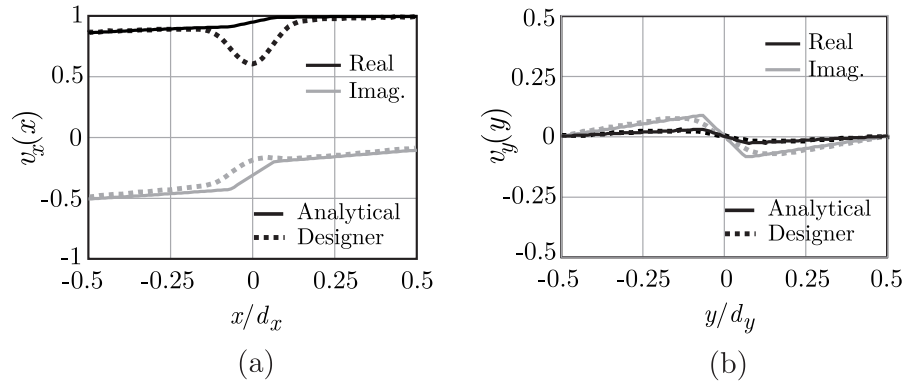

Figure 3.15: Normalized voltage distribution for TE incidence at 60° and plane of incidence $\phi = 0°$: (a) x-oriented slot, (b) y-oriented slot. The geometrical parameters are the same as in Fig. 3.14.

The results for the voltage are compared with simulation performed with the commercial software Ansoft Designer [78], which is based on small domain method of moments. The analytical expressions here derived agree well for all cases with the commercial solver. The deviation in the crossing region was explained by Fig. 3.7. From Fig. 3.15(b) it is clear that the basis function chosen to describe the voltage induced on the crossing slot is appropriate, as the distribution resembles the one in Fig. 3.5(b).

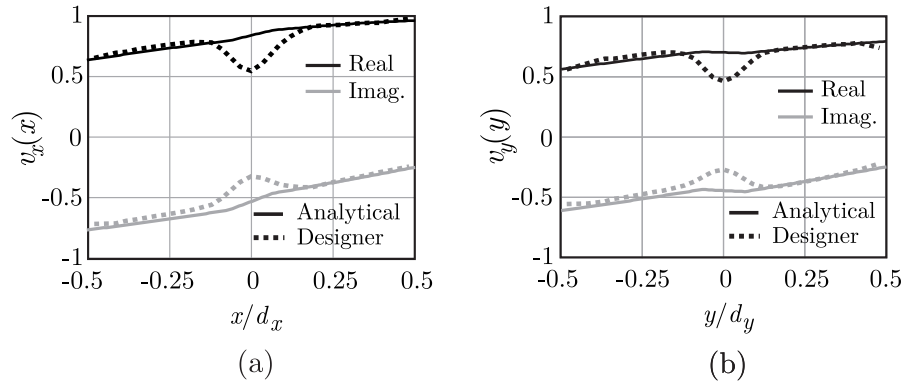

Figure 3.16: Normalized voltage distribution for TE incidence at 60° and plane of incidence $\phi = 40°$: (a) x-oriented slot, (b) y-oriented slot. The geometrical parameters are set as $w_x = w_y = 0.02\lambda_0$ and $d_x = d_y = 0.15\lambda_0$ with λ_0 being the wavelength at the calculation frequency.

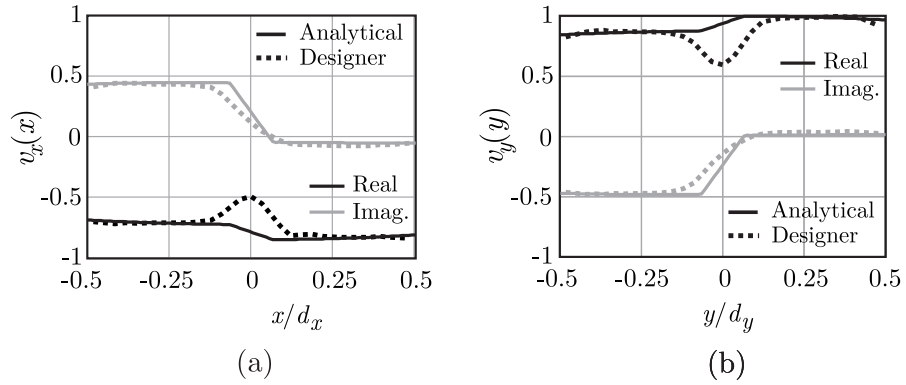

Figure 3.17: Normalized voltage distribution for TM incidence at 60° and plane of incidence $\phi = 40°$: (a) x-oriented slot, (b) y-oriented slot. The geometrical parameters are the same as in Fig. 3.16.

3.5 Conclusions

In this chapter, an analytical method is presented to describe the interaction between a generic plane wave and a square-mesh layer. In addition to previous works with similar scope, our approach allows to derive a closed-form expression for the magnetic current distribution on the array plane. Also, the decoupling properties of the TE and TM modes and the azimuthal independence of the structure were not assumed as initial hypotheses but they were demonstrated and characterized, with consequent gain in physical insight. Besides these new insights, thanks to the spectral representation used for the derivation, the way has also been paved for expanding the formulation for the analysis of closely spaced ADLs, which are treated in Ch. 4.

Chapter 4

Closed-Form Analysis of Patch-Type Artificial Dielectric Layers Part–II: Extension to Multiple Layers and Arbitrary Illumination

4.1 Introduction

In Ch. 3, we derived an analytical formulation to characterize the interaction between a generic plane wave and a single, electrically dense layer of periodic patches. The current distribution on the plane was derived in closed form, as well as the equivalent reactance of the layer. We rigorously demonstrated that, for array periods smaller than a quarter wavelength, the structure does not couple the transverse electric (TE) and the transverse magnetic (TM) modes. This property was shown to be due to a compensation of the self reactance of the slots by the reactive coupling occurring between orthogonal slots at the junction.

Artificial dielectric layers (ADLs) are obtained by cascading a multiplicity of such layers to realize equivalent dielectric slabs. These slabs are demonstrated to support much less surface waves than regular slabs of equivalent permittivity [80]. Since in realistic designs the layers are closely spaced, the inter-layer interaction is dominant and significantly changes the reactance that the layers would have in isolation. Thus, the formulation has to be generalized to account for this interaction if one wishes to use the analytical method for real ADL designs.

Analyses of homogeneous isotropic artificial materials made of spheres were given in [56,

81]. In this chapter, we concentrate on anisotropic artificial dielectrics (ADs) based on planar inclusions. A theory of planar ADs was reported by R. E. Collin in [55], valid for two-dimensional infinite periodic structures (arrays of strips). However, for realistic applications in integrated technology, the three-dimensional analysis of AD slabs with finite height is crucial. Simple analysis of the cascade of multiple layers were given in [82–86]. These theories neglected the higher-order coupling between adjacent layers, accounting only for the fundamental Floquet wave. Accordingly, these techniques fail when the distance between adjacent layer becomes small compared to the unit cell period. In realistic AD designs [80], such a distance can be in the order of one hundredth of the wavelength. Therefore, the reactive coupling between parallel adjacent layers must be rigorously taken into account to correctly characterize the structure. In theory, this can be done by adopting methods such as generalized admittance matrix and multi-mode equivalent networks [60, 87]. However, such methods lead to rather complex equivalent networks to represent the ensemble of metallic layers that constitute the AD, which renders the analysis difficult for arbitrary excitation. Recently, a method based on multi-modal equivalent network was presented in [88]. This method accounts for higher-order Floquet modes as lumped components, based on the assumption that the aperture field on the unit cell is known a priori.

In this chapter, we propose an analytical method to describe ADL slabs of finite thickness under generic field incidence. The form of the solution given for the single layer allows to easily extend the formulation to the multi-layer case to account for the reactive coupling between parallel layers in analytical form. Equivalent circuit models for finite AD slabs are given and used to investigate the dispersion characteristics and to evaluate the radiation patterns of a source located near to the ADL. Simulations performed with commercial software and measurements from a prototype antenna are also presented and show a good agreement with the theory developed here.

4.2 Infinite Number of Layers

ADLs are composed by several layers stacked together with very small electrical inter-layer distance, inducing a higher order interaction between adjacent sheets. In this section, we generalize the formulation presented in Ch. 3 to account for the coupling between the layers.

We first consider an infinite number of layers periodically spaced along z with inter-layer distance d_z, as shown in Fig. 4.1. By applying the equivalence theorem, we can setup an

integral equation similar to the one derived for a single layer [Ch. 3, Eq. 3.1]. The steps of the equivalence principle are explained in Fig. 4.2. When a plane wave is propagating through the infinite layer stack, it generates magnetic and electric fields on the slots (gaps between the patches) that satisfy periodic boundary conditions along z, as shown in Fig. 4.2(a). The wavenumber k_{zs} is still undefined and is related to the linear phase progression along z of the plane wave traveling in the ADL. We then apply the equivalence principle on the union of the surfaces indicated by S_{n_z} in Fig. 4.2(b), which enclose each layer. Equivalent magnetic currents can be introduced on the slot apertures, defined as in Fig. 4.2(c), while perfect electric conductor (P.E.C.) is filling the volume inside the surfaces S_{n_z}. We finally apply the image theorem to replace the P.E.C. with an infinite series of magnetic currents, as in Fig. 4.2(d).

The integral equation to be solved is obtained by imposing the continuity of the total transverse magnetic field at the interface between region 2 and region 1 in Fig. 4.2(d):

$$\sum_{n_z\text{even}} \int_{-\infty}^{\infty}\int_{-\infty}^{\infty} 4\mathbf{m}_0(\boldsymbol{\rho}')\mathbf{g}(\boldsymbol{\rho}-\boldsymbol{\rho}', n_z d_z, z=0)d\boldsymbol{\rho}' - \sum_{n_z\text{odd}} \int_{-\infty}^{\infty}\int_{-\infty}^{\infty} 2(e^{jk_{zs}d_z}+e^{-jk_{zs}d_z})\mathbf{m}_0(\boldsymbol{\rho}')\mathbf{g}(\boldsymbol{\rho}-\boldsymbol{\rho}', n_z d_z, z=0)d\boldsymbol{\rho}' = 2\mathbf{h}_i(\boldsymbol{\rho}, z=0) \quad (4.1)$$

where, without loss of generality, we impose the continuity condition of the fields at $z = 0$. The function $\mathbf{g}$ represents the dyadic Green's function which relates the magnetic field to a magnetic source. The factor 2 on the right hand side comes from the fact that the normals to the surface S_0 are equal and opposite in region 1 and region 2, i.e. $\mathbf{h}_i^{(1)} - \mathbf{h}_i^{(2)} = 2\mathbf{h}_i$, where the subscript indices refer to the corresponding region.

Since ADLs are characterized by electrically small inter-layer distance, the exponential functions in (4.1) can be approximated as $e^{jx} \approx 1 + x$ and therefore, after a few algebraic steps, the integral equation becomes

$$\sum_{n_z=-\infty}^{\infty}(-1)^{n_z}\int_{-\infty}^{\infty}\int_{-\infty}^{\infty} 2\mathbf{m}_0(\boldsymbol{\rho}')\mathbf{g}(\boldsymbol{\rho}-\boldsymbol{\rho}', n_z d_z, 0)d\boldsymbol{\rho}' = \mathbf{h}_i(\boldsymbol{\rho}, 0)\,. \quad (4.2)$$

We can solve Eq. (4.2) by applying the same procedure used for the single layer in Ch. 3 to calculate the equivalent sheet reactance. This consists of expanding the unknown magnetic current with three entire domain basis functions that describe the transverse electric (TE) and transverse magnetic (TM) components of the plane-wave-like magnetic

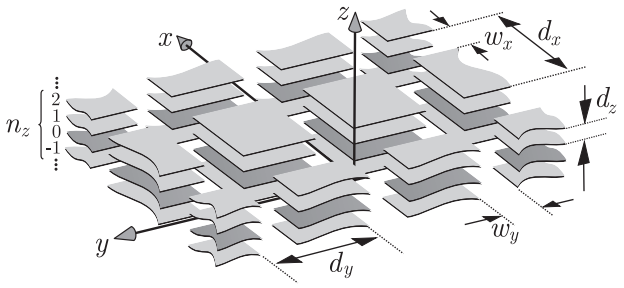

Figure 4.1: Multi-layer configuration, with highlighted the geometrical parameters.

current ($\mathbf{m}_{\mathrm{TE}}, \mathbf{m}_{\mathrm{TM}}$) and the coupling between orthogonal slots at the junction ($\mathbf{m}_{\mathrm{d}}$). By using Galerkin projection and calculating the mutual admittances, one can demonstrate, as for the single layer, that the mutual admittance between TE and TM currents can be neglected for electrically small patches (unit cell smaller than a quarter wavelength).

The only variation with respect to the single layer involves modifying the higher order Floquet modes of the Green's function, to account for the infinite sum on the indexes n_z arising from Eq. (4.2). This sum can be expressed in closed form, as described in the Appendix A.3:

$$\sum_{n_z=-\infty}^{\infty} (-1)^{n_z} e^{-jk_z|n_z|d_z} = j\tan\left(\tfrac{k_z d_z}{2}\right) \tag{4.3}$$

so that the slot susceptance in Eq. (3.22) of Ch. 3 becomes

$$B_{s\infty} = \frac{j2k_0}{\zeta_0} \sum_{m_y\neq 0} \frac{|\mathrm{sinc}(k_{ym}w_x/2)|^2}{|k_{ym}|} \tan\left(\frac{k_{zm}d_z}{2}\right) \tag{4.4}$$

where we used $k_{zm} \approx -j|k_{ym}|$ and we considered $k_{zm} \pm k_{zs} \approx k_{zm}$ for higher order Floquet modes, which is a fair assumption in virtue of the electrically dense periodicity of the structure along z. The analytical expression for the susceptance in (4.4) accounts for the higher-order interaction between layers and thus remains valid even for very small inter-layer distances. As one would expect, (4.4) tends, for increasing values of d_z, to the expression of the susceptance of the isolated layer (see Eq. (3.23) in Ch. 3): indeed, one can write $j\tan(k_{zm}d_z/2) = \tanh(|k_{ym}|d_z/2) \approx 1 - 2e^{-2\pi|m_y|d_z/d_y}$, and note that the exponential fastly tend to zero for higher order modes (increasing $|m_y|$) and even for the lowest order modes for growing values of d_z.

Analogously to the single layer case, we can write the reactance of a layer embedded in a periodic multi-layer environment as follows:

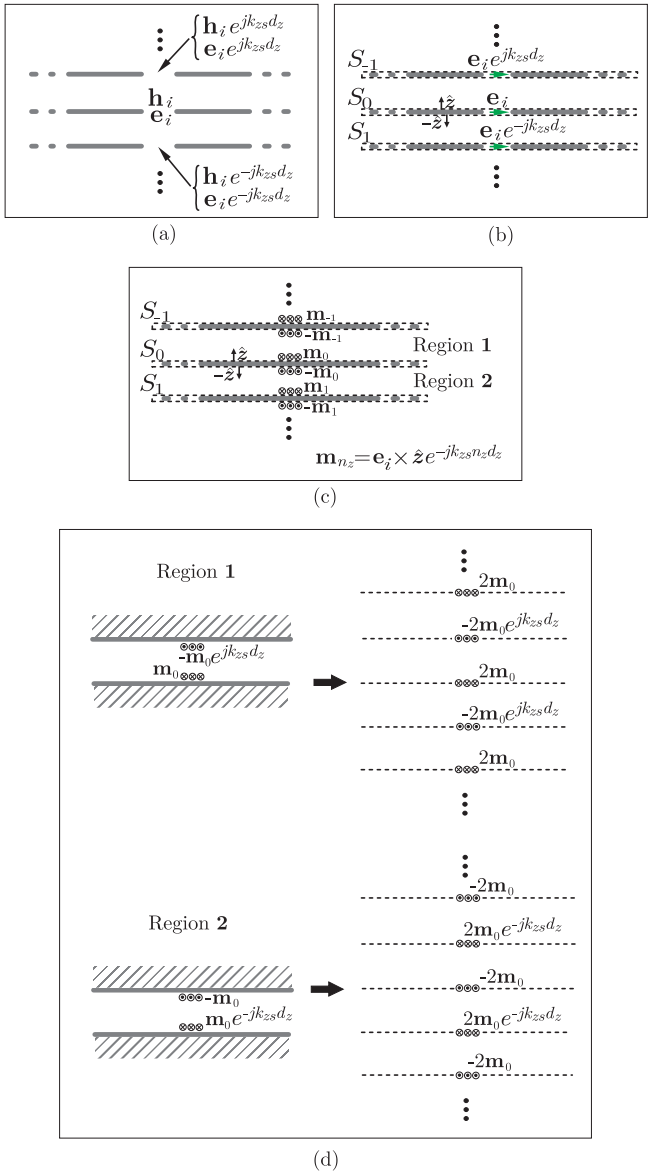

Figure 4.2: Steps of the equivalent theorem applied for the ADL: (a) original problem, (b) surface of the equivalence principle, (c) equivalent magnetic current on P.E.C. walls, (d) application of image theorem.

$$Z_{\infty,\mathrm{TM}} = \frac{-j}{B_{s\infty}}, \quad Z_{\infty,\mathrm{TE}} = \frac{-j}{B_{s\infty}(1-\frac{\sin^2\theta}{2})}\,. \tag{4.5}$$

The values of the equivalent reactance, obtained for TE and TM incidence, are shown in Fig. 4.3, for the geometrical parameters selected as $w_y = w_x = 0.03\lambda_0$, $d_y = d_x = 0.15\lambda_0$ and $d_z = 0.012\lambda_0$, with λ_0 being the wavelength at the frequency f_0. The reactance of

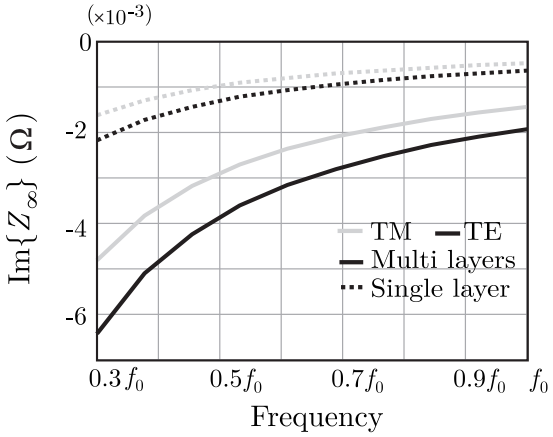

Figure 4.3: Equivalent capacitance of a layer embedded in an infinite cascade of layers along z with period $d_z = 0.012\lambda_0$, with λ_0 being the wavelength at the frequency f_0. Both TE and TM incidence from $\theta = 45°$ are considered, and the layer parameters are $w_y = w_x = 0.03\lambda_0$ and $d_y = d_x = 0.15\lambda_0$

the single layer is also reported for comparison. It can be observed that, for the same geometrical parameters, the equivalent reactance associated with an isolated layer significantly differs from the reactance of the same layer in a multi-sheet configuration, due to the reactive coupling occurring between closely spaced layers.

4.2.1 Equivalent Circuit and Effective Parameters

Once the equivalent impedance of a layer embedded in an infinite cascade is found, the ADL can be circuitally represented as a cascade of these equivalent impedances connected by transmission lines describing the plane-wave propagation through the structure. The equivalent circuit is shown in Fig. 4.4. The circuit model of a unit layer is the combination of transmission line sections and shunt loads, and can therefore be easily represented as ABCD matrix of a 2-port network. From the ABCD matrix, the effective permittivity of an homogenized dielectric medium can be easily retrieved as in [65, 66, 89] (see also Appendix B). A plot of the variation of the effective relative permittivity with the incidence angle for periodic homogenized ADL is shown in Fig. 4.5 for TE and TM incidence. Three different values of the patch size are considered, to highlight the relationship between equivalent permittivity and geometrical parameters. The structure is anisotropic, since the enhancement of the effective dielectric constant is maximum for normal incidence and decreases for oblique angles. For grazing incidence the ADLs become transparent for TM plane waves, but not for TE plane waves, being the electric field parallel to the patches.

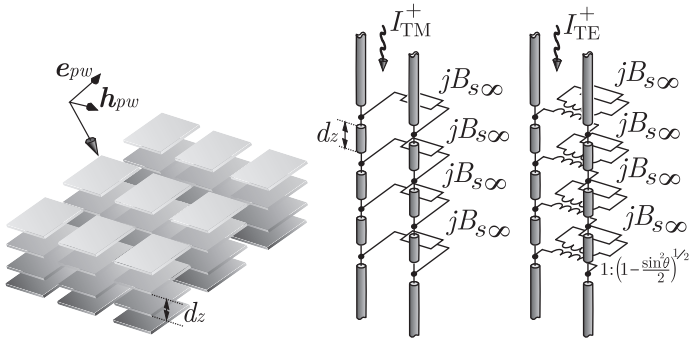

Figure 4.4: Equivalent circuit of ADL for plane wave incidence.

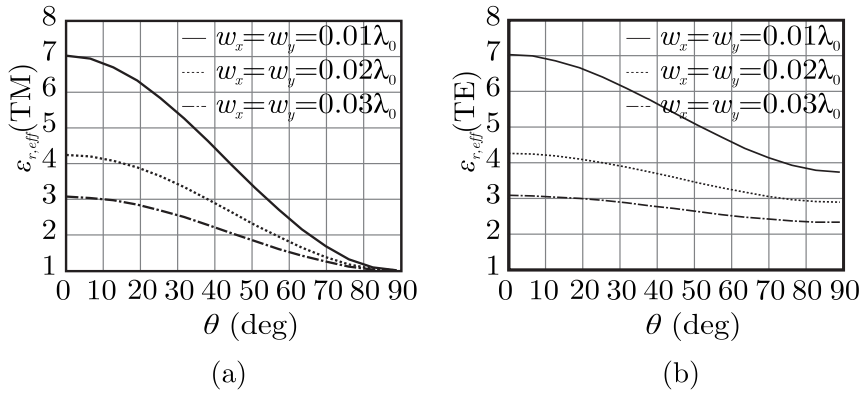

Figure 4.5: Effective relative permittivity of the homogenized ADL for z-periodic structure for (a) TM and (b) TE incidence. Array periods are set to $d_x = d_y = 0.0785\lambda_0$, with λ_0 being the wavelength at the calculation frequency. Three different sizes of patches are investigated.

4.3 Finiteness of the ADL Height

When considering a finite number of layers N_z, we can approximate the reactance of each layer with its infinite periodic solution. The results for the scattering parameters obtained with this approximation is compared in Fig. 4.6 with HFSS simulations [64]. The figure shows the magnitude and the phase of the reflection and transmission coefficients of a plane wave for normal incidence on a cascade of 4 layers. Although the comparison shows a fair agreement, the level of accuracy of our method can be further improved by accounting for truncation effects. With this goal, we propose a correction to the solution derived from the infinite case.

For each layer of the artificial dielectric, the reactive coupling with adjacent layers is mainly dominated by the coupling with the two layers immediately below and above. The infinite

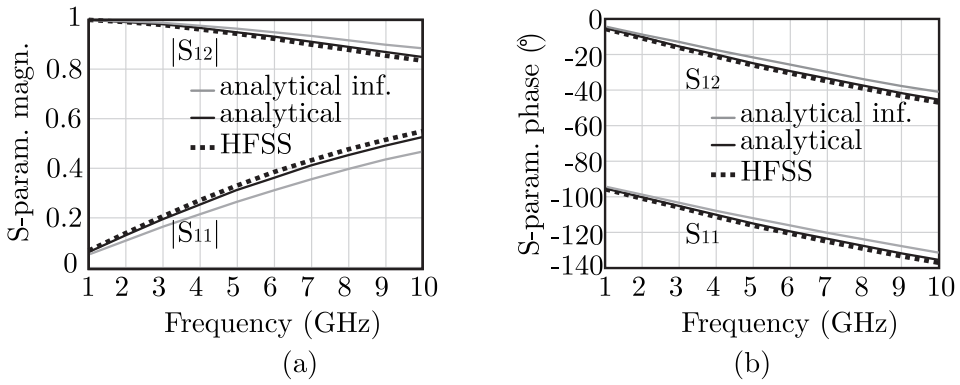

Figure 4.6: (a) Magnitude and (b) phase of the scattering parameters of a plane wave incident normal to a cascade of 4 layers. Dimensions are $w_x = w_y = 0.03\lambda_0$, $d_x = d_y = 0.15\lambda_0$, $d_z = 0.012\lambda_0$.

approximation of the admittance can be then considered a good approximation for inner layers in a finite structure. However, this is not the case for the first and the last layers (i.e. $n'_z = 0$ and $n'_z = N_z - 1$) of the finite stack. For these two elements, a semi-infinite solution would be more accurate, because it accounts for the truncation. The solution for a semi-infinite summation can be easily calculated in a closed form by modifying Eq. (4.3) as follows:

$$\sum_{n_z=-\infty}^{0}(-1)^{n_z}e^{jn_z k_z d_z} = \sum_{n_z=0}^{\infty}(-1)^{n_z}e^{-jn_z k_z d_z} = \frac{1+j\tan\left(\frac{k_z d_z}{2}\right)}{2} \tag{4.6}$$

where we used Eqs. (A.61) and (A.64) of the Appendix A. By considering these modified formulas, the expression of the susceptance of the first (i.e. $n'_z = 0$) and last layer (i.e. $n'_z = N_z - 1$) becomes

$$B_{s,\text{semi-}\infty} = \frac{k_0}{\zeta_0}\sum_{m_y\neq 0}\frac{|\text{sinc}(k_{ym}w_x/2)|^2}{|k_{ym}|}\left(1+j\tan\left(\tfrac{k_{zm}d_z}{2}\right)\right) \tag{4.7}$$

and the modified equivalent circuit for a cascade of four layers is shown in Fig. 4.7. This circuital representation yields a more accurate estimation of scattering parameters, as shown in Fig. 4.6. Indeed, it can be noted that the solution obtained with the correction, i.e. by using (4.7) for the edge layers, is closer to the one obtained with HFSS full-wave simulations. Also the case of a plane wave incident from the direction $\theta = 60°$ on the same 4-layer stack, both for TE and TM incidence, is reported in Fig. 4.8, showing a good agreement with HFSS simulated results.

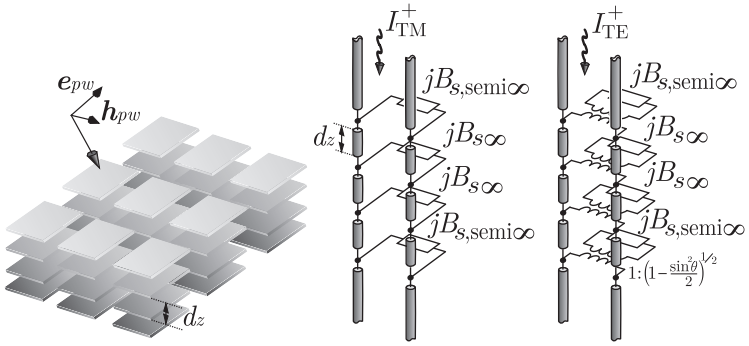

Figure 4.7: Equivalent circuit of ADL for plane wave incidence, considering semi-infinite solution for the edge layers.

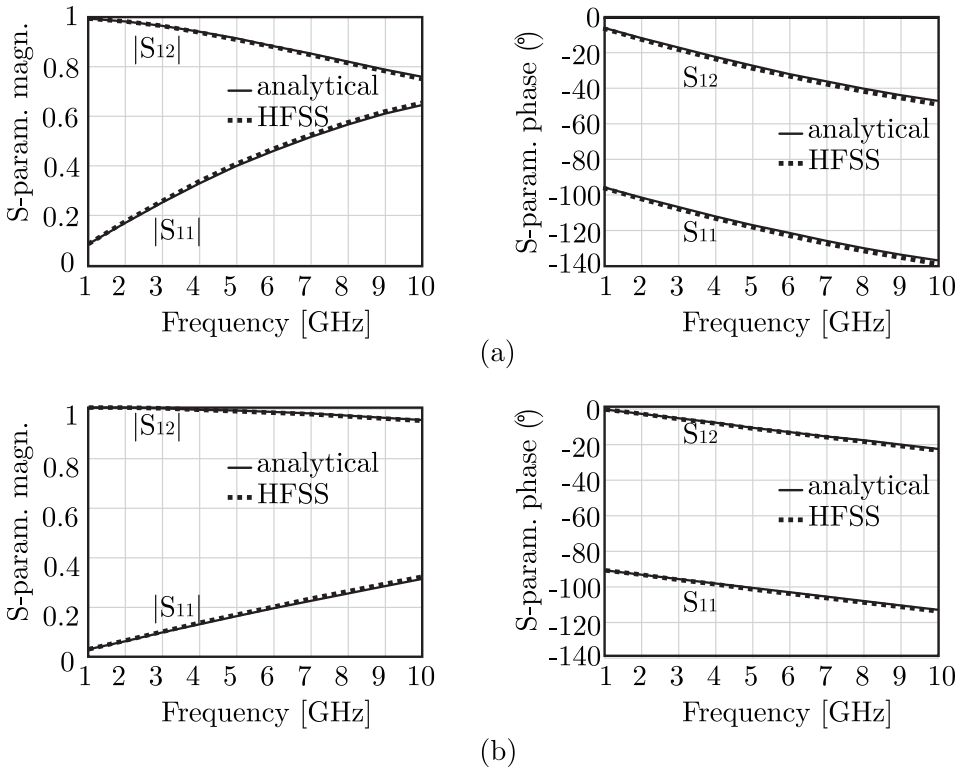

Figure 4.8: As in Fig. 4.6, but for (a) TE incidence from $\theta = 60°$ and (b) TM incidence from $\theta = 60°$.

4.4 Magnetic Current Distribution in ADL

The equivalent circuit in Fig. 4.7 can be used also to calculate the magnetic current distribution on each layer of the ADL slab. As for the single layer solution reported in Ch. 3, the magnetic current is written as the sum of three entire domain basis functions

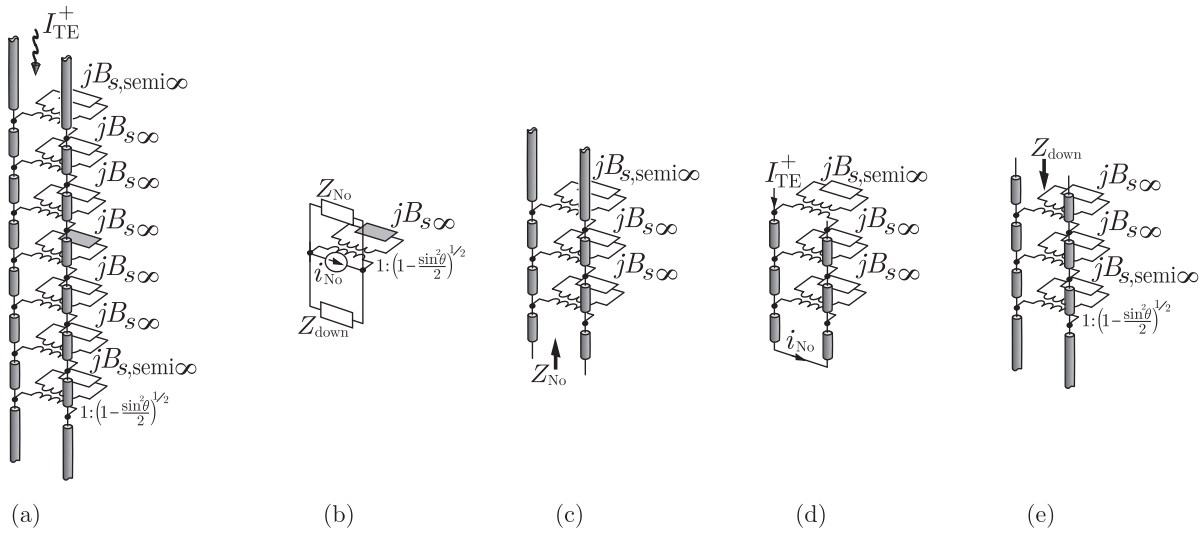

Figure 4.9: (a) Equivalent circuit of 7-layer ADL for TE plane wave incidence; (b) Norton equivalent circuit to calculate the magnetic current on a layer within the cascade; definition of the (c) equivalent Norton impedances, (d) the equivalent current generator and (e) the input impedance of the lower stratification.

weighted by the coefficient ($a_{\rm TE}$, $a_{\rm TM}$, $a_{\rm d}$).

Let us consider, as an example, a cascade of 7 layers illuminated by a TE incident plane wave. To calculate the magnetic current distribution on a layer (e.g. the central one $n_z = 3$), we can start from the equivalent circuit in Fig. 4.9(a) and apply the Norton equivalence as described in Fig. 4.9(b): the equivalent Norton impedances ($Z_{\rm No}$), the equivalent current generator ($i_{\rm No}$) and the input impedance of the lower stratification ($Z_{\rm down}$) can be easily evaluated from the circuit in Figs. 4.9(a), (b) and (c), respectively. The same procedure can be used for each layer in the cascade and for TM incidence.

Once the equivalent parameters of the Norton circuit are evaluated, the unknown weights for the basis function expansion of the magnetic current are then given by expressions very similar to (3.26) and (3.27) in Ch. 3:

$$\begin{aligned} a_{\rm TE} &= -2I_{\rm TE}\left(\tfrac{1}{Z_{\rm down}}+\tfrac{1}{Z_{\rm No}}+jB_{s\infty}\left(1-\tfrac{\sin^2\theta}{2}\right)\right)^{-1} \\ a_{\rm TM} &= -2I_{\rm TM}\left(\tfrac{1}{Z_{\rm down}}+\tfrac{1}{Z_{\rm No}}+jB_{s\infty}\right)^{-1} \end{aligned} \tag{4.8}$$

and

$$a_{\rm d} = \begin{cases} a_{\rm TE}\frac{jB_{s\infty}\sin\theta\cos(2\phi)}{2\widetilde{Y}} & \text{for TE incidence} \\ -a_{\rm TM}\frac{jB_{s\infty}\sin\theta\sin(2\phi)}{2\widetilde{Y}} & \text{for TM incidence} \end{cases} \tag{4.9}$$

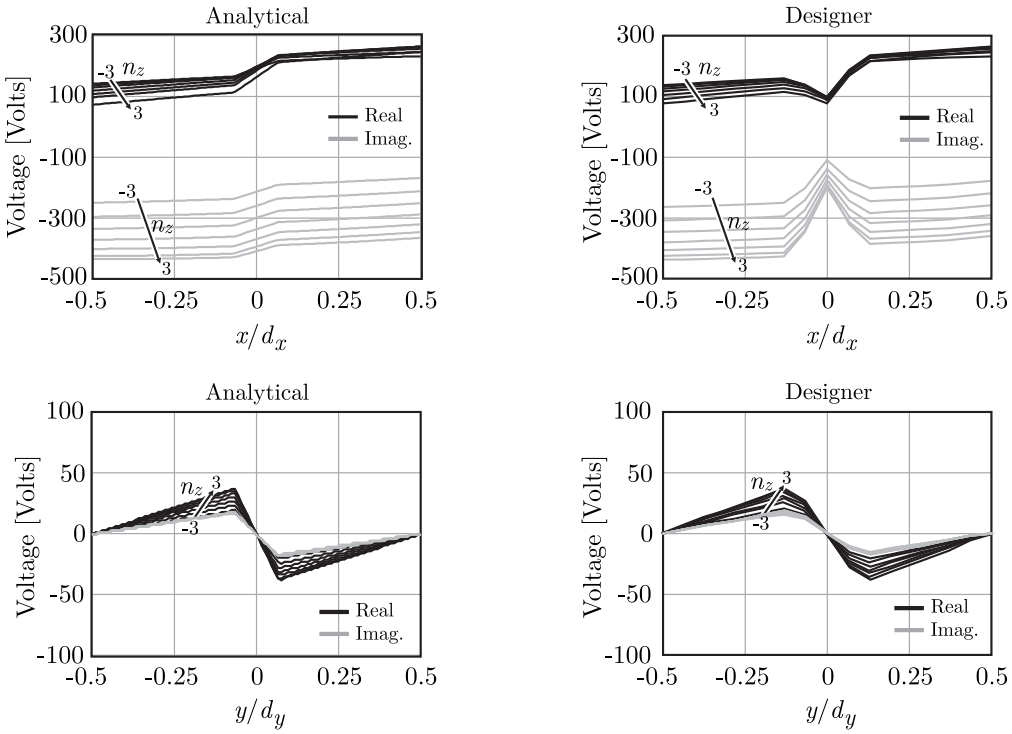

Figure 4.10: Voltages for TE incidence at $\theta = 60°$, $w_x = w_y = 0.01\lambda_0$, $d_x = d_y = 0.0785\lambda_0$ and $d_z = 0.012\lambda_0$.

where

$$\widetilde{Y} \approx \frac{-2}{\zeta_0 d_y} \sum_{m_y \neq 0} \operatorname{sgn}(k_{ym}) \operatorname{sinc}\left(\frac{k_{ym} w_x}{2}\right) \cdot B^*_{\mathrm{d},y}(-k_{ym}) \tan(k_{zm} d_z/2)\,. \tag{4.10}$$

The expression in (4.10) is similar to Eq. (3.27) in Ch. 3, but it is now valid for multi-layer structure. Figure 4.10 shows the voltage distribution along the x- and y- oriented slots on each array for a 7-layer cascade, under TE incidence at $\theta = 60°$. The geometrical parameters are $w_x = w_y = 0.01\lambda_0$, $d_x = d_y = 0.0785\lambda_0$ and $d_z = 0.012\lambda_0$. The results of our analytical circuit agree well with ANSYS Designer [78] simulations.

4.5 ADL Green's Function

So far we have analyzed artificial dielectrics under plane-wave illumination. We have described, by means of a simple equivalent circuit model, the scattering, propagation and transmission of an arbitrary plane wave through a finite-height stack of layers. The lumped elements of this equivalent circuit are analytical and depend on the specific polarization

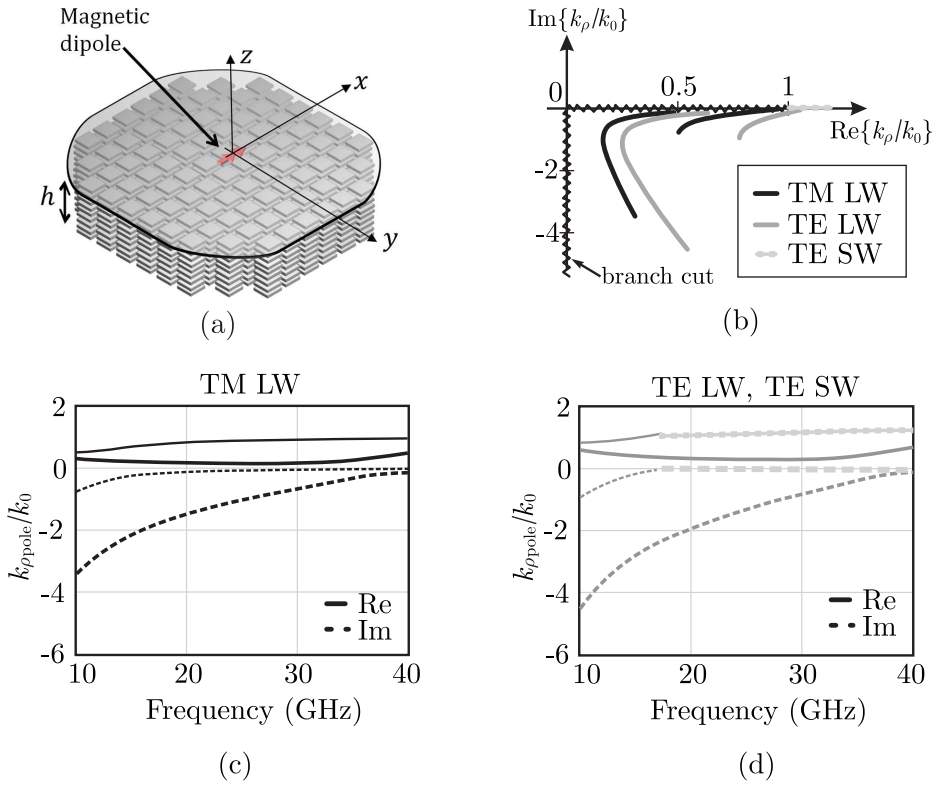

Figure 4.11: (a) ADL ground slab excited by a magnetic dipole; (b) polar singularities of the ADL Green's function on the complex k_ρ-plane; (c) and (d) dispersion curves of for TM and TE slab modes, respectively.

and angle of the incident plane wave, as well as on the geometrical parameters of the structure.

However, in realistic applications with integrated antennas, the field incident on these structures is not a plane wave but the near field of an antenna that is typically very close to the ADL. These more general cases can be also treated with our model, by expanding any generic incident field in a spectrum of plane waves and apply the analytical equivalent circuit to each of these plane waves.

We can then define a spectral Green's function of the ADL $\mathbf{G}^{\mathrm{ADL}}(k_\rho, \alpha, z)$ for a generic TE or TM plane wave with wavenumbers $k_x = k_\rho \cos\alpha$ and $k_y = k_\rho \sin\alpha$. This Green's function is provided analytically since is related to the current and voltage solutions of the equivalent transmission line models such as the one in Fig. 4.9(a).

4.5.1 Dispersion Characteristics of ADLs

Let us consider a x-oriented magnetic dipole located on a ground plane of a grounded ADL slab, as shown in Fig. 4.11(a). The polar singularities of the TE and TM component of the dyadic Green's function, i.e. the zeros of their inverse functions $1/G_{\mathrm{TE}}^{\mathrm{ADL}}$ and $1/G_{\mathrm{TM}}^{\mathrm{ADL}}$, can be found by applying a simple Newton method starting from an opportune initial point on the complex k_ρ-plane.

As an example, we consider a slab with 9 layers in free space with $d_x = d_y = 2$mm, $d_z = 0.26$mm and $w_x = w_y = 0.3$mm. The total height of the slab is $h = 2.34$mm, and the equivalent relative permittivity is 10 for normal incidence, in such a way that the artificial dielectric slab is effectively about a quarter-wave thick at 10 GHz. The zeros search leads to the polar singularities in Figs. 4.11 (b),(c),(d). It can be noted that, for TM incidence, the poles of the spectral Green's function are complex with an imaginary part, and therefore they are associated with the propagation of leaky waves. For increasing frequency the poles become dominantly real with smaller imaginary parts and tend to coincide with the branch point $\pm k_0$. Similar types of leaky waves are supported also for TE incidence. However additional, TE surface waves are present for slabs with electrically height $h > 0.3\lambda_{\mathrm{eff}}$. Such a kind of surface wave propagation is only occurring for TE incidence since the ADL is transparent for TM grazing incidence, while it still provides a permittivity enhancement for TE grazing incidence (Fig. 4.5).

The elementary magnetic dipole can be practically implemented as an electrically small slot aperture on the ground plane, with length l_s and width w_s. In this case, the spectrum of the magnetic current distribution in spectral polar coordinates can be expressed as

$$\mathbf{M}_s(k_\rho, \alpha) = \mathrm{sinc}\left(\frac{l_s}{2} k_\rho \cos\alpha\right) J_0\left(\frac{w_s}{2} k_\rho \sin\alpha\right) \hat{\mathbf{x}} \tag{4.11}$$

where the sinc function is the Fourier transform of the longitudinal distribution, assumed to be constant, whereas J_0 is the zeroth order Bessel function, which is the Fourier transform of the transverse edge singular distribution.

The radiated magnetic field in polar coordinates can be calculated as the following convolution integral

$$\mathbf{h}(\rho, \phi, z) = \frac{1}{4\pi^2} \int_{\infty}^{\infty} \int_{\infty}^{\infty} \mathbf{M}_s(k_\rho, \alpha) \cdot \mathbf{G}^{\mathrm{ADL}}(k_\rho, \alpha, z) e^{-jk_\rho \rho \cos(\alpha - \phi)} k_\rho dk_\rho d\alpha. \tag{4.12}$$

The Green's function $\mathbf{G}^{\mathrm{ADL}}$ links the magnetic field to the magnetic source. The electric field can be calculated in an analogous way by using the Green's function relating the electric field to the magnetic source.

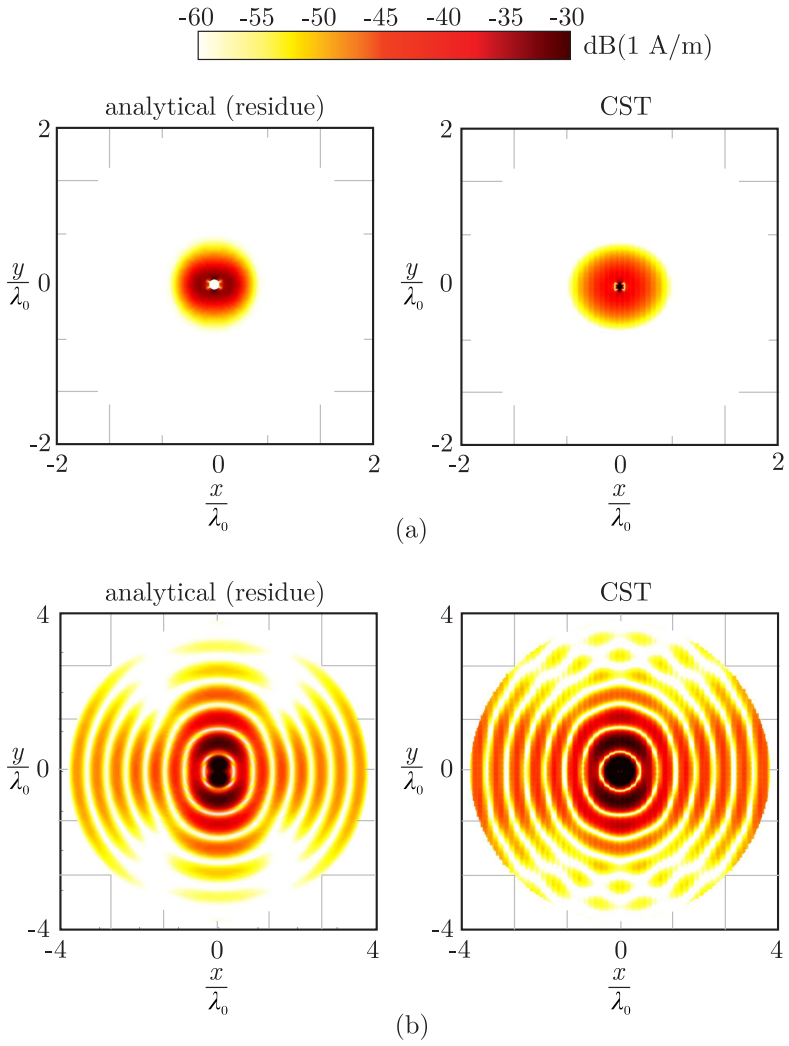

Figure 4.12: x-component of the magnetic field on the ground plane for the structure in Fig. 4.11(a). The comparison with CST simulations is shown at (a) 10 GHz and (b) 20 GHz.

The contributions of the integral (4.12) due to the polar singularities can be extracted in analytical form by applying the residue theorem. As an example, Fig. 4.12 shows x-component of the magnetic field on the ground plane for the structure in Fig. 4.11(a). The analytical residue contribution due to the dominant singularity of the Green's function is compared with CST simulations [69] at 10 GHz and 20 GHz. It can be noted that, for slab thickness of $h \approx \lambda_{\text{eff}}/4$ (at 10 GHz) no surface waves are supported by the slab and the field distribution is concentrate close to the feed. The field distribution at 20 GHz, for which $h \approx \lambda_{\text{eff}}/2$, is instead dominated by a TE surface wave and a slowly attenuating TM leaky wave.

4.5.2 Radiation Patterns from a Near Source

We describe in this section a method based on plane-wave expansion [90], aiming at calculating with minute computational efforts the radiation patterns radiated by the ADL-loaded antenna. A generic field radiated by the source can be expanded in a spectrum of plane waves. We assume that the known spectrum of the source current distribution is indicated by $M_{\mathrm{s}}(k_x, k_y)$ and oriented along x. We can apply the asymptotic evaluation of the radiation integrals for far-field observations. Defining the observation point as $(\mathbf{r}_o)$ or (θ_o, ϕ_o) or (x_o, y_o, z_o), we can write the generic ξ-component of the radiated magnetic field in the far-field region as follows:

$$h_\xi(\mathbf{r}_o) \approx 2jk_{zo} M_{\mathrm{s}}(k_{xo}, k_{yo}, z_o) G_{\xi x}^{\mathrm{ADL}}(k_{xo}, k_{yo}, z_o) \tag{4.13}$$

where $k_{xo} = k_0 \sin\theta_o \cos\phi_o$, $k_{yo} = k_0 \sin\theta_o \sin\phi_o$, and $k_{zo} = k_0 \cos\theta_o$. The field in Eq. (4.13) depends on the component of ADL Green's function $G_{\xi x}^{\mathrm{ADL}}$. Such Green's function is calculated as explained in Fig. 4.13. We first consider the equivalent transmission line of the ADL for a given plane wave direction (k_{xo}, k_{yo}) for a TE or TM mode, as depicted in Fig. 4.13(a). The circuit model for each plane wave can be conveniently represented in terms of its equivalent [ABCD] or impedance matrix (Fig. 4.13(b)). We then construct the equivalent Thevenin generator (with voltage V_{Th}) and impedance Z_{Th} to solve for the voltage and current at a generic observation point z_o on the transmission line, as shown in Fig. 4.13(c). Every component of the dyadic spectral Green's function is just a linear combination of the TE and TM voltage and current solutions on the line (the subscript 'Ti' in Fig. 4.13(c) can indicate TE or TM).

4.5.3 Validation of Radiation Pattern Calculation

As an example, we consider a short slot in the presence of an ADL slab, as depicted in Fig. 4.14. We assume a piecewise sinusoidal voltage distribution on the slot, characterized by a known spectrum $M_{\mathrm{PWS}}(k_x, k_y)$. Each layer of the artificial dielectric is characterized by the following geometrical parameters: $w_x = w_y = 0.01\lambda_0$ and $d_x = d_y = 0.0785\lambda_0$ with λ_0 being the wavelength at the calculation frequency. The distance between layers is $d_z = 0.012\lambda_0$. The source slot has width and length of $0.033\lambda_0$ and $0.133\lambda_0$, respectively, and it is etched on a ground plane at a distance of d_z from the ADL.

We calculate the radiation pattern from Eq. (4.13) and compare with results obtained with CST microwave studio [69] in Fig. 5.11. The results are in very good agreement.

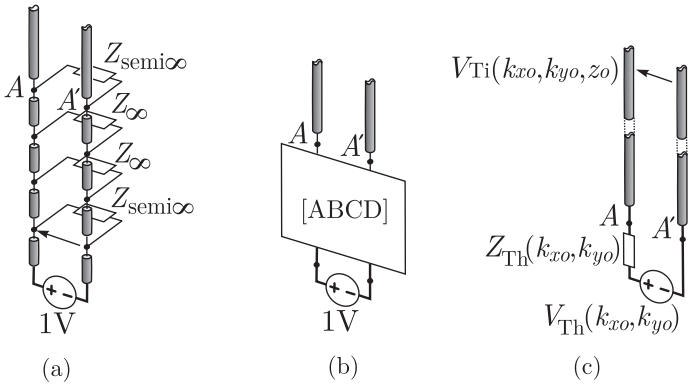

Figure 4.13: (a) Equivalent circuit of the ADL illuminated by an elementary magnetic dipole on a ground plane; (b) equivalent ABCD matrix of the ADL; (c) equivalent Thevenin representation of the source and the ADL.

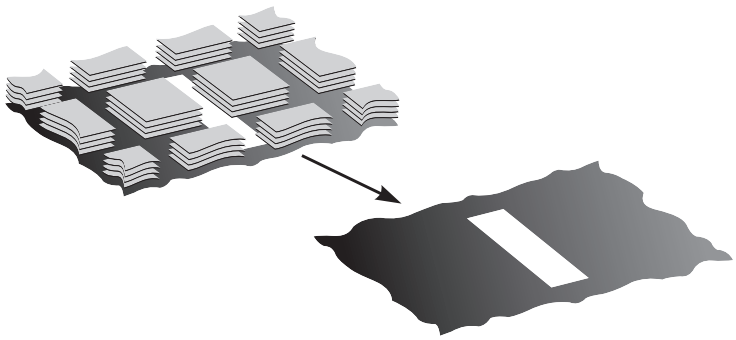

Figure 4.14: Slot in the presence of an ADL slab. The ADL parameters are $w_x = w_y = 0.01\lambda_0$ and $d_x = d_y = 0.0785\lambda_0$ with λ_0 being the wavelength at the calculation frequency. The distance between layers is $d_z = 0.012\lambda_0$. The slot has width and length of $0.033\lambda_0$ and $0.133\lambda_0$, respectively, and it is etched on a ground plane at a distance of d_z from the ADL.

We point out that in our method we have not considered the transverse finiteness of the structure, but just the finiteness along z. However, the CST simulation we are comparing with include also the transverse finiteness and do not show major discrepancy with our infinitely periodic model.

4.6 Conclusions

We proposed an analytical method for the characterization of artificial dielectric layers (ADL) of finite height, under arbitrary field illumination. The methods exploits a closed-

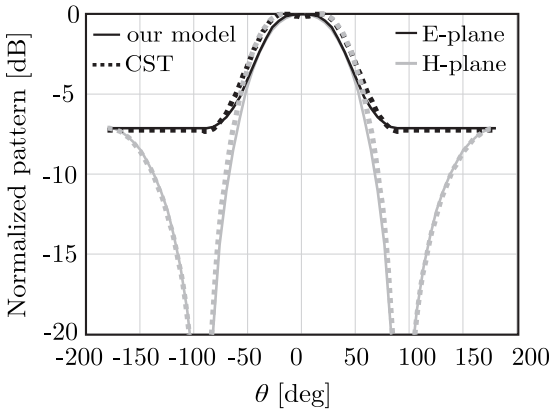

Figure 4.15: The far-field radiation pattern of a slot radiating in the presence of ADL geometry shown in Fig. 4.14.

form formulation developed in Ch. 3 to describe a single layer. The formulas valid for the single layer were generalized here to treat the cases of an infinite or semi-infinite cascade of layers. The reactive coupling between adjacent layers is rigorously taken into account in analytical form.

An equivalent circuit was derived, which can be used to calculate, on one hand, the effective parameters of the ADL and, on the other hand, the spectral Green's function of the ADL. This latter allows to evaluate the dispersion characteristic of finite slabs, and the patterns of a generic antenna in the presence of the ADL. The calculated patterns were validated with the simulations performed with commercial EM solvers.

Chapter 5

Front-to-Back Ratio Enhancement of Planar Printed Antennas by Means of Artificial Dielectric Layers

5.1 Introduction

Artificial dielectric layers (ADLs) based integrated solutions have been recently proposed for THz frequency domain spectroscopy [91] and THz anti-reflection coating [92]. In [57], authors have exploited the concept of ADLs in commercial complementary metal-oxide-semiconductor (CMOS) technology to reduce the size of on-chip passive components. The use of ADLs has also led to a significant reduction in ohmic losses, since they are directly proportional to the device physical dimensions. In [44,45], ADL have been used to minimize the volumetric occupation of the resonant cavities in so-called Fabry-Perot type antennas. Planarity and integrability render ADLs a promising candidate to be considered for the design of planar integrated antennas. In the design of such antennas, a good front-to-back radiation ratio ($>$ 10 dB) can be achieved by using a dense dielectric slab of thickness in the order of quarter wavelength $\lambda_d/4$. Here, λ_d represents the wavelength inside the dielectric of permittivity ε_r at the central frequency of the matching bandwidth. However, the surface wave efficiency of such antennas is quite poor and can severely deteriorate the quality of the radiation patterns [51, 52]. To overcome this problem, other planar solutions have been proposed, which typically shape the antenna elements themselves or their immediate surroundings. For instance, in [46] it has been shown that 99.9% radiation efficiency can be obtained by using a twin arc slot antenna, where the slots generate equal and opposite surface wave in every radial direction. The antenna is then backed by a cavity

to increase the front-to-back radiation ratio. A circularly symmetric electromagnetic band gap (EBG) based solution, again completely planar, has been presented in [51–53] to minimize the surface wave coupling between the neighboring elements of an antenna array. The design works over a bandwidth in the order of 20%. However, usage of the EBGs in array configuration results in limiting the scanning to only one plane because of the large radii of the proposed EBG rings.

5.2 Antenna Concept

In this chapter, the use of ADLs is proposed in order to enhance the performance of an antenna printed on a dielectric slab having $\varepsilon_r = 3.66$ and thickness in the order of $\lambda_d/10$. Since the slab is electrically thin, it supports minimal excitation of the surface waves, but the front-to-back radiation ratio of an antenna radiating in the presence of this slab is extremely poor. To increase the front-to-back ratio, the permittivity of this slab is enhanced by loading it with planar and periodically stacked ADL inclusions. The periodic metallic loading consists of multilayer non-resonant array of square patches which brings the effective dielectric constant (ε_{eff}) of the slab to 20 for the wave propagating normal to the stratification. In this way, a dielectric slab with effective height in the order of quarter wavelength can be realized on an electrically thin substrate. A double slot antenna, which is widely used at the THz frequencies [37], is then attached on the back side of this ADL loaded slab (see Figs. 5.2 and 5.9).

Thanks to the dielectric enhancing properties of the ADLs, a front-to-back radiation ratio greater than 10 dB over 10% bandwidth is achieved as it will be shown in the remainder of this chapter. The front-to-back ratio that can be achieved via the use of ADL materials is comparable to the one that can be achieved with the stacked patch antenna concept [41]. The advantage of solution presented here is that the ADL can be "designed" independently of the antenna. Whereas in the case of stack patches, the resonances of the multiple patches are needed to be tuned together. Also, ADLs can be manufactured and placed on top of an antenna without a fine alignment between the two. Furthermore, this concept can be extended to built two-dimensional arrays for scanning in both the planes, without incurring scan blindness introduced by the large periodicity or by surface waves.

The chapter is structured as follows. ADLs based planar antenna design is presented in Sec. 5.3 and the performance of this antenna is compared to the antenna design without the ADL inclusions. A prototype antenna was also manufactured and the measurement results are reported in Sec. 5.4.

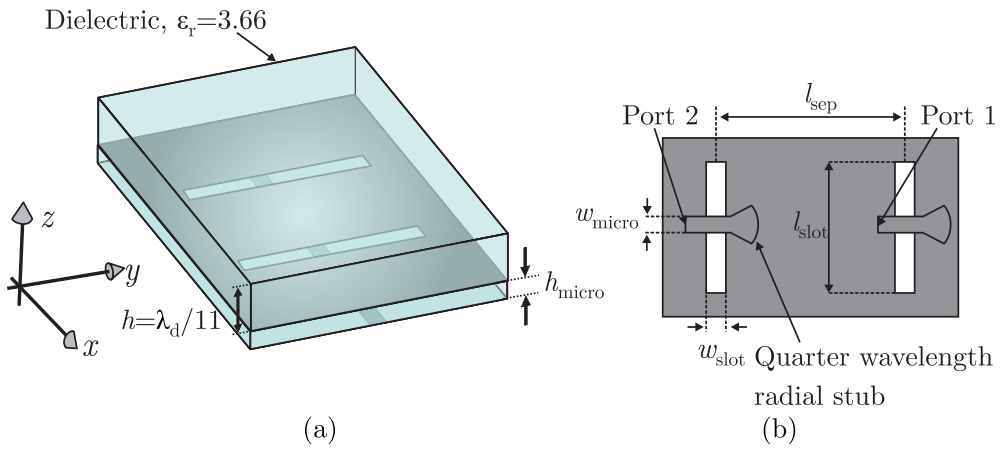

Figure 5.1: (a) A twin slot antenna radiating in a finite dielectric slab. (b) Two dimensional view of microstrip feed lines and the twin slots.

5.3 Antenna Design

The design of a twin slot antenna in X-Band is discussed in this section. The antenna is coupled to an electrically thin dielectric substrate, which is enhanced by an ADL.

5.3.1 A Double Slot Radiating in a Finite Dielectric Slab

As a starting point, let us consider, as shown in Fig. 5.1(a), a double slot antenna radiating in the presence of a dielectric slab of $\varepsilon_{\mathrm{r}} = 3.66$ and height $h = 1.42$ mm ($\lambda_d/11$). The parameter $\lambda_d = 15.7$ mm is the wavelength inside the dielectric at 10 GHz. The height of the dielectric slab is small enough to ensure that minimal amount of power is coupled to surface wave modes. The double slot antenna, as depicted in Fig. 5.1(b), consists of two identical slots of length $l_{\mathrm{slot}} = 19$ mm and width $w_{\mathrm{slot}} = 2.0$ mm which are separated by a distance $l_{\mathrm{sep}} = 11$ mm. These slots are oriented along the y-axis and the input signal is fed by two x-oriented microstrip lines each of width $w_{\mathrm{micro}} = 1.8$ mm. To avoid vertical pins, the coupling between the slots and the microstrip lines is achieved using quarter wavelength radial stubs. Moreover, the planes containing the microstrip feeding lines and the radiating slots are separated by a dielectric substrate of thickness $h_{\mathrm{micro}} = 0.355$ mm and $\varepsilon_{\mathrm{r}} = 3.66$. Also, the dielectric slab is considered to be lossless and finite conductivity material (Copper, $\sigma = 5.8 \times 10^7$ S/m) is assumed for all the metallic parts.

5.3.2 Double Slot Radiating in a Finite Dielectric in the Presence of ADLs

In Fig. 5.2, a double slot antenna similar to the one discussed in previous subsection is shown. This antenna also radiates in the presence of a dielectric slab that has the same permittivity and height as the one depicted in Fig. 5.1. However, this dielectric slab is now loaded by 4 layers of artificial dielectrics along the z-axis, separated by a distance $d_z = 0.355$ mm ($0.023\lambda_d$). These planar ADLs are composed of finite array of 17×17 electrically small square metallic patches. The width of the gap between neighboring patches is $w_x = w_y = 0.31$ mm ($0.02\lambda_d$) and the period is $d_x = d_y = 2.35$ mm ($0.15\lambda_d$). By using the formulation discussed in Ch. 3 and 4, the aforementioned geometrical dimensions of the ADLs result in an effective dielectric constant of $\varepsilon_{\text{eff}} = 20$ for the waves which are incident normal to the metallic layers. Therefore stacking four of these layers, as shown schematically in Fig. 5.2, leads to the realization of a dielectric slab that has an effective height in the order of quarter wavelength ($\approx 0.25\lambda_{eff}$). Moreover, to achieve the resonance around 10 GHz in the presence of ADLs, the parameters l_{slot} and l_{sep} are changed to 10.95 mm and 10 mm from 19 mm and 11 mm, respectively.

5.3.3 Simulation Results

The two antenna geometries, described above are then simulated using CST Microwave Studio [69]. The active reflection coefficient for both the cases is reported in Fig. 5.3. The -10 dB relative matching bandwidth is slightly smaller, in the order of 14%, for the case including the ADLs, when compared with the bandwidth of the antenna in absence of inclusions (20%). Figure 5.3 also reports S12, which is lower in case of ADL enhanced slab.

Figure 5.4 shows the radiation patterns (gain) calculated for the double slot antenna printed on a homogeneous dielectric and the ADLs enhanced slab. The far-field gain patterns are reported for three different frequencies in the E- and H-planes. It can be observed that the radiation patterns of the antenna without ADLs, despite the finite size of the slab is taken into account, do not show large oscillations. Such oscillations are typically associated with the surface waves being diffracted from the edges. This is because the dielectric slab is taken thin enough so that it does not support surface waves. Also, the far-field radiation patterns for both the antennas are qualitatively similar in the upper ($z > 0$) half spaces. However, in the case of ADL, the gain is significantly larger for observations in the upper half space. A clear difference instead appears in the radiation towards the lower ($z < 0$)

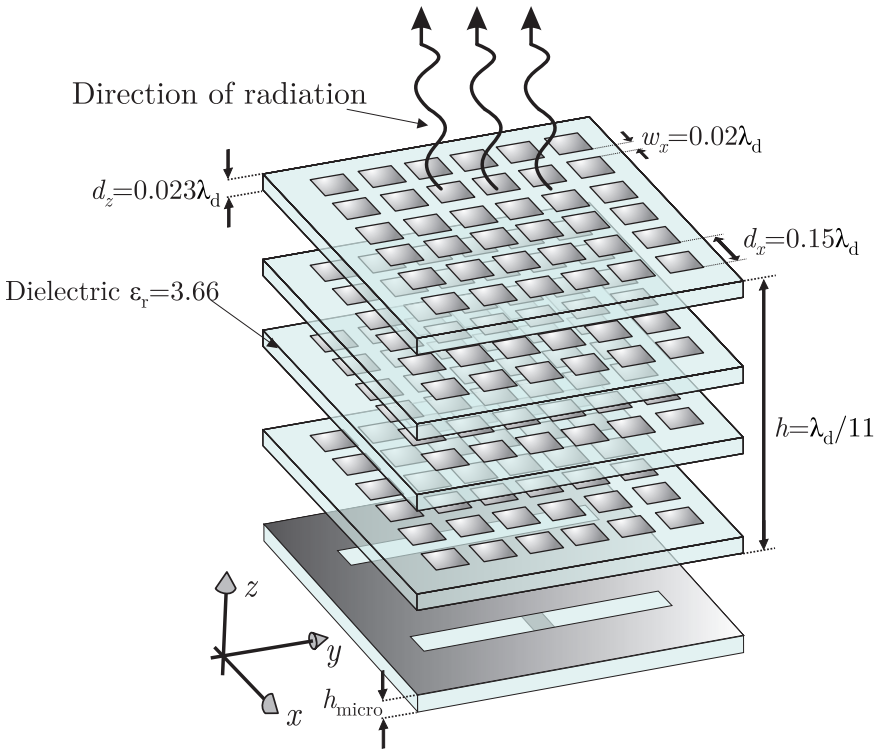

Figure 5.2: An exploded view of a twin slot antenna radiating in the presence of ADLs.

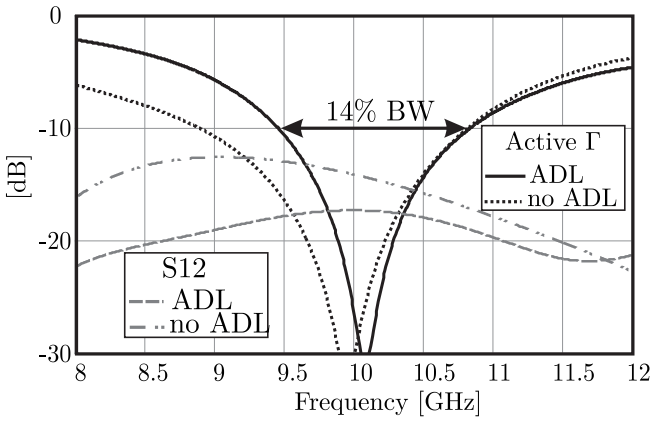

Figure 5.3: Simulated two port active reflection coefficient (Γ) and the mutual coupling (S12) between the two slots.

half space, where the ADL enhanced antenna is generating a very low back radiation. Consequently, as shown in Fig. 5.5, a front-to-back ratio greater than 10 dB over a wide frequency range can be achieved. This is the key advantage of using ADL enhanced slabs.

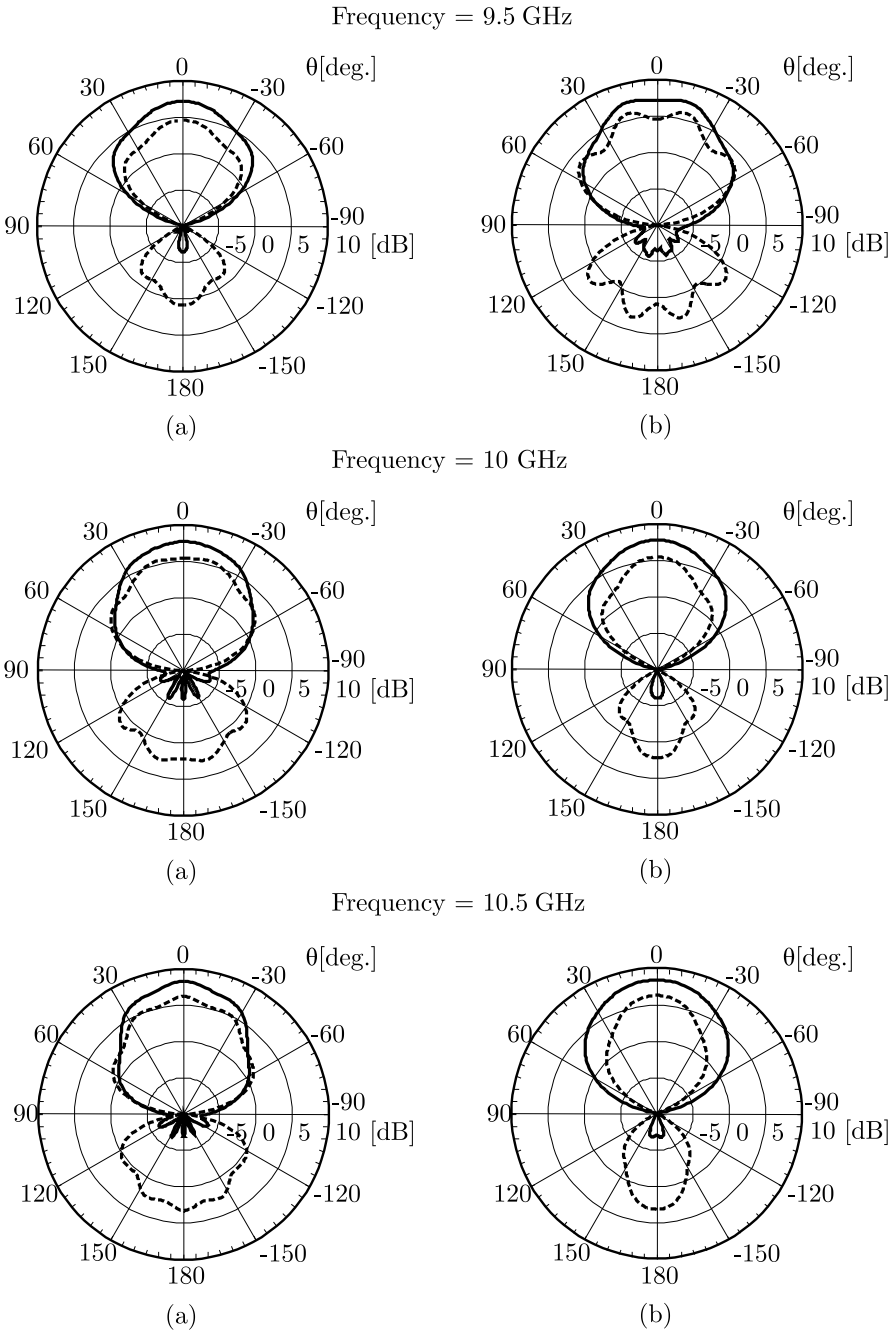

Figure 5.4: Far-field gain plots (expressed in dBi) of the antenna for different frequencies in (a) E- and; (b) H-plane. The dashed line $(--)$ represents the radiation pattern in the absence of ADL, whereas the solid line $(-)$ represents the radiation pattern in the presence of ADL.

This graph also shows that, in the absence of ADLs, the front-to-back ratio is in the order of 2.5-3 dB over the whole frequency range. As a result, the gain of the ADL enhanced

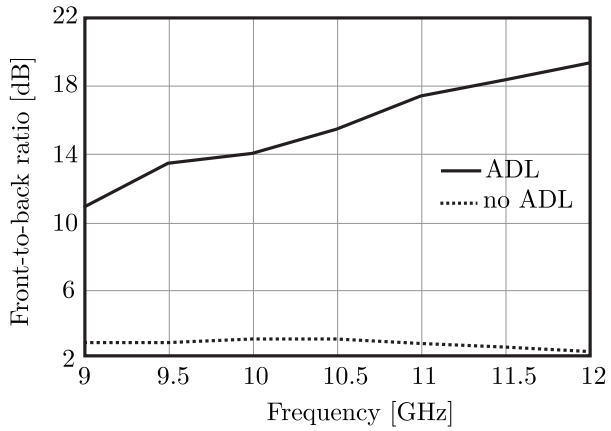

Figure 5.5: Simulated front-to-back radiation ratio.

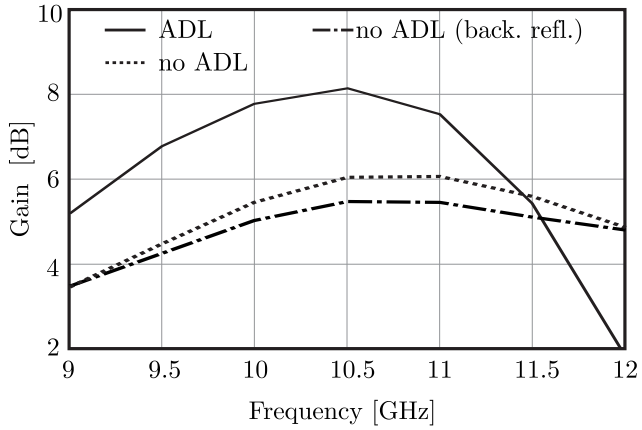

Figure 5.6: Simulated gain versus frequency. The values of the gain are along the broadside direction.

antenna, as depicted in Fig. 5.6, is increased by almost 2 dB over the matching bandwidth without compromising the pattern quality. Note that the broadside gains shown in Fig. 5.6 include ohmic as well as the mismatch losses. In the same graph, we also report the gain of the antenna without ADL (conceptually Fig.5.1) in the presence of a backing reflector. The latter is placed at a distance of $\lambda_0/4$ along the negative z-axis from the plane containing the double slot antenna. The gain in this case is even lower (< 6 dB), due to the excitation of parallel plate wave guide (PPW) modes, with the far-field patterns (not shown) having ripples in the main beam. The excitation of the PPW modes can only be avoided in a narrow frequency band by shaping the slots [46].

Finally, the curves in Fig. 5.7 show the simulated ohmic losses and the surface wave losses as a function of the frequency. The simulation results show that the ADL inclusions

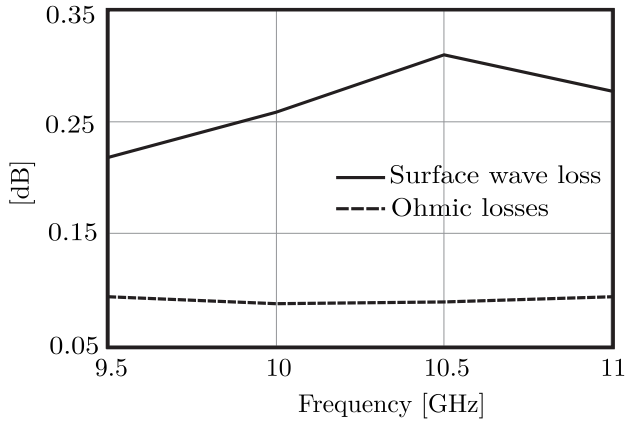

Figure 5.7: The simulated surface waves losses and the ohmic losses due to ADLs alone.

introduce very low (0.1 dB) ohmic losses, at least in the considered X-band. In addition to the low ohmic losses, the power which is being launched in surface waves when using a ADL enhanced slab is only 0.3 dB over the whole operating bandwidth. This value is the same and not better than that of the bare homogeneous slab, but with a much higher front-to-back ratio.

To further highlight the effect of ADLs on the surface waves, the induced magnetic field $|H|$ is plotted in Fig. 5.8. The scan is performed inside the dielectric slab at 10.5 GHz using CST [69]. This figure shows that for both the cases (i.e., with/without ADLs) the magnetic field peaks in the vicinity of the sources and decays with a certain geometrical distribution as the observation point moves away from the location of the source. At approximately half wavelength away from the center, the magnitude of the magnetic field has essentially the same magnitude for both the cases. This means that ADL do not suppress nor add any surface waves. The information that this graph provide also complements Fig. 2.6 and 2.7.

5.4 Prototype Demonstrator

A twin slot antenna electromagnetically coupled to an ADL enhanced slab has then been manufactured and a photo is shown in Fig. 5.9(a). The substrate material adopted is Rogers RO4350B, with dielectric constant $\varepsilon_r = 3.66$. The feeding has been realized via two microstrip lines utilizing a single Wilkinson power divider network as shown in Fig. 5.9(b). Since the input impedance of each of the slot is in the order of 25 Ω, the microstrip lines are tapered from 2.1 mm to 0.7 mm to match it to 50 Ω at the two output ports of

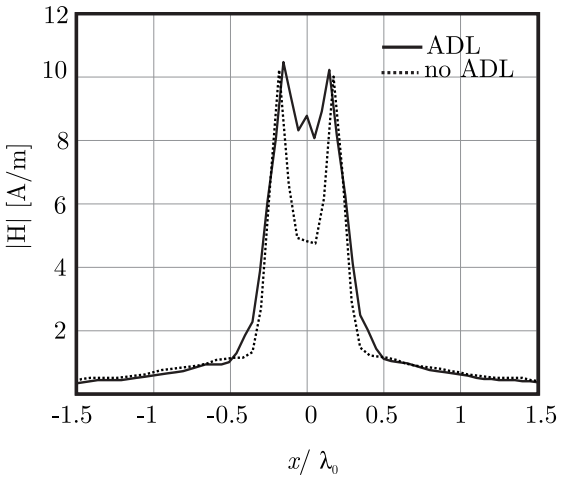

Figure 5.8: A 2-D scan of the near magnetic field radiated by a twin slot antenna in the presence and absence of ADL. This scan is performed at $z = 3.5\ d_z$ and $y = 0$.

the divider network. The geometrical dimensions of the antenna and the ADLs are the same as mentioned in the previous section. In order to obtain the desired height between the microstrip and the slots (i.e., h_{micro}), and separation between each layer consisting of planar ADL inclusions (i.e., d_z), homogeneous layers of RO4350 dielectric of thickness 0.254 mm are arranged in a multilayer PCB with 0.10 mm of RO4450F bonding material ($\varepsilon_{\text{r}} = 3.52$).

The measured reflection coefficient of the antenna is shown in Fig. 5.10. It can be seen that the -10 dB matching bandwidth is essentially the same as that of simulated one. The discrepancy in the resonance frequency between the simulations and the measurements can be attributed to the presence of the connector, which is not included in the simulations.

The simulated and the measured normalized far-field patterns in the E-, H- and the diagonal (D-) plane at 10 GHz are reported in Fig. 5.11(a), (b), and (c), respectively. In Fig. 5.11(c), the cross-polarization patterns in the diagonal plane is also shown which remains well below -13 dB with respect to the maximum of the co-pol. A good agreement is obtained between the simulated and the measured patterns and, as expected by using the ADLs the power radiated on the front (desired) direction of the antenna is 90% more than the power radiated on the back side (undesired) direction. Also, the patterns, as predicted by the simulations, are circularly symmetric with -3 dB beam width of about 70° in the E-, H and, D-plane. The agreement between simulations and the measurements implicitly validates the results in Fig. 5.7. The far-field patterns, as shown in Fig. 5.12(a) and (b) at 9.5 and 10.5 GHz respectively, remain qualitatively the same over the frequencies at which

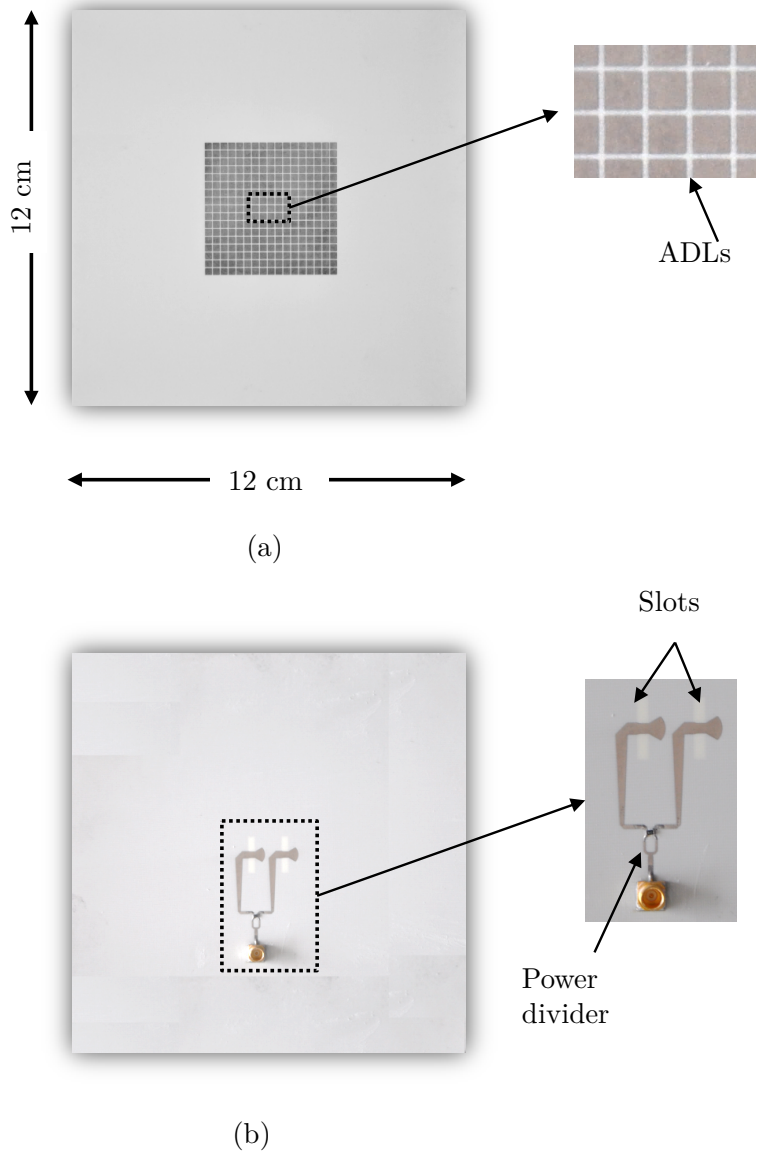

Figure 5.9: Prototype antenna. (a) The front view showing the top artificial dielectric layer and; (b) the back view showing the connector and the power dividing network.

the antenna is matched. Note that these graphs show the E-, H- and the D-plane (co- and cross-polarization) patterns. The cross polarization level in the E- and the H-plane is always below -25 dB over the whole frequency range (not shown).

The absolute measured gain is reported in Fig. 5.13 and is compared to the simulated gain. The two curves are superimposed within the limits of accuracy of our measurement setup.

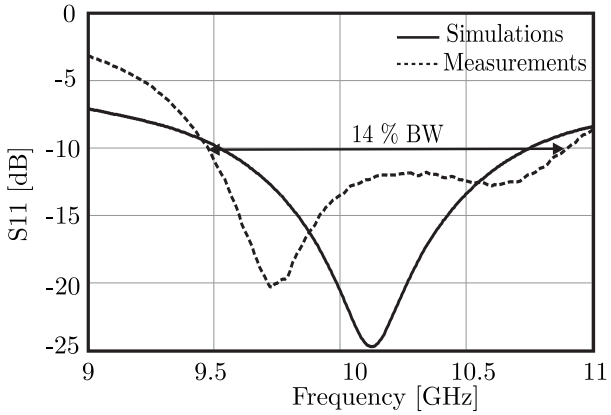

Figure 5.10: The simulated (without the inclusion of a connector) and the measured reflection coefficient.

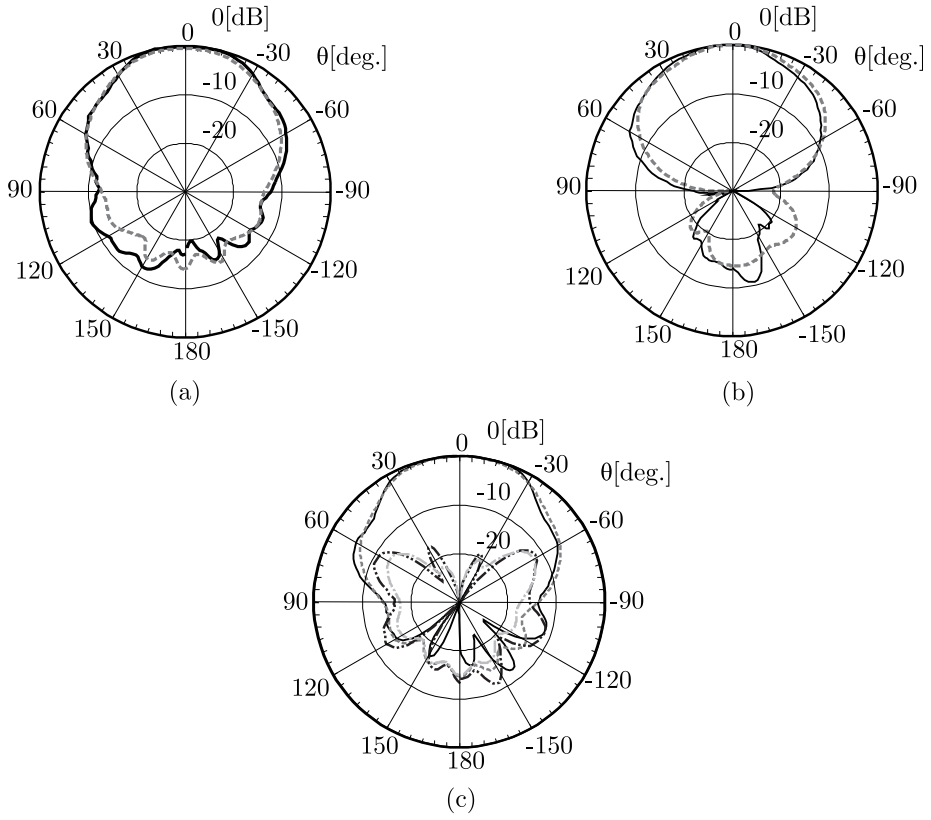

Figure 5.11: Normalized far-field radiation pattern at 10 GHz in (a) E-, (b) H- and (c) D-plane ($\phi = 45^0$). The dashed lines $(--)$ represent the simulated co-pol pattern, whereas the solid line $(-)$ represents measured co-pol pattern. For the $\phi = 45^0$ plane in (c) dotted gray $(-..)$ and black dashed dotted $(-.)$ represents the measured and the simulated cross-pol pattern respectively.

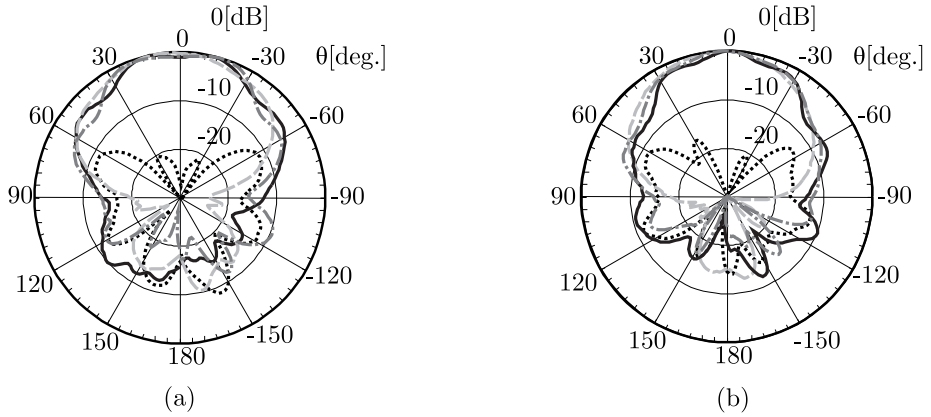

Figure 5.12: Normalized measured far-field radiation patterns at (a) 9.5 GHz and (b) 10.5 GHz. The solid blue line (−) represents the E-plane patterns, whereas the red dashed line (−−) represents the H-plane pattern. The co-polarized patterns in the diagonal plane are represented by the dashed dotted (−.) black line and the cross-polarized one is shown by a dotted (..) black line.

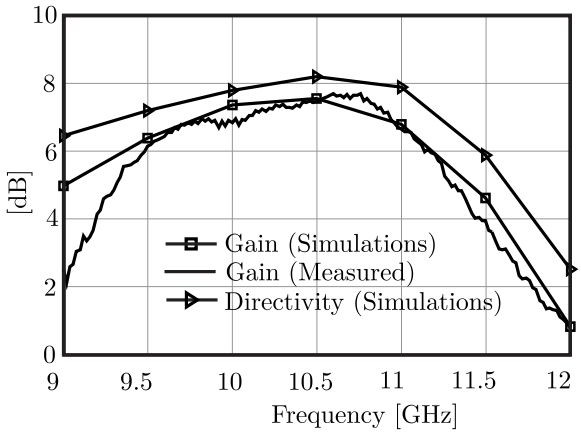

Figure 5.13: Broadside gain (measured and simulated) and directivity (simulated) versus frequency.

The plot of simulated directivity is also shown in the same plot to highlight the mismatch and the material losses. These losses are approximately 1.12 dB in the worst case (i.e., 9.5 GHz), out of which the material losses (ohmic) amount to 0.25 dB and reflection losses are in the order of 0.5 dB. Also, 0.32 dB of loss is incurred due to the power dividing network. Note that the difference between the calculated gains shown in Fig. 5.13 and Fig. 5.6 is because of the latter including the power divider and the long microstrip lines (see Fig.5.9(b)).

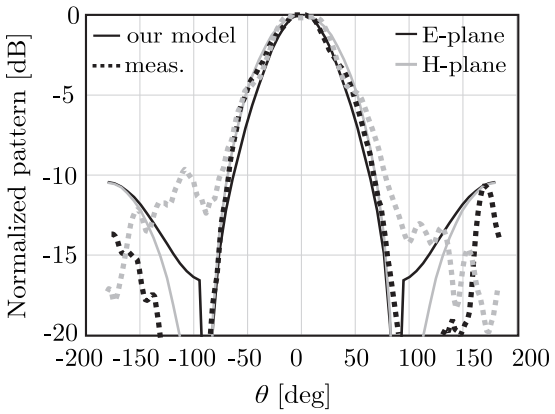

Figure 5.14: The measured far-field radiation pattern of a double-slot antenna at 10 GHz compared to the analytical model presented in Ch. 4.

Consideration on Losses

The losses estimated from measurements of the prototype at 10 GHz were too small to be given a realistic value, given the accuracy of the measurement setup. The main physical reason for the low impact of ohmic losses is that a very small electric currents is present on the metallic patches, because of the sub-wavelength nature of the patches. However, envisaging the effect of losses at the higher frequencies, the analysis of the scaled versions of the same antenna, operating at 300 GHz, is presented in Ch. 6.

5.5 Validation of the Measurements with the Analytical Method

As an additional validation we reproduce with our analytical method (see Ch. 4) the measured radiation patterns from the demonstrator presented in Sec. 5.4. The results of our method are compared with measurements in Fig. 5.14. Although the presence of the cable is affecting the symmetry of the measured back lobe, a good agreement can be observed in both the estimation of the beamwidth and the level of back radiation.

5.6 Conclusions

The design of planar integrated antennas benefiting from artificial dielectric layers (ADLs) is presented in this chapter. ADLs can be used to selectively enhance the effective dielec-

tric constant of dielectric slabs in specific directions, typically normal to the slab itself. Accordingly, an antenna can be printed on a thin isotropic dielectric slab that hosts the ADLs and achieve high front-to-back ratios that normally would only be associated with dense and thick dielectric slabs. The advantage is that, while a dense and thick isotropic layer would also support strong surface wave propagation, an artificially enhanced slab of equivalent normal permittivity does not.

In this chapter, we have shown that electrically thin substrate ($h \leq \lambda_d/10$) can be used to design integrated slot antennas with bandwidth in the order of 13% and front-to-back radiation ratio $\geq$ 10 dB, with virtually no power launched in to surface waves. This was experimentally verified.

Similar performances could be achieved by using slot coupled printed patch antennas on foam, such as those proposed in [41]. A key advantage of using ADLs with respect to these latter is that they can be used as an add-on component. This means there is no need to co-design as well as align the antenna and the ADLs.

Chapter 6

Design, Fabrication and Measurement of 0.3 THz On-Chip Double Slot Antenna Enhanced by Artificial Dielectric Layers

6.1 Introduction

The volumetric and the planar nature of ADLs renders them a promising candidate for the design of integrated and compact passive devices in commercial CMOS technologies [57]. However, we believe that these ADLs can be mostly beneficial when used as superstrates to enhance the radiation performance of on-chip antennas. The design of such antennas presents numerous challenges. First, the vertical thickness of the stack that can be used to design an antenna, depending on the specific technology used, is in the order of 10-12μm. To accommodate high-frequency active front ends, this stack is grown on top of a lossy doped silicon substrate of thickness 250-300μm. The electromagnetic coupling to the lossy substrate is avoided by shielding the antenna with a metal plane. At 0.3 THz, a substrate height of 10μm corresponds to an electrical thickness of $\lambda_d/50$, where λ_d is the wavelength in the silicon dioxide $\varepsilon_r \approx 4$. It is well known that any antenna printed on top of an electrically thin grounded dielectric slab exhibits a very low radiation efficiency. This is because the source and its image radiate out of phase. Recently, the use of a high impedance metasurface as a radiator at 94 GHz was proposed to mitigate this effect [93]. However, the efficiency of this antenna is still limited due to the close proximity of the radiator to the ground plane.

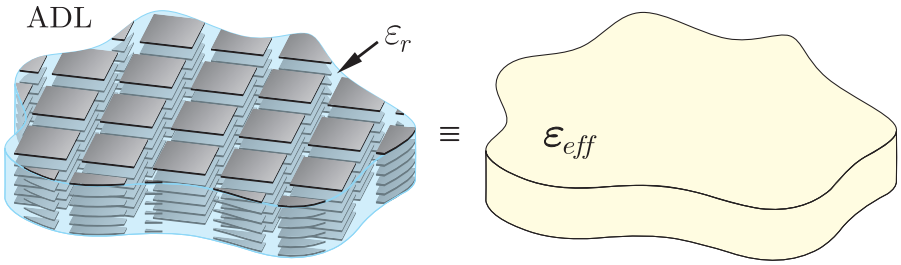

Figure 6.1: Artificial dielectric layers embedded in a host medium with relative permittivity ε_r to realize an equivalent effective homogenous medium. Each layer is composed by an array of electrically small patches.

A non-planar solution to the low radiation efficiency issue is to use a dielectric lens with matching layers. The matching layers are used to minimize the losses due to multiple reflections inside the lens [35–37]. A planar solution that can bypass a dielectric lens was presented in [94]. In this work, the antenna is printed on an additional low-loss quartz wafer, glued on the chip to increase the distance form the ground plane, and aperture-coupled to the feed structure. The antenna achieved a peak efficiency of 60%. The 40% loss in efficiency is due to the excitation of the substrate modes. Furthermore, a strict alignment accuracy is required between the antenna and the on-chip feed lines. A similar kind of solution has also been proposed for on-chip antenna arrays by the same authors in [95].

In Ch. 5, it was shown that ADLs can be exploited to increase the front-to-back radiation ratio of planar antennas printed on a electrically thin dielectric slabs, in X-band. Thanks to the enhanced anisotropic properties, virtually no power loss in surface waves was observed. To ensure that no surface waves are excited, the characterization of the dispersion properties of ADL slabs in Ch. 3 and Ch. 4 can be used, which is based on an analytical study of the spectral Green's function of these slabs.

In this chapter, we present a 0.3 THz version of the double-slot antenna enhanced by an ADL superstrate proposed in Ch. 5. The non-resonant patches composing the ADL, as depicted in Fig. 7.3, are hosted by an electrically thin silicon dioxide slab with relative permittivity $\varepsilon_{\text{host}} = 4$. Such value is increased by the presence of the ADLs to an equivalent relative dielectric constant $\varepsilon_{\text{eff}} = 32$, for normally incident waves. The ADL superstrate does not suffer from surface-wave losses. This is due to the fact that, in virtue of the anisotropy, the waves incident at angles towards the grazing do not feel the larger effective dielectric constant, which would otherwise induce surface-wave modes. The superstrate and the antenna have been fabricated using an in-house IC process and the silicon on the

Table 6.1: Physical Dimensions of the Antenna and ADL in μm

l_{slot}	l_{sep}	w_{slot}	w_1	w_2	w_3	d_{adl}	d_z	w_{adl}
195	300	25	46.5	1	8	95	5	10

back side of the antenna has been etched off. Measured results are reported and compared with simulations.

6.2 Antenna Design

The double-slot antenna is shown in Fig. 6.2(a), with a co-planar waveguide (CPW) feed. The antenna is loaded by artificial dielectrics superstrate placed at a distance of 5 μm above the antenna (see Fig. 6.2(b)). The dimensions of the antenna and the ADL are summarized in Tab. 7.1. The geometrical parameter have been selected so that the antenna is matched around the frequency of 300 GHz and the ADLs exhibit an effective dielectric constant of 32 for the waves which are incident along the broadside direction. The effective enhancement of the host material by the ADL, in an infinite homogeneous dielectric environment, is reported in Fig. 6.3.

The two curves represent the equivalent permittivities, as a function of the angle of incidence θ, for a transverse magnetic (TM) plane wave, with the electric field along $\hat{\boldsymbol{\theta}}$, and a transverse electric (TE) plane wave, with the electric field along $\hat{\boldsymbol{\varphi}}$. These values are derived using the procedure described in Appendix B. In Ch. 3 and Ch. 4, we have also shown that, for electrically small dimensions of the metallic inclusions, the TE and TM modes do not couple. Moreover, it was also demonstrated that the equivalent permittivity is independent of the azimuth plane (i.e. φ). This graph also shows that for a TM incident wave, the equivalent permittivity of the enhanced medium tends to the one of the host substrate, i.e. 4, when the angle of incidence tends to 90 degrees. However, in case of TE incidence, the dielectric constant tends to a higher value. The effects of this property were investigated in Ch. 4, where the dispersion characteristic of these slabs were described in detail by means of an analytical method.

The total height of the host silicon dioxide substrate is 35μm, which is electrically equivalent to $\lambda_d/14$. Within this slab, an ADL consisting of a stack of 7 layers, each separated by 5μm along the z-axis (see Fig. 6.2(b)), is realized. This results in a slab with effective height of $0.2\lambda_{eff}$ at 0.3 THz. A starting point for the design has been obtained by following the guidelines outlined in Ch. 5 and by using the tools described in Ch. 3 and 4. While this

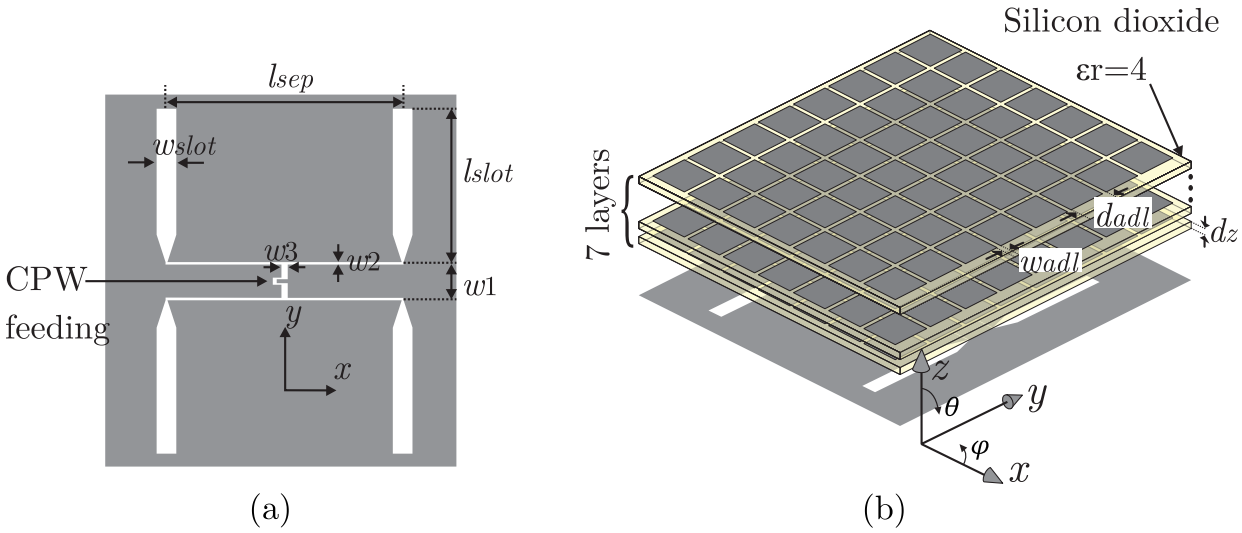

Figure 6.2: (a) 2D view of a double slot fed by CPW lines and (b) 3D view of the antenna loaded by the ADL superstrate. For the sake of clarity only 3 layers of the ADL stack are shown.

allows for a fast selection of quasi-optimal geometrical parameter, the final structure with the details of the feed has been fine tuned using a commercial EM solver [69].

6.2.1 Simulated Results

Figure 6.4 shows the simulated reflection coefficient with and without metal losses. As expected, the finite conductivity case (aluminum with conductivity $\sigma = 2.6 \times 10^7$ S/m) shows a broader bandwidth of the reflection coefficient, due to ohmic losses. In the fabricated device, the metal thickness of the antenna layer is 2μm, while it is 0.5μm for the ADL patches. In both cases, the thickness is well above the skin depth at 0.3 THz. The -10 dB impedance matching bandwidth of the antenna ranges from 295 till 320 GHz (8% relative bandwidth). This value is typical of a resonant double-slot antenna and not reduced by the presence of the ADL, which has broadband and non-resonant characteristics.

In order to quantify the advantage of using the ADL inclusions, a reference double-slot antenna loaded only with a 35μm slab of silicon dioxide has been designed and manufactured. This antenna without ADL is also matched at around 300 GHz, as shown in Fig. 6.4.

The simulated normalized radiation patterns of the antenna, with and without ADL, are reported in Fig. 6.5, at 305 GHz. It can be observed that the antenna with the ADL has a front-to-back ratio greater than 10 dB. On the contrary, the antenna in absence of the

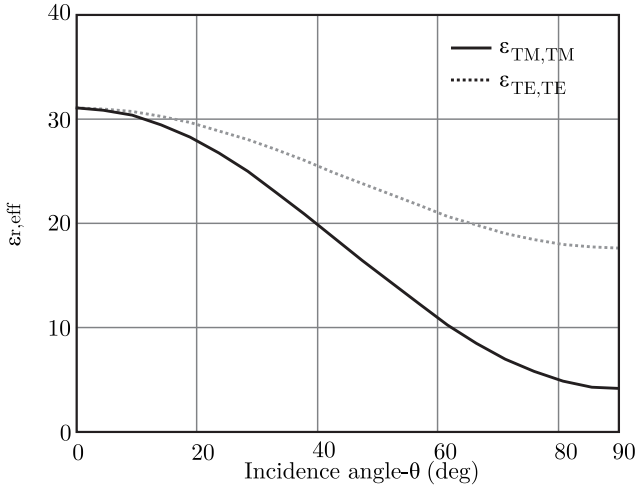

Figure 6.3: The value of the the equivalent dielectric constant for scanning angles 0 to 90 degrees.

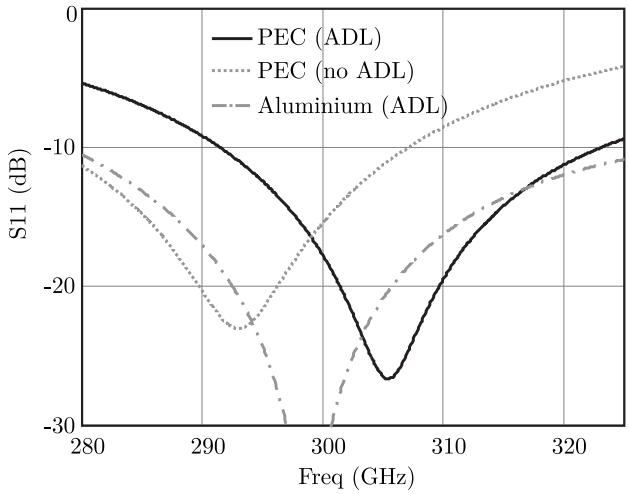

Figure 6.4: Simulated reflection coefficient.

ADL, loaded only by an electrically thin slab, exhibits a front-to-back ratio lower than 1 dB, since almost equal power is radiated in the two half spaces above and below the slot ground plane. Figure 6.6 shows the variation of the front-to-back ratio as a function of the frequency for the two antennas. The values for the ADL loaded antenna are higher than 10 dB over the whole matching bandwidth, and linearly increasing with frequency, due to the increasing electrical thickness of the ADL slab. Instead, the reference antenna has an almost frequency independent front-to-back ratio of about 0.7 dB.

In Fig. 6.7(a), we compare the gain and directivity for the antenna with and without

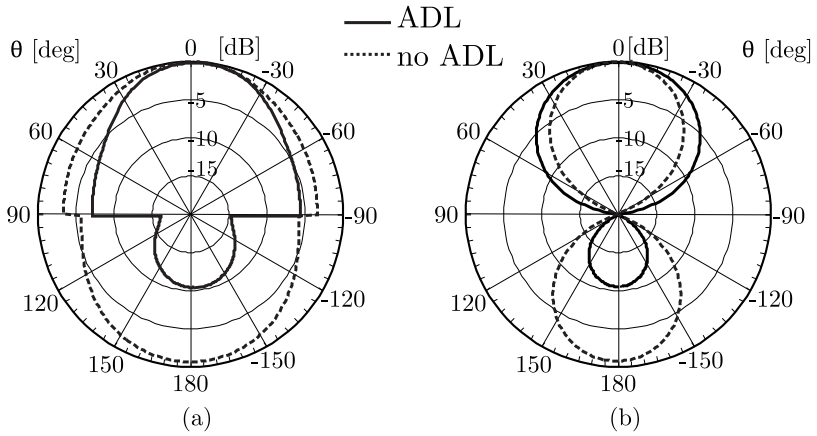

Figure 6.5: Normalized simulated (a) E-plane and (b) H-plane radiation pattern in dB at 305 GHz. The solid and the dashed line represent the antenna with and without the ADL, respectively.

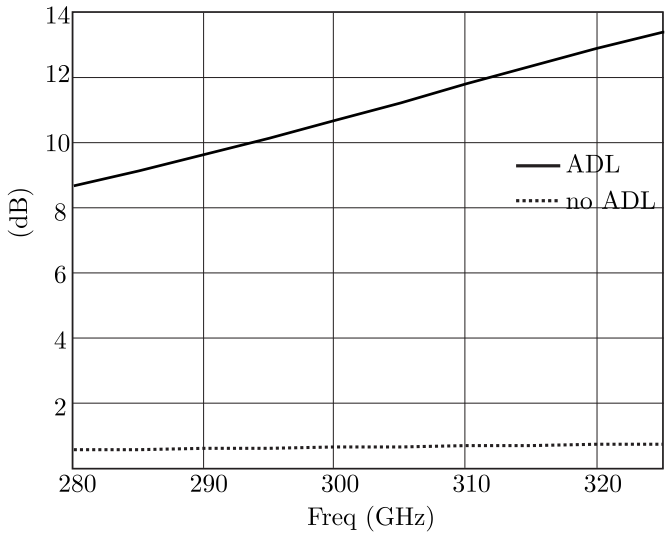

Figure 6.6: Simulated front to back radiation ratio.

ADL for the perfect electric conductor (PEC) case. This plot shows that the difference between the gain and directivity around the central frequency of the matching bandwidth for both antennas is negligible within the accuracy of the simulations. This means that surface waves, which in principle are allowed to propagate (TM_0 mode), are essentially not excited. The gain presented here also includes the mismatch losses. In the same graph, the comparison between the directivity of the two antenna reveals an enhancement of 2.2-2.6 dB for the ADL loaded antenna. This improvement occurs without compromising on pattern purity or surface wave efficiency. Note that, in simulations, surface wave losses are

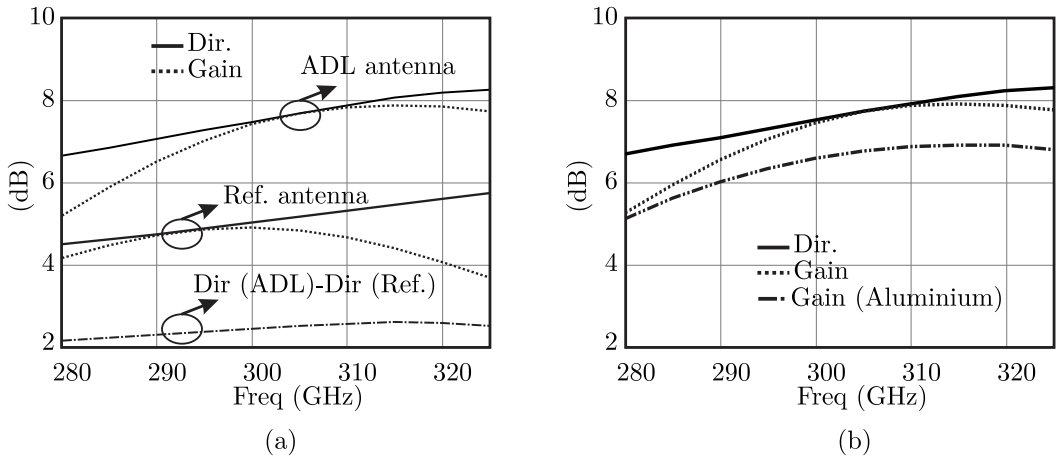

Figure 6.7: Simulated antenna efficiency: (a) comparison with a reference antenna (i.e., without ADL) for a PEC case; (b) evaluation of ohmic losses using aluminum.

too low to be estimated accurately despite the use of absorbing boundary conditions along the lateral directions (x and y).

The simulated gain obtained in the case of lossy metal (aluminum) for the ADL loaded antenna is shown in Fig.6.7(b). It is 2 dB lower than the PEC case. By means of numerical simulation, we estimated the ohmic losses accounts for 1.3 dB within the slot antenna and 0.7 dB within the ADL.

To feed the double-slot antenna, a 50 Ohm CPW line is used to carry the input power to the center of the H-slot from one side of the antenna, as depicted in Fig. 6.8(a). Such a feed introduces an asymmetry in the E-plane pattern (see Fig. 6.8(b)), due to the coupling of the CPW lines with the parallel lines forming the H-slot and with the ADL. However, this asymmetry is kept to a minimum, by designing the CPW as small as possible (strip width of 5 μm and slot width of 2 μm) so that the field is confined in a small region and couples weakly with the antenna structure. On the other hand, such approach comes at the cost of increased ohmic losses due to strong currents in the inner conductor of the CPW. The total losses due to the 860μm long line are estimated to be about 2 dB.

6.3 Fabrication

The combined antenna/ADL structure has been built using, as substrate, a high resistivity (3.5k$\Omega\cdot$ cm) n-type silicon (Si) wafer with 100 mm diameter, (100) crystal orientation and thickness of $500 \pm 25\mu$m. The use of a high-resistivity substrate is mandatory since the

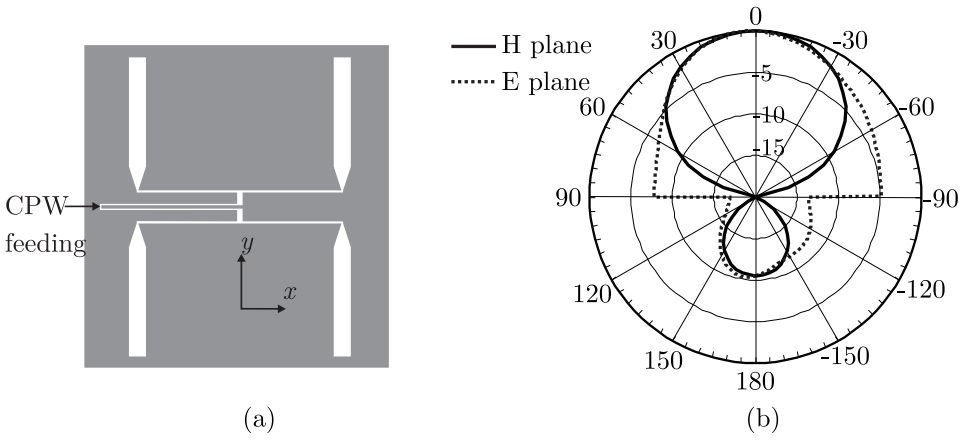

(a) (b)

Figure 6.8: (a) Schematic showing the extension of CPW line to feed the antenna. (b) The simulated radiation pattern in E and H-plane after inclusion of extended CPW.

charge carriers cause high losses and these losses are even higher in the THz frequency range [96, 97].

The devices are realized using a 20×20 mm die design (see Fig. 6.9), giving a total of 12 dies on a single wafer. To avoid any cross talk between antennas, the distance of radiating structures has been chosen to be larger than 4 mm. The die is divided in three parts: the antenna/ADL structure on the top left side, the reference antenna on the top right part and the test structures (used for de-embedding the feed lines) on the bottom part (see Fig. 6.9). Note that further details about the test structures are given in Sec. 6.4.

In Fig. 6.10, a schematic cross section of the device is shown. The structure can be divided in three main sections: the feeding/pads section (A), the feed transition (B) and the antenna/ADL one (C). A 2 mm long CPW with uniform width connects the contact-pads, where the wafer probe is landed, to a transition region. In this latter region, the CPW lines undergo a series of tapers and transitions to account for the different z-stratifications along the line. Finally, the feed line is connected to the double-slot antenna that radiates in the presence of the ADL. The antenna/ADL system is suspended by removing the silicon substrate, to avoid that the power is radiated into silicon and then to enhance the effect of the dielectric contrast given by the ADL.

A thin (100 nm) low-pressure chemical-vapor-deposition (LPCVD) low-stress silicon nitride (SiN) layer is firstly deposited on the silicon as hard mask for the back-side of the wafer, followed by 200 nm of plasma enhanced CVD (PECVD) silicon oxide. The antenna layer was realized using a 2 μm thick pure aluminum layer deposited by radio-frequency (RF) sputtering, using an SPTS Sigma 204 DC magnetron system. The deposition temperature

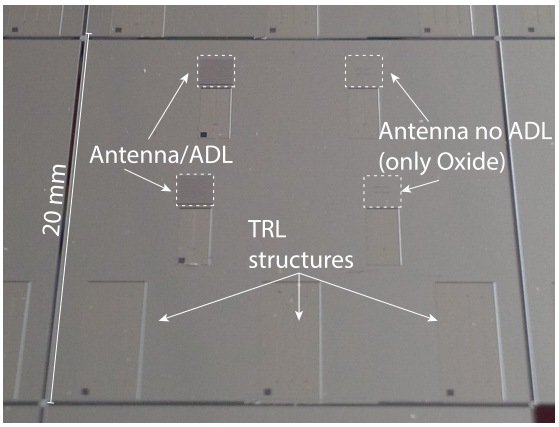

Figure 6.9: Top view of the die containing the antenna/ADL, the reference antenna and the calibration structures. The dashed area indicates where the silicon is removed from the back of the wafer.

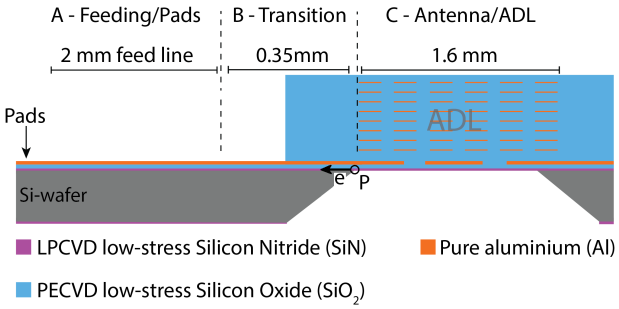

Figure 6.10: Schematic cross-section of the antenna/ADL structure. The device can be divided in three main parts: the feeding/pads area, the transition region and the antenna/ADL structure. The overall length of the structure is 4 mm, including the pads and the entire ADL length.

of the aluminum was 350°C, resulting in a layer conductivity of about $2.6 \cdot 10^7 \sigma$/m. The residual stress of this layer is 290 ± 23 MPa and has been measured using a TENCOR stress-meter.

The patterning of the metal layer is realized by first coating the wafer with a 2 μm layer of SPR 3017M positive photoresist and then using I-line lithography (ASML PAS 5500/80 wafer-stepper) to define the features.

After the photoresist development, a dry etching process based on chlorine chemistry has been used to remove the aluminum. The etching parameters, such as the gas ratio, etching time and depth uniformity, have been carefully optimized. This is because unwanted effects like over-etching or iso-etching could have resulted in larger features, compromising the impedance matching between the feed and the antenna. Moreover, any aluminum residuals in the thin slots could have shorted the antenna or the feeding lines in some points. For these reasons, accurate scanning electron microscope (SEM) inspections of the

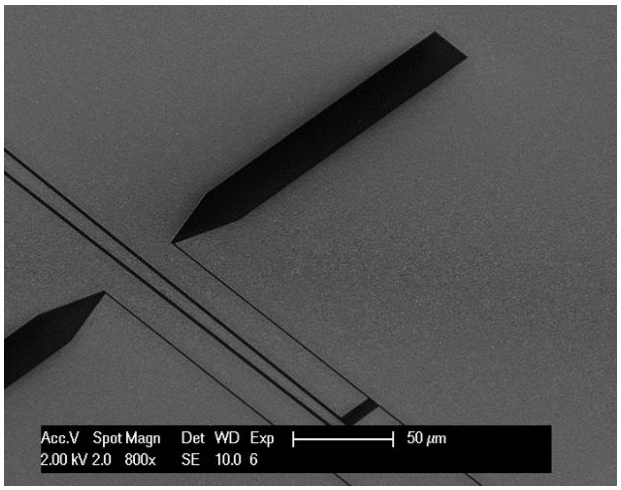

Figure 6.11: SEM picture showing the double slots antenna. The grey area is the pure aluminum layer while the dark area is the landing layer of PECVD silicon oxide.

thin slots have been performed after the etching and the resist stripping (see Fig. 6.12). The through, reflect and line (TRL) test structures have been realized on the same metal layer (see Fig. 6.9, bottom part), with the same etching process. The PECVD silicon oxide deposited under the antenna layer prevents any damaging of the silicon nitride during the metal etching.

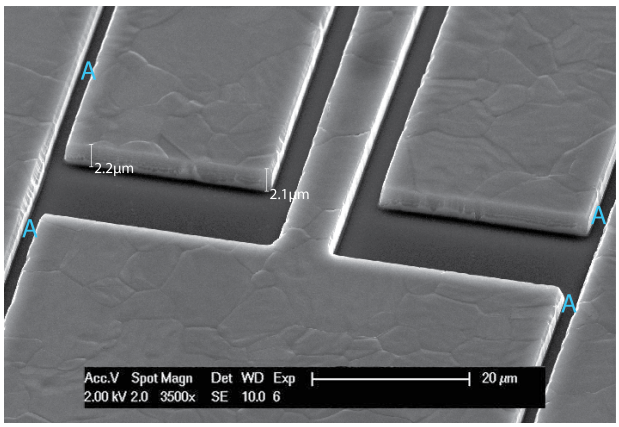

Figure 6.12: SEM picture showing a detail of the double slots antenna. The thick aluminum layer is clearly visible and the measurements confirm the thickness of 2μm. No visible aluminum residuals are present in the structure. The thin openings marked by A are only 1μm wide.

As explained in the previous sections, to ensure a correct matching between the slot antenna and the feeding lines, an accurate transition has been designed and the result is shown in Fig. 6.13. The structure in region B is designed to implement the transition between the

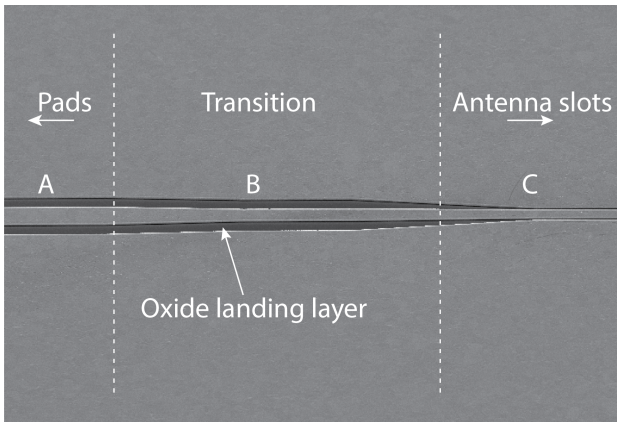

Figure 6.13: SEM picture of the transition region on the antenna feeding line.

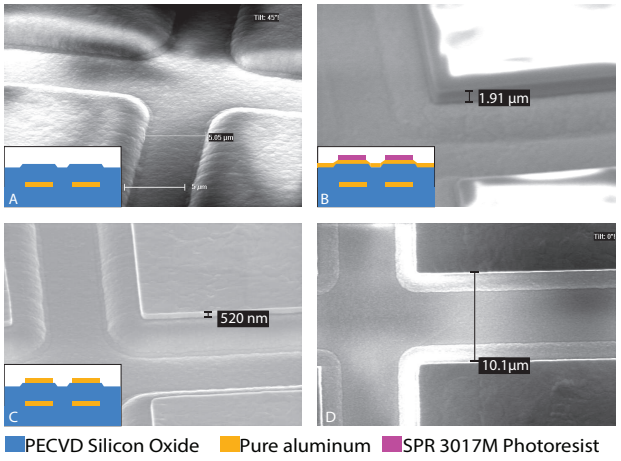

Figure 6.14: Series of SEM picture showing the ADL during the fabrication process. (A) The 5μm silicon oxide layer is deposited on top of a metal patch layer (see in the inset the layer stack). The brighter area in the figure are given by electron charging phenomena. After the silicon oxide coating, the aluminum layer is deposited and the patches defined by I-line lithography. In (B) the photoresist layer is clearly visible and the measured thickness is $\approx$ 2μm. Due to the non-conductive nature of the layer, electron charging phenomena are clearly visible. Using a dry etching process, the patch layer is defined (C) and the relative distance between the patched measured (D).

large CPW lines (region A), with a inner conductor width of 22μm, and the CPW lines feeding the antenna slots (region C), with a inner conductor width of 11μm.

After the antenna fabrication, a separation layer of 5μm of silicon oxide is deposited in a PECVD Novellus Concept-One reactor. The ADL consists of a stack of 7 metal layers embedded into a thick layer of PECVD silicon oxide. As first step, a pure aluminum layer (500 nm) is deposited using the same tool and deposition condition of the antenna layer. A layer of 2μm of SPR 3017M positive photoresist is used to define the ADL area. Each

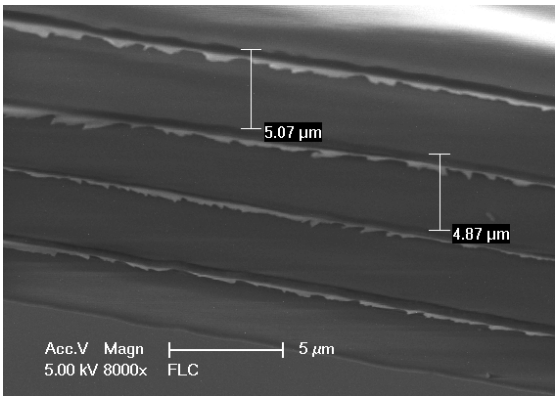

Figure 6.15: SEM cross-section showing a detail of the fabricated ADL stack. The overall ADL is $\approx 39\mu$m thick.

ADL layer consists of an array of 16×16 square patches that effectively cover the entire antenna radiation area. The patches are 85μm wide with a separation of 10μm in the xy plane. All the layers are patterned by means of I-line lithography and dry etching process. The details of the fabrication are shown in Fig. 6.14. After the patches definition, a layer of 5μm of low-stress (−30MPa) PECVD silicon oxide is deposited. Since the ratio between the height of the oxide layer and the metal patches is more than 10, step coverage is not an issue. After the oxide deposition, a new metal layer is deposited and etched. These process is repeated 7 times. A protective layer of 1μm of PECVD oxide is deposited to prevent possible damages of the ADL during the remaining process steps. The alignment of the different metal layers was done with a standard wafer-stepper, used in IC technology for accurate alignment of the various mask layers. The tool used in this process guarantees a maximum overlay error of 50 nm over the different deposited layers. Simulation have shown that such error has negligible effects on the antenna performance.

To achieve an effective enhancement of the dielectric constant, an accurate control of the oxide thickness and alignment of the metal patches is fundamental. By means of optical reflectometry (Leitz MPV-SP) measurements, the thickness of the layers was determined and carefully monitored during all process steps. A detail of a cross section (Fig. 6.15) clearly shows the metal patches embedded in the oxide layer. By measuring the oxide thickness, we estimated a maximum thickness deviation of about ∼80 nm on the entire wafer area. Numerical simulations have confirmed that such variations have negligible effects on the ADL properties.

Using a similar process, a reference test-antenna has been realized on the same substrate, to allow a comparison between the antenna gain with and without the ADL. This structure is similar to the one presented in Fig. 6.10 and visible on the right side of Fig. 6.9. These

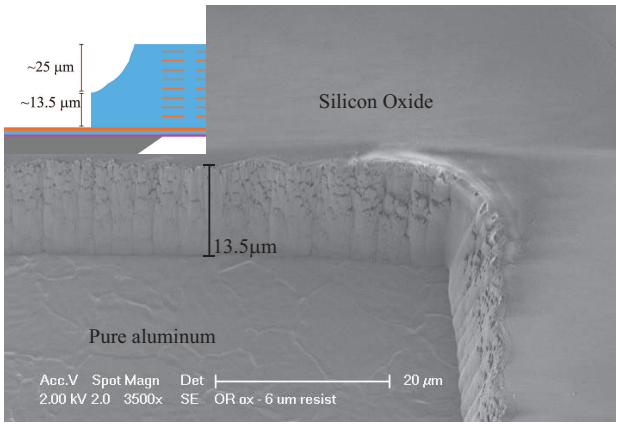

Figure 6.16: SEM cross-section showing a detail of the silicon oxide after the etching. The sample is here tilted of 45 to show the inner part of the cavity. The wet etching gives a round corner on the top of the silicon oxide layer (see the schematic in the inset). Approximately 25 μm of silicon oxide are removed with this process. The remaining 13.5μ m are removed by a final dry etching. This last process gives a vertical profile of the etched oxide, clearly visible at the corner.

antennas are covered only by the thick oxide layer used to realize the ADL, but no metal patches have been inserted in the fabrication flow.

After the ADL deposition, a final etching is required to remove the thick layer of silicon oxide that covers the antenna contact pads. Due to the large amount of oxide to etch, a single dry etch step would require a very thick photoresist layer to protect the structures and a very long (more than 1 hour) plasma etching. Such long process could cause unwanted phenomena such as photoresist burning or large non-uniformity in the etched layer. For these reasons, a wet/dry combined etching has been performed. To protect the structures, a 12 μm layer of SPR 3017M photoresist has been used to coat the wafer. After the resist patterning, the oxide is etched in a buffered hydrofluoric acid (BHF) 1:7 solution (etch rate 290 nm/min), for 75 minutes. This step removes approximately 2/3 of the oxide layer, with a very high uniformity on the wafer area. A final dry etching step is then performed in a Drytek Triode 384T oxide dry etcher. SEM inspection has been performed on the wafer (see Fig. 6.16) and clearly show the thick oxide being etched and the aluminum layer.

To release the antenna/ADL membrane and the test-antenna membrane, a silicon wet etching in a 33 wt % KOH at 85 °C has been lastly performed on the wafer. The wafer backside windows were previously patterned etching the LPCVD silicon nitride layer with a dry etching process. Then, using a special holder, the wafer front-side has been protected from the solution. After the etching (5 hours and 30 minutes), a final rinsing (HNO_3 and water) is performed to clean the wafer. The inspection of the etched cavity has shown that a small mismatch (e=$65 \pm 10\mu$m, Fig. 6.10) in the KOH opening position is present. This

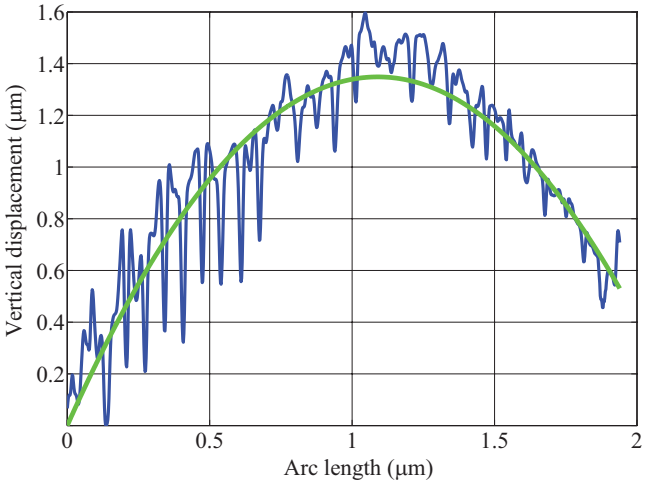

Figure 6.17: Membrane vertical displacement obtained by white light interferometry. The maximum deflection is $\approx 1.6\mu$m. The membrane shape can be well fitted by a parabolic trend (green curve).

is probably due to a variation of the wafer thickness and a front-to-back misalignment of the silicon nitride mask used to pattern the wafer backside.
The use of low-stress layer in the ADL fabrication is of fundamental importance to achieve a flat structure. To prove that only very small deflections are present, a white light interferometer has been used to map the vertical displacement of the structure. As shown in Fig. 6.17, the maximum deflection is measured at the center of the membrane, resulting in a maximum displacement of $\approx 1.6\mu$m, almost 10^{-3} times smaller than the membrane side length.

6.4 mm-Wave Measurements

The fabricated chip micrograph is shown in Fig. 6.18(a). The measurement setup consists of an Agilent vector network analyzer (PNA-X N5242A) working from 10 MHz to 26.5 GHz. Frequency extension modules, to operate the VNA in the WR03 band (i.e. 220-325 GHz) band from OML Inc. are used. The feeding to the antenna is realized by using GGB Cascade Infinity ground-signal-ground (GSG) waveguide probes with pitch equal to 100μm. The measured insertion loss of this probe is 1 dB and was calibrated out. The fabricated chip was placed on a metal chuck. A feeding pad to land coaxial probes on the chip of length 105μm and a feeding line was added on the back of the antenna, as labeled in the chip micrograph in Fig. 6.18(a). The length of this line was selected as 2 mm, to trade off loss levels with scan area: on the one hand, a too short line would cause the bulky

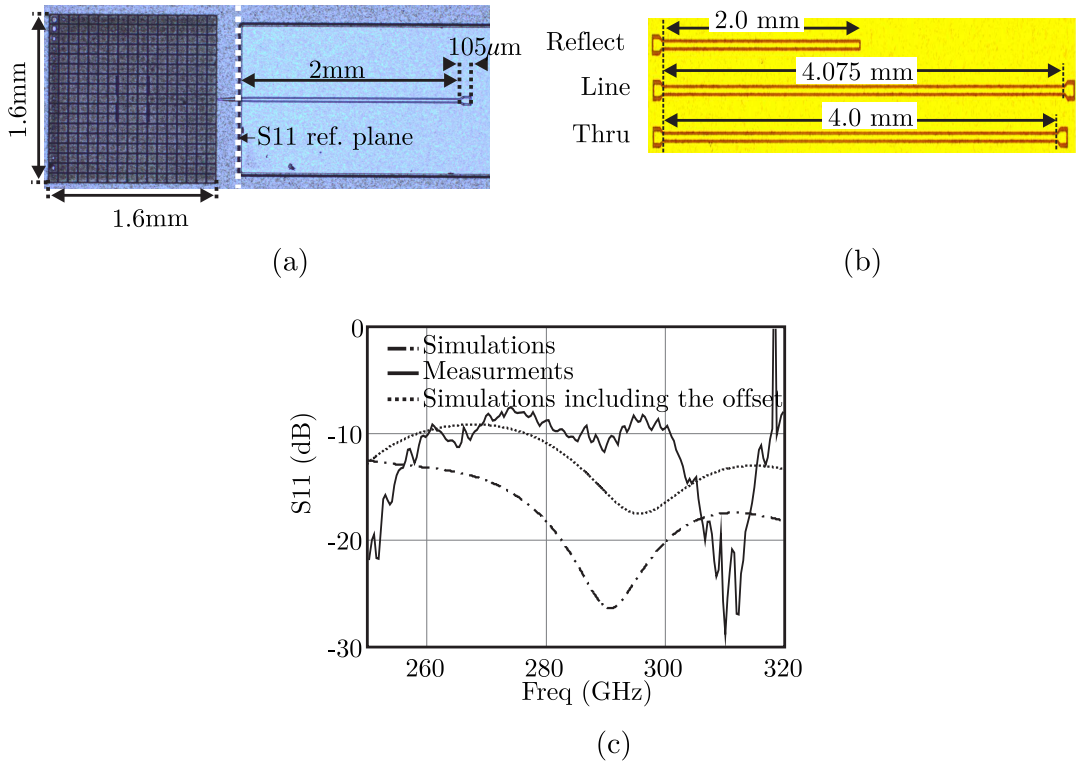

Figure 6.18: The fabricated (a) chip micrograph, (b) TRL structure, and (c) simulated and measured reflection coefficient.

wafer probe to be too close to the antenna, limiting the near-field scanning area needed for the radiation pattern measurements; on the other hand a line that is too long would introduce too high losses reducing the accuracy of the measurements.

The long line (i.e., 2mm) is de-embedded from the measured data employing a thru-reflect-line (TRL) technique [98]. Figure 6.18(b), shows on-chip test structure that are fabricated on the same die as that of the antenna (see Fig. 6.9) and are measured to apply TRL procedure. The measured de-embedded one port reflection coefficient is presented in Fig. 6.18(c), compared with the simulations. There is a frequency shift of 6% between the measured and the simulated results. As pointed out earlier in Sec.6.3, a mismatch during the KOH etching process has resulted in an offset of point P (see Fig. 6.10) by a distance e=65 $\pm$ 10μm. The S11, recomputed after including the above-mentioned mismatch in the simulation, is shown in Fig. 6.18(c). The error difference between simulation and the measurement is now reduced to 3%. Also, the measured and simulated reflection coefficients starts to show a similar trend at the low end of the frequency band (250-280 GHz).

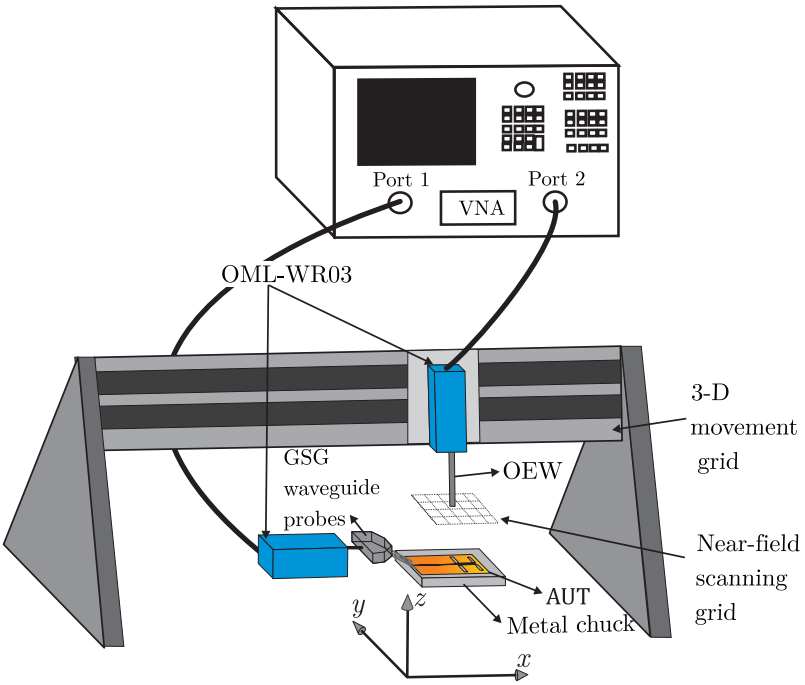

Figure 6.19: Schematics of the near-field measurement setup (not to the scale).

The far field radiation patterns are calculated using the near-field measurement setup depicted in Fig. 6.19 [99]. To avoid the reflections from the metal chuck, commercial absorbers (ECCOSORB MMI-U) are placed below the antenna. A linearly polarized, WR-03 open ended waveguide (OEW) is used to sample the near field of the antenna under test (AUT) on a rectangular grid, while the AUT is kept stationary. The distance between each spatial sample point was set to be $\lambda_0/8$ at 300 GHz, to obtain a high resolution data. The vertical distance (along the z-axis) of the OEW tip from the AUT is about 3.5 mm, i.e. radiative near-field region. The measured normalized amplitude and phase of the electric field radiated by the AUT in the presence of probe is shown in Fig. 6.20(a) and (b), respectively. Since the AUT and OEW are linearly polarized, only the x-component of the near field was measured. The scan area is rectangular and the maximum of the electric field is around $x = 0$ and $y = 0$, which denotes the center of the AUT. The acquisition of near field data along the $-x$-direction is limited by the presence of the GSG waveguide probe, which is an usual limitation in these type of measurements [93, 95, 100].

The effect of the OEW is de-embedded from the far-field pattern of the AUT by using a standard probe correction technique [101]. The far-field radiation patterns in the upper hemisphere, obtained by Fourier transform of the near-field data, are shown in Fig. 6.21,

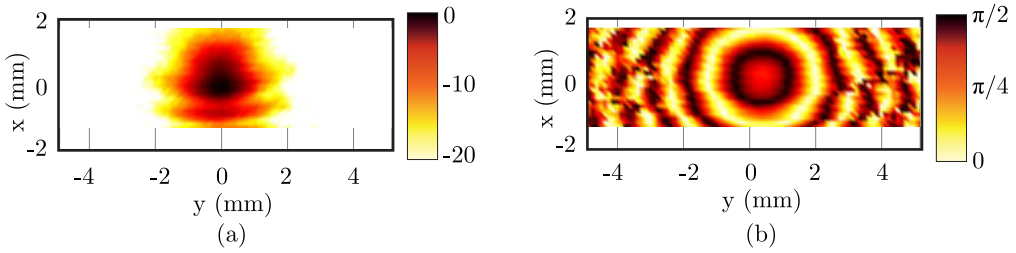

Figure 6.20: The measured near field at 300 GHz (a) normalized amplitude in dB and (b) phase in radians.

in the frequency range from 300-315 GHz. The patterns in the H-plane show an excellent agreement with the simulations. The E-plane patterns are asymmetric and oscillatory. The reason is the scattering from the probe, which interferes with the antenna. Also, the patterns are shown till $\pm 45°$, because the near-field scan area is restricted to ± 1.5 mm (see Fig. 6.20) by the presence of the wafer probe. Since the near-field area is limited along the x-direction the accuracy of the radiation pattern measurements decreases for angle greater than $\pm 23°$.

At a later moment, a scan over a bigger aperture in the direction where there is no feed probe was carried out. The measured near field data is shown in Fig. 6.22(a) at 300 GHz. A symmetric near field data is obtained artificially by mirroring the near field data (see Fig. 6.22(b)) with respect to the x-axis ($x = 0$). Exact symmetry conditions are also imposed on the simulated near field data from CST. The far field patterns after post-processing are shown in Fig.6.22(c) for both the cases. A better agreement can now be observed between the simulations and the measurements. This approach for artificially symmetrizing the pattern gives an indication of how the antenna would operate in a realistic application scenario, in which there would be no feeding probe.

Also the reference antenna without the ADL was measured. A comparison between the simulated and the measured far field radiation patterns is shown in Fig. 6.23, at 300 GHz. Although not shown for the sake of brevity, the radiation patterns at other frequencies show a similar agreement.

The relative difference between the broadside gain of the two antennas (with and without ADL) is presented in Fig. 6.24. Both simulations and measurements show an improvement of about 2 dB for the ADL loaded antenna with respect to the reference one. The measured results are presented in a frequency range of 20 GHz centered at 300 GHz, where the simulated reflection coefficient is well matched for both antenna (see Fig. 6.4).

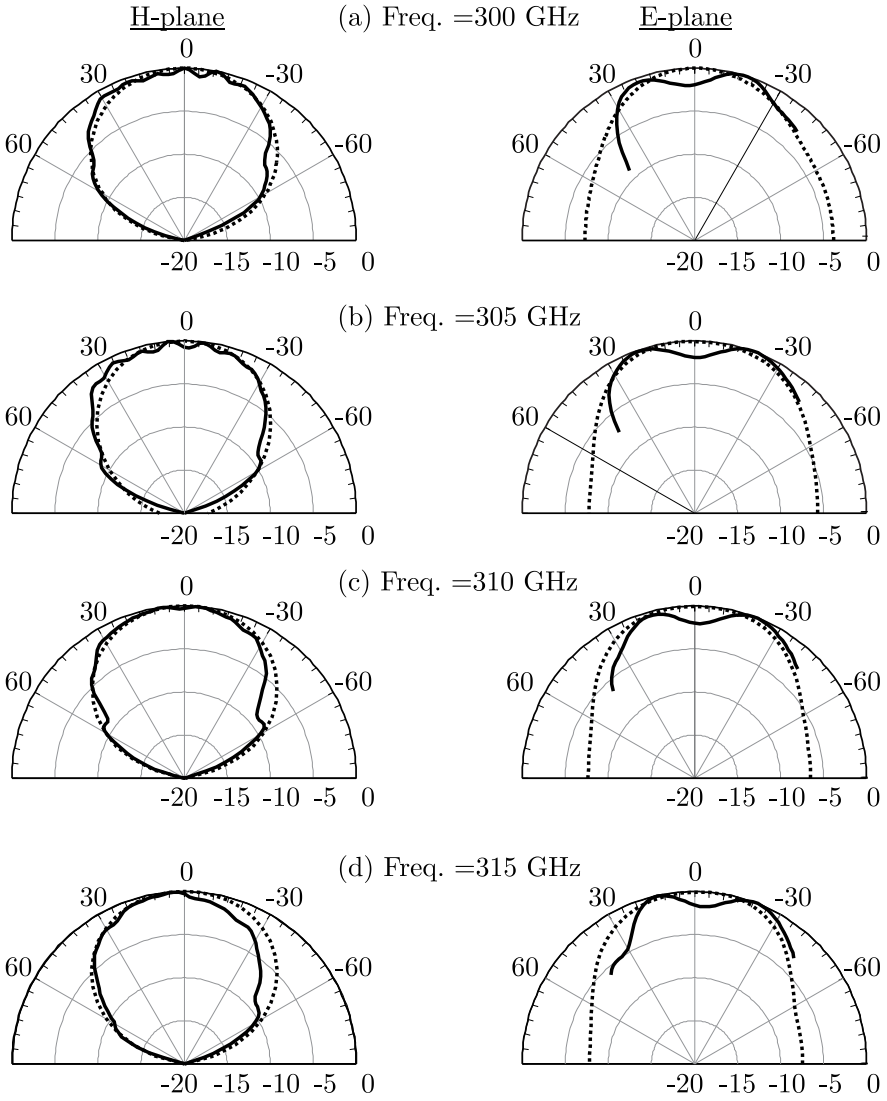

Figure 6.21: Measured(-) and the simulated (- -) radiation pattern (dB) with ADL.

6.5 Conclusions

On-chip integrated antennas typically radiate in the presence of either a lossy silicon substrate or an electrically thin grounded slab. This leads to either high dielectric losses or very narrow bandwidths of operation. To increase the radiation efficiency of such antennas, we demonstrate, at 300 GHz, the effectiveness of artificial dielectrics superstrates, previously proposed at lower frequencies, using printed circuit board technology. In this specific work, the conventional double slot antenna is loaded by an ADL superstrate that substantially increases the front-to-back ratio.

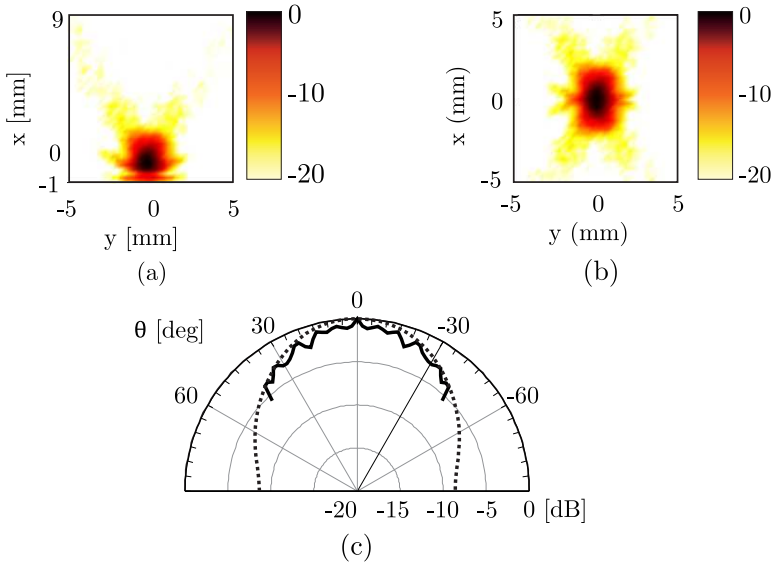

Figure 6.22: The near-field expressed in dB (a) measured, and (b) obtained after applying symmetry to the measured data. (c) Measured (-) and the simulated (- -) far-field radiation pattern (dB) in E-plane. The process of symmetry has also been applied for simulated antenna.

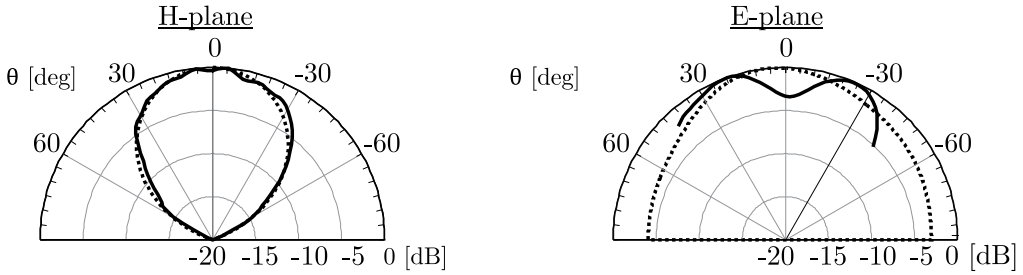

Figure 6.23: Measured (-) and the simulated (- -) radiation pattern of the antenna without ADL loading at 300 GHz.

For the fabrication of the antenna and the ADL superstrate, we developed a low-temperature CMOS back-end compatible process. By using pure aluminum as metal and silicon oxide as dielectric host matrix, the ADL was deposited on top of the antenna structure.

The anisotropic properties of the proposed artificial slab allows to achieve high surface-wave efficiency. This is because the ADL is dense and electrically thick for waves radiated by the slot in directions close to the normal, whereas it has lower permittivity and is electrically thin for the waves radiated in directions almost parallel to the slab.

The antenna has a front to back ratio larger than 10 dB, with essentially no power launched in to surface waves. Also an antenna without ADL loading has been fabricated and used

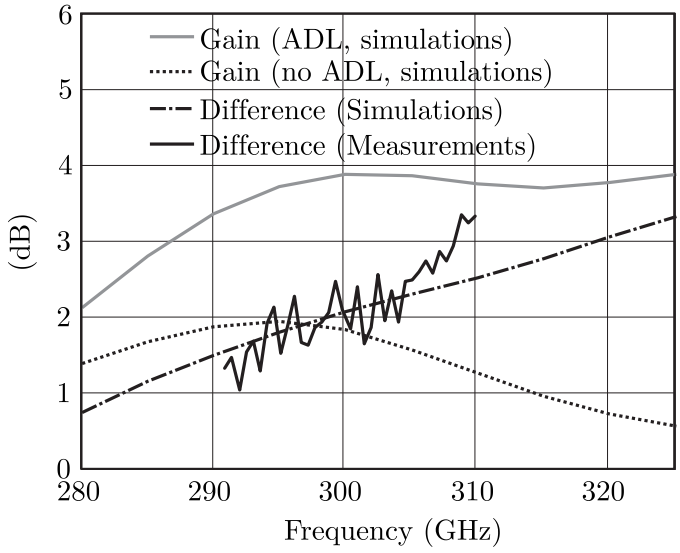

Figure 6.24: Simulated gain of the two antennas, with and without the ADL loading; the relative gain difference is also reported and compared with the measured one.

as a reference solution to quantify the enhancement due to the ADL. A improvement of about 2 dB in gain has been achieved both in simulations and measurements.
The key feature feature of the present ADL superstrate solution is that they can be designed and manufactured independently from the antenna and the IC's. They can be used as add-on components since no alignment is required between the antenna and the superstrate layers. Also, ADL are broadband because of their non-resonant periodic nature. This concept can be beneficial for any on-chip radiating structure, including antenna arrays.

Chapter 7

Wideband, Wide-Scan Planar Array of Connected Slots Loaded with Artificial Dielectric Superstrates

7.1 Introduction

Wideband, wide-scanning arrays have been receiving great attention in the last few decades for both commercial and military applications, such as satellite communications, radioastronomy and broadband radars.

The high number of coexisting systems that support various functionalities (e.g. tracking, surveillance or discrimination), for airborne military platform, has lead to an increasing interest in wideband arrays [102, 103]. In these scenarios, where space and weight are major constraints, it is beneficial to combine several functionalities in a single wideband, wide-scan antenna aperture. When such systems are required to support communication services, polarization purity is an important aspect to be accounted for. A dual-polarized wideband array with low cross-polarization was proposed in [104], for satellite communication applications. Another important application that benefits from wideband arrays is radio astronomy, e.g. the Square Kilometer Array (SKA) [105, 106].

The most typical antenna solutions used in wideband, wide-scanning arrays can be mainly classified in three categories: stacked patches, tapered slot antennas, and connected arrays. Stacked patches have been shown to achieve about an octave bandwidth, for a linearly polarized array, capable to scan up to 45° in all azimuth planes [30]. However, the maximum possible bandwidth achievable with this solution is limited by the resonant nature of the radiators. Tapered slots have been shown to achieve large bandwidth of operation (multi-

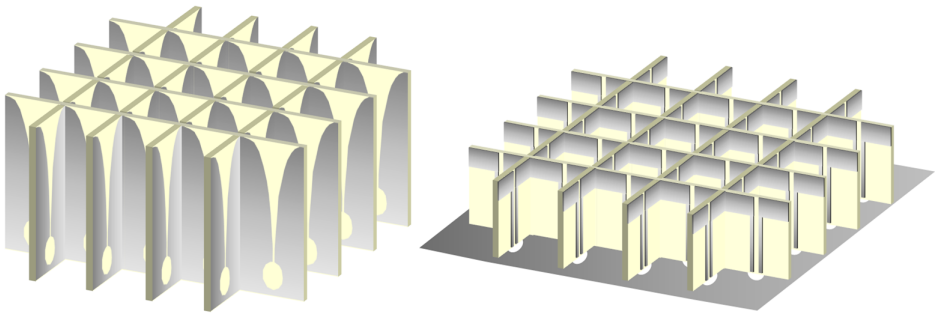

(a) (b)

Figure 7.1: Typical egg-crate configuration for wideband wide-scanning dual-polarized arrays: (a) tapered slot antenna array and (b) connected dipole array.

octave), over a wide scan volume [25, 102]. Despite the good performance in terms of impedance matching, the large bandwidth come often at the cost of degraded performance in terms of polarization purity, especially for scanning in the diagonal planes [107].

Connected arrays consist of arrays of either slots or dipoles which are electrically connected [108]. They have the advantage of being broadband and, at the same time, they exhibit low cross polarization. Unlike resonant antennas, which support sinusoidal and strongly frequency dependent current distributions, connected arrays are characterized by an almost flat, frequency independent current distribution, due to the electrical connection between adjacent antenna elements [109]. Practically the bandwidth of a connected array is limited by the presence of the backing reflector, which is needed to ensure unidirectional radiation [103].

In most of the state-of-the-art designs of dual-polarized Vivaldi and connected arrays [25–27], a complicate egg-crate configuration is implemented (see Fig. 7.1), which is costly to realize. In this assembly, vertical printed circuit boards (PCBs) are arranged in a three-dimensional lattice to provide unidirectional radiation. In Vivaldi arrays, a long vertical flaring is used in the element to increase the directivity. In connected arrays, a backing reflector is typically placed at about a quarter wavelength distance from the array plane [110], thus vertical feeding lines are needed to connect the elements to the connectors or electronic components located below the ground plane. These lines are usually too long to be implemented with standard PCB via-hole technology and thus they are printed on vertically oriented PCBs.

To overcome the drawbacks of the vertical arrangement of the antenna PCBs, it is convenient to implement the array in a completely planar structure that, as such, would be

low-cost and easier to manufacture. A planar solution for wideband phased array was presented in [29], where scanning up to 45° degrees was achieved. Here we propose a different concept that allows to further increase the scanning range, while maintaining good matching efficiency (active voltage standing wave ratio lower than 2) within a large frequency bandwidth.

7.1.1 Antenna Concept

In the proposed solution, we combine the connected array with artificial dielectric layers (ADLs). A connected array of slots in presence of a backing reflector is depicted in Fig. 7.2(a), with the respective geometrical parameters. Connected slots are selected as radiating elements, to avoid the use of differential feed lines, which can support undesired common-mode resonances. Indeed, the slot elements can be fed by unbalanced line, as opposed to dipole elements, which often require differential feeding lines and ad-hoc balanced-to-unbalanced (baluns) transitions [111, 112]. Such baluns are often the limiting factor for the bandwidth performance.

Figure 7.2(b) shows a unit cell of the connected array loaded with an ADL superstrate, located at a distance h_{gap}. ADLs consist of arrays of electrically small metallic patches included in a dielectric host medium to enhance its equivalent relative permittivity, as shown in Fig. 7.3. As discussed previously in Ch. 3 and 4, the factor by which the permittivity of a medium is increased depends on the physical dimensions of the metallic patches and the inter-layer distance. Moreover, ADLs have also been exploited in Ch. 5 and 6 to enhance the front-to-back ratio of planar antennas and to minimize the excitation of the surface waves. Loading the array with a single or multiple ADL slabs allows to significantly reduce the distance between the array and the backing reflector, in such a way to permit the implementation of the element feed by means of standard via-hole technology. Consequently, a fully planar implementation of the array is enabled by the proposed solution. The ADL slab is characterized by a high effective relative permittivity, thus increasing the radiation towards the positive z-direction. Consequently, the array 'feels' less the presence of the backing reflector, which can be located closer to it without strongly degrading the impedance matching properties.

The analysis of the array concept presented here is based on infinite array simulations. Several design examples are shown in the chapter, for both single-polarized and dual-polarized arrays targeting the frequency range of one octave, from 6.5 to 14.5 GHz, and scanning up to 50° in all azimuth planes. A possible implementation of the feed structure and the multi-layer stack is also investigated.

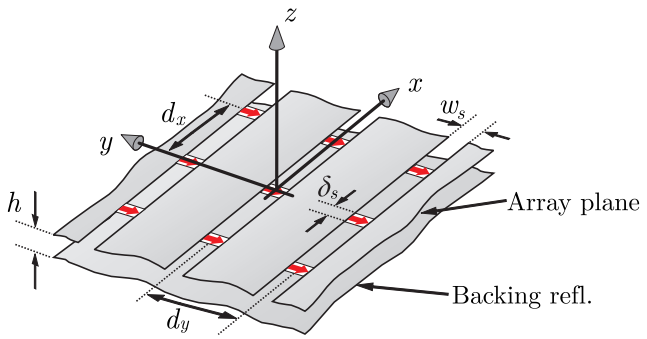

(a)

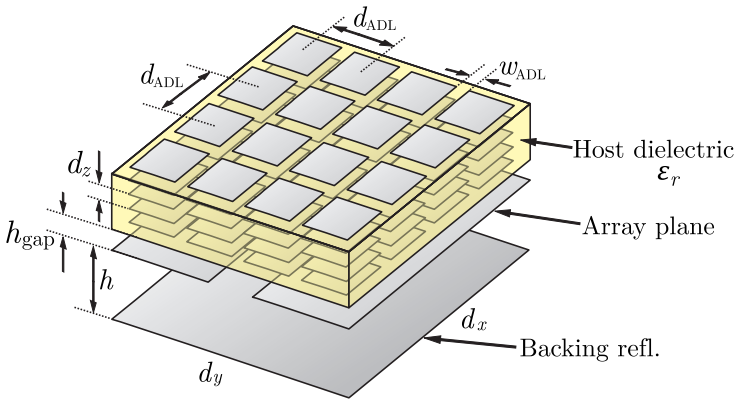

(b)

Figure 7.2: (a) Connected array of slots in the presence of a backing reflector and (b) unit cell of the array loaded with ADL.

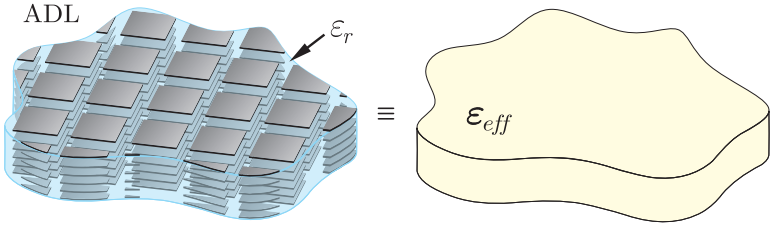

Figure 7.3: A planar ADL slab hosted by a homogeneous dielectric of permittivity ε_r to realize an equivalent anisotropic medium.

7.2 Analysis Tool

Simulating a structure like the one in Fig. 7.2(b) using commercial electromagnetic solvers is not a simple or fast process, due to the large number of layers composing the entire stack

and the electrically small geometrical features that require very fine meshes. Moreover, a high number of such simulations are needed for the optimization of the total structure in a design phase, with consequent demand for large computational resources. Therefore, an analytical tool was developed to estimate the performance of the connected array of slots loaded with ADL. The formulation exploits and combines the analytical spectral solutions of connected arrays [109] and ADLs (see Ch. 3 and 4). The analysis tool takes into account all the higher-order-mode interactions between adjacent layers composing the array plane and the ADL. This is required since the inter-layer distance is typically in the order of one hundredth of the wavelength.

The active input impedance of the connected array of slots can be expressed in closed-form as follows [109]:

$$z_{\text{slot}} = -\frac{1}{d_x} \sum_{m_x=-\infty}^{\infty} \frac{\text{sinc}^2(k_{xm}\frac{\delta_s}{2})}{D(k_{xm})}\,. \tag{7.1}$$

This is expressed as an infinite summation of Floquet modes (with indexes m_x and wave numbers $k_{xm} = k_{x0} - 2\pi m_x/d_x$, accounting for the periodicity along the x-axis. Here, $k_{x0} = k_0 \text{sin}\theta\text{cos}\phi$, where k_0 is the propagation constant in the free space and θ, ϕ are the angles towards which the array is pointing. The function $D(k_x)$ represents the transverse connected array Green's function [110] and accounts for the periodicity along the y-axis. It is expressed as a summation of Floquet modes with wave numbers $k_{ym} = k_{y0} - 2\pi m_y/d_y$ and $k_{y0} = k_0 \text{sin}\theta\text{sin}\phi$:

$$D(k_x) = \frac{1}{d_y} \sum_{m_y=-\infty}^{\infty} G_{xx}(k_x, k_{ym}) J_0\left(k_{ym}\frac{w_s}{2}\right). \tag{7.2}$$

The zeroth order Bessel function (J_0) is the Fourier transform of the transverse edge-singular magnetic current distribution along the slot. Moreover, G_{xx} is the spectral Green's function that represents the x-component of the magnetic field radiated by a x-oriented elementary magnetic dipole. This Green's function accounts for the stratification along the z-axis and it can be defined to include the ADL slab. It can be expressed in terms of the current solutions of equivalent transmission lines that represent the stratification [113], i.e.

$$G_{xx}(k_x, k_y) = -\frac{I_{\text{TE}}(k_x, k_y)k_x^2 + I_{\text{TM}}(k_x, k_y)k_y^2}{k_\rho^2} \tag{7.3}$$

where $k_\rho^2 = k_x^2 + k_y^2$. The currents I_{TE} and I_{TM} are given by

$$I_{Ti} = \frac{1}{Z_{\text{up},Ti}} + \frac{1}{Z_{\text{down},Ti}} \tag{7.4}$$

Table 7.1: Dimensions of the Array Unit Cell in Terms of the Free-Space Wavelength at the Maximum Frequency of Investigation f_0

$d_x = d_y$	w_s	δ_s	h	h_{gap}	d_{ADL}	w_{ADL}	d_z
$\frac{\lambda_0}{2.1}$	$\frac{\lambda_0}{48}$	$\frac{\lambda_0}{12}$	$\frac{\lambda_0}{12.5}$	$\frac{\lambda_0}{80}$	$\frac{\lambda_0}{11}$	$\frac{\lambda_0}{111}$	$\frac{\lambda_0}{158}$

where Ti can refer to either the transverse electric (TE) or the transverse magnetic (TM) mode. The impedances representing the upper and lower stratifications are calculated using the equivalent circuit models in Fig. 7.4. In these models, the transmission lines for the TE and the TM incidence have characteristic impedances $Z_{0\text{TE}} = \zeta k/k_z$ and $Z_{0\text{TM}} = \zeta k_z/k$, respectively, with ζ and k being the impedance and the wavenumber of the pertaining dielectric slab and with $k_z = (k^2 - k_{x0}^2 - k_{y0}^2)^{1/2}$. Each layer of the ADL is represented as an equivalent susceptance ($B_{s,\infty}$) defined in closed form in Eq. (4.4). The finite height of the ADL is taken into account using a semi-infinite solution for the top layer, represented as $B_{s,\text{semi}\infty}$ in Eq. (4.7). The transformer with turn ratio $1 - k_{\rho m}^2/(2k_{\text{layer}}^2)$ in the TE equivalent circuit in Fig. 7.4(b) was derived in Sec. 3.3. $k_{\rho m}^2$ can be written in terms of the incident angle for homogeneous plane waves (visible region) or, more in general, we consider $k_{\rho m}^2 = k_{xm}^2 + k_{ym}^2$ to treat also the cases of non-homogenous plane waves (higher order Floquet modes). In the expression of the transformer, k_{layer} represents the propagation constant of the medium in which the layer (array of patches) is embedded or it is an average propagation constant if the layer is located at the interface between two different media.

By implementing the equations (7.1) to (7.4) in a Matlab code, we obtain a simple analytical tool to estimate the matching performance of the array unit cell. As an example, a comparison between our tool and a commercial electromagnetic solver [69] is presented in Fig. 7.5. The figure reports the active input impedance of an ADL-loaded array with the geometrical dimensions summarized in Tab. 7.1. A total of 5 layers are used in the ADL design, realizing an effective dielectric constant of 8.4 for normal incidence. The dielectric of the host medium was taken to be free space $\varepsilon_r = 1$. A good comparison is obtained for broadside and scanning toward 50° in the E- , diagonal (D-) and H-planes, as shown in Fig. 7.5. The calculation of the active input impedance, for 15 frequency points and 3 scan angles, can be completed in 0.2 seconds with our code, while it requires about 180 minutes with CST, on the same computer.

The method described in Ch. 3 and 4 is, to our knowledge, the only analytical model accounting for the higher-order interaction between the multiple layers composing the ADL. To highlight the importance of taking into account the higher-order coupling, Fig.

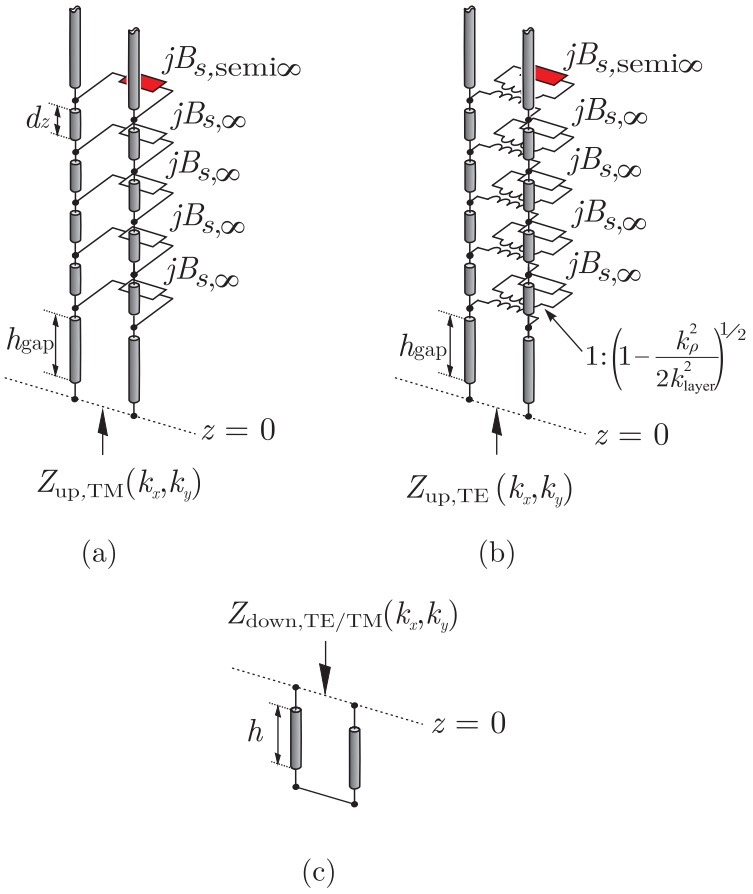

Figure 7.4: An equivalent transmission-line representation of a finite height ADL for a generic TE and TM plane wave.

7.5(a) also reports the result obtained by considering only the interaction of the propagating Floquet mode (above cutoff). The result does not agree anymore with the CST full-wave simulations, showing a 10% shift of the resonance peak.

7.3 Single-Pol Array Design

In this section, we present a design of a single-polarized connected array of slots matched over an octave bandwidth in the target frequency range from 7 to 14 GHz. To realize a broadband transformation between the free-space impedance (377 Ω) and the slot active input impedance (70 Ω), three ADL slabs are considered. Figure 7.6(a) depicts the unit-cell of connected slot array loaded with the multi-slab ADL stack.

To enable the possibility of implementing a feeding structure with PCB via-hole technol-

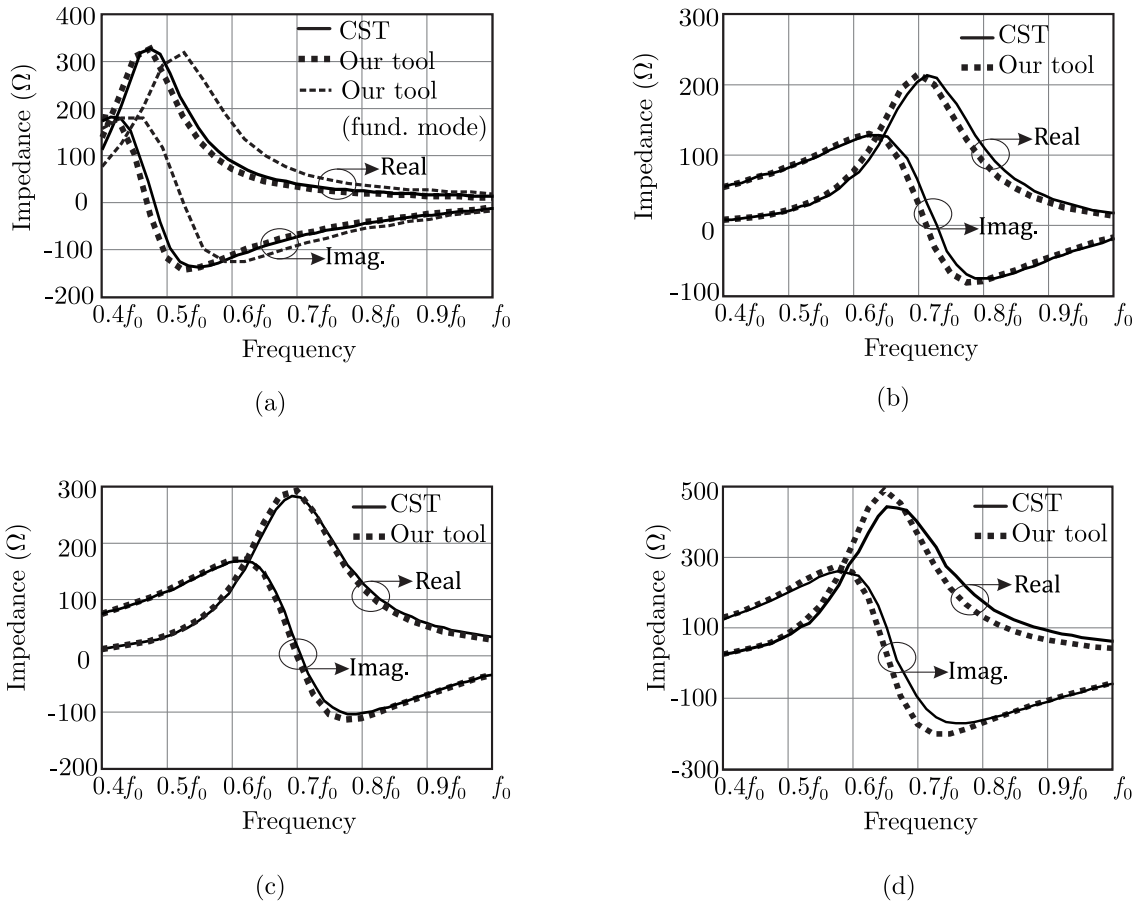

Figure 7.5: Comparison of the input impedance of the connected array of slots loaded with ADL for (a) broadside, scanning at 50° in (b) H- plane (c) D- plane and (d) E-plane.

ogy, we consider a dielectric slab (RO5880LZ) of permittivity $\varepsilon_{r5880\text{LZ}} = 1.96$ between the slot plane and the backing reflector. When compared with a foam substrate, such a slab degrades the matching performance of the array. Therefore, to reduce its effective permittivity, the dielectric can be milled in a grid configuration as shown in Fig. 7.6(b). The equivalent dielectric constant, calculated as in [66], is reduced to 1.4 and it remains almost independent of the angle of the incidence of the plane wave. Also, a substrate of relative permittivity ε_{r5880} =2.2 and thickness 0.254 mm is included for the possibility of realizing a microstrip feed line (see Fig. 7.6(b)).

The analytical tool has been used to optimize the geometrical parameters of the ADL slabs and the connected array, which are summarized in Tabs. 7.2 and 7.3. The grid is modeled in our analytical tool as a homogeneous dielectric of permittivity 1.4 and height of 1.746 mm. The three ADL slabs are characterized by a number of layers (n_z) of 5,

Table 7.2: Dimensions of the Three ADL Slabs

Parameter	Unit	Slab1	Slab2	Slab3
d_{ADL}	(mm)	1.862	1.862	1.862
w_{ADL}	(mm)	0.19	0.2	0.4
h_{gap}	(mm)	0.45	0.5	0.33
d_z	(mm)	0.127	0.333	2
n_z	–	5	6	3
$\varepsilon_{r\mathrm{eff}}$	–	16.5	5.5	1.72
ε_r	–	2.2	1	1

Table 7.3: Dimensions in mm of the Single-Pol Connected Array

$d_x = d_y$	w_s	δ_s	h
9.31	0.7	1.8	2.0

6 and 3, respectively, and relative permittivity, for normal plane-wave incidence, of 16.5, 5.5, and 1.72, respectively. These three different dielectric constants can be engineered by varying the geometrical parameters of the ADLs (refer to Ch. 4). It can be noted that the dimensions of the patches in the ADL slabs are less than one tenth of the wavelength i.e., $0.1\lambda_0$. Here, λ_0 is the wavelength in free space at the maximum frequency of investigation 14 GHz. Such a small size yields very low ohmic losses, in virtue of the non-resonant nature of the metal patches [114, 115]. Moreover, under the hypothesis of small periods, the analytical tool developed in Ch. 3 and 4 remains valid with high accuracy.

7.3.1 Matching Performance for Ideal Design

In Fig. 7.7, the active voltage standing wave ratio (VSWR) of the array normalized to 70 Ω is shown. The VSWR is lower than 2 for over more than one octave bandwidth, for broadside and for scanning to 50° in the E- and the H-planes. These results assume that the array elements are fed with ideal delta-gap excitations, as shown in Fig. 7.2. A fair agreement can be observed between the curves obtained with the presented analytical tool and the results obtained using a commercial electromagnetic solver [69].

Note that the distance from the backing reflector is remarkably low ($0.09\lambda_0$). This height is much lower than the typical value of $\approx \lambda_0/4$ required to maximize the bandwidth for slots with a backing reflector and without superstrates.

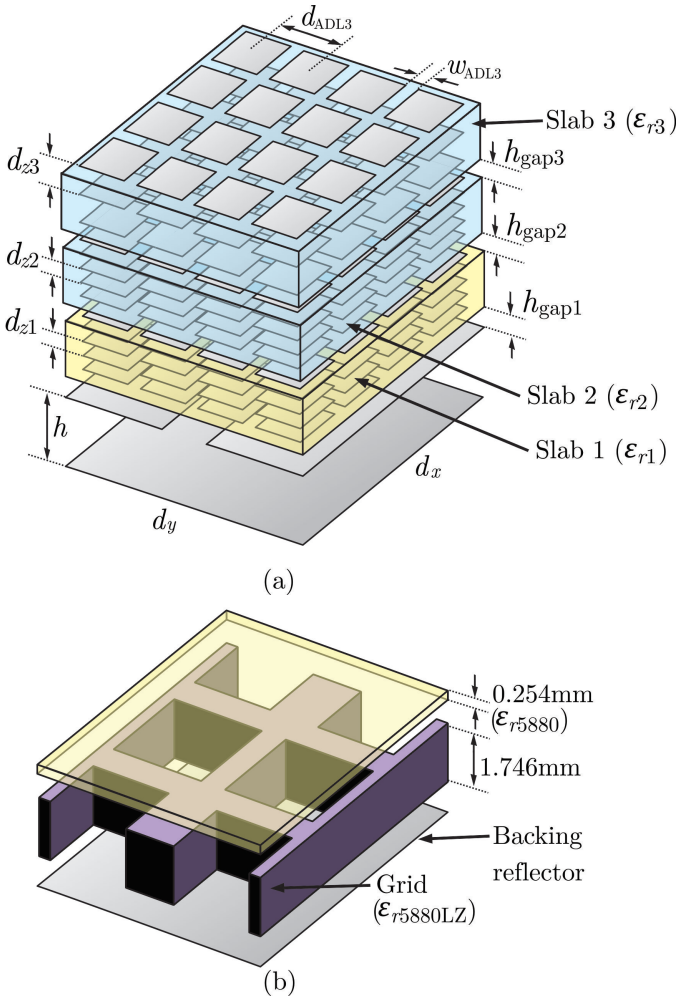

Figure 7.6: (a) A unit cell of connected array radiating in the presence of multi-layer ADL stack; (b) exploded view of the dielectric stratification on the back side of the antenna.

7.3.2 Inclusion of Bonding Layers

The practical realization of the multi-layer PCB composing the antenna array requires the use of bonding layers. A possible implementation of the layer stack is depicted in Fig. 7.8. The first ADL slab is realized using multiple Rogers RO5880 substrates ($\varepsilon_{r1} = 2.2$, thickness $t_1 = 0.127$ mm), in order to achieve very small inter-layer spacing, which would be too demanding for foam substrates. Arlon CuClad 6700 ($\varepsilon_{r6700} = 2.35$, $t_{6700} = 0.038$ mm) is used to bond the slabs together. Rohacell foam ($\varepsilon_{r2} = \varepsilon_{r3} = 1.06$) can be used to realize the other two ADL slabs, for which the inter-layer distance is greater than 330 μm. Since foam cannot be metalized, the metal patches can be printed on a thin dielectric film

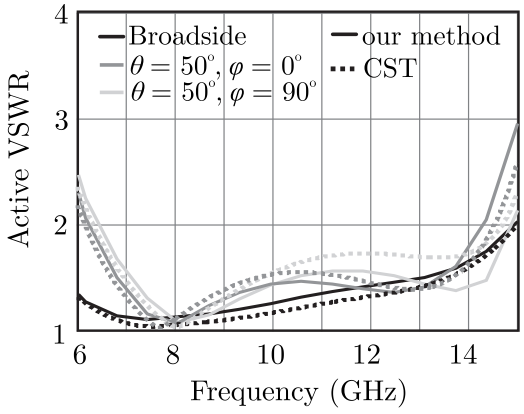

Figure 7.7: Active VSWR of the array for broadside, scanning at 50° in E- and H-plane.

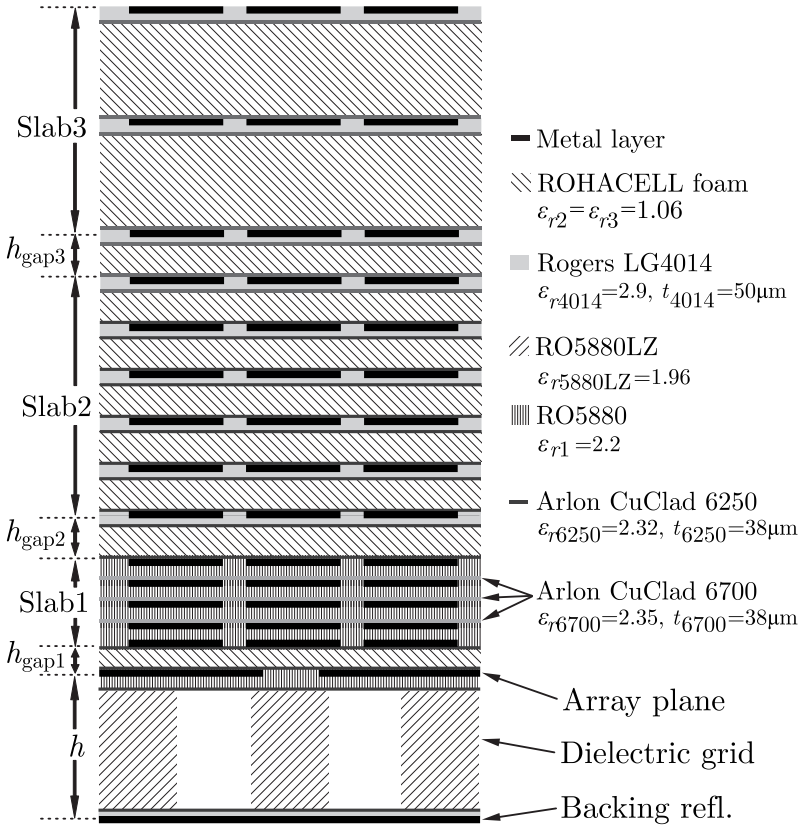

Figure 7.8: A two dimensional view of the stratification with the inclusion of the bonding layers.

(LG4014, $\varepsilon_{r4014} = 2.9$, $t_{4014} = 0.050$ mm) and this layer is glued to the foam using adhesive Arlon CuClad 6250 ($\varepsilon_{r6250} = 2.32$, $t_{6250} = 0.038$ mm), as done in [116].

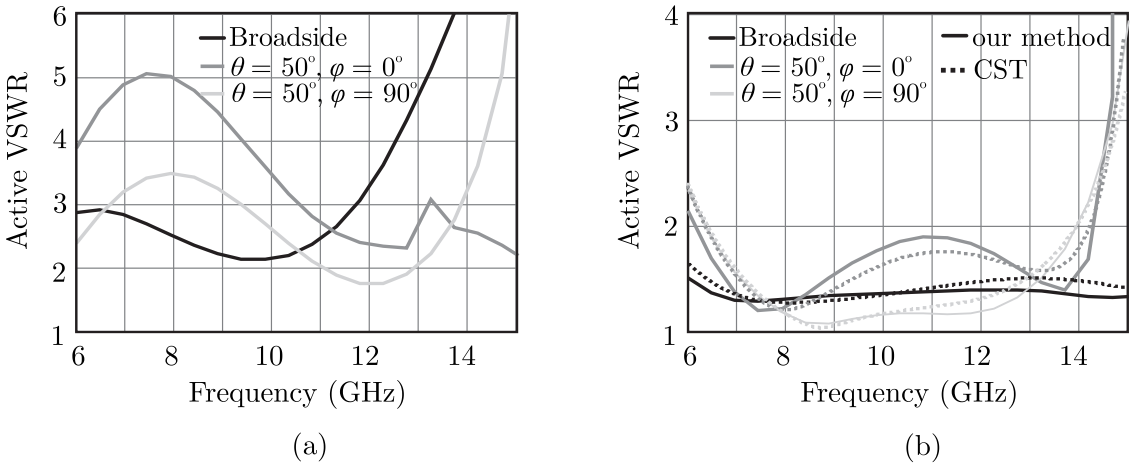

Figure 7.9: (a) Deteriorating effect of the bonds on the active VSWR of Fig. 7.7; (b) re-optimized VSWR, accounting the effect of the bonds.

The effect of the bonding layers onto the array performance is investigated in Fig. 7.9(a), which shows the active VSWR of the array with the inclusions of the glue. It can be observed that the presence of the bonds strongly degrades the matching efficiency of the array. For the specific targeted frequency range, the thickness of the adhesive layers is not negligible with respect to the total height, which increases by about 15% (from 7.1 to 8.1 mm). Smaller impact of the glue is expected for lower frequency designs.
However, this effect can be accounted for in the analytical model of the entire structure, which can be re-optimized including the presence of the adhesive layers. The optimization process resulted in a new set of geometrical parameters of the array and the ADL, which leads to performance similar to the case without bonding. The active VSWR of the array is reported in Fig. 7.9(b), reporting an active VSWR<2 from 6.3 to 14 GHz. CST simulations are also included in the figure for comparison. The optimized dimensions of the ADL and the connected array are listed in Tab. 7.4 and 7.5, respectively.

7.4 Design of the Feeding Structure

The slot element of the array is fed with a microstrip line terminated by a shorting via. A microstrip-to-coaxial transition is implemented to feed the elements with coaxial connectors, located underneath the backing reflector. The transmission coefficient (S_{12}) of the transition, shown in Fig. 7.10, is higher than -0.15 dB over the desired frequency band. Moreover, the transition is designed to implement a quarter wavelength section that

Table 7.4: ADL Dimensions After the Inclusion of Adhesive Films.

Parameter	Unit	Slab1	Slab2	Slab3
d_{ADL}	(mm)	1.862	1.862	1.862
w_{ADL}	(mm)	0.19	0.2	0.4
h_{gap}	(mm)	0.424	0.474	2.1
d_z	(mm)	0.127	0.374	1.47
n_z	–	3	5	2
ε_r	–	2.2	1	1

Table 7.5: Dimensions in mm of the Single-Pol Connected Array

$d_x = d_y$	w_s	δ_s	h
9.25	3.8	1.8	2.0

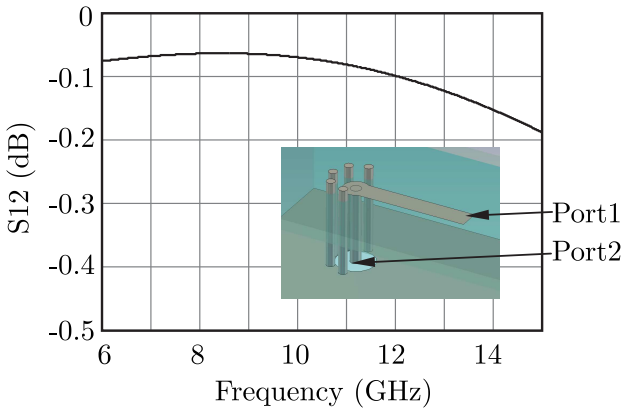

Figure 7.10: The transmission between ports 1 and 2 of the microstrip-to-coaxial transition (shown in the inset).

transforms the input impedance at the slot (70 Ω) to 50 Ω at the connector.

7.4.1 Undesired PPW-Mode Excitation Due to Common-Mode

When including the transition in the array unit cell, simulations exhibit strong resonances within the operative bandwidth, as reported in Fig. 7.11(a), for broadside and scanning in the main planes. Such resonances are caused by common-mode currents, excited on the integrated coaxial feed lines. This effect is described in Fig. 7.11(b), where two adjacent array elements are shown. The current impressed in one element of the array can flow

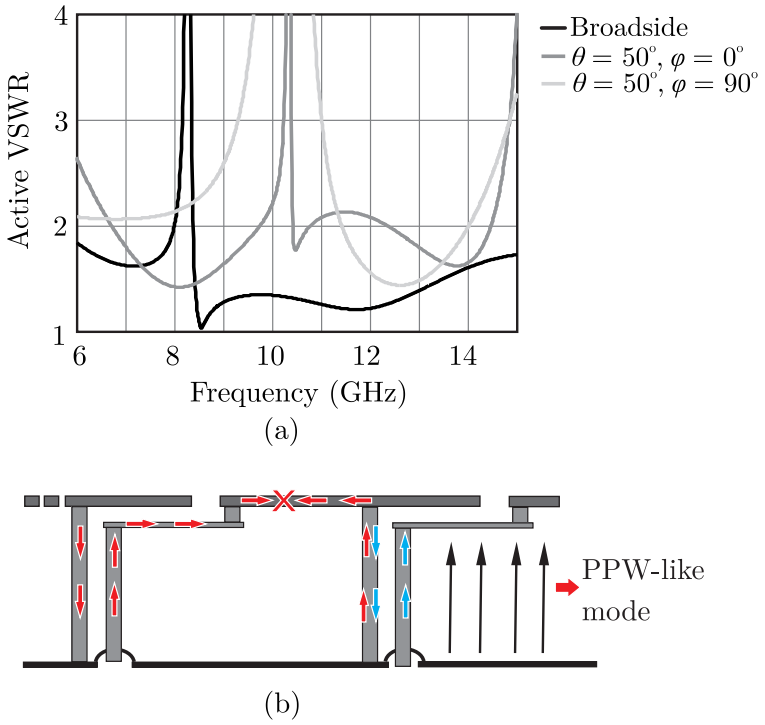

Figure 7.11: (a) Common-mode resonances in the active VSWR of the array due to common-mode current excitation in the vertical feed lines; (b) schematic description of the common-mode current excitation.

to the vertical feed lines of the neighboring element generating unbalanced currents. The common-mode component of these currents excites parallel plate waveguide (PPW) modes within the array substrate, resulting in the resonances observed in Fig. 7.11(a).

7.4.2 Solution to the Common-Mode Resonance

The PPW mode can be suppressed by positioning continuous metallic walls in a configuration as shown in Fig. 7.12(a). The walls prevent the excitation of PPW-like modes, thus representing a choke for the common-mode current. The metal walls are parallel to the slot and are placed in the centers between adjacent slots. This configuration allows to minimize the influence of the metal wall on the slot impedance, since the currents flowing in the metal walls due to neighboring elements cancels out, giving a close-to-zero net current. This behavior is shown in Fig. 7.12(b). A practical implementation of the metal walls is obtained with metal plated vias in the dielectric grid. The via holes, as depicted in Fig. 7.13, are spaced closely enough in terms of wavelength to emulate the properties of a continuous metal wall.

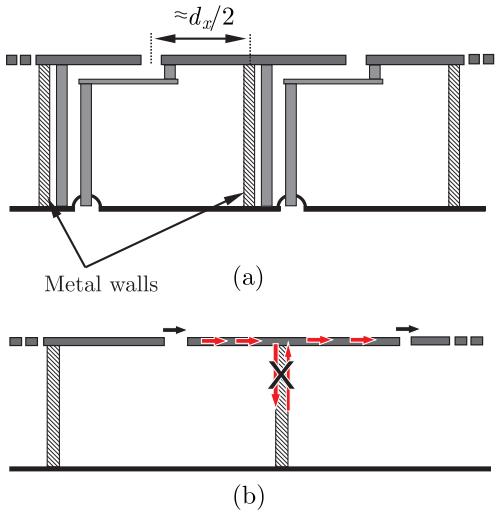

Figure 7.12: (a) Introduction of the metallic walls to inhibit the propagation of the PPW modes; (b) current cancellation on the walls due to neighboring slots.

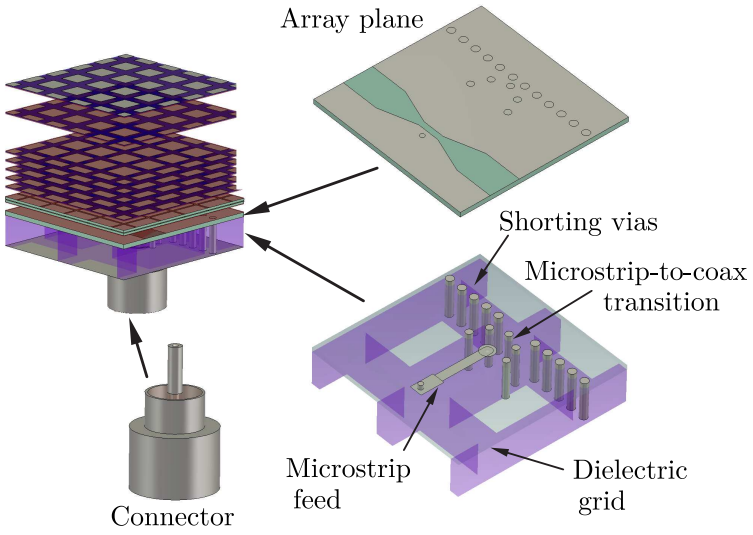

Figure 7.13: A complete three-dimensional view of the unit cell array including the mini-SMP connector.

7.4.3 Array Performance

The simulations of the array including the details of the feed network have been performed with CST [69]. The active VSWR, including the metal wall as well the mini-SMP connector (see Fig. 7.13), is shown in Fig. 7.14. It can be observed that the presence of the walls eliminates the resonances highlighted in Fig. 7.11, resulting in a VSWR of less than 2 from

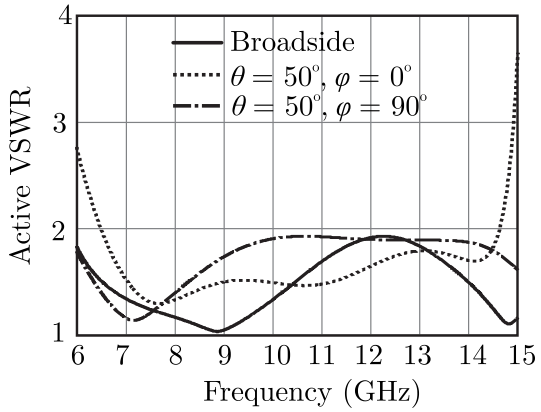

Figure 7.14: Active VSWR of the array shown in Fig. 7.13.

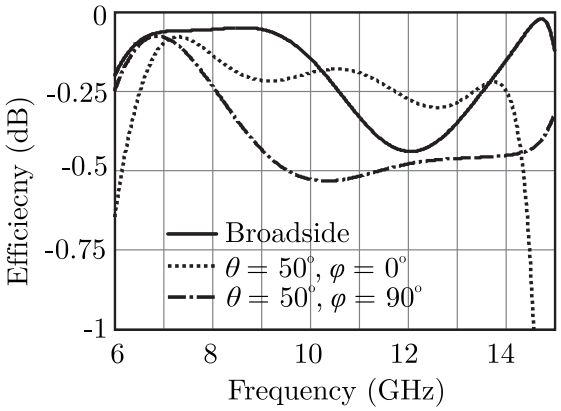

Figure 7.15: The simulated efficiency of the array including ohmic and mismatch losses.

6.5 to 14.6 GHz.

Simulation assuming the finite conductivity of the metal have been performed to estimate the ohmic losses. The total efficiency of the array, under infinite array approximation, is reported in Fig. 7.15. The curves show that the efficiency of the array is higher than 88% for all scanning angles. The main cause of losses is impedance mismatch, while negligible ohmic losses are predicted by the simulations. This distinctive property of the ADL was experimentally verified in Ch. 5.

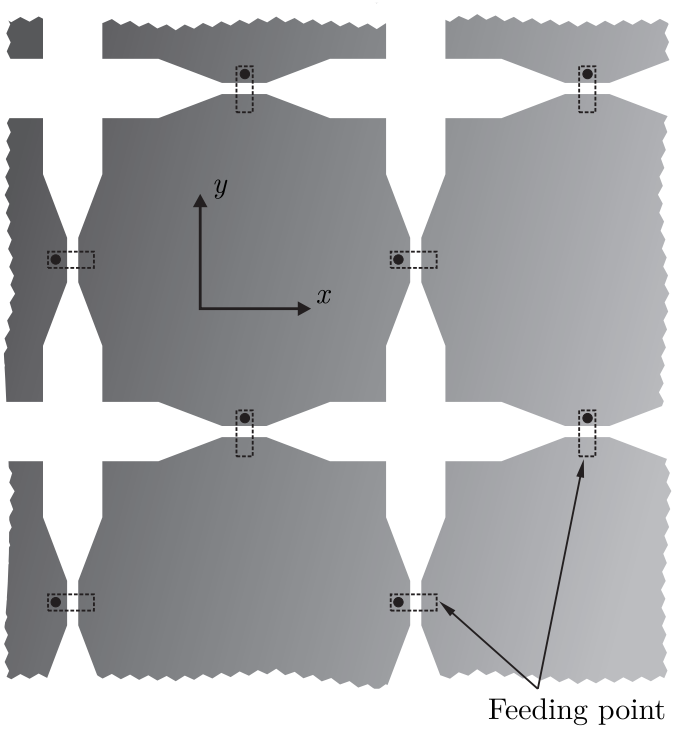

Figure 7.16: Top view of the dual-polarized connected array of slots.

7.5 Dual-Pol Array Design

In this section we investigate the possibility of generalizing the proposed antenna concept to dual-polarized designs. Figure 7.16 shows a top view of slot array for a dual-polarized array. To analyze the effect of the presence of the crossing slots on the matching performance, we only include the feeding microstrip lines in the simulations. The active VSWR of the array, normalized to 70 Ω, is shown in Fig. 7.17(a) and it is below the desired value of 2 from 6.5 to 14.3 GHz.

The cross polarization level is reported in Fig. 7.17(b) for scanning in the diagonal plane and for different values of θ from 0° to 50°. The simulated value is about −10 dB for the worst case i.e, $\theta = 50°$ in the operative frequency band. It is 5 dB higher than the ideal value of a perfectly linearly polarized antenna. This effect is expected in the presence of high permittivity slabs [117].

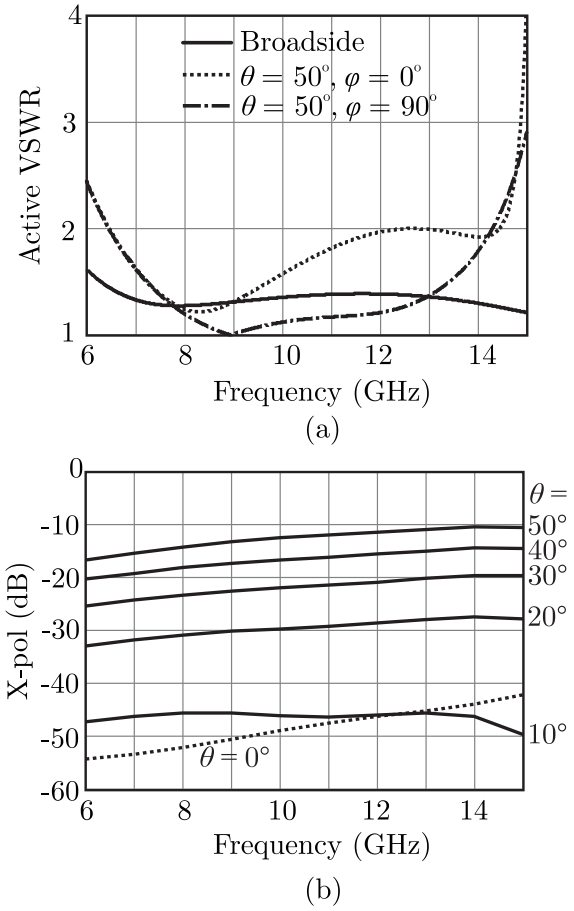

Figure 7.17: (a) Active VSWR of the dual-polarized array and; (b) and cross-polarization performance of array when scanning from θ = 0-50° in the diagonal plane.

7.6 Conclusions

We presented a novel concept for wideband wide-scanning phased array designs, based on connected arrays of slots loaded with ADL superstrates. The proposed structure has two main advantages with respect to the existing solutions. Firstly, it is completely planar and realized with a single multi-layer PCB, with consequent reduction of the cost and the complexity of the array. Secondly, ADLs are used in place of real dielectric superstrates, to achieve much better efficiency in terms of surface-wave loss. The design of a wideband feed structure was also proposed, which does not require balanced-to-unbalanced (balun) transitions that limit the matching bandwidth.

For the design of the array loaded with ADL, including the adhesive layers, an analytical tool can be used which allows to estimate the performance of the array with minimal

computational resources.

The presented array design has VSWR lower than 2 from 6.5 to 14.6 GHz for the single-polarized array, and from 6.5 to 14.3 GHz for the dual-polarized array. The array can scan up to 50° in all azimuth planes with a radiation efficiency higher than 88%. The maximum cross-pol level of the dual-pol array is −10 dB for scanning to 50° in the D-plane.

Chapter 8

Conclusions and Future Prospects

The research work reported in this dissertation was carried out over a period of four years spanning from March 2011 till February 2015 at Delft University of Technology, Delft, Netherlands. The scope of this thesis was the development of an innovative planar antenna concept, which can be characterized by high surface-wave efficiency and unidirectional radiation patterns.

In the design of planar antennas, good front-to-back radiation ratio can be achieved by loading the radiating element with an electrically thick and dense dielectric slab. However, this leads to significant coupling of power into surface wave modes, via those rays that are radiated by the antenna at angles greater than the critical angle, thus deteriorating the antenna radiation performances.

In this dissertation, a planar methodology to solve the issue of surface waves is presented, which can be used to obtain simultaneously high radiation efficiency and good front-to-back radiation ratio. This consists in engineering anisotropic equivalent materials, referred to as artificial dielectric layers (ADL), and use them to enhance the performance of planar antennas. A practical planar realization of this concept can be achieved by embedding inside the host dielectric a periodic array of sub-wavelength square metal patches in a multilayer configuration. In this work, the main aspects pertaining to the theoretical development and the practical implementation of ADLs are investigated.

The most significant results achieved in this thesis work are summarized in the subsequent sections.

8.1 Analysis of ADLs

The analysis of ADLs has been extensively developed within this project. The modeling of ADL structure was first implemented for two-dimensional structures, and then generalized for three dimensional ADLs. The closed-form expressions derived with the formalism described in the thesis are very beneficial in the design phase, since they can be used to predict the performance of antennas in the presence of ADLs with minimal computational resources.

8.1.1 Analysis of Two-Dimensional (Strip-Type) ADLs

In Ch. 2, an analytic formula is presented, which is derived in a two-dimensional case and allows to estimate analytically the effective dielectric constant as a function of the ADL geometrical parameters. Although the derived closed-form expressions hold only for a transverse magnetic (TM) polarized incident wave, it highlights an important physical mechanism: ADL is an equivalent dense material for the plane waves incident in directions close to the normal, whereas it exhibits lower effective permittivity for the waves that are incident close to the grazing angle. This peculiar anisotropy, characteristic of ADLs, is a key property for the design of high-efficiency superstrates.
To study the effect of a near-source radiating in the presence of a finite ADL slab, an in-house developed method of moments tool is built. The numerical results confirm that the ADL inclusions do not support additional surface waves, with respect to the hosting homogeneous dielectric slab.

8.1.2 Analysis of Three-Dimensional (Patch-Type) ADLs

The formulation derived for the description of three-dimensional ADLs was presented in Ch. 3 and Ch. 4. The method was first introduced for a single layer, aiming at describing the interaction between a generic plane wave and a square-mesh layer. In addition to previous works in literature, the adopted approach allows to derive a closed-form expression for the magnetic current distribution on the array plane. The method leads to the derivation of an equivalent circuit that is useful to highlight the characteristic properties of the structure and to define the frequency range of validity of the representation. Also, the decoupling properties of the TE and TM modes and the azimuthal independence of the structure, previously only empirically observed, were here rigorously demonstrated, with consequent gain in physical insight.

One great advantage of the theoretical derivation proposed for the single layer is the convenient generalization of the method to the case of an infinite or semi-infinite cascade of layers. The reactive coupling between adjacent layers is rigorously taken into account in analytical form, for arbitrarily small inter-layer separation. An equivalent circuit was derived, which can be used to calculate, on one hand, the constitutive parameters of the ADL and, on the other hand, the spectral Green's function of the ADL. This latter allows to evaluate the dispersion characteristic of finite slabs, as well as the patterns of a generic antenna in the presence of the ADL. The calculated patterns were validated both with simulations performed with commercial EM solvers and with measured results.

8.2 Practical Demonstration of ADL Based Antenna Design

In this dissertation, two prototypes at X-band and at 0.3 THz were developed to demonstrate the advantages of ADLs. This study has highlighted that the ADL superstrates can be designed and manufactured independently from the antenna and the circuit. Consequently, this allows their use as add-on components, since no accurate alignment is required between the antenna and the superstrate layers. Moreover, ADL are broadband because of their non-resonant nature. This concept can be beneficial for any planar radiating structure, including on-chip antennas as well as antenna arrays.

8.2.1 X-Band Antenna Design

In Ch. 5, a design of a planar integrated antenna, which is realized in printed circuit board technology and benefits from ADL, is presented at 10 GHz. The ADL can be used to selectively enhance the effective dielectric constant of the slabs in specific directions, typically normal to the slab itself. Accordingly, an antenna can be printed on a thin isotropic dielectric slab that hosts the ADL and achieve high front-to-back ratios that normally would only be associated with the dense and thick dielectric slabs. The advantage is that while a dense and thick isotropic layer would also support strong surface wave propagation, an artificially enhanced slab of equivalent normal permittivity does not.
It was shown, with the help of experimental verification, that an electrically thin substrate ($h \leq \lambda_d/10$) can be used to design integrated slot antennas with the matching bandwidth in the order of 13% and front-to-back radiation ratio $\geq$ 10 dB, with virtually no power launched into surface waves.

8.2.2 0.3 THz Antenna Design

On-chip integrated antennas typically radiate in the presence of either a lossy silicon substrate or an electrically thin grounded slab. This leads to either high dielectric losses or very narrow bandwidths of operation. To increase the radiation efficiency of such antennas, we demonstrate, at 300 GHz, the effectiveness of artificial dielectrics superstrates, previously proposed at lower frequencies with printed circuit board technology.

For the fabrication of the antenna and the ADL superstrate, a low-temperature CMOS back-end compatible process was developed within a parallel Ph.D. project. By using pure aluminum as metal and silicon oxide as dielectric host matrix, the ADL was deposited on top of the antenna structure.

Also antenna without ADL loading has been fabricated and used as a reference solution to quantify the enhancement due to the ADL. An improvement of about 2 dB in gain due to the ADL was achieved both in simulations and measurements.

8.3 Connected Array Loaded With ADL Superstrates

In Ch. 7, a novel concept for wideband wide-scanning phased array designs was presented, based on connected arrays of slots loaded with ADL superstrates. The proposed structure has two main advantages with respect to the existing solutions. Firstly, it is completely planar and realized with a single multilayer PCB, with consequent reduction of the cost and the complexity of the array. Secondly, ADLs are used in place of real dielectric superstrates, to achieve much better efficiency in terms of surface-wave loss. The design of a wideband feed structure was also proposed, which does not require balanced-to-unbalanced (balun) transitions that limit the matching bandwidth. For the design of the array loaded with ADL, including the adhesive layers, an analytical tool can be used which allows to estimate the performance of the array with minimal computational resources.

The presented array design has VSWR lower than 2 from 6.5 to 14.6 GHz for the single-polarized array, and from 6.5 to 14.3 GHz for the dual-polarized array. The array can scan up to 50° in all azimuth planes with a radiation efficiency higher than 88%. The maximum cross-pol level of the dual-pol array is -10 dB for scanning to 50° in the D-plane.

Although wider bandwidths are claimed in literature, e.g. in [27, 29], these performances are obtained accepting much lower efficiency in terms of matching (VSWR < 3). If we restrict the comparison with the state-of-the-art to high efficiency designs (VSWR ≤ 2), the designs presented in this thesis achieve performance that is among the best ever reported.

8.4 Future Prospects

Some important benefits of ADL have been highlighted and demonstrated in this thesis. Possible future research directions that can motivate further developments of the concept, are enlisted below:

- The antenna loaded with ADL superstrates was characterized at 0.3 THz when the silicon layer behind the antenna is removed. This additional step adds complexity to the fabrication. As a future work, the enhancing capability of the ADL superstrates should also be assessed for the case of shielded silicon slabs, with the ground plane located electrically close to the antenna.

- The possibility of realizing flat lenses based on the ADL concept can be investigated. A non-uniform geometrical arrangement of the metallic inclusion can be designed to bend the rays propagating through the structure. Such a planar structure would achieve focusing properties typical of three-dimensional bulky dielectric lenses. The fabrication of these flat lenses is an important aspect, due to the likelihood of an high number of layers required.

- The potential advantages of ADLs in the design of antennas can be further exploited for integrated low-cost front ends. The realization of ADLs at frequency higher than 100 GHz, for which the PCB based solutions are too inefficient, will require a parallel research effort in the field of enabling fabrication technologies, such as low temperature co-fired ceramics (LTCC) or novel silicon (e.g. CMOS/Bi-CMOS) processes.

8.5 The Research Impact

The proposed concept has great potential for a number of applications. The most important ones that are envisaged to benefit from improved efficiency of integrated or planar antennas, are the following:

- *"Terabit" wireless communication*: cost-effective ultra-fast wireless communication at unprecedented data rates can be achieved only by tapping the unlicensed THz frequency band. In spite of the availability of the spectrum in this frequency regime, the research in the field of the generation and the detection of the THz waves is driven mainly by high-end applications such as space. These scenarios allow for

costly, complex, bulky and power hungry THz systems, which would not be suitable for viable commercial applications.

Thanks to the recent advancements in the field of commercial silicon technologies (e.g., CMOS/Bi-CMOS, SiGe), the gap between the usage of THz spectrum and its commercial applicability is being bridged. The aforementioned novel manufacturing techniques are making it possible to fabricate transistors with cutoff frequencies reaching as high as 0.5 THz [118, 119]. However, these solutions are still limited in sensitivity due to the poor conversion capabilities between the electrical (on-chip) and the radiated (off-chip) signal and vice versa. The reason behind is that the available on-chip solutions are inefficient either due to the narrow matching bandwidth of the antenna or due to the coupling of power in the substrate modes. These bottlenecks can be overcome by employing the antenna concepts presented in this thesis.

- *The next generation wideband wide-scanning planar connected arrays*: there is an ever-increasing demand for wide bandwidth, large scanning range and planarity in the design of phased arrays. A couple of applications for such arrays are satellite communication [104, 120] and military radars [103]. Connected arrays [27, 103, 109, 111] have recently gain popularity as an efficient solution to meet these stringent requirements. The state-of-the-art connected array designs, available in the literature, usually employ three-dimensional egg-crate configurations to realize the feed networks. Furthermore, the bandwidth is also often limited by the balun used to realize the conversion between unbalanced and balance feeding lines that drive the differential antenna elements. However, a completely planar design would substantially reduce the cost and the complexity of fabrication. Also, to obtain a cost effective solution, the design should be realizable using commercial fabrication techniques e.g., printed circuits boards (PCB).

  In this thesis, an antenna concept for designing the next generation of completely planar connected arrays is presented in Ch. 7. The reported array is matched over more than an octave bandwidth, and is capable of scanning up to $\pm$ 50° in all the azimuth planes. The array is loaded with the ADL superstrates, which enhances the front radiation and also helps to realize the feeding structure by means of an integrated coaxial line. The array can be fabricated using a single multilayer PCB, and uses slots instead of dipoles as the radiating elements to avoid the need of narrowband baluns.

8.5.1 Thesis Outcome

The research work discussed in thesis has resulted in a number of conference and journal publications (refer to p. 159). Moreover, the research has been performed under the framework of the following two projects:

- Integrated Artificial Dielectric for mm-Wave Applications: this project is supported by the Dutch Technology Foundation (STW) under the project code 10709.
- Advanced Antenna Architectures for THz Sensing Instruments (AAATSI): this project is supported by European Research Council starting grants ERC-2011-StG Grant and AAATSI 278794.

Within this thesis project, two antenna prototypes were also fabricated and measured. Furthermore, the manufacturing and the measurement campaign of the third antenna prototype, which pertains to the antenna array discussed in Ch. 7, is also expected in the near future.
The work discussed in Ch. 3 and Ch. 4 was selected as one of the ten finalist for the *Best Student Paper Award* at the 7th edition of European Conference on Antennas and Propagation (EUCAP), Gothenburg, Sweden. Moreover, the results presented in Ch. 2 and Ch. 5 were awarded with the *"Best Poster Award"* at the Annual Netherlands Antenna Research Framework (NARF) Workshop, Delft, Netherlands. Finally, the work presented in Ch. 6 has been awarded with the *"Special Mention for the Excellent Presentation"* in the *Best Student Paper Contest* at the 9th edition of EUCAP, Lisbon, Portugal.

Appendix A

Closed Form Solution of the Elements of the Admittance Matrix

A.1 Reaction Integrals

The purpose of this appendix is to derive closed-form solutions of the reaction integrals arising from the Galerkin projection in Eq. (3.14). The mutual admittances have been defined as follows:

$$Y_{p,q} = \langle \mathbf{g} * \mathbf{m}_p, \mathbf{m}_q \rangle = \int_{-\infty}^{\infty}\int_{-\infty}^{\infty}\int_{-\infty}^{\infty}\int_{-\infty}^{\infty} \mathbf{m}_p(\boldsymbol{\rho'})\mathbf{g}(\boldsymbol{\rho},\boldsymbol{\rho'})\mathbf{m}_q^*(\boldsymbol{\rho})d\boldsymbol{\rho'}d\boldsymbol{\rho} \tag{A.1}$$

where p and q can indicate any of the subscripts 'TE', 'TM' or 'd'. In the spectral domain the quadruple integral can be written as a double Floquet summation by applying the Poisson formula:

$$Y_{p,q} = \frac{1}{d_x d_y}\sum_{m_x=-\infty}^{\infty}\sum_{m_y=-\infty}^{\infty} \mathbf{M}_p(k_{xm},k_{ym})\mathbf{G}(k_{xm},k_{ym})\mathbf{M}_q^*(-k_{xm},-k_{ym}) \tag{A.2}$$

where $k_{xm} = k_{x0} - (2\pi m_x)/d_x$ and $k_{ym} = k_{y0} - (2\pi m_y)/d_y$ are the Floquet wavenumbers, and capital letters indicate Fourier transforms. The elements of the admittance matrix, described in Eq. (3.14), can also be expressed in the matrix form as follows:

$$\mathbf{Y} = \begin{pmatrix} Y_{TE,TE} & Y_{TE,TM} & Y_{TE,d} \\ Y_{TM,TE} & Y_{TM,TM} & Y_{TM,d} \\ Y_{d,TE} & Y_{d,TM} & Y_{d,d} \end{pmatrix}. \tag{A.3}$$

A.1.1 The Basis Functions

The spectral domain expressions of the basis functions, indicated as $\mathbf{M}$ in Eq. (A.2), can be found by applying the Fourier transform to Eqs. (3.11) to (3.13):

$$\mathbf{M}_{\mathrm{TE}}(k_{xm}, k_{ym}) = d_x\delta(m_x)\mathrm{sinc}(k_{ym}\tfrac{w_x}{2})\cos\phi\hat{\mathbf{x}} + d_y\delta(m_y)\mathrm{sinc}(k_{xm}\tfrac{w_y}{2})\sin\phi\hat{\mathbf{y}} \tag{A.4}$$

$$\mathbf{M}_{\mathrm{TM}}(k_{xm}, k_{ym}) = -d_x\delta(m_x)\mathrm{sinc}(k_{ym}\tfrac{w_x}{2})\sin\phi\hat{\mathbf{x}} + d_y\delta(m_y)\mathrm{sinc}(k_{xm}\tfrac{w_y}{2})\cos\phi\hat{\mathbf{y}} \tag{A.5}$$

$$\mathbf{M}_{\mathrm{d}}(k_{xm}, k_{ym}) = B_{\mathrm{d},x}(k_{xm})\mathrm{sinc}(k_{ym}\tfrac{w_x}{2})\hat{\mathbf{x}} - B_{\mathrm{d},y}(k_{ym})\mathrm{sinc}(k_{xm}\tfrac{w_y}{2})\hat{\mathbf{y}} \tag{A.6}$$

where $\delta(m)$ is a Kronecker delta-function equal to 1 for the integer $m = 0$ and 0 otherwise. Also, $B_{\mathrm{d},x}$ and $B_{\mathrm{d},y}$ are the Fourier transform of the doublet basis functions defined in (3.13). The explicit expression of $B_{\mathrm{d},x}$ is the following:

$$\begin{aligned} B_{\mathrm{d},x}(k_x) = &- \frac{e^{-j(k_x+k_0)\frac{w_y}{2}} - e^{-j(k_x+k_0)\frac{d_x}{2}}}{j(k_x+k_0)} - \Gamma\frac{e^{-j(k_x-k_0)\frac{w_y}{2}} - e^{-j(k_x-k_0)\frac{d_x}{2}}}{j(k_x-k_0)} \\ &+ \frac{e^{j(k_x-k_0)\frac{d_x}{2}} - e^{j(k_x-k_0)\frac{w_y}{2}}}{j(k_x-k_0)} + \Gamma\frac{e^{j(k_x+k_0)\frac{d_x}{2}} - e^{j(k_x+k_0)\frac{w_y}{2}}}{j(k_x+k_0)} \\ &+ C\frac{k_x w_y\cos(k_x\frac{w_y}{2}) - 2\sin(k_x\frac{w_y}{2})}{jk_x^2}\,. \end{aligned} \tag{A.7}$$

In Eq. (A.7), C is a constant equal to $(2/w_x)(e^{-jk_0w_x/2} + \Gamma e^{jk_0w_x/2})$ and Γ represents the reflection coefficient at the shorts ($\Gamma = -e^{-jk_0d_x}$).

Asymptotic behavior of $B_{\mathrm{d},x}(k_x)$

It is convenient to evaluate the asymptotic expression, for k_x large, of the Fourier transform $B_{\mathrm{d}}(k_x)$, which is associated with the coupling between the voltage distributions on the two orthogonal slots at the junction. By approximating $j(k_x \pm k_0) \approx jk_x$ for the value of $k_x \to \infty$, the right hand side (RHS) of Eq. (A.7) can be expressed as

$$\begin{aligned} \frac{1}{jk_x}\Bigg[&- \left(e^{-j(k_x+k_0)\frac{w_y}{2}} - e^{-j(k_x+k_0)\frac{d_x}{2}}\right) - \Gamma\left(e^{-j(k_x-k_0)\frac{w_y}{2}} - e^{-j(k_x-k_0)\frac{d_x}{2}}\right) \\ &+ \left(e^{j(k_x-k_0)\frac{d_x}{2}} - e^{j(k_x-k_0)\frac{w_y}{2}}\right) + \Gamma\left(e^{j(k_x+k_0)\frac{d_x}{2}} - e^{j(k_x+k_0)\frac{w_y}{2}}\right)\Bigg] \\ &+ \mathrm{C}\frac{k_x w_y\cos(k_x\frac{w_y}{2}) - 2\sin(k_x\frac{w_y}{2})}{jk_x^2}\,. \end{aligned} \tag{A.8}$$

After a few algebraic steps, Eq. (A.8) can be written as

$$\frac{1}{jk_x}\Bigg[\left(-e^{-j(k_x+k_0)\frac{w_y}{2}}+e^{-j(k_x+k_0)\frac{d_x}{2}}+e^{j(k_x-k_0)\frac{d_x}{2}}-e^{j(k_x-k_0)\frac{w_y}{2}}\right)$$
$$+\Gamma\left(-e^{-j(k_x-k_0)\frac{w_y}{2}}+e^{-j(k_x-k_0)\frac{d_x}{2}}+e^{j(k_x+k_0)\frac{d_x}{2}}-e^{j(k_x+k_0)\frac{w_y}{2}}\right)\Bigg]$$
$$+\mathrm{C}\frac{k_x w_y\cos(k_x\frac{w_y}{2})-2\sin(k_x\frac{w_y}{2})}{jk_x^2} \tag{A.9}$$

and, by using the Euler's formula, one can write

$$\frac{1}{jk_x}\Bigg[\left(-e^{-jk_0\frac{w_y}{2}}2\cos\left(k_x\frac{w_y}{2}\right)+e^{-jk_0\frac{d_x}{2}}2\cos\left(k_x\frac{d_x}{2}\right)\right)$$
$$+\Gamma\left(-e^{jk_0\frac{w_y}{2}}2\cos\left(k_x\frac{w_y}{2}\right)+e^{jk_0\frac{d_x}{2}}2\cos\left(k_x\frac{d_x}{2}\right)\right)\Bigg]$$
$$+\mathrm{C}\frac{k_x w_y\cos(k_x\frac{w_y}{2})-2\sin(k_x\frac{w_y}{2})}{jk_x^2}\,. \tag{A.10}$$

Substituting $\Gamma=-e^{-jk_0d_x}$ in Eq. (A.10), we obtain

$$\frac{2}{jk_x}\Bigg[\left(-e^{-jk_0\frac{w_y}{2}}\cos\left(k_x\frac{w_y}{2}\right)+\cancel{e^{-jk_0\frac{d_x}{2}}\cos\left(k_x\frac{d_x}{2}\right)}\right)$$
$$+\left(e^{jk_0(\frac{w_y}{2}-d_x)}\cos\left(k_x\frac{w_y}{2}\right)-\cancel{e^{-jk_0\frac{d_x}{2}}\cos\left(k_x\frac{d_x}{2}\right)}\right)\Bigg]$$
$$+\mathrm{C}\frac{k_x w_y\cos(k_x\frac{w_y}{2})-2\sin(k_x\frac{w_y}{2})}{jk_x^2} \tag{A.11}$$

which simplifies to

$$\cancel{-\frac{2\cos\left(k_x\frac{w_y}{2}\right)}{jk_x}(e^{-jk_0\frac{w_y}{2}}+\Gamma e^{jk_0\frac{w_y}{2}})}+\cancel{\mathrm{C}\frac{w_y\cos(k_x\frac{w_y}{2})}{jk_x}}+2j\mathrm{C}\frac{\sin(k_x\frac{w_y}{2})}{k_x^2}\,. \tag{A.12}$$

Finally, the Fourier transform of the doublet function is asymptotically given by

$$\boxed{B_{\mathrm{d,asy}}(k_x)\sim 2jC\frac{\sin(k_x w_y/2)}{k_x^2}}\,. \tag{A.13}$$

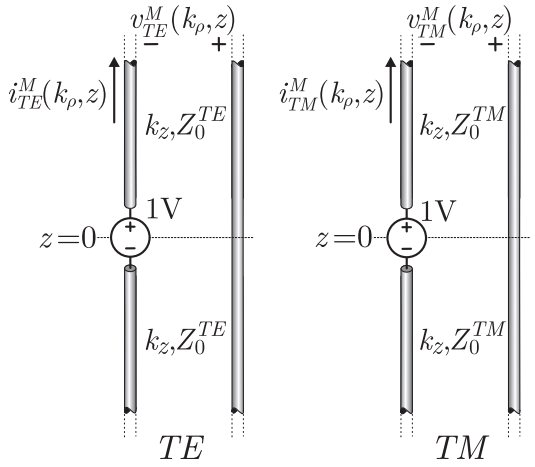

Figure A.1: Equivalent z-transmission lines pertaining to TE and TM modes for a magnetic dipole placed in the (x, y)-plane in free space.

A.1.2 The Green's Function

The explicit matrix form of the dyadic spectral Green's function ($\mathbf{G}$) in Eq. (A.2), which gives the magnetic field (H) radiated by an elementary magnetic current (M), is given as follows [68]:

$$\underline{\underline{G}}^{HM}(k_x,k_y,z) = \begin{pmatrix} G^{HM}_{xx} & G^{HM}_{xy} & G^{HM}_{xz} \\ G^{HM}_{yx} & G^{HM}_{yy} & G^{HM}_{yz} \\ G^{HM}_{zx} & G^{HM}_{zy} & G^{HM}_{zz} \end{pmatrix} = \begin{pmatrix} -\frac{i^M_{TE}k_x^2+i^M_{TM}k_y^2}{k_\rho^2} & \frac{(i^M_{TM}-i^M_{TE})k_xk_y}{k_\rho^2} & 0 \\ \frac{(i^M_{TM}-i^M_{TE})k_xk_y}{k_\rho^2} & -\frac{i^M_{TM}k_x^2+i^M_{TE}k_y^2}{k_\rho^2} & 0 \\ \frac{k_x}{\zeta k}v^M_{TE} & \frac{k_y}{\zeta k}v^M_{TE} & 0 \end{pmatrix}. \tag{A.14}$$

In Eq. (A.14), each entry of the dyad, as shown in Fig. A.1, is expressed as the linear combination of the current and voltage on a transmission line along z. Since we are only interested in planar sources, the dyadic components of the Green's function (GF) related to the magnetic currents in the (x, y)-plane are reported. In the case of free-space, the currents and the voltages in the transmission line can be found using

$$\begin{aligned} i_{TM}(\boldsymbol{k}_\rho) &= \frac{1}{2Z^{TM}(\boldsymbol{k}_\rho)} \\ i_{TE}(\boldsymbol{k}_\rho) &= \frac{1}{2Z^{TE}(\boldsymbol{k}_\rho)} \end{aligned} \tag{A.15}$$

where $\boldsymbol{k}_\rho = k_x\hat{\boldsymbol{x}} + k_y\hat{\boldsymbol{y}}$. Moreover, Z^{TM} and Z^{TE} are the characteristic impedance of the transmission lines shown in Fig. A.1 for TE and TM modes, respectively. They are given by:

$$\begin{aligned} Z^{TM}(\boldsymbol{k}_\rho) &= \zeta_0 \frac{k_z}{k_0} \\ Z^{TE}(\boldsymbol{k}_\rho) &= \zeta_0 \frac{k_0}{k_z}\,. \end{aligned} \tag{A.16}$$

The z-oriented propagation constant is given by $k_z = \sqrt{k_0^2 - k_x^2 - k_y^2}$, where k_0 is the free-space wavenumber, and ζ_0 is the impedance of free-space. By substituting Eq. (A.16) into (A.15), the elements of the free-space (FS) dyadic spectral GF that are required for the solution of $\mathbf{Y}$ (see Eq. (A.2) and (A.3)) can be obtained as follows:

$$\boxed{\begin{aligned} G^{HM}_{xx,\mathrm{FS}}(k_x,k_y) &= -\frac{1}{2k_0\zeta_0}\frac{k_0^2-k_x^2}{k_z} \\ G^{HM}_{yy,\mathrm{FS}}(k_x,k_y) &= -\frac{1}{2k_0\zeta_0}\frac{k_0^2-k_y^2}{k_z} \\ G^{HM}_{yx,\mathrm{FS}}(k_x,k_y) = G^{HM}_{xy,FS}(k_x,k_y) &= \frac{1}{2k_0\zeta_0}\frac{k_xk_y}{k_z} \end{aligned}} \tag{A.17}$$

A.1.3 Evaluation of Y

This subsection describes the mathematical steps required to derive the closed-form solutions of the elements of the admittance matrix given in Eq. (A.3).

Solution of $Y_{\mathrm{TE,TE}}$ and $Y_{\mathrm{TM,TM}}$

In accordance with Eq. (A.2), $Y_{TE,TE}$ can be defined in spectral domain as follows:

$$Y_{\mathrm{TE,TE}} = \frac{1}{d_x d_y}\sum_{m_x=-\infty}^{\infty}\sum_{m_y=-\infty}^{\infty}\mathbf{M}_{TE}(k_{xm},k_{ym})\mathbf{G}(k_{xm},k_{ym})\mathbf{M}^*_{TE}(-k_{xm},-k_{ym})\,. \tag{A.18}$$

An explicit representation of Eq. (A.18) can be obtained by substituting $\mathbf{M}_{TE}$ from Eq. (A.5) and using the definition of the dyadic spectral GF given in Eq. (A.14). Thus, we have

$$
\begin{aligned}
Y_{\mathrm{TE,TE}} &= \cos^2\phi \frac{1}{d_x d_y} \sum_{m_x=-\infty}^{\infty} \sum_{m_y=-\infty}^{\infty} d_x^2 \delta(m_x) \left|\mathrm{sinc}(k_{ym}\frac{w_y}{2})\right|^2 G_{xx}^{HM}(k_{xm}, k_{ym}) \\
&\quad + \sin^2\phi \frac{1}{d_x d_y} \sum_{m_x=-\infty}^{\infty} \sum_{m_y=-\infty}^{\infty} d_x^2 \delta(m_y) \left|\mathrm{sinc}(k_{xm}\frac{w_x}{2})\right|^2 G_{yy}^{HM}(k_{xm}, k_{ym}) \\
&+ \sin\phi\cos\phi \frac{2}{d_x d_y} \sum_{m_x=-\infty}^{\infty} \sum_{m_y=-\infty}^{\infty} d_x d_y \delta(m_x)\delta(m_y) \,\mathrm{sinc}(k_{ym}\frac{w_y}{2}) \,\mathrm{sinc}(-k_{xm}\frac{w_x}{2}) G_{xy}^{HM}(k_{xm}, k_{ym}) \,.
\end{aligned}
\tag{A.19}
$$

Then, by exploiting the properties of the Kronecker δ-function, and by taking $d_y = d_x$, one obtains

$$
\begin{aligned}
Y_{\mathrm{TE,TE}} &= \cos^2\phi \left(\sum_{m_y=-\infty}^{\infty} \left|\mathrm{sinc}(k_{ym}\frac{w_y}{2})\right|^2 G_{xx}^{HM}(k_{x0}, k_{ym}) \right) \\
&+ \sin^2\phi \left(\sum_{m_x=-\infty}^{\infty} \left|\mathrm{sinc}(k_{xm}\frac{w_x}{2})\right|^2 G_{yy}^{HM}(k_{xm}, k_{y0}) \right) \\
&+ 2\sin\phi\cos\phi \left(\mathrm{sinc}(k_{y0}\frac{w_y}{2}) \,\mathrm{sinc}(k_{x0}\frac{w_x}{2}) G_{xy}^{HM}(k_{x0}, k_{y0}) \right) \,.
\end{aligned}
\tag{A.20}
$$

A convenient way of simplifying Eq. (A.20) is to treat each term on its RHS (inside the parenthesis) separately. Let us consider the first term, which can also be expressed by splitting up the summation in m_y in the fundamental Floquet mode ($m_y = 0$) and higher order modes ($m_y \neq 0$) as follows:

$$
\begin{aligned}
\sum_{m_y=-\infty}^{\infty} \left|\mathrm{sinc}(k_{ym}\frac{w_y}{2})\right|^2 G_{xx}^{HM}(k_{x0}, k_{ym}) &= \left|\mathrm{sinc}(k_{y0}\frac{w_y}{2})\right|^2 G_{xx}^{HM}(k_{x0}, k_{y0}) \\
&\quad + \sum_{m_y\neq 0} \left|\mathrm{sinc}(k_{ym}\frac{w_y}{2})\right|^2 G_{xx}^{HM}(k_{x0}, k_{ym}) \,.
\end{aligned}
\tag{A.21}
$$

The dyadic GF ($\boldsymbol{G}$) can be related with the free-space GF (presented in Eq. (A.17)) using $\boldsymbol{G} = 4\boldsymbol{G}_{FS}$. A factor of 4 arises when the boundary conditions which are necessary to treat a single layer of the ADL are applied (refer to Sec. 3.2). Thus, we have

$$
\mathrm{RHS} = -\left|\mathrm{sinc}(k_{y0}\frac{w_y}{2})\right|^2 \frac{2}{k_0\zeta_0}\frac{k_0^2 - k_{x0}^2}{k_{z0}} - \sum_{m_y\neq 0} \left|\mathrm{sinc}(k_{ym}\frac{w_y}{2})\right|^2 \frac{2}{k_0\zeta_0}\frac{k_0^2 - k_{x0}^2}{k_{zm}} \,.
\tag{A.22}
$$

An equivalent compact representation of Eq. (A.22) is given by

$$\sum_{m_y=-\infty}^{\infty} \left|\mathrm{sinc}(k_{ym}\frac{w_y}{2})\right|^2 G_{xx}^{HM}(k_{x0},k_{ym}) \approx -\frac{k_0^2-k_{x0}^2}{k_0\zeta_0}\left(\frac{2}{k_{z0}}+jB_s\frac{\zeta_0}{k_0}\right) \tag{A.23}$$

where the function B_s represents the slot-susceptance and is defined as

$$B_s = \frac{-2jk_0}{\zeta_0}\sum_{m_y\neq 0}\frac{|\mathrm{sinc}(k_{ym}w_y/2)|^2}{k_{zm}} = \frac{-2jk_0}{\zeta_0}\sum_{m_x\neq 0}\frac{|\mathrm{sinc}(k_{xm}w_x/2)|^2}{k_{zm}}\,. \tag{A.24}$$

Here the higher order Floquet mode summations, which refer to the x- and y-periodicity, are considered to be equal. This is because ADL has square unit cells. Hence, for Floquet modes $m_x \neq 0$ and $m_y \neq 0$ we can use the approximation $k_{zm} \approx -j|2\pi m_y/d_y|$ and $k_{zm} \approx -j|2\pi m_x/d_x|$, respectively. Also, we made use of the small-argument approximation of the sinc function, which implies that

$$\mathrm{sinc}\left(k_{y0}\frac{w_y}{2}\right) \approx \mathrm{sinc}\left(k_{x0}\frac{w_x}{2}\right) \approx 1\,. \tag{A.25}$$

Note that the approximation in Eq. (A.25) is valid as long as the width of the slots is much smaller than the wavelength ($w_y \ll \lambda$). Furthermore, analogous steps can be followed to obtain the explicit expression of the second summation.

$$\sum_{m_x=-\infty}^{\infty} \left|\mathrm{sinc}(k_{xm}\frac{w_x}{2})\right|^2 G_{yy}^{HM}(k_{xm},k_{y0}) \approx -\frac{k_0^2-k_{y0}^2}{k_0\zeta_0}\left(\frac{2}{k_{z0}}+jB_s\frac{\zeta_0}{k_0}\right)\,. \tag{A.26}$$

The third term in Eq. (A.20) can be expressed as

$$\mathrm{sinc}(k_{y0}\frac{w_y}{2})\,\mathrm{sinc}(k_{x0}\frac{w_x}{2})G_{xy}^{HM}(k_{x0},k_{y0}) \approx \frac{2}{k_0\zeta_0}\frac{k_{x0}k_{y0}}{k_{z0}}\,. \tag{A.27}$$

Substituting Eq. (A.23), (A.26) and (A.27) in (A.20), one obtains

$$\begin{aligned} Y_{\mathrm{TE,TE}} = -\cos^2\phi\frac{k_0^2-k_{x0}^2}{k_0\zeta_0}\cdot\left(\frac{2}{k_{z0}}+jB_s\frac{\zeta_0}{k_0}\right) - \sin^2\phi\frac{k_0^2-k_{y0}^2}{k_0\zeta_0}\cdot\left(\frac{2}{k_{z0}}+jB_s\frac{\zeta_0}{k_0}\right) \\ + 4\sin\phi\cos\phi\frac{1}{k_0\zeta_0}\frac{k_{x0}k_{y0}}{k_{z0}} \end{aligned} \tag{A.28}$$

By replacing $k_{x0} = k_0\sin\theta\cos\phi$, $k_{y0} = k_0\sin\theta\sin\phi$ in Eq. (A.28), the following closed form expression of $Y_{\mathrm{TE,TE}}$ is obtained:

$$\boxed{Y_{\mathrm{TE,TE}} \approx -\frac{2}{Z_{0TE}} - jB_s(1-\frac{\sin^2\theta}{2}) + jB_s\frac{\sin^2\theta\cos^2(2\phi)}{2}}\,. \tag{A.29}$$

The admittance $Y_{\mathrm{TM,TM}}$ can also be calculated in a similar way. For the sake of brevity, we present here only the final result, which is given by

$$\boxed{Y_{\mathrm{TM,TM}} \approx -\frac{2}{Z_{0TM}} - jB_s + jB_s \frac{\sin^2\theta \cos^2(2\phi)}{2}} \tag{A.30}$$

The impedances Z_{0TE} and Z_{0TM} in Eq. (A.29) and (A.30) can be calculated using Eq. (A.16).

Solution of $Y_{\mathrm{TE,TM}} = Y_{\mathrm{TM,TE}}$

The admittance terms which describe the coupling between the TE and TM modes can be written as follows:

$$Y_{\mathrm{TM,TE}} = Y_{\mathrm{TE,TM}} = \frac{1}{d_x d_y} \sum_{m_x=-\infty}^{\infty} \sum_{m_y=-\infty}^{\infty} \mathbf{M}_{TE}(k_{xm}, k_{ym}) \mathbf{G}(k_{xm}, k_{ym}) \mathbf{M}^*_{TM}(-k_{xm}, -k_{ym})\,. \tag{A.31}$$

By substituting the description of TE and TM magnetic currents (see Eq. (A.4) and (A.5)) in Eq. (A.31), we obtain the following expression

$$\begin{aligned} Y_{\mathrm{TE,TM}} = & -\sin\phi\cos\phi \sum_{m_y=-\infty}^{\infty} \left|\mathrm{sinc}(k_{ym}\frac{w_y}{2})\right|^2 G^{HM}_{xx}(k_{x0}, k_{ym}) \\ & +\sin\phi\cos\phi \sum_{m_x=-\infty}^{\infty} \left|\mathrm{sinc}(k_{xm}\frac{w_x}{2})\right|^2 G^{HM}_{yy}(k_{xm}, k_{y0}) \\ & +(\sin^2\phi - \cos^2\phi)\,\mathrm{sinc}(k_{y0}\frac{w_y}{2})\,\mathrm{sinc}(k_{x0}\frac{w_x}{2}) G^{HM}_{xy}(k_{x0}, k_{y0}) \end{aligned} \tag{A.32}$$

which, by using Eq. (A.17) and Eqs. (A.23)-(A.27) and performing some tedious algebraic steps, can be expressed in the following compact form:

$$\boxed{Y_{\mathrm{TM,TE}} \approx Y_{\mathrm{TE,TM}} \approx -jB_s \frac{\sin^2\theta \sin(2\phi)\cos(2\phi)}{2}}\,. \tag{A.33}$$

Solution of $Y_{\mathbf{d,d}}$

Using Eq. (A.2) and (A.6), $Y_{\mathrm{d,d}}$ can be expressed as follows:

$$Y_{\mathrm{d,d}} = \frac{1}{d_x d_y} \sum_{m_x=-\infty}^{\infty} \sum_{m_y-\infty}^{\infty} \left(B_{\mathrm{d},x}(k_{xm}) \mathrm{sinc}(k_{ym}\frac{w_x}{2})\hat{\mathbf{x}} - B_{\mathrm{d},y}(k_{ym}) \mathrm{sinc}(k_{xm}\frac{w_y}{2})\hat{\mathbf{y}} \right) \\ \mathbf{G}(k_{xm}, k_{ym}) \left(B_{\mathrm{d},x}(-k_{xm}) \mathrm{sinc}(-k_{ym}\frac{w_x}{2})\hat{\mathbf{x}} - B_{\mathrm{d},y}(-k_{ym}) \mathrm{sinc}(-k_{xm}\frac{w_y}{2})\hat{\mathbf{y}} \right) \quad \text{(A.34)}$$

By performing the product between the vectors and the dyadic GF, we obtain

$$Y_{\mathrm{d,d}} = \frac{1}{d_x d_y} \sum_{m_x=-\infty}^{\infty} \sum_{m_y=-\infty}^{\infty} |B_{\mathrm{d},x}(k_{xm})|^2 |\mathrm{sinc}(k_{ym}\frac{w_y}{2})|^2 G_{xx}^{HM}(k_{xm}, k_{ym}) \\ + \frac{1}{d_x d_y} \sum_{m_x=-\infty}^{\infty} \sum_{m_y=-\infty}^{\infty} |B_{\mathrm{d},y}(k_{ym})|^2 |\mathrm{sinc}(k_{xm}\frac{w_x}{2})|^2 G_{yy}^{HM}(k_{xm}, k_{ym}) \\ - \frac{2}{d_x d_y} \sum_{m_x=-\infty}^{\infty} \sum_{m_y=-\infty}^{\infty} B_{\mathrm{d},x}(k_{xm}) \mathrm{sinc}(k_{ym}\frac{w_x}{2}) B_{\mathrm{d},y}(-k_{ym}) \mathrm{sinc}(-k_{xm}\frac{w_y}{2}) G_{xy}^{HM}(k_{xm}, k_{ym}) \quad \text{(A.35)}$$

As shown in Fig. A.2, the Fourier transforms of the doublet basis functions for the fundamental Floquet mode (i.e., $m_x = 0$ and $m_y = 0$) can be approximated equal to zero.

$$B_{\mathrm{d},x}(k_{x0}) \approx B_{\mathrm{d},y}(k_{y0}) \approx 0\,. \quad \text{(A.36)}$$

The reason is that they are quasi-odd functions and vanish close to the origin. Also, it can be seen observed from Fig. A.2 that

$$B_{\mathrm{d},x}(k_{xm}) \simeq B_{\mathrm{d},y}(k_{ym}) \quad \forall (m_x, m_y)\,. \quad \text{(A.37)}$$

Equations (A.36) and (A.37) imply that

$$\frac{1}{d_x d_y} \sum_{m_x=-\infty}^{\infty} \sum_{m_y=-\infty}^{\infty} |B_{\mathrm{d},x}(k_{xm})|^2 |\mathrm{sinc}(k_{ym}\frac{w_y}{2})|^2 G_{xx}^{HM}(k_{xm}, k_{ym}) \approx \\ \frac{1}{d_x d_y} \sum_{m_x=-\infty}^{\infty} \sum_{m_y=-\infty}^{\infty} |B_{\mathrm{d},y}(k_{ym})|^2 |\mathrm{sinc}(k_{xm}\frac{w_x}{2})|^2 G_{yy}^{HM}(k_{xm}, k_{ym})\,. \quad \text{(A.38)}$$

Therefore, Eq. (A.35) can also be expressed as follows:

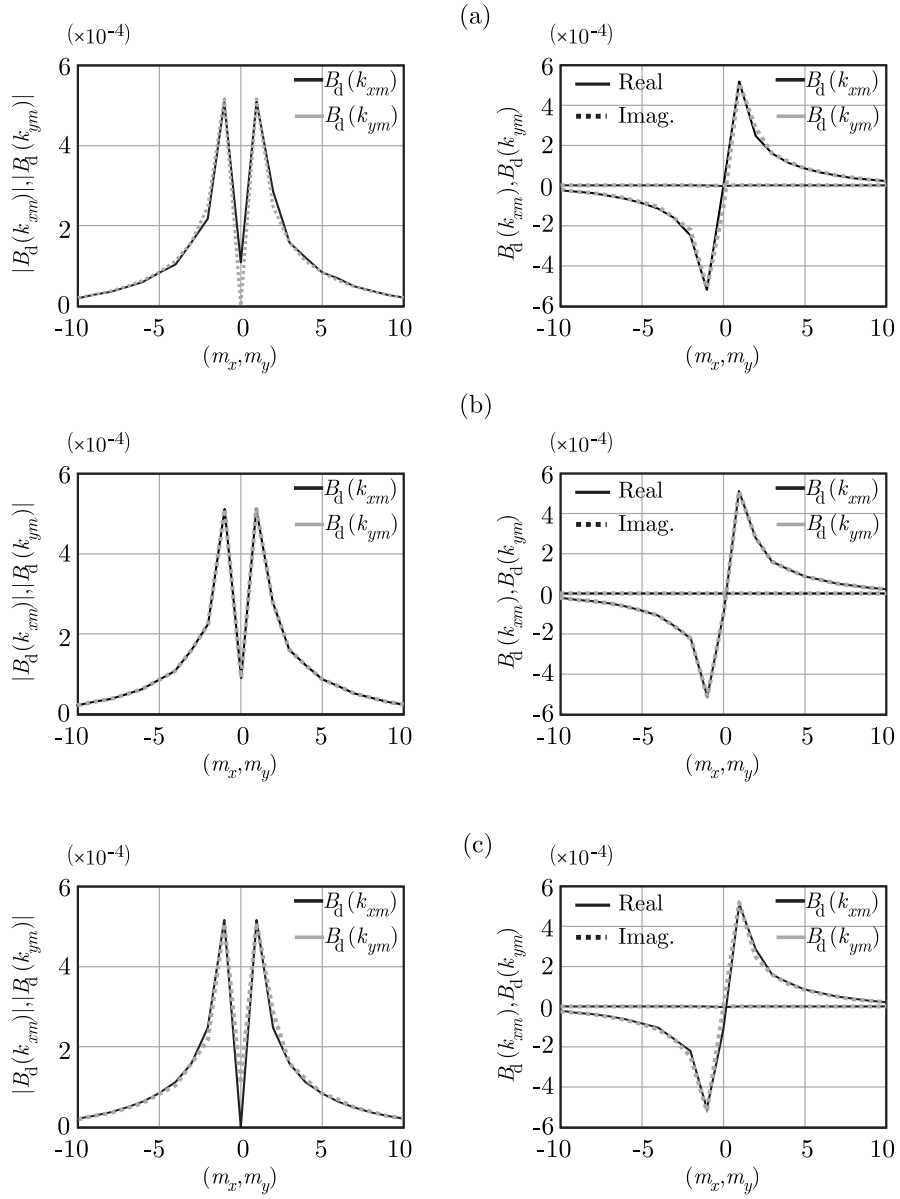

Figure A.2: Fourier transform of the doublet basis function considering $d_x = d_y = 0.15\lambda_0$, $w_x = w_y = 0.01\lambda_0$, $\theta = 60°$, and (a) $\phi = 0°$, (b) $\phi = 45°$ and, (c) $\phi = 90°$.

$$Y_{\mathrm{d,d}} \approx \frac{2}{d_x d_y} \sum_{m_x=-\infty}^{\infty} \sum_{m_y=-\infty}^{\infty} |B_{\mathrm{d},x}(k_{xm})|^2 |\mathrm{sinc}(k_{ym}\frac{w_y}{2})|^2 G_{xx}^{HM}(k_{xm}, k_{ym}) - \frac{2}{d_x d_y} \sum_{m_x=-\infty}^{\infty} \sum_{m_y=-\infty}^{\infty} B_{\mathrm{d},x}(k_{xm}) \mathrm{sinc}(k_{ym}\frac{w_x}{2}) B_{\mathrm{d},y}(-k_{ym}) \mathrm{sinc}(-k_{xm}\frac{w_y}{2}) G_{xy}^{HM}(k_{xm}, k_{ym}) \,. \tag{A.39}$$

By splitting up the summation over m_x and m_y into the fundamental mode and higher order modes, one obtains

$$Y_{\mathrm{d,d}} \approx \frac{2}{d_x d_y} \sum_{m_x \neq 0} B_{\mathrm{d},x}(k_{xm}) \cdot \Bigg[\Bigg\{ B_{\mathrm{d},x}(-k_{xm}) |\mathrm{sinc}(k_{y0}\frac{w_y}{2})|^2 G_{xx}^{HM}(k_{xm}, k_{y0}) - \mathrm{sinc}(k_{y0}\frac{w_x}{2}) \cancelto{0}{B_{\mathrm{d},y}(-k_{y0})} \mathrm{sinc}(-k_{xm}\frac{w_y}{2}) G_{xy}^{HM}(k_{xm}, k_{y0}) \Bigg\} + \sum_{m_y \neq 0} \Bigg\{ B_{\mathrm{d},x}(-k_{xm}) |\mathrm{sinc}(k_{ym}\frac{w_y}{2})|^2 G_{xx}^{HM}(k_{xm}, k_{ym}) - \mathrm{sinc}(k_{ym}\frac{w_x}{2}) B_{\mathrm{d},y}(-k_{ym}) \mathrm{sinc}(-k_{xm}\frac{w_y}{2}) G_{xy}^{HM}(k_{xm}, k_{ym}) \Bigg\} \Bigg] . \quad \text{(A.40)}$$

It can be proved that the sum for $m_y \neq 0$ in Eq. (A.40) is equal to zero.

$$\sum_{m_y \neq 0} \Bigg(B_{\mathrm{d},x}(-k_{xm}) |\mathrm{sinc}(k_{ym}\frac{w_y}{2})|^2 G_{xx}^{HM}(k_{xm}, k_{ym}) - \mathrm{sinc}(k_{ym}\frac{w_x}{2}) B_{\mathrm{d},y}(-k_{ym}) \mathrm{sinc}(-k_{xm}\frac{w_y}{2}) G_{xy}^{HM}(k_{xm}, k_{ym}) \Bigg) \approx 0 \quad \text{(A.41)}$$

Proof of Eq. (A.41)

Using Eq. (A.13) and (A.17), (Eq. A.41) can be written as follows:

$$\approx 2jC \frac{2}{k_0 \zeta_0} \sum_{m_y \neq 0} \Bigg(\frac{\sin(k_{xm}\frac{w_x}{2})}{k_{xm}^2} |\mathrm{sinc}(k_{ym}\frac{w_y}{2})|^2 \frac{-k_{xm}^2}{k_{zm}} - \mathrm{sinc}(k_{ym}\frac{w_x}{2}) \frac{\sin(-k_{ym}\frac{w_y}{2})}{k_{ym}^2} \mathrm{sinc}(-k_{xm}\frac{w_y}{2}) \frac{k_{xm} k_{ym}}{k_{zm}} \Bigg)$$

which then simplifies further to

$$\approx \frac{4jC}{k_0 \zeta_0} \sum_{m_y \neq 0} \Bigg(\sin(k_{xm}\frac{w_x}{2}) |\mathrm{sinc}(k_{ym}\frac{w_y}{2})|^2 \frac{-1}{k_{zm}} - \mathrm{sinc}(k_{ym}\frac{w_x}{2}) \frac{\sin(-k_{ym}\frac{w_y}{2})}{k_{ym}} \frac{\sin(-k_{xm}\frac{w_y}{2})}{(-k_{xm}\frac{w_y}{2})} \frac{k_{xm}}{k_{zm}} \Bigg) .$$

Since we assume that $w_y = w_x$, we have

$$\frac{4jC}{k_0\zeta_0}\sum_{m_y\neq 0}\left(\sin(k_{xm}\frac{w_x}{2})|\mathrm{sinc}(k_{ym}\frac{w_y}{2})|^2\frac{-1}{k_{zm}}+|\mathrm{sinc}(k_{ym}\frac{w_x}{2})|^2\sin(k_{xm}\frac{w_y}{2})\frac{1}{k_{zm}}\right)=0\,.$$

Finally, Eq. (A.40) reduces to

$$Y_{\mathrm{d,d}}=\frac{2}{d_xd_y}\sum_{m_x\neq 0}|B_{\mathrm{d},x}(k_{xm})|^2G_{xx}^{HM}(k_{xm},k_{y0}) \tag{A.42}$$

where the small argument approximation of the sinc function is also used (refer to Eq. (A.25)). By replacing $G_{xx}^{HM}=4G_{xx,\mathrm{FS}}^{HM}$ (see Eq. (A.17)) in (A.42) leads to

$$Y_{\mathrm{d,d}}=-\frac{2}{k_0\zeta_0}\frac{2}{d_xd_y}\sum_{m_x\neq 0}|B_{\mathrm{d},x}(k_{xm})|^2\frac{k_0^2-k_{xm}^2}{k_{zm}}\,. \tag{A.43}$$

As pointed out earlier, for the higher order Floquet modes, one can, use the following two approximations:

- $k_{zm}\approx\sqrt{-k_{xm}^2}=-j|k_{xm}|$
- $k_0^2-k_{xm}^2\approx -k_{xm}^2\,.$

Therefore, Eq. (A.43) takes the following form:

$$\boxed{Y_{\mathrm{d,d}}\approx\frac{4j}{k_0\zeta_0}\frac{1}{d_xd_y}\sum_{m_x\neq 0}|B_{\mathrm{d},x}(k_{xm})|^2|k_{xm}|}\,. \tag{A.44}$$

Solution of $Y_{\mathrm{TE,d}}$ and $Y_{\mathrm{TM,d}}$

Let us now define $Y_{\mathrm{TE,d}}$ using Eq. (A.2):

$$\begin{aligned}Y_{\mathrm{TE,d}}=\frac{1}{d_xd_y}\sum_{m_x=-\infty}^{\infty}\sum_{m_y-\infty}^{\infty}&\left(d_x\delta(m_x)\mathrm{sinc}(k_{ym}\tfrac{w_x}{2})\cos\phi\hat{\mathbf{x}}+d_y\delta(m_y)\mathrm{sinc}(k_{xm}\tfrac{w_y}{2})\sin\phi\hat{\mathbf{y}}\right)\\&\mathbf{G}(k_{xm},k_{ym})\left(B_{\mathrm{d},x}(-k_{xm})\mathrm{sinc}(-k_{ym}\frac{w_x}{2})\hat{\mathbf{x}}-B_{\mathrm{d},y}(-k_{ym})\mathrm{sinc}(-k_{xm}\frac{w_y}{2})\hat{\mathbf{y}}\right)\end{aligned} \tag{A.45}$$

It can written more explicitly as follows:

$$
\begin{aligned}
Y_{\mathrm{TE,d}} = & \\
& \cos\phi \frac{1}{d_x d_y} \sum_{m_x=-\infty}^{\infty} \sum_{m_y=-\infty}^{\infty} d_x \delta(m_x) \mathrm{sinc}(k_{ym} \tfrac{w_x}{2}) G_{xx}^{HM}(k_{xm}, k_{ym}) B_{\mathrm{d},x}(-k_{xm}) \mathrm{sinc}(k_{ym} \tfrac{w_y}{2}) \\
& - \sin\phi \frac{1}{d_x d_y} \sum_{m_x=-\infty}^{\infty} \sum_{m_y=-\infty}^{\infty} d_y \delta(m_y) \mathrm{sinc}(k_{xm} \tfrac{w_y}{2}) G_{yy}^{HM}(k_{xm}, k_{ym}) B_{\mathrm{d},y}(-k_{ym}) \mathrm{sinc}(-k_{xm} \tfrac{w_x}{2}) \\
& - \sin\phi \frac{1}{d_x d_y} \sum_{m_x=-\infty}^{\infty} \sum_{m_y=-\infty}^{\infty} d_x \delta(m_x) \mathrm{sinc}(k_{ym} \tfrac{w_x}{2}) G_{xy}^{HM}(k_{xm}, k_{ym}) B_{\mathrm{d},y}(-k_{ym}) \mathrm{sinc}(-k_{xm} \tfrac{w_x}{2}) \\
& + \cos\phi \frac{1}{d_x d_y} \sum_{m_x=-\infty}^{\infty} \sum_{m_y=-\infty}^{\infty} d_y \delta(m_y) \mathrm{sinc}(k_{xm} \tfrac{w_y}{2}) G_{yx}^{HM}(k_{xm}, k_{ym}) B_{\mathrm{d},x}(-k_{xm}) \mathrm{sinc}(-k_{ym} \tfrac{w_y}{2})
\end{aligned}
\tag{A.46}
$$

Using the approximations given in Eq. (A.25) and (A.36), and exploiting the properties of Dirac-delta function, Eq. (A.46) becomes

$$
\begin{aligned}
Y_{\mathrm{TE,d}} = & \cos\phi \frac{1}{d_y} \cancelto{0}{B_{\mathrm{d},x}(-k_{x0})} \sum_{m_y=-\infty}^{\infty} |\mathrm{sinc}(k_{ym} \tfrac{w_y}{2})|^2 G_{xx}^{HM}(k_{x0}, k_{ym}) \\
& - \sin\phi \frac{1}{d_x} \cancelto{0}{B_{\mathrm{d},y}(-k_{y0})} \sum_{m_x=-\infty}^{\infty} |\mathrm{sinc}(k_{xm} \tfrac{w_x}{2})|^2 G_{yy}^{HM}(k_{xm}, k_{y0}) \\
& - \cos\phi \frac{1}{d_y} \cancelto{1}{\mathrm{sinc}(-k_{x0} \tfrac{w_x}{2})} \sum_{m_y \neq 0} \mathrm{sinc}(k_{ym} \tfrac{w_x}{2}) G_{xy}^{HM}(k_{x0}, k_{ym}) B_{\mathrm{d},y}(-k_{ym}) \\
& + \cos\phi \frac{1}{d_x} \cancelto{1}{\mathrm{sinc}(-k_{y0} \tfrac{w_y}{2})} \sum_{m_x \neq 0} \mathrm{sinc}(k_{xm} \tfrac{w_y}{2}) G_{yx}^{HM}(k_{xm}, k_{y0}) B_{\mathrm{d},x}(-k_{xm}) \,.
\end{aligned}
\tag{A.47}
$$

By substituting the explicit expression of the free-space spectral GF times a factor 4 as well as the definition of the wave numbers (k_{x0}, k_{y0}), one obtains

$$
\begin{aligned}
Y_{\mathrm{TE,d}} = \frac{\sin\theta}{\zeta_0} \Bigg(& \frac{2}{d_y} \sum_{m_y \neq 0} \mathrm{sinc}(k_{ym} \frac{w_x}{2}) \frac{k_{ym} \sin^2\phi}{k_z} B_{\mathrm{d},y}(-k_{ym}) - \\
& \frac{2}{d_x} \sum_{m_x \neq 0} \mathrm{sinc}(k_{xm} \frac{w_y}{2}) \frac{k_{xm} \cos^2\phi}{k_z} B_{\mathrm{d},x}(-k_{xm}) \Bigg)
\end{aligned}
\tag{A.48}
$$

We can define an admittance $\widetilde{Y}$ as

$$\widetilde{Y} = \frac{2}{d_y}\sum_{m_y\neq 0}\mathrm{sinc}(k_{ym}\frac{w_x}{2})\frac{k_{ym}}{k_{zm}}B_{\mathrm{d},y}(-k_{ym}) = \frac{2}{d_x}\sum_{m_x\neq 0}\mathrm{sinc}(k_{xm}\frac{w_y}{2})\frac{k_{xm}}{k_{zm}}B_{\mathrm{d},x}(-k_{xm}) \quad \text{(A.49)}$$

which can also be expressed in the following form by using the definition of the sign function (sgn).

$$\widetilde{Y} = \frac{2}{d_y}\sum_{m_y\neq 0}\mathrm{sinc}(k_{ym}\frac{w_x}{2})\mathrm{sgn}(k_{ym})B_{\mathrm{d},y}(-k_{ym}) = \frac{2}{d_x}\sum_{m_x\neq 0}\mathrm{sinc}(k_{xm}\frac{w_y}{2})\mathrm{sgn}(k_{xm})B_{\mathrm{d},x}(-k_{xm}) \quad \text{(A.50)}$$

Thus, we have after few algebraic steps

$$\boxed{Y_{\mathrm{TE,d}} \approx -\sin\theta\cos 2\phi\widetilde{Y}}. \quad \text{(A.51)}$$

Analogously, the other mutual admittance term is given by

$$\boxed{Y_{\mathrm{TM,d}} \approx \sin\theta\sin 2\phi\widetilde{Y}}. \quad \text{(A.52)}$$

A.1.4 Summary

The closed form expressions of the admittance elements derived in the previous sections are summarized as follows:

$$\boxed{\begin{aligned} Y_{\mathrm{TM,TM}} &\approx -\tfrac{2}{Z_{0TM}} - jB_s + jB_s\tfrac{\sin^2\theta\sin^2(2\phi)}{2} \\ Y_{\mathrm{TE,TE}} &\approx -\tfrac{2}{Z_{0TE}} - jB_s(1-\tfrac{\sin^2\theta}{2}) + jB_s\tfrac{\sin^2\theta\cos^2(2\phi)}{2} \\ Y_{\mathrm{TE,TM}} &\approx -jB_s\tfrac{\sin^2\theta\sin(2\phi)\cos(2\phi)}{2} \\ Y_{\mathrm{TM,d}} &\approx \sin\theta\sin(2\phi)\widetilde{Y} \\ Y_{\mathrm{TE,d}} &\approx -\sin\theta\cos(2\phi)\widetilde{Y} \\ Y_{\mathrm{d,d}} &\approx \tfrac{j4}{\zeta_0 k_0}\tfrac{1}{d_x d_y}\sum_{m_x\neq 0}|k_{xm}||B_{\mathrm{d},x}(k_{xm})|^2 \end{aligned}} \quad \text{(A.53)}$$

where we define the slot-susceptance as

$$B_s = \frac{-2jk_0}{\zeta_0}\sum_{m_y\neq 0}\frac{|\mathrm{sinc}(k_{ym}w_x/2)|^2}{k_{zm}} \quad \text{(A.54)}$$

and the admittance $\widetilde{Y}$ as

$$\widetilde{Y} \approx \frac{2j}{\zeta_0 d_y} \sum_{m_y \neq 0} \mathrm{sgn}(k_{ym}) \mathrm{sinc}\left(\frac{k_{ym} w_x}{2}\right) B^*_{\mathrm{d},y}(-k_{ym})\,. \tag{A.55}$$

Note that the approximations in Eq. (A.53) are related to the following three assumptions:

- Firstly, for the small width of the slot, $\mathrm{sinc}(k_{x0} w_x/2) \approx \mathrm{sinc}(k_{y0} w_y/2) \approx 1$.
- Secondly, it was assumed that the Fourier transforms of the doublet functions are $B_{\mathrm{d},x}(k_{x0}) \approx B_{\mathrm{d},y}(k_{y0}) \approx 0$, since they are quasi-odd functions and vanish close to the origin.
- Thirdly, for well sampled arrays, we approximate $k_{zm} \approx -j|k_{ym}|$ and $k_{zm} \approx -j|k_{xm}|$ for the Floquet summations referring to the x- and y-periodicity, respectively.

A.2 Exact and Asymptotic Expressions of the TE-TM Coupling Admittance

The expression of the admittance term Y_c, which describes the modal coupling between TE and TM Floquet waves, is given by

$$Y_c = jB_s - \frac{2\widetilde{Y}^2}{Y_{\mathrm{d,d}}}\,. \tag{A.56}$$

In this section, we aim at proving that, asymptotically, for k_x and k_y large, the coupling term Y_c vanishes: $Y_c \sim 0$. This condition is equivalent to the following:

$$\frac{jB_s Y_{\mathrm{d,d}}}{2} \approx \widetilde{Y}^2\,. \tag{A.57}$$

By substituting the expressions of $Y_{\mathrm{d,d}}$, B_s and $\widetilde{Y}$ (given in Eqs. (A.53)-(A.55)) into (A.57), we obtain

$$\sum_{m_x \neq 0} \sum_{m_y \neq 0} \frac{|k_{xm}| |\mathrm{sinc}(\frac{k_{ym} w_y}{2})|^2 |B_{\mathrm{d},x}(k_{xm})|^2}{|k_{ym}|} \approx \sum_{m_x \neq 0} \sum_{m_y \neq 0} \frac{k_{xm} \mathrm{sinc}(\frac{k_{xm} w_x}{2}) B^*_{\mathrm{d},x}(k_{xm})}{|k_{xm}|} \frac{k_{ym} \mathrm{sinc}(\frac{k_{ym} w_y}{2}) B^*_{\mathrm{d},y}(k_{ym})}{|k_{ym}|} \tag{A.58}$$

By using the asymptotic evaluation in Eq. (A.13), it is then straightforward to verify the condition Eq. (A.58), which is equivalent to the decoupling condition $Y_c \approx 0$.

A.3 Closed Form Solutions for Infinite Sums

When setting up the integral equation for a plane wave incident on an infinite number of layers (see geometry in as in Fig. 4.1), an infinite sum on the indexes n_z is present:

$$\sum_{n_z=-\infty}^{\infty} (-1)^{n_z} e^{jk_{z0}n_z d_z} e^{-jk_z|n_z|d_z} \,. \tag{A.59}$$

It is convenient to split the sum into three contributions, as follows

$$\sum_{n_z=-\infty}^{\infty} (-1)^{n_z} e^{jk_{z0}n_z d_z} e^{-jk_z|n_z|d_z} = 1+ \sum_{n_z=-\infty}^{-1} (-1)^{n_z} e^{j(k_z+k_{z0})n_z d_z} + \sum_{n_z=1}^{\infty} (-1)^{n_z} e^{-j(k_z-k_{z0})n_z d_z} \,. \tag{A.60}$$

The semi-infinite sum over positive indexes can be expressed in a closed form as

$$\sum_{n_z=1}^{\infty} (-1)^{n_z} e^{-j(k_z-k_{z0})n_z d_z} = -\frac{1}{2} + \frac{j}{2} \tan\left(\frac{(k_z-k_{z0})d_z}{2}\right) \tag{A.61}$$

where we used the following identity [55]:

$$\sum_{n=1}^{\infty} (-1)^n e^{jkn} = -\frac{1}{2} - \frac{j}{2} \tan(k/2) \,. \tag{A.62}$$

The sum over negative indexes can be expressed in a similar form by substituting $n'_z = -n_z$:

$$\sum_{n_z=-\infty}^{-1} (-1)^{n_z} e^{j(k_z+k_{z0})n_z d_z} = \sum_{n_z=1}^{\infty} (-1)^{-n'_z} e^{-j(k_z+k_{z0})n_z d_z} \tag{A.63}$$

and thus, by using (A.62),

$$\sum_{n_z=-\infty}^{-1} (-1)^{n_z} e^{j(k_z+k_{z0})n_z d_z} = -\frac{1}{2} + \frac{j}{2} \tan\left(\frac{(k_z+k_{z0})d_z}{2}\right) \,. \tag{A.64}$$

Appendix B

Extraction of Effective Permittivity

This appendix discusses the procedure for calculating the effective permittivity values plotted in Figs. 4.5 and 6.3. To every angle of incidence θ, one can associate a transverse spectral wave number $k_\rho = k\sin\theta$. The parameter k is the propagation constant inside the host medium, $k = k_0\sqrt{\varepsilon_r}$. By solving the equivalent analytical transmission lines for TE and TM modes shown in Fig. B.1(b), characterized by $k_z = k\cos\theta$ one can then derive $k_{z\text{eff},TE}$ and $k_{z\text{eff},TM}$ (see Fig.B.1(c)) respectively using the known expressions for periodically loaded transmission lines [121]:

$$k_{z\text{eff,Ti}} = \frac{1}{d_z}\cos^{-1}\left(\cos(k_z d_z) + j\frac{Z_{\text{Ti}}}{2Z_{\text{ADL,Ti}}}\sin(k_z d_z)\right) \tag{B.1}$$

where Ti can refer to either the TE or TM mode respectively. The formula for calculating

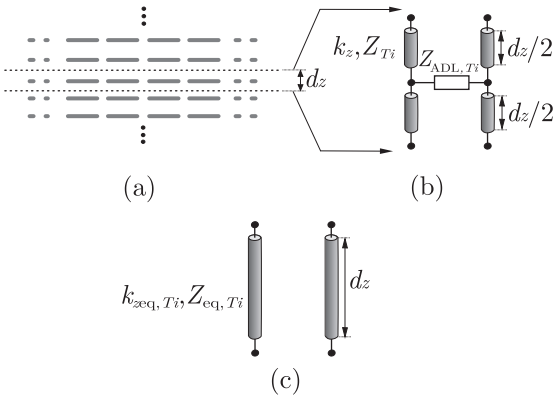

Figure B.1: (a) A 2D view of ADL; (b) a transmission line based representation of a unit cell to retrieve the effective permittivity for TE and TM incidence; and (c) the equivalent transmission line representation of ADL unit cell. Note that Ti can refer to either the TE and TM mode respectively.

$Z_{ADL,Ti}$ is analytically derived in closed-form in Ch. 4 (see Eq. 3.23), and it refers to the impedance of a single layer of ADL in an infinite cascade of artificial dielectric layers as depicted in Fig. B.1(a). Moreover, the impedance Z_{TE} and Z_{TM} are equal to $\zeta k/k_z$ and $\zeta k_z/k$ respectively, where $\zeta = 120\pi/\sqrt{\varepsilon_r}$ is the impedance of the medium hosting the ADL. The equation to compute the effective permittivity $\varepsilon_{\mathrm{Ti,Ti}}$ is then:

$$\varepsilon_{\mathrm{Ti,Ti}} = \frac{k_{z\mathrm{eff,Ti}}^2 + k_\rho^2}{k_0^2} \,. \tag{B.2}$$

Bibliography

[1] D. M. Pozar and D. H. Schaubert, *Microstrip antennas: the analysis and design of microstrip antennas and arrays*, Wiley-IEEE Press, 1995.

[2] P. Bhartia, I. Bahl, R. Garg, and A. Ittipiboon, "Microstrip antenna design handbook," *Norwood, MA, Artech House*, 2000.

[3] P. Smulders, "Exploiting the 60 GHz band for local wireless multimedia access: prospects and future directions," *IEEE Communications Magazine*, vol. 40, no. 1, pp. 140–147, Jan. 2002.

[4] C. H. Doan, S. Emami, A. M. Niknejad, and R. W. Brodersen, "Millimeter-wave CMOS design," *IEEE J. Solid-State Circuits*, vol. 40, no. 1, pp. 144–155, Jan. 2005.

[5] S. K. Reynolds, B. A. Floyd, U. R. Pfeiffer, T. Beukema, J. Grzyb, C. Haymes, B. Gaucher, and M. Soyuer, "A silicon 60-GHz receiver and transmitter chipset for broadband communications," *IEEE J. Solid-State Circuits*, vol. 41, no. 12, pp. 2820–2831, Dec. 2006.

[6] Y.-P. Zhang and D. Liu, "Antenna-on-chip and antenna-in-package solutions to highly integrated millimeter-wave devices for wireless communications," *IEEE Trans. Antennas Propag.*, vol. 57, no. 10, pp. 2830–2841, Oct. 2009.

[7] H. H. Meinel, "Commercial applications of millimeterwaves: history, present status, and future trends," *IEEE Trans. Microwave Theory Techn.*, vol. 43, no. 7, pp. 1639–1653, Jul. 1995.

[8] H. Li, H.-M. Rein, T. Suttorp, and J. Bock, "Fully integrated SiGe VCOs with powerful output buffer for 77-GHz automotive radar systems and applications around 100 GHz," *IEEE J. Solid-State Circuits*, vol. 39, no. 10, pp. 1650–1658, Oct. 2004.

[9] B. Schoenlinner, X. Wu, J. P. Ebling, G. V. Eleftheriades, and G. M. Rebeiz, "Wide-scan spherical-lens antennas for automotive radars," *IEEE Trans. Microwave Theory Techn.*, vol. 50, no. 9, pp. 2166–2175, Sep. 2002.

[10] V. Jain, F. Tzeng, Z. Lei, and P. Heydari, "A single-chip dual-band 22-29-GHz/77-81-GHz BiCMOS transceiver for automotive radars," *IEEE J. Solid-State Circuits*, vol. 44, no. 12, pp. 3469–3485, Dec. 2009.

[11] S. T. Nicolson, P. Chevalier, B. Sautreuil, and S. P. Voinigescu, "Single-chip W-band SiGe HBT transceivers and receivers for doppler radar and millimeter-wave imaging," *IEEE J. Solid-State Circuits*, vol. 43, no. 10, pp. 2206–2217, Oct. 2008.

[12] B.-H. Ku, O. Inac, M. Chang, H.-H. Yang, and G. M. Rebeiz, "A high-linearity 76−85-GHz 16-element 8-transmit/8-receive phased-array chip with high isolation and flip-chip packaging," *IEEE Trans. Microwave Theory Techn.*, vol. 62, no. 10, pp. 2337–2356, Oct. 2014.

[13] S. Y. Kim, O. Inac, C.-Y. Kim, D. Shin, and G. M. Rebeiz, "A 76− 84-GHz 16-element phased-array receiver with a chip-level built-in self-test system," *IEEE Trans. Microwave Theory Techn.*, vol. 61, no. 8, pp. 3083–3098, Aug 2013.

[14] F. Golcuk, T. Kanar, and G. M. Rebeiz, "A 90- 100-GHz 4 x 4 SiGe BiCMOS polarimetric transmit/receive phased array with simultaneous receive-beams capabilities," *IEEE Trans. Microwave Theory Techn.*, vol. 61, no. 8, pp. 3099–3114, Aug 2013.

[15] A. Arbabian, S. Callender, S. Kang, M. Rangwala, and A. M. Niknejad, "A 94 GHz mm-wave-to-baseband pulsed-radar transceiver with applications in imaging and gesture recognition," *IEEE J. Solid-State Circuits*, vol. 48, no. 4, pp. 1055–1071, Apr. 2013.

[16] A. Tessmann, S. Kudszus, T. Feltgen, M. Riessle, C. Sklarczyk, and W. H. Haydl, "Compact single-chip W-band FMCW radar modules for commercial high-resolution sensor applications," *IEEE Trans. Microwave Theory Techn.*, vol. 50, no. 12, pp. 2995–3001, Dec. 2002.

[17] S. Raman, N. S. Barker, and G. M. Rebeiz, "A W-band dielectric-lens-based integrated monopulse radar receiver," *IEEE Trans. Microwave Theory Techn.*, vol. 46, no. 12, pp. 2308–2316, Dec. 1998.

[18] M. Jahn, R. Feger, C. Wagner, Z. Tong, and A. Stelzer, "A four-channel 94-GHz SiGe-based digital beamforming FMCW radar," *IEEE Trans. Microwave Theory Techn.*, vol. 60, no. 3, pp. 861–869, March 2012.

[19] D. M. Pozar, "Considerations for millimeter wave printed antennas," *IEEE Trans. Antennas Propag.*, vol. 31, no. 5, pp. 740–747, Sep 1983.

[20] D. Liu, U. R. Pfeiffer, J. Grzyb, and B. Gaucher, *Advanced millimeter-wave technologies: antennas, packaging and circuits*, John Wiley & Sons, 2009.

[21] J. Hasch, E. Topak, R. Schnabel, T. Zwick, R. Weigel, and C. Waldschmidt, "Millimeter-wave technology for automotive radar sensors in the 77 GHz frequency band," *IEEE Trans. Microwave Theory Techn.*, vol. 60, no. 3, pp. 845–860, Mar. 2012.

[22] J. Schoebel, T. Buck, M. Reimann, M. Ulm, M. Schneider, A. Jourdain, G. J. Carchon, and H. A. C. Tilmans, "Design considerations and technology assessment of phased-array antenna systems with RF MEMS for automotive radar applications," *IEEE Trans. Microwave Theory Techn.*, vol. 53, no. 6, pp. 1968–1975, Jun. 2005.

[23] G. Chattopadhyay, C.-L. Kuo, P. Day, J. J. Bock, J. Zmuidzinas, and A. E. Lange, "Planar antenna arrays for cmb polarization detection," in *Joint 32nd Int. Conf. on Infrared and Millimeter Waves, and the 15th Int. Conf. on THz Electronics. IRMMW-THz.*, Sept 2007, pp. 184–185.

[24] A. Orlando et al., "Antenna-coupled TES bolometer arrays for BICEP2/Keck and SPIDER," *Millimeter, Submillimeter, and Far-Infrared Detectors and Instrument ation for Astronomy*, 2010.

[25] D. H. Schaubert, S. Kasturi, A. O. Boryssenko, and W. M. Elsallal, "Vivaldi antenna arrays for wide bandwidth and electronic scanning," in *Proc. Eur. Conf. Antennas Propag.*, Edinburgh, U.K., 11-16 Nov. 2007.

[26] D. Cavallo, A. Neto, and G. Gerini, "Common-mode resonances in ultra wide band connected arrays of dipoles: Measurements from the demonstrator and exit strategy," in *Proc. Int. Conf. Electromagnetics Advanced Applications*, Turin, Italy, 14-18 Sep. 2009, pp. 435–438.

[27] J. P. Doane, K. Sertel, and J. L. Volakis, "A wideband, wide scanning tightly coupled dipole array with integrated balun (TCDA-IB)," *IEEE Trans. Antennas Propag.*, vol. 61, no. 9, pp. 4538–4548, Sep. 2013.

[28] R. B. Waterhouse, "Design and performance of large phased arrays of aperture stacked patches," *IEEE Trans. Antennas Propag.*, vol. 49, no. 2, pp. 292–297, Feb. 2001.

[29] S. S. Holland, D. H. Schaubert, and M. N. Vouvakis, "A 7-21 GHz dual-polarized planar ultrawideband modular antenna (PUMA) array," *IEEE Trans. Antennas Propag.*, vol. 60, no. 10, pp. 4589–4600, Oct. 2012.

[30] L. Infante, A. De Luca, and M. Teglia, "Low-profile ultra-wide band antenna array element suitable for wide scan angle and modular subarray architecture," in *Proc. IEEE Int. Symp. Phased Array Systems Tech.*, 12-15 Oct. 2010, pp. 157–163.

[31] T. A. Milligan, *Modern antenna design*, John Wiley & Sons, 2005.

[32] D. Marcuse, "Theory of dielectric waveguides," *Academic, New York*, 1974.

[33] F. Mesa, C. Di Nallo, and D. R. Jackson, "The theory of surface-wave and space-wave leaky-mode excitation on microstrip lines," *IEEE Trans. Microwave Theory Techn.*, vol. 47, no. 2, pp. 207–215, Feb 1999.

[34] N. Llombart, *Development of integrated printed array antennas using EBG substrates*, Ph.D. thesis, University of Valencia, 2006.

[35] S. Raman and G. M. Rebeiz, "Single- and dual-polarized millimeter-wave slot-ring antennas," *IEEE Trans. Antennas Propag.*, vol. 44, no. 11, pp. 1438–1444, Nov. 1996.

[36] S. Raman, N. S. Barker, and G. M Rebeiz, "A W-band dielectric-lens-based integrated monopulse radar receiver," vol. 46, no. 12, pp. 2308–2316, Dec. 1998.

[37] D. F. Filipovic, S. S. Gearhart, and G. M. Rebeiz, "Double-slot antennas on extended hemispherical and elliptical silicon dielectric lenses," *IEEE Trans. Microwave Theory Techn.*, vol. 41, no. 10, pp. 1738–1749, Oct. 1993.

[38] A. Neto, "UWB, non dispersive radiation from the planarly fed leaky lens antenna-Part I: Theory and design," *IEEE Trans. Antennas Propag.*, vol. 58, no. 7, pp. 2238–2247, Jul. 2010.

[39] A. Neto, S. Monni, and F. Nennie, "UWB, non dispersive radiation from the planarly fed leaky lens antenna-Part II: Demonstrators and measurements," *IEEE Trans. Antennas Propag.*, vol. 58, no. 7, pp. 2248–2258, Jul. 2010.

[40] N. Llombart and A. Neto, "THz time-domain sensing: The antenna dispersion problem and a possible solution," *IEEE Trans. THz Science and Tech.*, vol. 2, no. 4, pp. 416–423, Jul. 2012.

[41] S. D. Targonski, R. B. Waterhouse, and D. M. Pozar, "Design of wide-band aperture-stacked patch microstrip antennas," *IEEE Trans. Antennas Propag.*, vol. 46, no. 9, pp. 1245–1251, Sep. 1998.

[42] W. S. T. Rowe and R. B. Waterhouse, "Theoretical investigation on the use of high permittivity materials in microstrip aperture stacked patch antennas," *IEEE Trans. Antennas Propag.*, vol. 51, no. 9, pp. 2484–2486, Sep. 2003.

[43] R. Gardelli, M. Albani, and F. Capolino, "Array thinning by using antennas in a fabry-perot cavity for gain enhancement," *IEEE Trans. Antennas Propag.*, vol. 54, no. 7, pp. 1979–1990, Jul. 2006.

[44] H. Attia, L. Yousefi, M. M. B. Suwailam, M. S. Boybay, and Omar M. Ramahi, "Enhanced-gain microstrip antenna using engineered magnetic superstrates," *IEEE Antennas Wireless Propag. Letters*, vol. 8, pp. 1198–1201, Nov. 2009.

[45] A. Foroozesh and L. Shafai, "Investigation into the effects of the reflection phase characteristics of highly-reflective superstrates on resonant cavity antennas," *IEEE Trans. Antennas Propag.*, vol. 58, no. 10, pp. 3392–3396, Oct 2010.

[46] M. Qiu and G. V. Eleftheriades, "Highly efficient unidirectional twin arc-slot antennas on electrically thin substrates," *IEEE Trans. Antennas Propag.*, vol. 52, no. 1, pp. 53–58, Jan. 2004.

[47] D. R. Jackson, J. T. Williams, A. K. Bhattacharyya, R. L. Smith, S. J. Buchheit, and S. A. Long, "Microstrip patch designs that do not excite surface waves," *IEEE Trans. Antennas Propag.*, vol. 41, no. 8, pp. 1026–1037, Aug. 1993.

[48] G. P. Gauthier, A. Courtay, and G. M. Rebeiz, "Microstrip antennas on synthesized low dielectric-constant substrates," *IEEE Trans. Antennas Propag.*, vol. 45, no. 8, pp. 1310–1314, Aug. 1997.

[49] I. Papapolymerou, R. F. Drayton, and L. P. B. Katehi, "Micromachined patch antennas," *IEEE Trans. Antennas Propag.*, vol. 46, no. 2, pp. 275–283, Feb. 1998.

[50] D. Sievenpiper, L. Zhang, R. F. J. Broas, N. G. Alexopolous, and E. Yablonovitch, "High-impedance electromagnetic surfaces with a forbidden frequency band," *IEEE Trans. Microwave Theory Techn.*, vol. 47, no. 11, pp. 2059–2074, Nov. 1999.

[51] A. Neto, N. Llombart, G. Gerini, and P. de Maagt, "On the optimal radiation bandwidth of printed slot antennas surrounded by EBGs," *IEEE Trans. Antennas Propag.*, vol. 54, no. 4, pp. 1074–1083, April 2006.

[52] N. Llombart, A. Neto, G. Gerini, and P. de Maagt, "Planar circularly symmetric EBG structures for reducing surface waves in printed antennas," *IEEE Trans. Antennas Propag.*, vol. 53, no. 10, pp. 3210–3218, Oct. 2005.

[53] N. Llombart, A. Neto, G. Gerini, and P. de Maagt, "1-D scanning arrays on dense dielectrics using PCS-EBG technology," *IEEE Trans. Antennas Propag.*, vol. 55, no. 1, pp. 26–35, Jan. 2007.

[54] W. E. Kock, "Metallic delay lenses," *Bell System Technical Journal*, vol. 27, no. 1, pp. 58–82, 1948.

[55] R. E. Collin, *Field theory of guided waves*, IEEE/OUP series on electromagnetic wave theory. IEEE Press, New York, 1991.

[56] M. Albani and F. Capolino, "Wave dynamics by a plane wave on a half-space metamaterial made of plasmonic nanospheres: a discrete wiener–hopf formulation," *J. Opt. Soc. Amer. B*, vol. 28, no. 9, pp. 2174–2185, Sept. 2011.

[57] D. Huang, W. Hant, N.-Yi Wang, T. W. Ku, G. Qun, R. Wong, and M.-C. F. Chang, "A 60GHz CMOS VCO using on-chip resonator with embedded artificial dielectric for size, loss and noise reduction," in *IEEE ISSCC Dig. Tech. Paper*, Feb. 2006, pp. 1218–1227.

[58] P. Clemmow, *The Plane Wave Spectrum Representation of Electromagnetic Fields*, Wiley-IEEE Press, 1997.

[59] C. M. Butler, "General solutions of the narrow strip (and slot) integral equations," *IEEE Trans. Antennas Propag.*, vol. 33, no. 10, pp. 1085–1090, Oct. 1985.

[60] E. Martini, G. M. Sardi, and S. Maci, "Homogenization processes and retrieval of equivalent constitutive parameters for multisurface-metamaterials," *IEEE Trans. Antennas Propag.*, vol. 62, no. 4, pp. 2081–2092, April 2014.

[61] C. R. Simovski, "Material parameters of metamaterials (a Review)," *Opt. and Spectroscopy*, vol. 107, no. 5, pp. 726–753, 2009.

[62] J. B. Pendry, A. J. Holden, D. J. Robbins, and W. J. Stewart, "Magnetism from conductors and enhanced nonlinear phenomena," *IEEE Trans. Microwave Theory Techn.*, vol. 47, no. 11, pp. 2075–2084, Nov. 1999.

[63] P. A. Belov, R. Marques, S. I. Maslovski, I. S. Nefedov, M. Silveirinha, C. R. Simovski, and S. A. Tretyakov, "Strong spatial dispersion in wire media in the very large wavelength limit," *Phys. Rev. B*, vol. 67, pp. 113103, Mar. 2003.

[64] "Ansoft HFSS, ansoft corporation," Pittsburgh, PA, [Online]. Available: http://www.ansoft.com/.

[65] D. R. Smith, D. C. Vier, Th. Koschny, and C. M. Soukoulis, "Electromagnetic parameter retrieval from inhomogeneous metamaterials," *Phy. Rev. E*, vol. 71, no. 3, pp. 036617, Mar. 2005.

[66] C. Menzel, C. Rockstuhl, T. Paul, F. Lederer, and T. Pertsch, "Retrieving effective parameters for metamaterials at oblique incidence," *Phys. Rev. B*, vol. 77, no. 19, pp. 195328, May 2008.

[67] D. M. Pozar and D. H. Schaubert, "Scan blindness in infinite phased arrays of printed dipoles," *IEEE Trans. Antennas Propag.*, vol. 32, no. 6, pp. 602–610, Jun. 1984.

[68] D. Cavallo, *Connected array antennas: Analysis and design*, Ph.D. thesis, University of Eindhoven, 2011.

[69] "CST Microwave Studio 2012," Available: http://www.cst.com.

[70] N. Marcuvitz, *Waveguide handbook*, Lexington, MA: Boston Technological Publisher, 1964.

[71] J. R. Wait, *Theories of scattering from wire-grid and mesh structures*, P.L.E. Uslenghi, Ed. New York: Academic, 1978.

[72] L. B. Whitbourn and R. C. Compton, "Equivalent-circuit formulas for metal grid reflectors at a dielectric boundary," *Appl. Opt.*, vol. 24, no. 2, pp. 217–220, Jan. 1985.

[73] R. C. Compton and D. B. Rutledge, "Approximation techniques for planar periodic structures," *IEEE Trans. Microwave Theory Techn.*, vol. 33, no. 10, pp. 1083–1088, Oct. 1985.

[74] O. Luukkonen, C. Simovski, G. Granet, G. Goussetis, D. Lioubtchenko, A. V. Raisanen, and S.A. Tretyakov, "Simple and accurate analytical model of planar grids and high-impedance surfaces comprising metal strips or patches," *IEEE Trans. Antennas Propag.*, vol. 56, no. 6, pp. 1624–1632, June 2008.

[75] S. A. Tretyakov, *Analytical modeling in applied electromagnetics*, Artech House: London, 2003.

[76] A. Neto and S. Maci, "Green's function for an infinite slot printed between two homogeneous dielectrics. part I: magnetic currents," *IEEE Trans. Antennas Propag.*, vol. 51, no. 7, pp. 1572–1581, July 2003.

[77] A. Neto and J. J. Lee, "Ultrawide-band properties of long slot arrays," *IEEE Trans. Antennas Propag.*, vol. 54, no. 2, pp. 534–543, Feb 2006.

[78] "Ansoft Designer, ansoft corporation," Pittsburgh, PA, [Online]. Available: http://www.ansoft.com/.

[79] D. Cavallo, A. Neto, and G. Gerini, "Green's function based equivalent circuits for connected arrays in transmission and in reception," *IEEE Trans. Antennas Propag.*, vol. 59, no. 5, pp. 1535–1545, May 2011.

[80] W. H. Syed and A. Neto, "Front-to-back ratio enhancement of planar printed antennas by means of artificial dielectric layers," *IEEE Trans. Antennas Propag.*, vol. 61, no. 11, pp. 5408–5416, Nov. 2013.

[81] R. A. Shore and A. D. Yaghjian, "Traveling waves on two-and three-dimensional periodic arrays of lossless scatterers," *Radio Sci.*, vol. 42, no. RS6S21, Dec. 2007.

[82] S. B. Cohn, "Electrolytic-tank measurements for microwave metallic delay-lens media," *J. Appl. Phys.*, vol. 21, no. 1, pp. 674–680, Jul. 1950.

[83] J. Brown, "The design of metallic delay dielectrics," *Proceedings of the IEE - Part III: Radio and Communication Engineering*, vol. 97, no. 45, pp. 45–48, Jan. 1950.

[84] V. P. Shestopalov Z. S. Agranovich, V. A. Marchenko, "Diffraction of a plane electromagnetic wave from plane metallic lattices," *Sov. Phys. Tech. Phys.*, vol. 7, no. 4, pp. 277–281, 1962.

[85] V. B. Kazanskii, L.N. Litvineuko, and V. P. Shestopalov, "The equivalent dielectric properties of an infinite two-dimensionally periodic tape structure," *Radiophysics and Quantum Electronics*, vol. 14, no. 10, pp. 1221–1232, 1971.

[86] C. S. R. Kaipa, A. B. Yakovlev, F. Medina, F. Mesa, C. A. M. Butler, and A. P. Hibbins, "Circuit modeling of the transmissivity of stacked two-dimensional metallic meshes," *Optics express*, vol. 18, no. 13, pp. 13309–13320, Jun. 2010.

[87] S. Monni, G. Gerini, A. Neto, and A. G. Tijhuis, "Multimode equivalent networks for the design and analysis of frequency selective surfaces," *IEEE Trans. Antennas Propag.*, vol. 55, no. 10, pp. 2824–2835, Oct. 2007.

[88] R. Rodrguez-Berral, F. Mesa, and F. Medina, "Circuit model for patch/slot-based frequency selective surfaces under conical incidence," in *Proc. Eur. Conf. Antennas Propag.*, Apr. 2014, pp. 1714–1718.

[89] M. A. Antoniades, *Microwave devices and antennas based on negative-refractive-index transmission-line metamaterials*, Ph.D. thesis, University of Toronto, 2009.

[90] F. Capolino, D. R. Jackson, D. R. Wilton, and L. B. Felsen, "Comparison of methods for calculating the field excited by a dipole near a 2-d periodic material," *IEEE Trans. Antennas Propag.*, vol. 55, no. 6, pp. 1644–1655, Jun. 2007.

[91] S. C. Saha, J. P. Grant, Y. Ma, A. Khalid, F. Hong, and D. R. S. Cumming, "Terahertz frequency-domain spectroscopy method for vector characterization of liquid using an artificial dielectric," *IEEE Trans. THz Sci. and Tech.*, vol. 2, no. 1, pp. 113–122, Jan. 2012.

[92] J. Zhang, P. A. R. Ade., P. Mauskopf, L. Moncelsi, G. Savini, and N. Whitehouse, "New artificial dielectric metamaterial and its application as a terahertz antireflection coating," *Applied optics*, vol. 48, no. 35, pp. 6635–6642, 2009.

[93] S. Pan, F. Caster, P. Heydari, and F. Capolino, "A 94-GHz extremely thin metasurface-based bicmos on-chip antenna," *IEEE Trans. Antennas Propag.*, vol. 62, no. 9, pp. 4439–4451, Sept. 2014.

[94] Y.-C. Ou and G. M. Rebeiz, "On-chip slot-ring and high-gain horn antennas for millimeter-wave wafer-scale silicon systems," *IEEE Trans. Microwave Theory Techn.*, vol. 59, no. 8, pp. 1963–1972, Aug. 2011.

[95] Y.-C. Ou and G. M. Rebeiz, "Differential microstrip and slot-ring antennas for millimeter-wave silicon systems," *IEEE Trans. Antennas Propag.*, vol. 60, no. 6, pp. 2611–2619, Jun. 2012.

[96] T. Makita, I. Tamai, and S. Seki, "Coplanar waveguides on high-resistivity silicon substrates with attenuation constant lower than 1 db/mm for microwave and millimeter-wave bands," *IEEE Trans. Electron Devices*, vol. 58, no. 3, pp. 709–715, Mar. 2011.

[97] C. Schollhorn, W. Zhao, M. Morschbach, and E. Kasper, "Attenuation mechanisms of aluminum millimeter-wave coplanar waveguides on silicon," *IEEE Trans. Electron Devices*, vol. 50, no. 3, pp. 740–746, Mar. 2003.

[98] G. F. Engen and C. A. Hoer, "Thru-reflect-line: An improved technique for calibrating the dual six-port automatic network analyzer," *IEEE Trans. Microwave Theory Techn.*, vol. 27, no. 12, pp. 987–993, Dec. 1979.

[99] M. J. Pelk, "Near field characterization of integrated antenna's at (sub)/mm-wave frequencies," in *Workshop WFS06 (EuMC/EuMIC) silicon characterization from MHz to THz*, 2010, vol. 90, p. 30.

[100] S. Pan, L. Gilreath, P. Heydari, and F. Capolino, "Investigation of a wideband BiCMOS fully on-chip W-band bowtie slot antenna," *IEEE Antennas Wireless Propag. Lett.*, vol. 12, pp. 706–709, June 2013.

[101] J. J. Lee, E. M. Ferren, D. P. Woollen, and K. M. Lee, "Near-field probe used as a diagnostic tool to locate defective elements in an array antenna," *IEEE Trans. Antennas Propag.*, vol. 36, no. 6, pp. 884–889, June 1988.

[102] J. J. Lee, S. Livingston, and R. Koenig, "A low-profile wide-band (5:1) dual-pol array," *IEEE Antennas Wireless Propag. Lett.*, vol. 2, no. 1, pp. 46–49, 2003.

[103] J. J. Lee, S. Livingston, R. Koenig, D. Nagata, and L. L. Lai, "Compact light weight UHF arrays using long slot apertures," *IEEE Trans. Antennas Propag.*, vol. 54, no. 7, pp. 2009–2015, Jul. 2006.

[104] D. Cavallo, G. Gerini, R. Bolt, D. Deurloo, R. Grooters, A. Neto, G. Toso, and R. Midthassel, "Ku-band dual-polarized array of connected dipoles for satcom terminals: Theory and hardware validation," in *Proc. Eur. Conf. Antennas Propag.*, Gothenburg, Sweden, Apr. 2013, pp. 459–460.

[105] "The SKA website," Available: http://www.skatelescope.org/.

[106] D. H. Schaubert, A. O. Boryssenko, A. Van Ardenne, J. G. B. de Vaate, and C. Craeye, "The square kilometer array (SKA) antenna," in *Proc. IEEE Int. Symp. Phased Array Systems Tech.*, 14-17 Oct. 2003, pp. 351–358.

[107] Y.-S. Kim and K. S. Yngvesson, "Characterization of tapered slot antenna feeds and feed arrays," *IEEE Trans. Antennas Propag.*, vol. 38, no. 10, pp. 1559–1564, Oct. 1990.

[108] R. C. Hansen, "Linear connected arrays," *IEEE Antennas Wireless Propag. Lett.*, vol. 3, no. 1, pp. 154–156, Dec. 2004.

[109] A. Neto and J. J. Lee, "Infinite bandwidth long slot array antenna," *IEEE Antennas Wireless Propag. Lett.*, vol. 4, pp. 75–78, 2005.

[110] A. Neto, D. Cavallo, G. Gerini, and G. Toso, "Scanning performances of wideband connected arrays in the presence of a backing reflector," *IEEE Trans. Antennas Propag.*, vol. 57, no. 10, pp. 3092–3102, Oct. 2009.

[111] D. Cavallo, A. Neto, G. Gerini, A. Micco, and V. Galdi, "A 3- to 5-GHz wideband array of connected dipoles with low cross polarization and wide-scan capability," *IEEE Trans. Antennas Propag.*, vol. 61, no. 3, pp. 1148–1154, Mar. 2013.

[112] D. Cavallo, A. Neto, and G. Gerini, "A 10.5-14.5 GHz wide-scanning connected array of dipoles with common-mode rejection loops to ensure polarization purity," in *Proc. IEEE Int. Symp. Antennas Propag. Soc.*, Toronto, ON, Canada, 11-17 Jul. 2010.

[113] D. Cavallo and A. Neto, "A connected array of slots supporting broadband leaky waves," *IEEE Trans. Antennas Propag.*, vol. 61, no. 4, pp. 1986–1994, Apr. 2013.

[114] S. Maci, G. Minatti, M. Casaletti, and M. Bosiljevac, "Metasurfing: Addressing waves on impenetrable metasurfaces," *IEEE Antennas Wireless Propag. Lett.*, vol. 10, pp. 1499–1502, 2011.

[115] G. Minatti, M. Faenzi, E. Martini, F. Caminita, P. De Vita, D. Gonzalez-Ovejero, M. Sabbadini, and S. Maci, "Modulated metasurface antennas for space: Synthesis, analysis and realizations," *IEEE Trans. Antennas Propag.*, vol. 63, no. 4, pp. 1288–1300, Apr. 2015.

[116] D. Cavallo, A. Neto, and G. Gerini, "Green's function based equivalent circuits for connected arrays in transmission and in reception," *IEEE Trans. Antennas Propag.*, vol. 59, no. 5, pp. 1535–1545, May 2011.

[117] A. Hoorfar, K. C. Gupta, and D. C. Chang, "Cross-polarization level in radiation from a microstrip dipole antenna," *IEEE Trans. Antennas Propag.*, vol. 36, no. 9, pp. 1197–1203, Sep. 1988.

[118] R. Al Hadi, H. Sherry, J. Grzyb, Y. Zhao, W. Forster, H. M. Keller, A. Cathelin, A. Kaiser, and U.R. Pfeiffer, "A 1 k-pixel video camera for 0.7-1.1 terahertz imaging applications in 65-nm CMOS," *IEEE J. Solid-State Circuits*, vol. 47, no. 12, pp. 2999–3012, Dec. 2012.

[119] R. Al Hadi, J. Grzyb, B. Heinemann, and U. R. Pfeiffer, "A terahertz detector array in a SiGe HBT technology," *IEEE J. Solid-State Circuits*, vol. 48, no. 9, pp. 2002–2010, Sept. 2013.

[120] R. Bolt K. Kegel, "Actife, advanced antenna concepts for Aircraft in-Flight Entertainment, Identification antenna requirements," *European Spase Agency, Noordwijk, Netherland, Tech. Rep. 3 WP 0300, ESA Contract no. C19865*, May 2007.

[121] W. Rotman, "Plasma simulation by artificial dielectrics and parallel-plate media," *IRE Trans. Antennas Propag.*, vol. 10, no. 1, pp. 82–95, Jan. 1962.

List of Publications

Journal Papers

J1. W. H. Syed and A. Neto, "Front to back ratio enhancement of planar printed antennas by means of artificial dielectric layers," *IEEE Trans. Antennas Propag.*, vol. 61, no. 11, pp. 5408-5416, Nov. 2013.

J2. D. Cavallo, W. H. Syed, and A. Neto, "Closed-form analysis of artificial dielectric layers−Part I: Properties of a single layer under plane-wave incidence," *IEEE Trans. Antennas Propag.*, vol. 62, no. 12, pp. 6256-6264, Dec. 2014.

J3. D. Cavallo, W. H. Syed, and A. Neto, "Closed-form analysis of artificial dielectric layers−Part II: Extension to multiple layers and arbitrary illumination," *IEEE Trans. Antennas Propag.*, vol. 62, no. 12, pp. 6265-6273, Dec. 2014.

J4. W. H. Syed, G. Fiorentino, D. Cavallo, M. Spirito, P. M. Sarro, and A. Neto, "Design, fabrication and measurements of a 0.3 THz on-chip double sot antenna enhanced by artificial dielectrics," *IEEE Trans. THz Science and Tech.*, vol. 5, no. 2, pp. 288-298, Mar. 2015.

J5. W. H. Syed, D. Cavallo, H. Thippur Shivamurthy, and A. Neto, "Wideband, wide-scan planar array of connected slots loaded with artificial dielectric superstrates," *IEEE Trans. Antennas Propag.*, under review.

Conference Papers

C1. W. H. Syed and A. Neto, "Near field excitation of artificial dielectric layers: Field distributions and electrical properties," *6th European Conference on Antennas and Propagation (EUCAP 2012)*, Prague, Czech Republic, pp. 395-397, Mar. 26-30, 2012.

C2. W. H. Syed and A. Neto, "Artificial dielectric layers for the performance enhancement of slot antennas on a dielectric lens," *IEEE Antennas and Propagation Society International Symposium (APSURSI 2012)*, Chicago, IL, USA, Jul. 8-14, 2012.

C3. G. Fiorentino, W. H. Syed, P. M. Sarro, and A. Neto, "Artificial dielectric layer as sub-mm wave antenna super-strates," *IEEE Antennas and Propagation Society International Symposium (APSURSI 2012)*, Chicago, IL, USA, Jul. 8-14, 2012.

C4. W. H. Syed, D. Cavallo, and A. Neto, "Artificial dielectric layers for efficient feeding of lens antennas: Rigorous analysis and experimental validation," *7th European Conference on Antennas and Propagation (EUCAP 2013)*, Gothenburg, Sweden, Apr. 8-12, 2013. (**Finalist for the best student paper award**)

C5. W. H. Syed, D. Cavallo, and A. Neto, "Artificial dielectric layers as surface-waveless antenna substrate," *Annual Netherlands Antenna Research Framework (NARF) Workshop*, Delft, Netherlands, May 31, 2013. (**Awarded with the best poster prize**)

C6. W. H. Syed, D. Cavallo, and A. Neto, "An analytical approach to describe plane-wave propagation in finite artificial dielectric layers," *IEEE Antennas and Propagation Society International Symposium (APSURSI 2013)*, Orlando, FL, USA, Jul. 7-13, 2013.

C7. D. Cavallo, A. Visweswaran, N. Llombart, M. Spirito, W. H. Syed, A. Neto, and J. Long, "Design of wideband and high-efficiency antenna array on chip at 1.1 terahertz," *8th European Conference on Antennas and Propagation (EUCAP 2014)*, The Hague, Netherlands, Apr. 6-11, 2014. (**convened paper**)

C8. W. H. Syed, D. Cavallo, A. Neto, and P. van Zeijl, "Artificial dielectric based connected array of slots at 60 GHz," *8th European Conference on Antennas and Propagation (EUCAP 2014)*, The Hague, Netherlands, Apr. 6-11, 2014.

C9. D. Cavallo, W. H. Syed, and A. Neto, "Closed-form expressions for the analysis of finite-height artificial dielectric layers," *8th European Conference on Antennas and Propagation (EUCAP 2014)*, The Hague, Netherlands, Apr. 6-11, 2014.

C10. D. Cavallo, W. H. Syed, and A. Neto, "Closed-form analysis of the decoupling properties of artificial dielectric layers," *IEEE Antennas and Propagation Society International Symposium (APSURSI 2014)*, Memphis, TN, USA, Jul. 6-11, 2014.

C11. W. H. Syed, G. Fiorentino, D. Cavallo, M. Spirito, P. M. Sarro, and A. Neto, "Front-to-back ratio enhancement of on-chip antenna using artificial dielectrics at 300 GHz," *IEEE Antennas and Propagation Society International Symposium (APSURSI 2014)*, Memphis, TN, USA, Jul. 6-11, 2014.

C12. W. H. Syed, D. Cavallo, A. Neto, and P. van Zeijl, "Design of connected array loaded with artificial dielectrics at 60 GHz," *IEEE Antennas and Propagation Society International Symposium (APSURSI 2014)*, Memphis, TN, USA, Jul. 6-11, 2014.

C13. W. H. Syed, G. Fiorentino, D. Cavallo, M. Spirito, P. M. Sarro, and A. Neto, "Enhancement of front-to-back ratio of on chip antenna by artificial dielectrics at 300 GHz," *39th International Conference on Infrared, Millimeter, and Terahertz Waves*, Tucson, AZ, USA, Sept. 14-19, 2014.

C14. W. H. Syed, G. Fiorentino, D. Cavallo, P. M. Sarro, and A. Neto,"On-chip double slot antenna at 300 GHz enhanced by artificial dielectrics," *9th European Conference on Antennas and Propagation (EUCAP 2015)*, Lisbon, Portugal, Apr. 12-17, 2015. (Awarded with **"Special Mention for the Excellent Presentation"**)

C15. W. H. Syed, D. Cavallo, H. Thippur Shivamurthy, and A. Neto, "Design of wideband, wide-scan planar arrays by combining connected arrays and artificial dielectrics," *9th European Conference on Antennas and Propagation (EUCAP 2015)*, The Hague, Netherlands, Apr. 12-17, 2015.

C16. D. Cavallo, W. H. Syed, and A. Neto, "Closed-form solutions for the analysis of artificial dielectric layers under generic field incidence," *IEEE Antennas and Propagation Society International Symposium (APSURSI 2015)*, Vancouver, Canada, Jul. 19-24, 2015. (**invited paper**)

C17. D. Cavallo, W. H. Syed, H. Thippur Shivamurthy, and A. Neto, "A planar wideband wide-scan phased array: Connected array loaded with artificial dielectric layers," *IEEE Antennas and Propagation Society International Symposium (APSURSI 2015)*, Vancouver, Canada, Jul. 19-24, 2015.

C18. W. H. Syed, G. Fiorentino, D. Cavallo, M. Spirito, P. M. Sarro and A. Neto, "Performance enhancement of 300 GHz on-chip double slot antenna by means of artificial dielectrics," *45th European Microwave Week*, Paris, France, Sept. 6-11, 2015.

Thesis Co-Supervised

T1. H. Thippur Shivamurthy, "Wideband, Wide-Scan Planar Connected Slot Array Enhanced with Artificial Dielectrics," M.Sc. thesis, Delft University of Technology, Delft, Netherlands, 2014.

T2. Wenda Zhu, "mm-Wave Antenna in Package for Short-Range Car Radar Application," M.Sc. thesis, Delft University of Technology, Delft, Netherlands, 2015.

Awards

A1. *"Special Mention for the Excellent Presentation"* in the *Best Student Paper Contest* at the 9th edition of European Conference on Antennas and Propagation (EUCAP), Lisbon, Portugal (12-17 Apr. 2015), with the paper **C.14** listed in the conference publications.

A2. *"Best Poster Prize"* at the Annual Netherlands Antenna Research Framework (NARF) Workshop, Delft, Netherlands (31st May 2013), with the paper **C.5** listed in the conference publications.

Summary

On the Control of Surface Waves in Integrated Antennas: Analysis and Design Exploiting Artificial Dielectric Layers

Planar printed antenna technologies, due to their light weight, low profile, cost effectiveness and ease of connection with the active devices (e.g., amplifiers etc.), are becoming an attractive solution for the commercial data-hungry applications, such as 60 GHz high-data rate communication. Another commercial application of planar antennas includes the exponentially growing lucrative industry of automotive radars. Such radar systems not only require highly reliability since human lives are involved, but also extreme integration to serve the purpose of compactness and cost. Therefore, it is desirable to have all the system functionalities on a single silicon chip, which can then easily be combined with either off- or on-chip antennas/antenna arrays. In such scenarios, planar printed antennas/arrays, because of their low profile and ability to be integrated, are emerging as an alternative to the bulky and expensive dielectric lenses.

Although planar antennas show advantageous properties, there are two major challenges associated with their design, namely surface waves and front-to-back radiation ratio. In this thesis, a innovative planar methodology is presented to solve the aforementioned bottlenecks. The proposed technique can be used to obtain simultaneously high radiation efficiency (i.e., minimal surface wave excitation) and good front-to-back radiation ratio. This solution consist of engineering anisotropic equivalent materials, referred to as artificial dielectric layers (ADLs), and using them to enhance the performance of planar antennas. A practical planar realization of this concept can be achieved by embedding inside the host dielectric a periodic array of sub-wavelength square metal patches in a multilayer configuration. In this work, the main aspects pertaining to the theoretical development and the practical implementation of ADLs are investigated.

The analysis of ADLs is extensively investigated in this thesis in order to understand the physical phenomena characterizing these structures. Moreover, this study also provides the guidelines to design such kind of engineered materials. The modeling of ADLs is first

implemented for two-dimensional structures, and then generalized to three-dimensional geometries. A rigorous analytical formulation is presented to model ADLs of finite height by including the higher-order interaction between parallel sheets in closed form. From the equivalent impedance of the layers, a transmission line model that provides the spectral Green's function of ADLs is constructed. This allows to characterize the propagation through finite ADLs and to study their dispersion characteristics. The analysis shows that an ADL slab is equivalent to a dense material for the plane waves incident in directions close to the normal, whereas it exhibits lower effective permittivity for the waves that are incident close to the grazing angle. This peculiar anisotropic property can be exploited to design antenna superstrates which, one one hand, exhibit high surface-wave efficiency over a wide band and, on the other hand, provide high front-to-back ratio.

The advantages of using ADL superstrates in the antenna designs is experimentally demonstrated by the development of two prototype demonstrators. The first design operates at X-band and is realized using commercial printed circuit board (PCB) technology. The second prototype consists of an on-chip antenna working at 0.3 THz, which is fabricated using an in-house integrated circuit process. This study highlights that the ADL superstrates can be designed and manufactured independently from the antenna and the circuit. This allows their use as add-on components, since no accurate alignment is required between the antenna and the superstrate layers. Moreover, ADL are broadband because of their non-resonant nature.

The last part of this thesis deals with a novel concept of wideband wide-scanning phased array designs, based on connected arrays of slots loaded with ADL superstrates. The proposed structure has two main advantages with respect to the existing solutions. Firstly, it is completely planar and realized with a single multilayer PCB, with consequent reduction of the cost and the complexity of the array. Secondly, ADLs are used in place of real dielectric superstrates, to achieve much better efficiency in terms of surface-wave loss. For the design of the array loaded with ADL, including the adhesive layers, an analytical tool, based on spectral Green's function, is used. This tool allows to estimate the performance of the array with minimal computational resources. The design of a wideband feed structure is also proposed, which does not require balanced-to-unbalanced (balun) transitions that limit the matching bandwidth.

Samenvatting

Over de Onderdrukking van Oppervlaktegolven in Geïntegreerde Antennes: Analyse en Ontwerp, Exploiteren van Artificiële Diëlektrische Lagen

Planair geprinte antenne technologieën worden door hun lichte gewicht, lage profiel, kosten effectiviteit en gemakkelijke verbinding met actieve elementen (bijv. versterkers enz.), een aantrekkelijke oplossing voor commerciële data-intensieve applicaties, zoals 60 GHz hogedatasnelheid communicatie. Een andere commerciële toepassing van planaire antennes omvat de exponentieel groeiende en lucratieve industrie van autoradars. Zulke radarsystemen vereisen niet alleen een hoge betrouwbaarheid, omdat er mensenlevens bij betrokken zijn, maar ook een extreme integratie ter bevordering van de compactheid en vermindering van de kosten. Daarom is het wenselijk om alle systeem functionaliteiten op een enkele silicium chip te hebben, welke dan gemakkelijk gecombineerd kan worden met zowel off- en on-chip antennes/antennestelsels. In dergelijke scenario's zijn planair geprinte antennes/antennestelsels in opkomst als een alternatief voor grote en dure dilektrische lenzen. Redenen hiervoor zijn hun lage profiel en geschiktheid voor integratie.
Hoewel planaire antennes gunstige eigenschappen vertonen, zijn er twee grote uitdagingen in verband met hun ontwerp, namelijk oppervlaktegolven en voor-achter-stralingsverhouding. In dit proefschrift wordt een innovatieve planaire methodologie gepresenteerd om de hiervoor genoemde knelpunten op te lossen. De voorgestelde techniek kan worden gebruikt om tegelijkertijd een hoge radiatie efficiëntie (d.w.z. minimale oppervlaktegolf excitatie) en een goede voor-achter-stralingsverhouding te verkrijgen. De oplossing bestaat uit het ontwikkelen van anisotrope equivalente materialen, aangeduid als artificiële diëlektrische lagen (ADLs), en ze vervolgens te gebruiken om de prestatie van planaire antennes te verbeteren. Een praktische planaire realisatie van dit concept kan worden bereikt door in de gast-diëlektriek een periodiek structuur te inbedden bestaande uit sub-golflengte vierkante metalen lappen in een meerlaagse configuratie. In dit werk worden de belangrijkste aspecten met betrekking tot de theoretische ontwikkeling en praktische uitvoering van ADLs onderzocht.

Dit proefschrift onderzoekt uitvoerig de fysische verschijnselen in ADLs, om die kunnen begrijpen. Bovendien geeft deze studie ook richtlijnen voor het ontwerp van zulke gemanipuleerde materialen. Het modelleren van ADLs is eerst toegepast in twee dimensionale structuren en dan gegeneraliseerd voor drie dimensionale geometrien. Een rigoureuze analytische formulering wordt gepresenteerd om ADLs met een eindige hoogte te modelleren. Dit wordt gedaan door het, in gesloten vorm, in beschouwing nemen van de hogere-orde interacties tussen de parallelle lagen van een ADL. Uit de equivalente impedantie van de lagen wordt een transmissielijn model geconstrueerd dat resulteert in de spectrale Green's functies van ADLs. Dit maakt het mogelijk om de propagatie in eindige ADLs en zijn dispersie eigenschappen te bestuderen. Deze analyse laat zien dat een ADL equivalent is aan een materiaal met een hoge dichtheid voor golven inkomend in richtingen dichtbij de normale, terwijl het een lagere permittiviteit vertoont voor de golven komend uit richtingen dichtbij de "grazing angle". Deze eigenaardige anisotrope eigenschap kan worden benut bij het ontwerpen van antenne-superstraten welke, aan de ene kant, over een brede frequentieband een hoge oppervlaktegolf efficintie hebben, en aan de andere kant, een hoge voor-achter-stralingsverhouding verstrekken.

De voordelen van het gebruiken van ADL superstraten in antenne-ontwerpen is experimenteel aangetoond met de ontwikkeling van twee prototypen. Het eerste ontwerp werkt in de X-band en is gerealiseerd door gebruik te maken van printed circuit board (PCB) technologie. Het tweede prototype bestaat uit een on-chip antenne die werkt op 0.3 THz, welke is gefabriceerd met behulp van in-huis geïntegreerde circuit-processen. Deze studie benadrukt dat de ADL superstraten onafhankelijk van de antenne en het circuit ontworpen en gefabriceerd kunnen worden. Dit maakt het mogelijk dat ADLs gebruikt kunnen worden als add-on componenten aangezien er geen accurate uitlijning benodigd is tussen de antenne en de superstraat lagen. Bovendien zijn ADLs breedbandig dankzij hun niet-resonante karakter.

Het laatste gedeelte van dit proefschrift behandelt een nieuw concept van breedband, breedgestuurd, fasegestuurde antennestelsel ontwerp, gebaseerd op de verbonden stelsels ("connected arrays") van sleuven welke zijn geladen met ADL superstraten. Het voorgestelde ontwerp heeft twee belangrijke voordelen ten opzichte van bestaande oplossingen. Ten eerste is het ontwerp volledig planair en is het gerealiseerd met een enkel-laags PCB, met als gevolg een vermindering van de kostprijs en complexiteit van het antennestelsel. Ten tweede worden ADLs gebruikt in plaats van echte dïelektrische superstraten om veel hogere efficiëntie te verkrijgen door oppervlaktegolf verliezen te onderdrukken. Voor het ontwerp van het antennestelsel geladen met ADL, inclusief de lijmlagen, wordt een analytische tool gebruikt die is gebaseerd op de spectrale Green's functies. Deze tool maakt het mogelijk om

de prestaties van het antennestelsel te schatten met minimale rekenhulpmiddelen. Ook het ontwerp van een breedband voedings-structuur is voorgesteld, welke geen gebalanceerde-naar-ongebalanceerde (balun) transities vereist die de gekoppelde bandbreedte limiteren.

About the Author

Waqas H. Syed was born on January 24, 1986 in Rawalpindi, Pakistan. He received his B.Sc. degree with distinction in Electrical (Telecommunication) Engineering from COMSATS Institute of Information Technology (CIIT), Islamabad, Pakistan in September 2007. At the completion of his B.Sc. degree he was awarded the institute and the campus silver medal for securing the second highest cumulative grade point average (CGPA) in the whole batch. He received his M.Sc. degree in Communication Engineering for RWTH Aachen University, Aachen, Germany in December 2010. His M.Sc. thesis and internship were carried out at PHILIPS Research Europe, Eindhoven, Netherlands from April to November 2010 . The project dealt with the analysis and design of non-linear transmission lines in 65-nm CMOS technology for THz power generation, under the supervision of dr. L. Tripodi (he was then with the PHILIPS Research, Eindhoven, he is now with ASML, Veldhoven).

In March 2011 he started working towards the Ph.D. degree in the Tera-Hertz Sensing group, Delft University of Technology, Delft, Netherlands. Here, he worked on the analysis and design of artificial dielectrics and their applicability for the planar antenna designs. This research has been carried out in under the supervision of prof. dr. ir. A. Neto and co-supervised by dr. ir. D. Cavallo. This work resulted in two manufactured prototype demonstrators, 5 journal publications and 18 conference papers.

He was awarded with the *"Special Mention for the Excellent Presentation"* in the *Best Student Paper Contest* at the 9th edition of European Conference on Antennas and Propagation (EUCAP), Lisbon, Portugal (12-17 Apr. 2015). He also received *"Best Poster Prize"* at the Annual Netherlands Antenna Research Framework (NARF) Workshop, Delft, Netherlands (31st May 2013)). He was also selected as one of the ten finalist to compete for the *Best Student Paper Award* at the 7th edition of EUCAP, Gothenburg, Sweden (8-12 Apr. 2013).

During his Ph.D, he has co-supervised two M.Sc. students, H. Thipur Shivamurthy (TU-

Delft) and Wenda Zhu (TU-Delft). He is currently serving as a reviewer for *IEEE Transactions on Antennas and Propagation*, *IEEE Transactions on Terahertz Science and Technology* and *IEEE Antennas and Wireless Propagation Letters*.

Acknowledgements

If I have seen further; it is by standing on the shoulders of giants

Sir Isaac Newton

This thesis work would not have been accomplished without the help, support and guidance of many people.

First and foremost, I would like to thank my supervisor Prof. Andrea Neto for accepting me to work on this thesis. Since the beginning of my thesis he has played an instrumental role and invested a lot of his time in teaching me the technical topics. He is an inspiring mentor and an exceptional teacher, who is always enthusiastic about the work and demands the best a student can do. His attitude and dedication towards the work has taught me that I should always strive for the best and that I shouldn't settle for the mediocre or average. His firm grasp on the extremely complex concepts of electromagnetism (EM) and his ability to apply them to solve complex EM problems will be the guiding principles in my future career. It has been a real pleasure and honor to have him as my PhD advisor and I will be always seeking his advice in the future regarding my career. (*I hope that I have been able to be part of his team of Spartans!*)

The second person who made this thesis work possible is my daily supervisor dr. Daniele Cavallo. He has been a great mentor and a good friend at the same. His deep understanding of antennas, electromagnetics, and extreme control over the programming tools and the commercial EM solvers has always been inspirational to me. I was always taken aback by his ability to draw breath-taking pictures of the complex EM phenomena, and I have tried my level best to master it (*but, I still have to undertake a long journey before reaching his level of perfection*). I would also like to express my gratitude for his patience in reading and reviewing this dissertation. I have learned a lot from him and will always be indebted for the things he has taught me in my professional life.

I would like to thank Prof. Pasqualina M. Sarro for her guidance in the realization of the

antenna prototype presented in Ch. 6 of this PhD thesis. A bundle of thanks and gratitude goes to my fellow colleague Giuseppe Fiorentino, who invested countless number of hours in the clean room and made the fabrication of the on-chip antenna possible. Furthermore, without the interest and the physical presence of dr. Marco Spirito in the measurement lab, it would near to impossible to perform the measurements of the antenna at 0.3 THz. I am really thankful to him for his support and guidance during the whole measurement campaign.

I would like to thank my PhD defense committee members for taking out their valuable time and accepting to be a part of the PhD commission. I am especially grateful to Prof. A. Yarovoy and dr. P.T.M. van Zeijl for their careful review of this dissertation.

I would like to express my gratitude to STW user committee members dr. S. Monni (TNO), dr. P. T. M. van Zeijl (Omniradar), ir. A. de Graauw (NXP), and dr. L. Tripodi (ASML) for periodically attending the user committee meetings over the course of four years and providing useful suggestions to improve the quality of the work. I would also like to thank Dr. Nuria Llombart for her valuable inputs regarding the analysis and design of artificial dielectrics throughout the course of my PhD thesis.

I would also like to thank the two master students, whom I co-supervised. Firstly to M.Sc H. Thippur Shivamurthy, for performing the time consuming simulations of the antenna array in Ch. 7. Secondly to Wenda Zhu, for helping me to simulate the feeding structure for the antenna array.

I would like to thank my office mates O. Yurduseven, B. Blazquez, and A. Garufo (*my Italian teacher*), thank you very much guys for being helpful and supportive all the time. I would like to express my gratitude to Sven van Berkel (*the only Dutch man in our group*) for translating the summary and the propositions of my thesis into Dutch. I would also like to thank my other fellow colleagues at the THz Sensing Group: dr. I. E. Lager, dr. E. Gandini, dr. G. Carluccio, dr. M. Alonso, S. Dabironezare and S. Zhou. I have to say that our group is like an extended family and it has been a real pleasure working and going out with all of you. I would like to express my gratitude to our group secretary X. Tober for her help and support.

I would like to thank my friend Venkat who has been a great friend, since I came to Delft in 2011. I would also like to thank my flat mates Girish and Zubair for their great friendship and cooking tasty meals. I would like to take this occasion to thank all my Pakistani friends in Delft: Shahzad (*like my elder brother*), Laiq, Abrar, Sami, Imran and, Fahim for their friendship and support.

I would like to dedicate this thesis work to my parents for their unconditional love and support. It is quite difficult for me to sum up in words the pain and the efforts that both

of you undertook so that I can study. I remember sending me abroad to study, seven years ago, thousands of kilometers away from home, has been one of the toughest decision in your lives. I will always remain indebted to the guidance of my father (*my hero*) in helping me with every important decision in my professional as well as personal life.

I love you Mom and Dad. I hope I made you proud!

I would like to say bundles of thanks to my brother (Usman) and sister (Omama) for their love and support during the course of my life. I would also like to thank all my extended family members, my uncles (Sarwar and Zafar), my aunts (Asma, Aniqa and Talat) and my cousins (Ifrah, Faiz, Tooba, Aleeza, Eman, Amna) for being there for my parents in my absence, in the hour of joy and sorrow. In the end, I would like to thank my to-be-wife (Qurrat Ul Ain) for loving me and caring for me. *I am very excited and looking forward to spend the rest of my life with you.*